ISSN 2712-8172

MAGAZINE OF CIVIL ENGINEERING

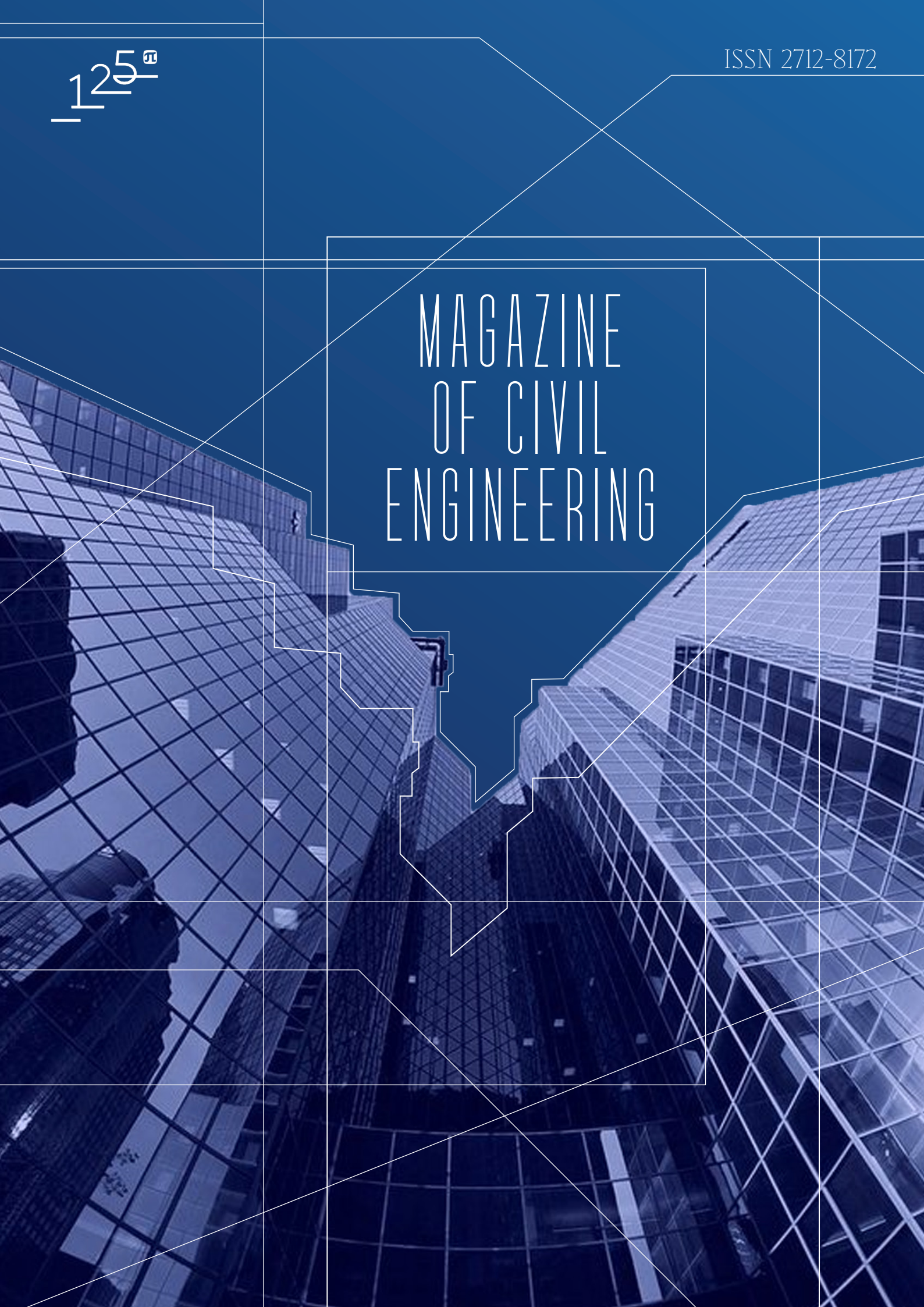

Magazine of Civil Engineering

ISSN 2712-8172

Online peer-reviewed open-access scientific journal in the field of Civil and Construction Engineering

Founder and Publisher: Peter the Great St. Petersburg Polytechnic University

This journal is registered by the Federal Service for Supervision of Communications, Information Technology, and Mass Media (ROSKOMNADZOR) in 2020. Certificate El No. FS77-77906 issued February 19, 2020.

Periodicity: 8 issues per year

Publication in the journal is open and free for all authors and readers.

Indexing: Scopus, Web of Sceince (ESCI, RSCI), DOAJ, Compendex, Google Academia, Index Copernicus, ProQuest, Ulrich's Serials Analysis System, CNKI

Corresponding address: 29 Polytechnicheskaya st., Saint Petersburg, 195251, Russia

Chief science editor: D.S. in Engineering, Galina L. Kozinetc

Deputy chief science editors:
D.S. in Engineering, Sergey V. Korniyenko

Executive editor: Ekaterina A. Linnik

Translator, editor: Irina Ye. Lebedeva

Proofreader: Philipp Chrysanthes S. Bastian

DT publishing specialist:
Anastasiya A. Kononova

Contacts:
E-mail: mce@spbstu.ru
Web: http://www.engstroy.spbstu.ru

Date of issue: 01.07.2024

Contents

Magazine of Civil Engineering

ISSN 2712-8172

journal homepage: http://engstroy.spbstu.ru/

Research article

UDC 624

DOI: 10.34910/MCE.128.1

Behavior of partially connected piled raft foundation under seismic loading

***M. Karkush*[1] ✉, *A.D. Almurshedi*[2], *K.A. AlSaadi*[1], *A.M.S. Al-Salakh*[3]**

[1] *Civil Engineering Department, University of Baghdad, Baghdad, Iraq*
[2] *Surveying Engineering Department, University of Baghdad, Baghdad, Iraq*
[3] *Department of Structures and Water Resources, University of Kufa, Kufa, Iraq*

✉ *mahdi_karkush@yahoo.com*

Keywords: partially connected piled raft, disconnected piled raft, seismic loading, piled-raft, cushion layer

Abstract. A partially connected piled raft foundation is a new modification for the fully connected or disconnected piled raft foundation. The characteristics of the connected piles could transfer loads from the superstructure to the underlying soils. The disconnected piled raft foundation has an effective advantage for reducing the dynamic motion that is transmitted to the high-rise superstructures. However, the dynamic behavior of the partially connected piled raft foundation system under a strong earthquake in medium sand soil has not been thoroughly understood. In this study, the effect of the distribution of piles patterns, number of connected piles (CP), and number of disconnected piles (DP) through a series of seismic experimental model tests have been investigated. These tests were performed with 1, 4, 5, and 9 piles under different static loads. Vertical and horizontal displacements, acceleration, and variation of bending moment of soil and piles are monitored through the experimental tests. The results showed that increasing the number of CP compared with DP contributed to an effective way to reduce the horizontal displacement of the piled raft foundation system. The advantage of DP in resisting seismic loading appears when the number of DP is more than the number of CP. Due to the structural connection of the raft-pile-soil system, the CP was subjected to high values of the seismic acceleration and bending moment. The reduction in the bending moment of DP within the partially connected piles group depended on the number of CP and increasing the thickness of the cushion layer.

Citation: Karkush, M., Almurshedi, A.D., AlSaadi, K.A., Al-Salakh, A.M.S. Behavior of partially connected piled raft foundation under seismic loading. Magazine of Civil Engineering. 2024. 2024. 17(4). Article no. 12801. DOI: 10.34910/MCE.128.1

1. Introduction

Among different types of foundations, piled raft foundation has been of great importance to practical researchers and studies. Heavy building construction on weak soils required the model piled raft foundation technique [1–4]. According to the connection behavior between pile and raft, connected and disconnected piled raft foundations are studied which will be responsible about sharing the load to the underlying layers [5]. Most of the previous works studied the effect of the cushion layer on the behavior of piles under static loads using experimental modeling. The disconnected piled raft is efficient in reducing the axial stress along the pile compared with that related to the connected piled raft [6]. Two cushion mechanisms could be observed through loading, the negative friction for the upper part and positive friction for the lower part of a pile. The stiffness of the disconnected piled raft foundation system depends on the stiffness of the cushion layer [7].

The performance of the piled raft system under seismic loading is of great concern to geotechnical practitioners to avoid probable damage in the piled raft system [3, 4]. Different researchers and studies explained the behavior of piled raft foundation under large and heavy structures subjected to earthquake

loadings. Earthquake usually creates additional loading situations on the piled raft which need special attention [1, 8, 9]. In addition, the piled raft foundation becomes an alternative in cases where soil layers are incapable to carry the applied loads and prevent excessive settlement [10, 11]. Earthquakes or seismic loading make a complex interaction for the pile-raft-soil-foundation components system. Saadatinezhad et al. [12] concluded that different factors could affect the response of the disconnected piled raft foundation such as L/D (slenderness ratio).

Through the centrifuge test was clarified that the disconnected pile located at the edge of the foundation can reduce the effect of the bending moment under seismic loading. At the same time, it was explained that one of the limitations of using disconnected piles is that it cannot provide sufficient tensile force of the raft foundation. On the other side, using a disconnected pile is one of the effective and economical design factors [13]. According to reference [14], it was concluded that using a connected piled raft system under increasing the excitation to 0.15 g and 0.32 g compared to 0.05 g will increase the total settlement of piled raft system by 30 % and 85 %, respectively. Similar to total settlement, differential settlement increases with increasing excitation. One of the disadvantages of using a fully connected piled raft foundation is that higher excitation produces higher irregular forces leading to irregular motions resulting in higher differential settlement.

Rasouli and Fatahi [15] investigated the behavior of disconnected piled raft foundation to protect high-rise buildings under the effect of the normal fault rapture. In this study, there was a comparison between connected and disconnected piled raft foundation systems. The results assessed different parameters such as permanent inter-story drifts, raft displacement, rocking, forces, and bending moments in piles and raft. As expected from this study, the piles near the hanging wall have not avoided the bending effect with 0.5 m differential settlement. Also, it experienced a maximum bending moment of about 7.3 MN.m that passed the maximum design bending moment 3 MN.m. The maximum differential settlement of the raft foundation was 0.292 m that reduced to 0.1 m when the disconnected piled raft foundation had been used.

From the literature data, it can be established that the provision of the partially connected piled raft foundation system reduces the vertical settlement for disconnected piles and increases the vertical settlement and reduces the horizontal settlement for connected piles. It was observed also that the highest value of bending moment for connected one and lowest value for disconnected one at the top part of piles head below the cushion layer. Only a very few studies deal with partially connected piles. Therefore, it is essential to evaluate partially connected piled raft foundation systems under seismic loading with different parameters such as thickness of cushion layer, no. of piles, L/D ratio for connected piles, and different distribution patterns of piles. The covered dynamic response parameters include vertical settlement of the foundation, horizontal displacement of the foundation, acceleration distribution inside the soil media, and a bending moment of piles for different cases.

2. Methods and Materials

2.1. Earthquake Loading System

To simulate the earthquake loading in the laboratory, there are several techniques and methods, one of them being using a shaking table. The shaking table is essential laboratory equipment that simulates the loading that occurs during dynamic excitation as in an earthquake [16]. In this study, the uniaxial sinusoidal motion was adopted by applying a suitable frequency using a shaking table device shown in Fig. 1. The dimension of the shaking plate is 1 × 1 m and 1 ton loading capacity. According to [17], the scale factors are important to select the suitable dimensions of experimental modeling. The motion was executed by using a 3-phase electrical motor connected to a mechanical gearbox to change the rotating direction, and regulate the motor speed and this motor was also connected to an AC-drive regulator. The motor operated to make a slow-motion rotation, then the gearbox operated the motion arm. Many options could be changed such as minimum, maximum, fixed, acceleration, and deceleration frequencies. All these factors affect the motion type and behavior, the range of available frequency is 0–20 Hz. In addition to the AC drive, there were time governor and protection devices shown in Fig. 1 by which the shaking time could be selected and the emergency circumstances could be avoided.

Figure 1. Shaking table and soil box with complete setup.

2.2. Recording Data and Instrumentation

To adjust the exact applied acceleration magnitude a calibration process must be done, this process was executed as follows: for a specific period, the number of back-and-forth cycles was recorded and compared with the results of the software, the result of the software was the acceleration obtained by changing the velocity speed of the motion as shown in Fig. 2. Thus, for a specific value of velocity, it is easy to select the correct number value of the acceleration in the software. The applied value of acceleration was selected and compared with the data from El Centro earthquake history. These data were calibrated using an accelerometer (Acc1) fixed on the base plate of the model after filling the steel model box with soil. Fig. 3 illustrates the calibration results of the applied speed of the electrical motor and the resulting acceleration. Different sensors were used in this study to get the actual behavior of a partially connected piled raft foundation system. These sensors were: 5 accelerometers, 3 strain gauges along each pile length to calculate bending moments values, and 3 LVDTs to calculate the horizontal, vertical, and base displacements.

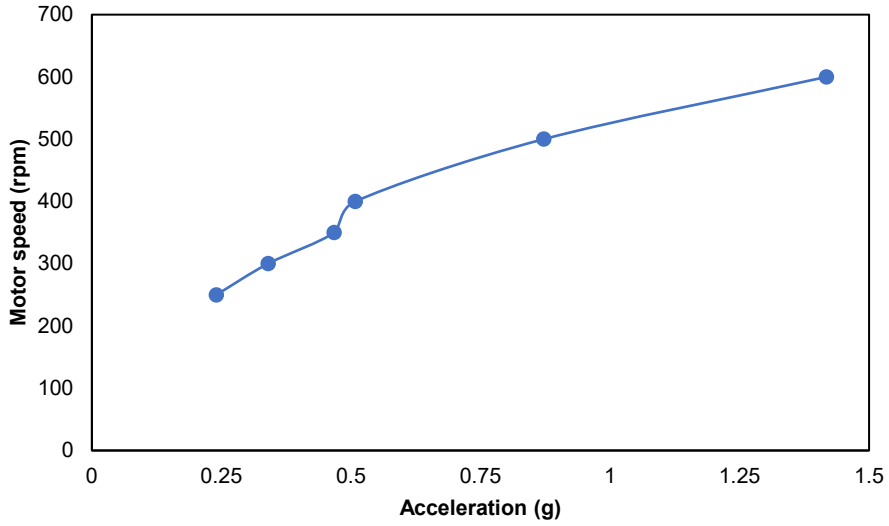

Figure 2. The calibration of motor speed (rpm) and acceleration.

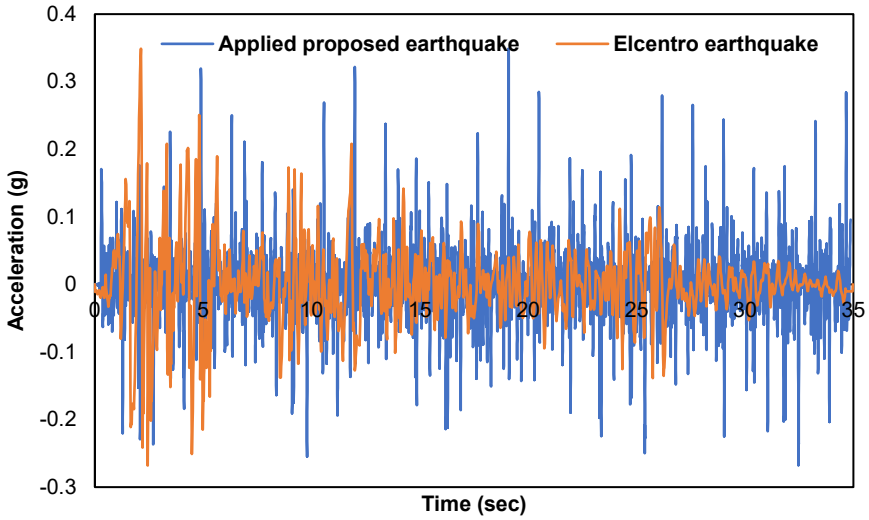

Figure 3. Time history of the applied acceleration on the base of the model compared with El Centro earthquake.

2.3. Materials

2.3.1. Bed Soil

The bed soil used in the model was dry sand obtained from Al-Najaf city (Iraq). A summary of the test results with standard specifications are presented in Table 1. According to the grain size distribution results, it can be seen that the sand consists of fine grains. This sand is categorized as poorly graded sand (SP) according to the Unified Soil Classification System (USCS), while the cushion layer soil is classified as well-graded sand soil (SW).

Table 1. Laboratory tests for model and cushion sand soil.

Property	Standard	Value (Cushion soil)	Value (Model soil)
Specific gravity	ASTM D854	2.68	2.64
Maximum dry unit weight (kN/m^3)	ASTM D4253	18.65	17.20
Minimum dry unit weight (kN/m^3)	ASTM D4254	14.45	13.89
Experimental dry unit weight (kN/m^3) (at Dr =50%)	------	16.28	15.36
D_{10} (mm)		0.13	0.5
D_{30} (mm)		0.44	0.65
D_{60} (mm)	ASTM D422	1.18	0.76
Coefficient of uniformity (Cu)		9.07	1.52
Coefficient of curvature (Cc)		1.26	1.11
Angle of internal friction (Ø) (Direct shear test)	ASTM D3080	35.4	29

2.3.2. Pile and Raft Models

The pile model used in the current study was made of aluminum alloy and had a hollow square cross-section of 14 mm outside dimension and a wall thickness of 1.5 mm. The embedded pile length was 350 mm used to model the disconnected pile and 370 mm to model the connected pile. For connected piled raft model tests a bolt of diameter 10 mm and 30 mm long was provided at the top head of each pile to fix the piles with raft and fastened with a nut. While the piles end was closed with a square aluminum piece of side dimension 14 mm and 2 mm thickness. A square steel plate, of side dimensions (210 × 210) mm and a thickness of 10 mm was used as a raft. The values of the poison's ratio and modulus of elasticity for soil, raft, and piles are displayed in Table 2.

Table** 2**. Mechanical properties for soil, pile, and raft foundation.

Property Name	Soil	Pile	Raft
Poisson's ratio, ν	0.31	0.28	0.31
Modulus of elasticity, E (MPa)	12.3	4.8×10^4	2.3×10^5

2.4. Tests Preparation and Procedure

To reconstitute or prepare the sand samples for experimental model tests, several ways were used such as raining, vibration, or tamping. In general, to provide relatively homogenous sand samples and to get the required relative density, the raining procedure is considered the best among these ways. Many trials were performed to draw a relationship between the falling height and the corresponding dry density as shown in Fig. 4. From the curve, it is clear that the falling height should be about 20 cm to get the required dry density of 16.28 kN/m^3 for bedding soil in the physical model and 10 cm to get the density of 15.36 kN/m^3 for the soil of cushion layer. Fig. 5 shows the raining of bedding soil used in this study. The raining technique used in this work consisted of a steel hopper of height 45 cm with a valve at the bottom to control sand raining manually. A sieve of 4.75 mm opening size is attached to the bottom of the funnel and connected to the hopper by a plastic joint to distribute the sand uniformly as shown in Fig. 5. The inside walls of the container were divided into 6 intervals, each of 15 cm thickness, to ensure that the desired dry density was obtained properly. To produce a homogenous sample overall in the container, the required quantity of sand for each layer was weighted such that the designed dry density could be obtained. For conditions of connected and disconnected piled raft model tests, a template provided by the steel mesh method was used. Piles were tied with the steel mesh placed previously inside the container by the plastic tie as shown in Fig. 5. The steel mesh was lifted up when the level of raining sand reached it.

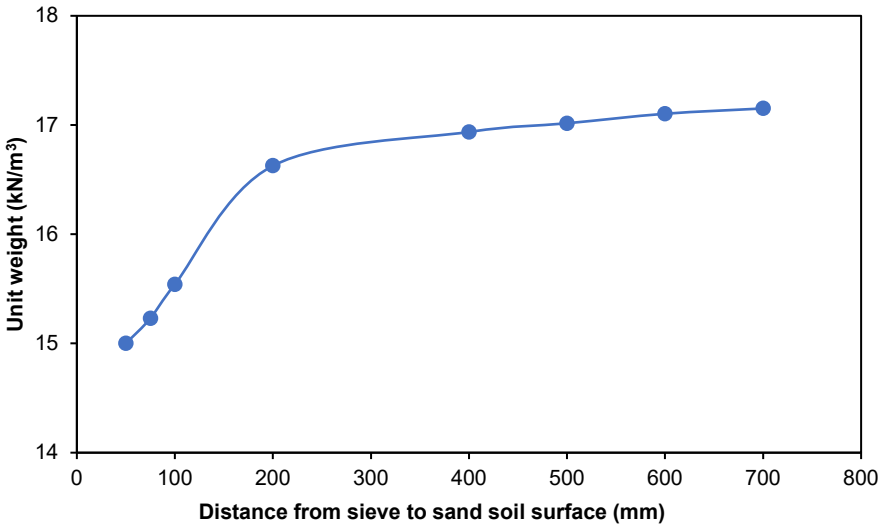

Figure 4. The relationship between the height of falling and the dry density of sand.

Figure 5. Raining tool and positions of the piles within steel mesh.

Several conditions of piles with raft were studied in this work to show the effects of partially connected piles on the behavior of building foundation under seismic loading. The proposed technique of partially connected piles mixes the advantages of both connected piled raft systems and disconnected piled raft systems. The studied patterns are shown in Fig. 6. The notations used in Fig. 6 are defined in Table 3.

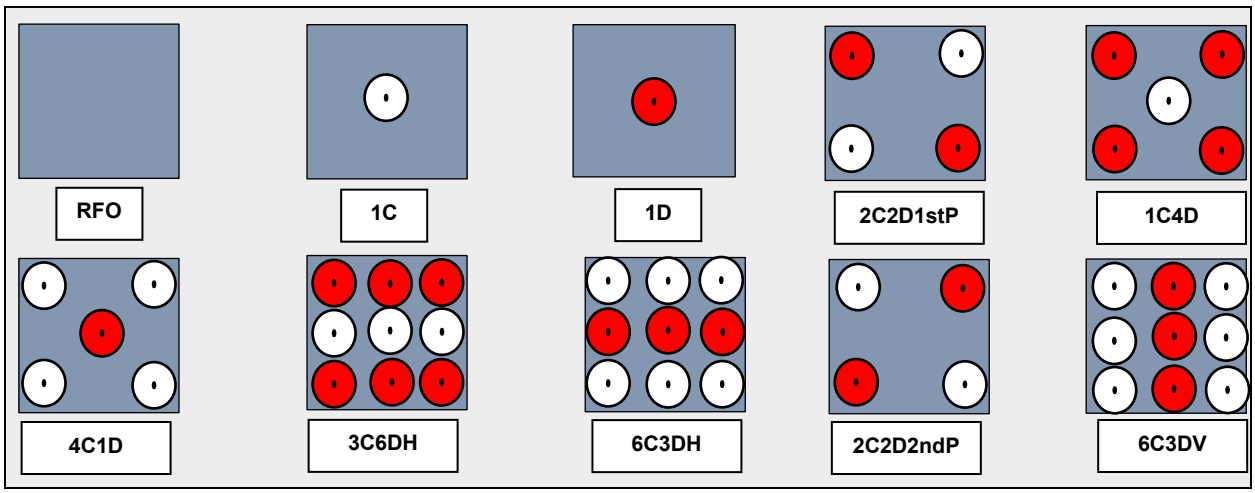

Figure 6. Patterns of piles and raft studied in this work.

The total settlement (horizontal and vertical) of the raft resulting from earthquake excitation was measured using LVDTs connected to the raft model supported on the shaking table. This variation was studied for single and group piles conditions under different static loads. Table 3 shows the details and notifications of conducted experimental tests. The loading was applied on the piles in two stages, the first stage referred to the vertical static axial load on the raft-pile surface with different values depending on the calculated ultimate capacity of the foundation as a guide. During the second stage the horizontal seismic load was applied with constant static loads.

Table 3. Details and notations of the conducted experimental tests.

Test No.	Symbol	Details		No. of dis-connected piles (D)	No. of connected piles (C)	Max vertical displacement failure ratio (δ_{rf})	Static load (kg)
1	RFO	Raft foundation only		----------	----------	1.06D	21.69
2	1C	37cmV*or H**	L/D1=23.41	----------	1	1.04D	2.41
3		39cmV or H	L/D2=24.68			0.87D	
4		41cmV or H	L/D3=25.94			0.81D	
5	1D	C2cmV or H	Cushion 2cm	1	----------	0.94D	2.41
6		C6cmV or H	Cushion 6cm			0.945D	
7	2C2D	1stP***V or H	Cushion 2cm	2	2	0.3D	9.64
8			Cushion 6cm			0.7D	
9		2ndP****V or H	Cushion 2cm			0.15D	
10			Cushion 6cm			0.67D	
11	1C4D	C2cmV or H	Cushion 2cm	4	1	0.52D	12.05
12		C6cmV or H	Cushion 6cm			0.31D	
13	4C1D	C2cmV or H	Cushion 2cm	1	4	0.33D	12.05
14		C6cmV or H	Cushion 6cm			0.41D	
15	3C6DH	C2cmV or H	Cushion 2cm	6	3	0.47D	21.69
16		C6cmV or H	Cushion 6cm			0.38D	
17	6C3DV	C2cmV or H	Cushion 2cm	3	6	0.35D	21.69
18		C6cmV or H	Cushion 6cm			0.30D	
19	6C3DH	C2cmV or H	Cushion 2cm	3	6	0.59D	21.69
20		C6cmV or H	Cushion 6cm	3	6	0.79D	

V*– Vertical displacement, H*– Horizontal displacement, V – Vertical distribution of piles, H – Horizontal distribution of piles, 1stP***–First pattern, 2ndP****–second pattern.

3. Results and Discussion

Fig. 7–12 show the variation of raft settlement with time for a different number of piles (1, 4, 5, and 9) in the piled raft system. Fig. 7 shows that the maximum vertical displacement of the raft foundation without piles is 16.76 mm under 21.69 kg as static building load. Increasing in length to diameter ratio of piles from 23.41 to 24.68 and 25.94 mm decreases the displacement amplitude of the piled-raft system by 19.83 % and 22.59 %, respectively. This reduction is related to the effect of the shaft and lateral resistance of piles. Using of disconnected piled raft produced good stability and resistance for vertical displacement till 15–20 sec from the start of the effect of earthquake excitation as shown in Fig. 8. Using one disconnected pile instead of one connected pile and increasing the thickness of the cushion layer from 2 to 6 cm had a small effect in reducing the vertical displacement. Fig. 9 shows the benefit of using 2C2D1stP instead of

2C2D2ndP by dropping the vertical displacement with 2 cm cushion layer from 4.85 to 2.47 mm. For 6 cm cushion thickness, the displacement was dropped from 11.13 to 10.57 mm. Generally, using of 6 cm cushion thickness is useless to reduce the displacement. 1C4D1stP with 6 cm cushion layer reduced the vertical settlement compared with using 1C4D1stP with 2 cm cushion layer from 8.29 to 4.84 mm. In the same time, the results of 4C1D2ndP for 2 cm and 6 cm cushion layers were equivalent. From these results, it could be concluded that increasing the number of connected piles within a well-compacted cushion layer increases the vertical displacement.

The variation of vertical displacement with time for the pattern of five piles is shown in Figю 10, the vertical displacement was reduced from 8.29 to 5.33 mm when the patterns were changed from 1C4D to 4C1D with 2 cm cushion layer respectively. Increasing the thickness of the cushion layer to 6 cm was not efficient in reducing the vertical displacement of the foundation system. It can confirm for the 9 piles condition that increasing the numbers of connected piles compared with disconnected piles could increase the vertical displacement. This appeared clearly by reducing the displacement from 9.38 to 7.52 mm with changing the pattern from 6C3DH to 3C6DH with 2 cm cushion layer, respectively. Increasing the thickness of the cushion layer to 6 cm slightly affected the vertical displacement of 3C6DV and 6C3DV due to the seizing of the connected piles to the cushion material on the top of the disconnected piles. According to Fig. 11, by increasing the thickness of the cushion layer from 2 to 6 cm, the maximum vertical displacement was reduced from 5.60 to 4.83 mm for the pattern 6C3DV. Also, the maximum vertical displacement of 3C6DV decreased from 7.52 to 6.04 mm by increasing the thickness of the cushion layer from 2 to 6 cm. This reduction in displacement could be attributed to the role of the 6 disconnected piles in the same direction of earthquake vibration. Fig. 12 illustrates the variation of the maximum displacement for all patterns as discussed in Figs. 7–11. Also, in Table 3, the maximum vertical displacement failure ratio (δ_{rf}) compared with the equivalent diameter of the pile (D) is displayed for each test.

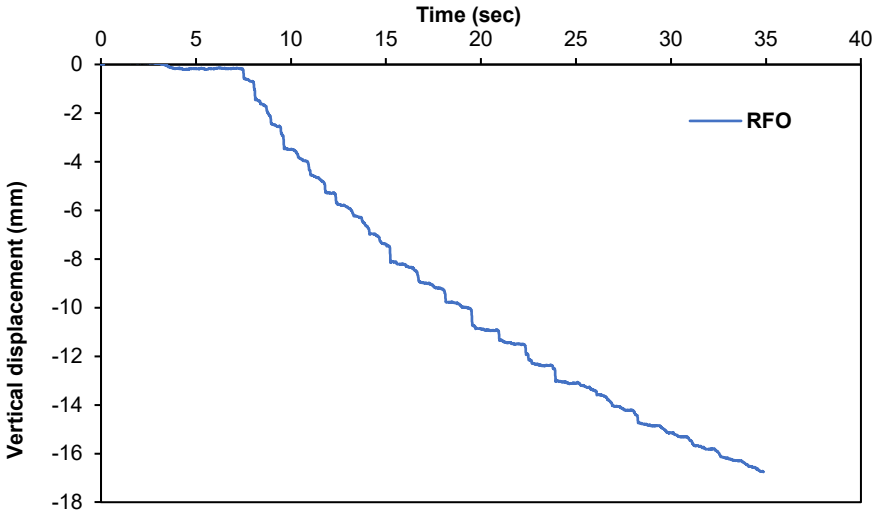

Figure 7. Variation of vertical displacement time for raft foundation only (RFO).

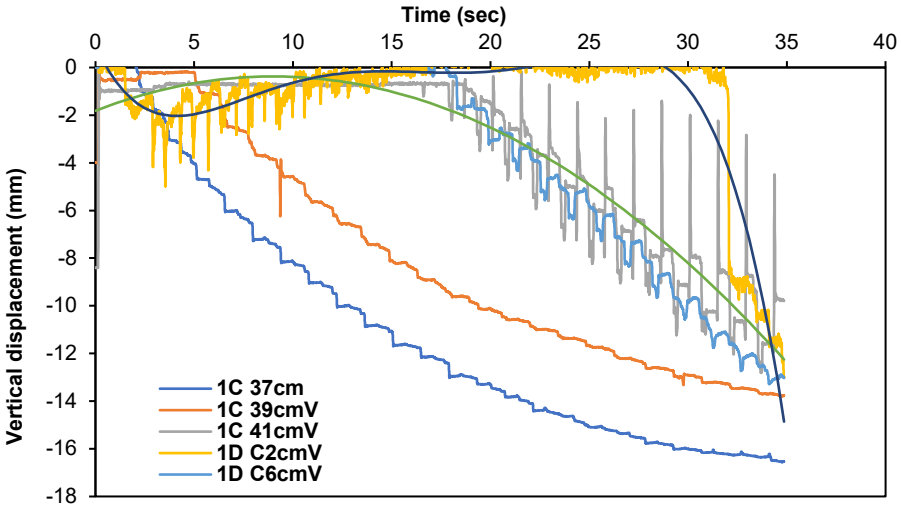

Figure 8. Variation of vertical displacement time for the system of one connected and one disconnected piled-raft.

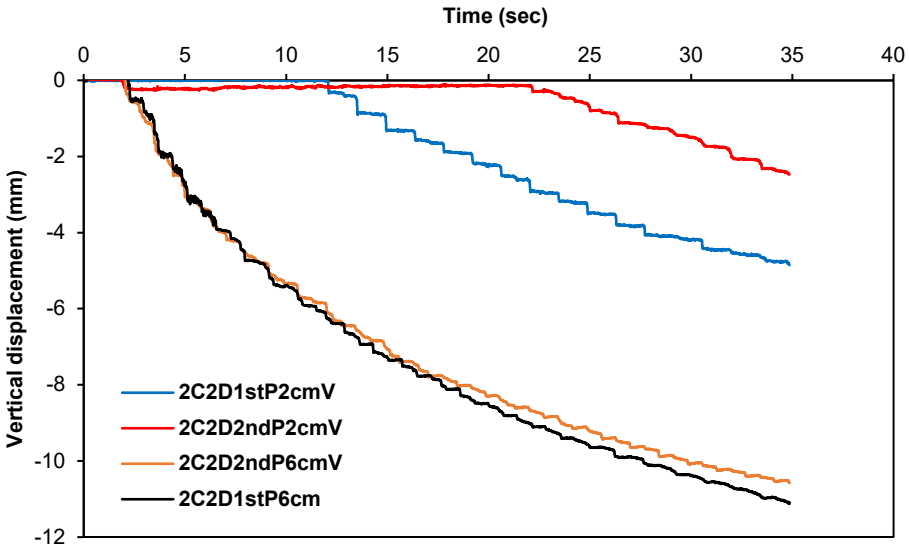

Figure 9. Variation of vertical displacement time for 1st and 2nd patterns of 2 connected and 2 disconnected piled-raft systems.

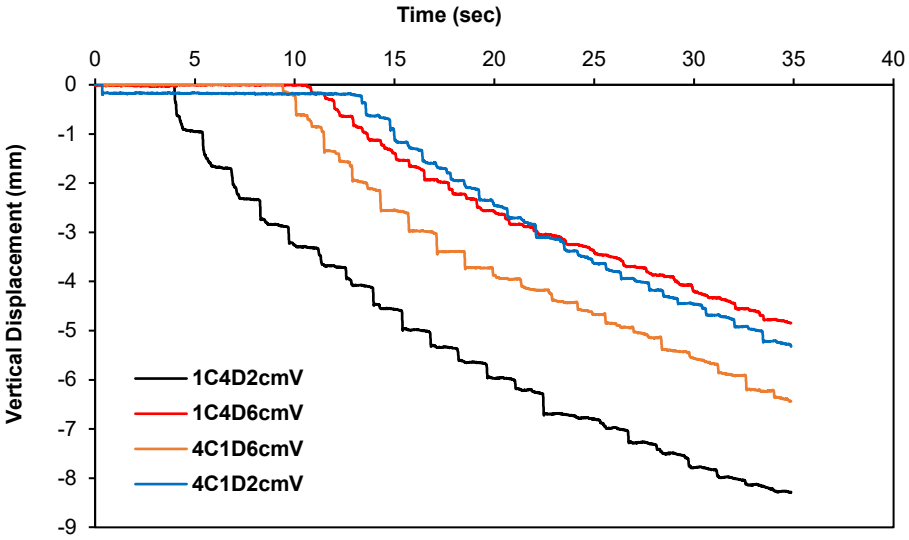

Figure 10. Variation of vertical displacement time for 1 disconnected, 4 connected, and 1 connected, 4 disconnected piled-raft systems.

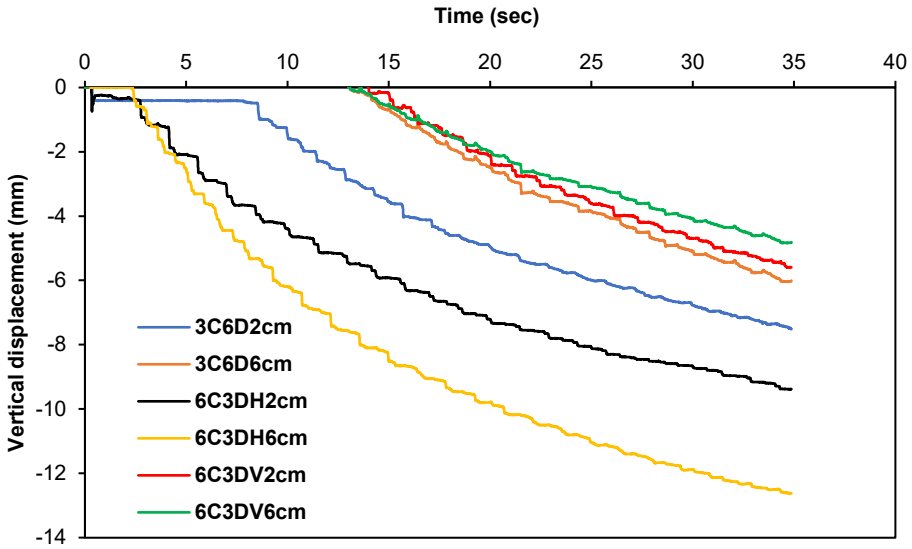

Figure 11. Variation of vertical displacement time for 3 disconnected, 6 connected, and 3 connected, 6 disconnected piled-raft systems.

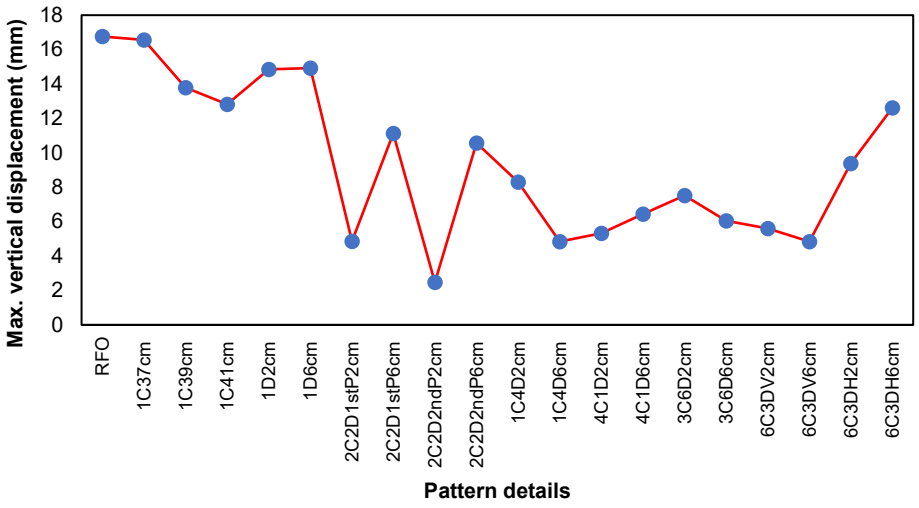

Figure 12. Variation of maximum vertical displacement for tested models.

Fig. 13–15 show the variation of the horizontal displacements measured at the raft foundation with time for several tested models. Increasing the number of connected piles compared with the number of disconnected piles increased the overall stiffness of the piled raft foundation system [12]. The lowest negative and positive horizontal displacements are 22.813 and 38.598 mm measured for the soil model 6C3DV with cushions 2 cm and 6 cm thickness, respectively. It can also be seen that the highest value of the horizontal displacement was 78.372 mm for 3C6DH with a cushion of 6 cm thickness. Generally, the small number of connected piles causes less stiffness as mentioned above. The summary of the lowest and highest horizontal displacements for all patterns of tested models is displayed in Fig. 16.

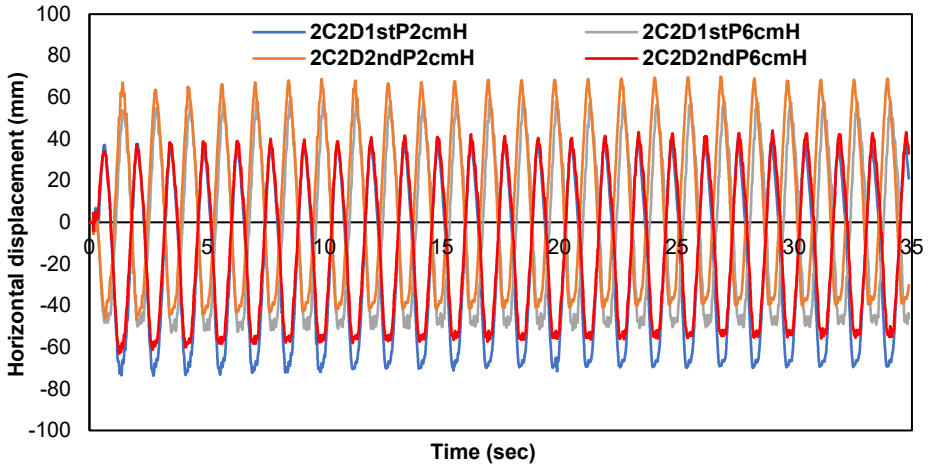

Figure 13. Variation of horizontal displacement with a time of 1st and 2nd patterns of 2 connected and 2 disconnected piled-raft systems.

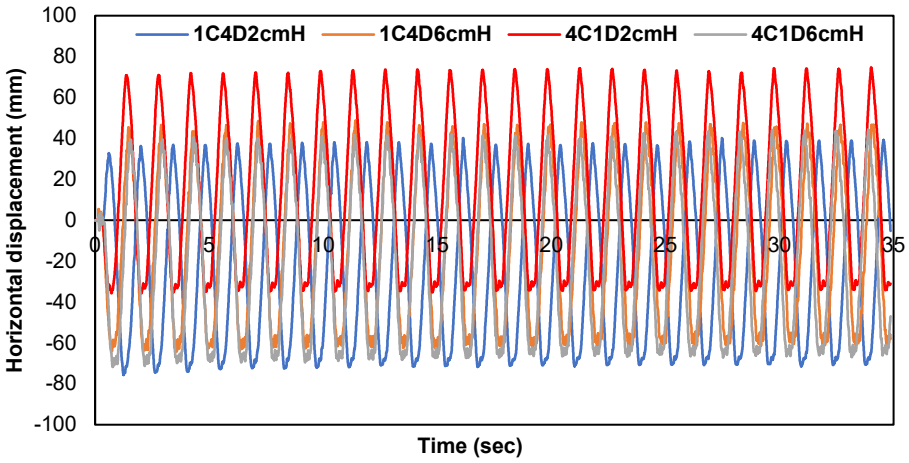

Figure 14. Variation of horizontal displacement with a time of 1 disconnected, 4 connected, and 1 connected, 4 disconnected piled-raft systems.

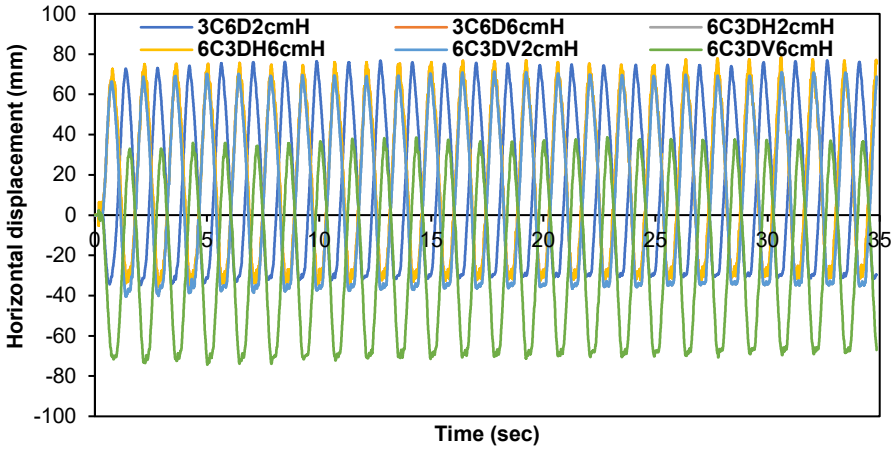

Figure 15. Variation of horizontal displacement with a time of 3 disconnected, 6 connected, and 3 connected, 6 disconnected piled-raft systems.

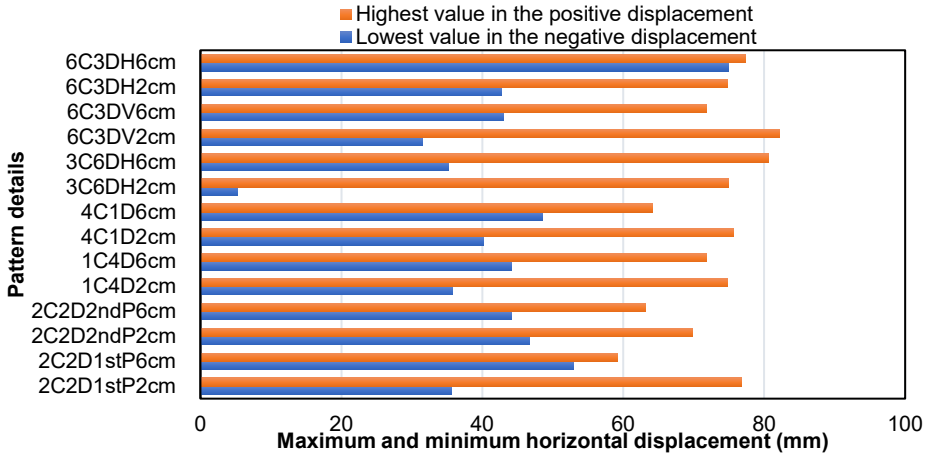

Figure 16. Maximum and minimum horizontal displacements for all patterns of tested models.

The bending moment caused in the piles depends on the pile's connection with the raft foundation, cushion thickness, and locations of the piles within the raft foundation. The profiles of bending moment along the pile length due to earthquake loading for one connected (CP) and one disconnected pile (DP) are clarified in Fig. 17 and 18. It is observed with a strong earthquake (0.35 g), the maximum bending moment occurred at the middle and top of the connected piles. In this study, the maximum bending moment increased when the length of the CP increased. The maximum bending moments were – 425, – 460, and – 486.68 N.mm for pile lengths of 37, 39, and 41 cm, respectively. The maximum bending moment was observed in the top part of the connected pile due to fixed-free ends, on the contrary, when the cushion thickness increased from 2 to 6 cm, the maximum bending moment had changed from + 335.76 N.mm to + 184.54 N.mm. All the maximum bending moments occurred at the top-middle part of the DP due to free-free ends at the top-tip ends respectively. For the pattern 2C2D, the highest reduction in the maximum bending moment was achieved when the pattern 2C2D2ndPC2cm had been used and the lowest reduction was achieved when the pattern 2C2D2ndPC6cm had been used as indicated in Fig. 18. This is more prominent for DP with a higher thickness of the cushion layer, where the stiffness of DP decreases the overall stiffness of the foundation-pile system.

For two patterns 1C4D and 4C1D, in Fig. 19, the bending moment of the CP (center) in the pattern 1C4DC6cm was less than the bending moment of the CP (center) in the pattern 1C4DC2cm. Also, the bending moment of the DP (corner) in the pattern 1C4DC2cm proved to be more bending compared with the DP (corner) in the pattern 1C4DC6cm. With increasing the number of the connected piles, it can be observed that the bending moment increased from + 403.63 N.mm to – 558.35 N.mm for the CP (corner) and it decreased from +105.69 N.mm to – 83.106 N.mm for the DP (center). This observation can be pronounced as a "shadowing phenomenon". This phenomenon is used to contract the effect of the interaction of the inner piles compare with the outer piles of the pile group under static or dynamic loads. As an important factor in the design of a partially connected piled raft foundation, the location and number of the connected pile's CP can be considered for the patterns 3C6DH, 6C3DH, and 3C6DH. As displayed in Fig. 20, in the pattern 3C6DH, the number of CP is less than the number of DP, and the CP (center) shows more bending moment than the CP (edge). On the contrary, the DP (edge) shows more bending moments than the DP (center). Here, the effect of shadow phenomena has more effect on disconnected

piles compared with connected piles depending on the number of piles. For the pattern 6C3DH, the number of CP is more than the number of DP, therefore increasing the number of connected piles will increase the stiffness of the system. In this pattern, the bending moment of the CP (edge) is more than the bending moment of the CP (corner). In the patterns 6C3DHC2cm and 6C3DHC6cm, the DP (center) sustained a small bending moment due to the shadow effect of the surrounding connected piles. For the last patterns 6C3DVC2cm and 6C3DVC6cm, the CP (edge) and CP (corner) show the highest values of the maximum bending moment. As expected, the DP (center) appeared the least values of the bending moment for the same reason as the pattern 6C3DH. It is preferable to mention here, for the DP, during a strong earthquake, must be compared between the destructive and designed bending moment. It is necessary to prepare suitable reinforcement according to the arrangement of the DP in the group.

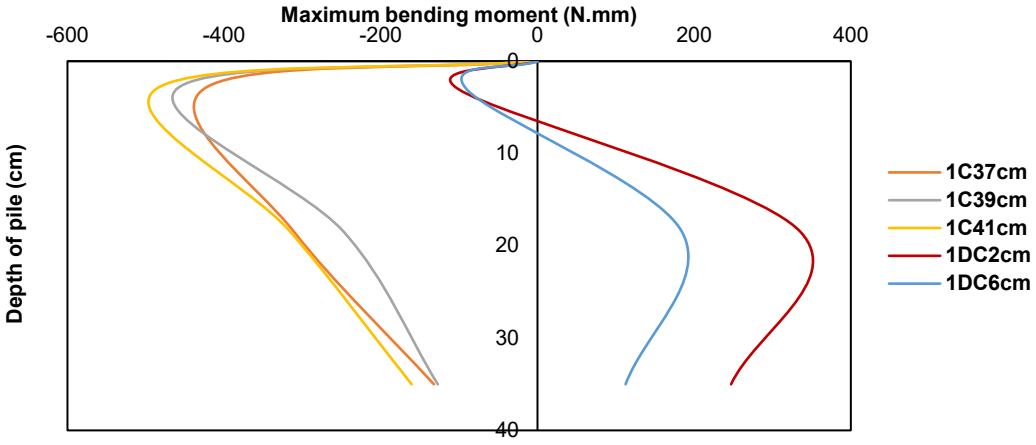

Figure 17. Variation of bending moment with the depth of pile for the single pile patterns (connected and disconnected).

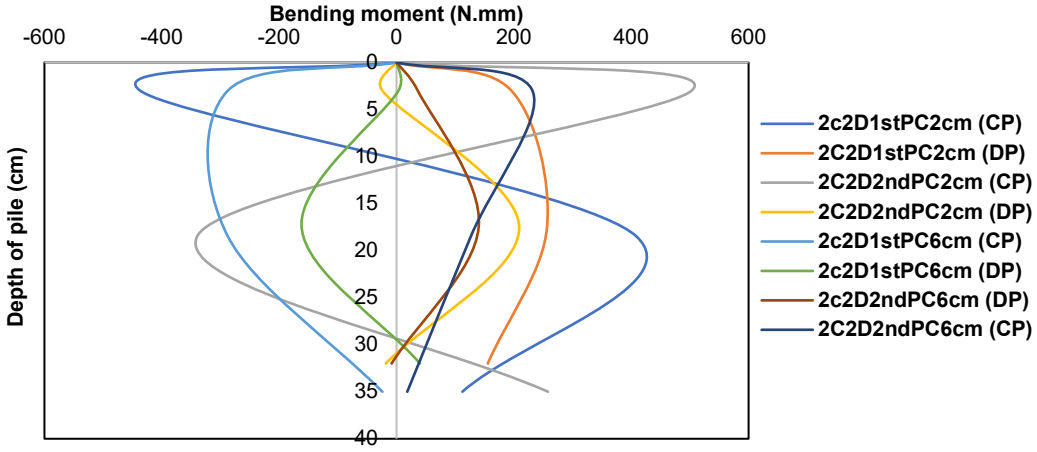

Figure 18. Variation of bending moment with the depth of pile for 2C2D1stP and 2C2D2ndP patterns (connected and disconnected).

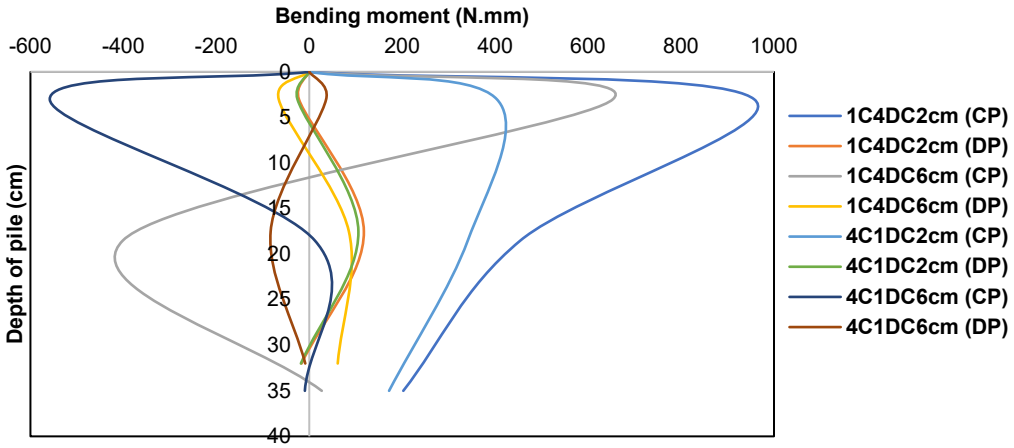

Figure 19. Variation of maximum bending moment with the depth of pile for 4C1D and 1C4D patterns (connected and disconnected) piles.

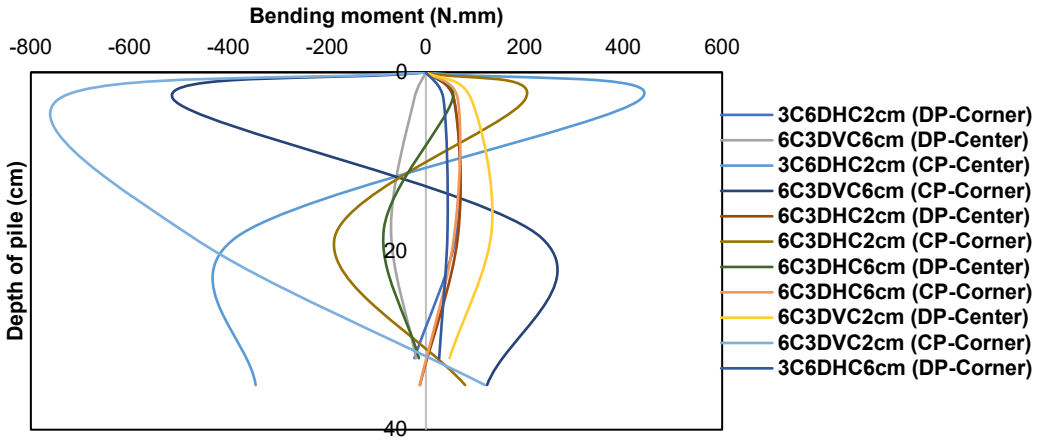

Figure 20. Variation of maximum bending moment with the depth of pile for 3C6DH, 6C3DH, and 6C3DV patterns (connected and disconnected) with RFO.

The acceleration induced by earthquake input motions on the base of the shaking table (Acc1) and within soil layer strata were measured using three digital accelerometers: Acc4 at a depth of 20 cm, Acc5 at a depth of 30 cm, one accelerometer at a cushion layer (Acc3). Also, additional accelerometer was placed on the top of the foundation surface (Acc2). The experimental results of the acceleration variation along the pile depth are presented in Fig. 21–24. For the single pile condition as shown in Fig. 21, the applied acceleration on the base of the shaking model is ranged from 0.31 to 0.38 g. For the CP, the model 1C39cm is recognized as the lowest value of acceleration 0.34 g on the top surface of the foundation.

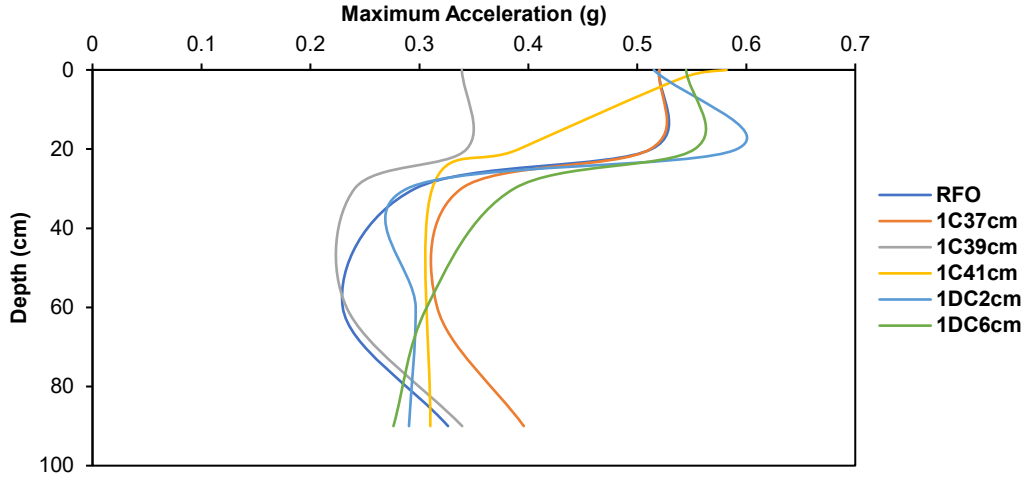

Figure 21. Variation of acceleration with the depth of pile for single pile patterns (connected and disconnected) compares with RFO.

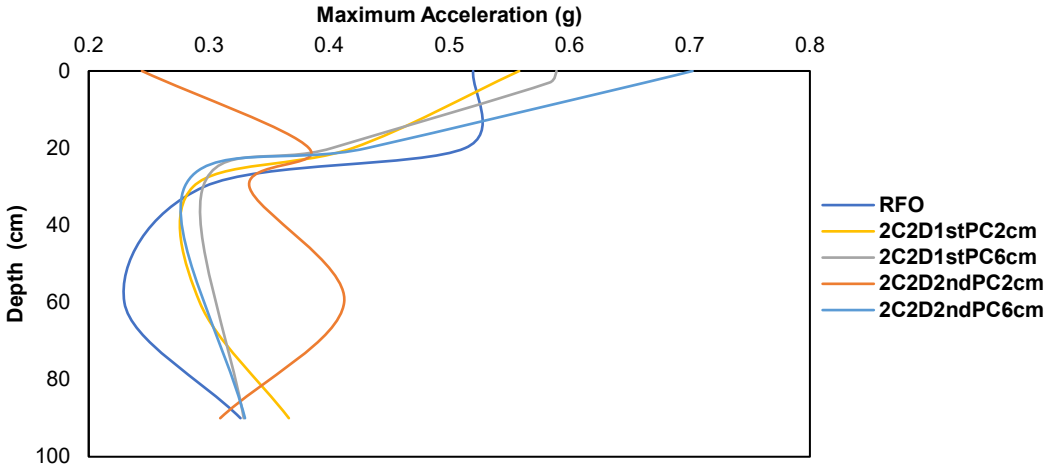

Figure 22. Variation of acceleration with the depth of pile for 2C2D1stP and 2C2D2ndP patterns (connected and disconnected) piles compared with RFO.

The DP 1DC6cm is recognized as the highest value of acceleration 0.544 g. Increasing the thickness of the cushion increased the stiffness of the system, which caused an increase in the value of the acceleration through the cushion layer. For DP conditions, the seismic response of the DP raft foundation system decreased the acceleration as the thickness of the cushion layer increases. This is due to the de-amplification of the raft motion to the free-field ground response. Here, two behaviors of the raft foundation (sliding and kinematic behavior) were observed [18–25]. As shown in Fig. 21 and 22, the seismic acceleration response below the soil depth of 30 cm is less than the acceleration at depth of 20 cm below the soil surface due to the effect of soil pressure. The pattern 2C2D2ndPC6cm showed the highest acceleration on the top of the foundation. At the same time, the pattern 2C2D1sPC6cm with the same cushion thickness had the same acceleration 0.589 g through the cushion and top surface of the foundation.

For the five piles patterns, it is observed from Fig. 23, the reduction in the seismic response (acceleration effect) of the raft (Acc3) for the pattern 1C4D with a cushion thickness of 2 cm and less reduction with cushion thickness of 6 cm. During a strong earthquake (peak ground acceleration of more than 0.35 g), the main reason to reduce the acceleration of the raft foundation is due to the kinematic interaction than due to the sliding behavior of the raft foundation. The patterns 1C4D and 4C1D with a cushion thickness of 6 cm showed less variation between the acceleration of the cushion layer and raft foundation surface. For the nine pile patterns, as shown in Fig. 24, the results were in reasonable agreement. It is confirmed that, when the number of connected piles was more than the number of disconnected piles in the system, there was less variation between the acceleration recorded in the cushion and raft foundation surface. This variation also depended on the cushion thickness. The higher thickness of the cushion layer showed more reduction as noted with the patterns 6C3DH and 6C3DV. The pattern 3C6DHC2cm displayed the lowest value of acceleration in the cushion layer. The pattern 6C3DVC2cm displayed the lowest value of acceleration on the surface of the raft foundation. This is due to a straight relationship between the thickness of the cushion layer and the stiffness that relates to the number of connected piles.

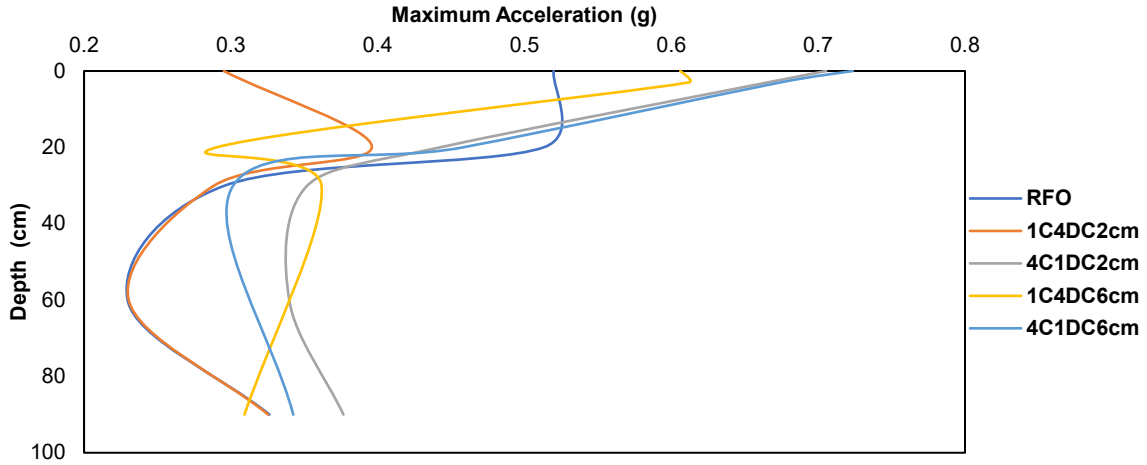

Figure 23. Variation of acceleration with the depth of pile for 4C1D and 1C4D patterns (connected and disconnected) piles with RFO.

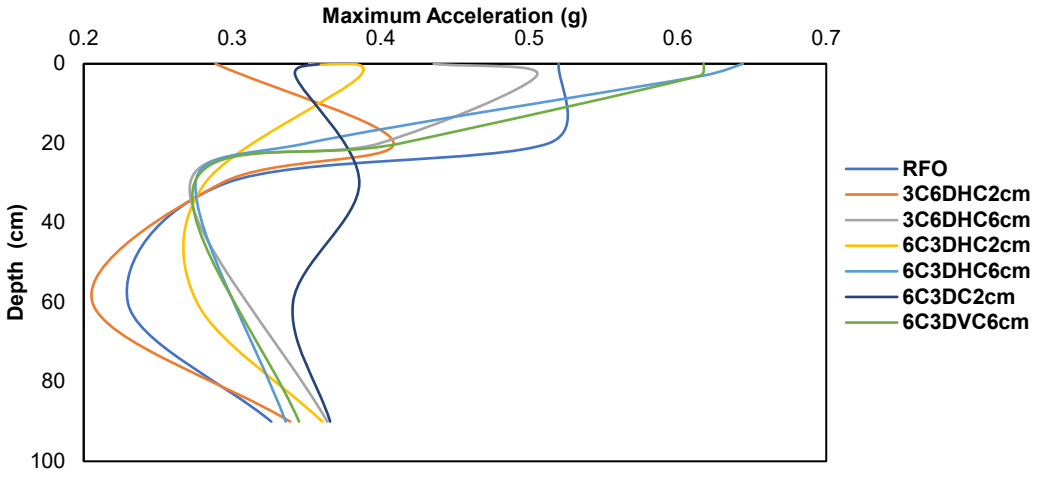

Figure 24. Variation of acceleration with the depth of pile for 3C6DH, 6C3DH, and 6C3DV patterns (connected and disconnected) piles.

4. Conclusions

In this study, the seismic response of the partially connected single and a group of piles under different static loads was evaluated using shaking table centrifuge tests. An experimental model was designed to depend on a virtual prototype dimension. Single and groups of 1, 4, 5, and 9 piles under different patterns for connected and disconnected piles were made from aluminum material. Two thicknesses of cushion layer were used in this study. Earthquake model tests were conducted by calibration depending on data of peak ground acceleration (0.35 g) of El Centro earthquake. Based on the results of the horizontal and vertical displacements, and acceleration of the piled raft foundation system with the seismic bending moment analyses, the following findings and observations were summarized:

- The DP as a single pile or group of piles can appear with less seismic acceleration and bending moment during strong earthquakes. Due to the structural connection of the foundation-pile-soil system, the CP appeared high values of the seismic acceleration and bending moment.
- The connection between the pile's head and the raft foundation was controlling the values of the bending moment. The CP appeared a larger bending moment at the top of the pile while the DP always appeared the maximum bending moment at the mid part of the pile length within partially connected piles. This is depending on the structural connection for each pile, whether it is fixed-free or free-free ends. For single DP conditions, increasing the cushion thickness reduced the variation of the bending moment. For single CP conditions, increasing the length of the pile increased the variation of the bending moment. The reduction in the bending moment of the DP within the partially connected piles group depended on the number of CP within partially connected piles group when the thickness of the cushion layer was increased. The CP in the center and corner had larger bending moments for the patterns 1C4D and 4C1D, respectively. For the pattern 3C6DH, the CP in the center had a larger bending moment than the CP in the edge. On the contrary for the same pattern, the DP in the edge had a larger bending moment than the DP in the corner. The DP in the center and edge and the CP in the corner and edge of the pattern 6C3DH showed less difference in the peak bending moment. Also, The CP in the edge and corner presented little difference from the pattern 6C3DV.
- Using a raft foundation only presented a high value of vertical displacement. Increasing the length of a single connected pile decreased the vertical displacement. When the number of connected piles is equal to disconnected piles, increasing the cushion thickness is useless. The advantages of DP for seismic design are concluded in foundation behavior when the number of disconnected piles is more than the number of connected piles.
- The pattern 2C2D2ndP showed less variation in the horizontal movement. For the other patterns, increasing the number of connected piles compared with disconnected piles contributed as an effective way to reduce the horizontal variation of the piled raft foundation system.

References

1. Maltseva, T., Nabokov, A., Chernykh, A. Reinforced sandy piles for low-rise buildings. Procedia Engineering. 2015. 117. Pp. 239–245. DOI: 10.1016/j.proeng.2015.08.156
2. Mackevicius, R. Possibility for stabilization of grounds and foundations of two valuable ancient cathedrals on weak soils in Baltic Sea region with grouting. Procedia Engineering. 2013. 57. Pp. 730–738. DOI: 10.1016/j.proeng.2013.04.092
3. Karkush, M.O., Aljorany, A.N. Numerical evaluation of foundation of digester tank of sewage treatment plant. Civil Engineering Journal. 2019. 5(5). Pp. 996–1006. DOI: 10.28991/cej-2019-03091306
4. Karkush, M.O., Aljorany, A.N. Analytical and numerical analysis of piled-raft foundation of storage tank. Construction in Geotechnical Engineering. 2020. Pp. 373–384.
5. Ghanbar Dezfouli, M., Dehghani, M., Asakereh, A., Kalantari, B. Behavior of geogrid reinforced and unreinforced non-connected pile raft foundation. International Journal of Civil Engineering. 2019. 17(6). Pp. 709–722. DOI: 10.1007/s40999-018-0362-4
6. Alhassani, A.M.J., Aljorany, A.N. Parametric study on unconnected piled raft foundation using numerical Modelling. Journal of Engineering. 2020. 26 (5). Pp. 156–71. DOI: 10.31026/j.eng.2020.05.11
7. Fioravante, V., Giretti, D. Contact versus noncontact piled raft foundations. Canadian Geotechnical Journal. 2010. 47(11). Pp. 1271–1287. DOI: 10.1139/T10-021
8. Chaudhary, M.T.A., Abé, M., Fujino, Y. Identification of soil-structure interaction effect in base-isolated bridges from earthquake records. Soil Dynamics and Earthquake Engineering. 2001. 21 (8). Pp. 713–25. DOI: 10.1016/S0267-7261(01)00042-2
9. Jebur, M.M., Ahmed, M.D., Karkush, M.O. Numerical analysis of under-reamed pile subjected to dynamic loading in sandy soil. IOP Conference Series: Materials Science and Engineering. 2020. 671 (1). 012084. DOI: 10.1088/1757-899X/671/1/012084
10. Chaudhary, M.T.A. FEM modelling of a large piled raft for settlement control in weak rock. Engineering Structures. 2007. 29(11). Pp. 2901–2907. DOI: 10.1016/j.engstruct.2007.02.001

11. Al-Saidi, A. Correction Factor for Methods of Installation of Piles Group in Sandy Iraqi Soils. Journal of Engineering. 2016. 22(9). Pp. 172–181. DOI: 10.31026/j.eng.2016.09.11
12. Saadatinezhad, M., Lakirouhani, A., Asli, S.J. Seismic response of non-connected piled raft foundations. International Journal of Geotechnical Engineering. 2021. 15(1). Pp. 66–80. DOI: 10.1080/19386362.2019.1565392
13. Ko, K.W., Park, H.J., Ha, J.G., Jin, S., Song, Y.H., Song, M.J., Kim, D.S. Evaluation of dynamic bending moment of disconnected piled raft via centrifuge tests. Canadian Geotechnical Journal. 2019. 56(12). Pp. 1917–1928. DOI: 10.1139/cgj-2018-0248
14. Karkush, M.O., Mohsin, A.H., Saleh, H.M., Noman, B.J. Numerical analysis of piles group surrounded by grouting under seismic load. Geotechnical Engineering and Sustainable Construction. 2022. Pp. 379–389. DOI: 10.1007/978-981-16-6277-5_30
15. Rasouli, H., Fatahi, B. A novel cushioned piled raft foundation to protect buildings subjected to normal fault rupture. Computers and Geotechnics. 2019. 106. Pp. 228–248. DOI: 10.1016/j.compgeo.2018.11.002
16. Prasad, S.K., Towhata, I., Chandradhara, G.P., Nanjundaswamy, P. Shaking table tests in earthquake geotechnical engineering. Current science. 2004. 87(10). Pp. 1398–404. http://www.jstor.org/stable/24109480
17. Meymand, P.J., Riemer, M.F., Seed, R.B. Large scale shaking table tests of seismic soil-pile interaction in soft clay. 12th World Conference on Earthquake Engineering (12WCEE). 2000. 0915.
18. Stewart, J.P. Variations between foundation-level and free-field earthquake ground motions. Earthquake Spectra. 2000. 16(2). Pp. 511–532. DOI: 10.1193/1.1586124
19. Karkush, M.O., Ali, S.D., Saidik, N.M., Al-Delfee, A.N. Numerical modeling of sheet pile quay wall performance subjected to earthquake. Geotechnical Engineering and Sustainable Construction. 2022. Pp. 355–365. DOI: 10.1007/978-981-16-6277-5_28
20. Karkush, M.O., Jihad, A.G., Jawad, K.A., Ali, M.S., Noman, B.J. Seismic analysis of floating stone columns in Soft Clayey Soil. E3S Web of Conferences. 2021. 318. 01008. DOI: 10.1051/e3sconf/202131801008
21. Khalaf, A.A., Al-hadidi, M.T. Numerical Analysis of the Stability of Bridge Foundation Pile under Earthquakes Effect. Journal of Engineering. 2023 Oct 2;29(10):150-64. DOI: 10.31026/j.eng.2023.10.09
22. Jihad, A.G., Karkush, M. Performance of geosynthetics-strengthened unconnected piled raft foundations under seismic loading. Magazine of Civil Engineering. 2024. 17(3). Pp. 12704. DOI: 10.34910/MCE.127.4
23. AlSaadi, K.A., Almurshedi, A.D., Karkush, M. Effect of geosynthetics-reinforced cushion on the behavior of partial connected piled raft foundation in dry and saturated sandy soil using shaking table. Indian Geotechnical Journal. 2024. 21. Pp. 1–4. DOI: 10.1007/s40098-024-00890-0
24. Alhassani, A.M., Aljorany, A.N. Parametric study on unconnected piled raft foundation using numerical modelling. Journal of Engineering. 2020. 26(5). Pp. 156–171. DOI: 10.31026/j.eng.2020.05.11
25. Jihad, A., Karkush, M. Behavior of geosynthetics-strengthened saturated cushion layer in disconnected piled-raft system under seismic loading. Indian Geotechnical Journal. 2024.14. Pp. 1–4. DOI: 10.1007/s40098-024-00877-x

Information about the authors:

Mahdi Karkush, *Doctor of Technical Sciences*
ORCID: https://orcid.org/0000-0003-1304-0303
E-mail: mahdi_karkush@yahoo.com

Alaa Almurshedi**,** *Doctor of Technical Sciences*
ORCID: https://orcid.org/0000-0003-1594-3979
E-mail: a.salman1001@coeng.uobaghdad.edu.iq

Karrar AlSaadi, *Doctor of Technical Sciences*
E-mail: karrar.jawad2001d@coeng.uobaghdad.edu.iq

Ahmed Al-Salakh, *Doctor of Technical Sciences*
E-mail: ahmedm.alsalakh@uokufa.edu.iq

Received: 04.02.2023. Approved after reviewing: 12.07.2023. Accepted: 29.11.2023.

Magazine of Civil Engineering

ISSN 2712-8172

journal homepage: http://engstroy.spbstu.ru/

Research article

UDC 624.04

DOI: 10.34910/MCE.128.2

The beam finite element with five nodal degrees of freedom

Yu.Ya. Tyukalov ✉

Vyatka State University, Kirov, Russian Federation

✉ *yutvgu@mail.ru*

Keywords: finite element, five degrees of freedom, reinforced concrete beam, physical nonlinearity, deformation, axis curvature, failure load

Abstract. The article presents comparative calculations of reinforced concrete beams using two types of beam finite elements: with three and five nodal degrees of freedom. Calculations were performed both taking into account the concrete and reinforcement physical nonlinearity, and without taking it into account. The expressions for stiffness matrix elements and the load vector were obtained for the finite element with five nodal degrees of freedom. Calculations taking into account physical nonlinearity were performed using the variable elasticity parameters method. As a structure for comparing solutions obtained by the two types of finite elements, a single-span clamped horizontal and inclined reinforced concrete beam were used. The accuracy of calculating beam axis deformations and curvature depending on the number and type of finite elements was assessed. It was shown that when performing linear calculations, bending moments, longitudinal forces and displacements do not depend on the number of finite elements with five degrees of freedom into which the beam had been divided. When solving physically nonlinear problems, if we refine the finite element mesh, the solutions obtained for elements with three degrees of freedom tend to the solutions obtained for a smaller number of elements with five degrees of freedom. The proposed beam finite element with five nodal degrees of freedom makes it possible to determine more accurately the axis curvature and deformation, which is especially important when solving physically nonlinear problems.

Citation: Tyukalov, Yu.Ya. The beam finite element with five degrees of node's freedoms. Magazine of Civil Engineering. 2024. 17(4). Article no. 12802. DOI: 10.34910/MCE.128.2

1. Introduction

The bending beams, compressed-bending and tensile rods are widely used in the building structures for various purposes. A large number of scientific articles are devoted to the use of finite element method (FEM) for calculation of such structures.

In [1], to calculate the beams on an elastic foundation, a finite element with three degrees of freedom at the nodes was used. The article notes the simplicity of the mathematical apparatus and the clarity of the diagram, which make the simplified FEM under consideration very flexible and allow us to solve the basic problems of calculating beams on an elastic foundation and other problems.

Article [2] is devoted to the three-dimensional nonlinear finite element analysis of inflatable beams. The beams under consideration are made of modern textile materials and, when inflated, can be used as load-bearing beams or arches. A three-noded spatial element was used, which has five degrees of each node freedom: an axial displacement along the beam element local axis, two transverse displacements along the two main axes, and two rotation angles. It was shown that the beam models had been in good agreement with the nonlinear thin-shell model.

In [3], the study develops a finite element formulation for the distortional buckling of I-beams. The formulation characterizes the distribution of the lateral displacement along the web height by superposing (a) two linear modes intended to capture classical non-distortional lateral-torsional behavior and (b) any

number of user-specified Fourier terms intended to capture additional web distortion. All displacement fields characterizing the lateral displacements are taken to follow a cubic distribution in the longitudinal direction.

Currently, volumetric finite elements are often used to study reinforced concrete bars. In [4, 5], a reinforced concrete beam is modeled using volumetric finite elements, taking into account the possible slipping of reinforcing bars and fibers. Based on the results of the study, recommendations were made on the reinforcement anchorage length.

In [6], a curved beam three-node finite element with nine degrees of freedom at each node was used to model multilayer beams with an arbitrary cross-section. It was noted that the numerical results indicate the effectiveness of the proposed contact solution to problems entailing various contact configurations.

Article [7] presents the formulation of strain-based finite elements for modelling composite beams with finger joints considering slip between the layers. The finite elements were derived in accordance with Reissner beam theory based on the modified virtual work principle where the displacements and rotations had been eliminated from the problem and axial deformation, shear deformation and curvature of the layers remain only functions to be approximated within the finite element. It was noted that the numerical model had been thoroughly tested and the results had shown that the presented finite element formulation had been an efficient tool for practical calculations.

Article [8] was devoted to the modeling of the nonlinear behavior of reinforced concrete structures subject to transverse shear or torsion under monotonic and cyclic loading. The fiber beam element approach was improved for shear effects. The 3D beam element was improved by adding an additional degree of freedom, which represented the deformation displacements of the cross-section. The element formulation was verified using an analytical solution for transverse shear, and 3D simulations of beams subject to shear and torsion.

Article [9] presents a new finite element formulation for the nonlinear analysis of two-layer composite planar frames with an interlayer slip. For each layer the geometrically nonlinear Reissner beam theory was assumed. As shown in one of the numerical examples, the use of the geometrically linear theory instead of the nonlinear one can lead to an error in determining the axial forces and bending moments in each layer as big as 20–80 %.

To calculate reinforced concrete and steel concrete beams taking into account physical nonlinearity, volumetric finite elements are often used [10–13]. A simply supported concrete fiber-reinforced beam was modeled using nonlinear volumetric eight-node finite elements in [10]. The work made an important conclusion: the presence of some fiber type in mortars can reduce compressive and flexural strength. This can be attributed to several factors: a decrease in the density of specimens, weak interfacial adhesion and negatively affected cement hydration, etc.

The principal purpose of [14] was to compare three different ways of determination of critical moment, also in the context of structural sensitivity analysis with respect to the structural element length. Sensitivity gradients were determined using the analytical solution, the finite difference and the finite element methods. The most important conclusion drawn from the computational analysis carried out in this paper was good agreement of all available methods, i.e., analytical methods, finite difference, and finite element methods, to determine the critical moment in thin-walled single-span structures.

Article [15] presents numerical and experimental studies of T-shaped reinforced concrete beams.

The various finite elements types were used to model the performance of box girder bridges [16–18]. Article [16] formulated a novel one-dimensional refined beam FEM that takes into account non-uniform distortional warping and secondary distortional moment deformation effect to analyze the deformation of thin-walled multi-cell box beams. This finite element was based on an extended version of generalized Vlasov's thin-walled beam theory. The proposed one-dimensional beam elements demonstrated desirable predictions for the deformation behavior of thin-walled single- or multi-cell box beams with constant or variable depth. The accuracy and reliability of these predictions were compared to shell finite element calculations.

Article [19] for the multilayer beams analysis proposes a finite element based on nonlinear Reissner beam theory. The connection between the layers was specified by an arbitrary function of the stiffness of springs, continuously distributed along the element length. The displacement field on which the stiffness function depends upon was expressed in a local, deformed basis. The large movements and rotations were taken into account. Distributed force which resulted from the interaction between layers, was included in the governing equations to avoid the need for additional interface elements and to integrate the equations using a single numerical method. The predicted deflection curve of each beam was compared to its experimental counterpart over the entire load range up to failure, and the two curves were found to be in reasonable agreement. A distinctive feature of the present analysis is that it captures not only the onset

and propagation of the delamination process, but also the total post-peak load or softening response of each beam.

Article [20] studied beam finite elements that use absolute nodal coordinates to express deformations. Such finite elements use strain gradient components rather than rotational degrees of freedom, resulting in a consistent and constant mass matrix. The article noted that most of the considered methods for eliminating locking gave the expected results compared to classical finite elements.

Article [21] presented a method for determining all six stress components for a cantilever-type beam that was subjected to concentrated end loads. The method considered an inhomogeneous cross-section and used the cylindrically orthotropic properties of the material. The solution was based on a displacement field formulation that includes unknown in-plane distortion and warping functions. A simple FEM procedure was then used. The efficacy of the method was confirmed by a series of numerical examples corresponding to the analytical results.

Article [22] addresses contact problems associated with large deformations of curved beams. Noted, the contact was difficult to analyze due to uncertainty of the contact positions and strong nonlinearity. A new adaptive differential quadrature element method was proposed to predict the contact positions of a curved beam with a finite number of contact points. The simulation results showed that the proposed element method significantly improved the efficiency and accuracy of solving the curved beam large-deformation contact problem.

Article [23] proposes a general procedure of actions aimed at increasing the seismic resistance of the foundations of turbine units. Implementation of the proposed methodology was carried out on a specific example of a vibroisolated foundation: the dependences of seismic accelerations and displacements were obtained for different variants of seismic isolation.

The beam finite elements are often used for the analysis of various multilayer's types [24–26] and multi-stage beams [27]. Article [24] presents a beam finite element for modal analysis of a double symmetric cross-section made of a functionally graded material. The material properties in a real beam can vary continuously in longitudinal direction, while the variation with respect to the transversal and lateral directions was assumed to be symmetric in a continuous or discontinuous manner. The influence of shear force deformation was taken into account, as well as the influence of longitudinally varying inertia and rotational inertia.

Article [28] aims to study the influences of the viscoelastic and anisotropic properties of a material on the dynamical behavior of the plate. For the first time, an integral model is used to consider the viscoelastic properties of materials of an anisotropic structure. The integral mode correctly describes the rheological processes occurring in the studied structure during the entire time. The presented mathematical model makes it possible to obtain sufficiently accurate solutions that are well combined with experimental results.

Articles [29–31] presented finite elements constructed based on the stress's approximations. The solutions were based on the additional energy functional, to which algebraic equilibrium equations were added using Lagrange multipliers. The stresses or forces can be approximated over the finite element domain by constant or piecewise constant functions. In [32], a beam finite element with five degrees of freedom was proposed to solve problems of beam systems stability. A deformation and axis curvature were added to the standard nodal degrees of freedom. These works show that such finite element makes it possible to more accurately determine critical forces with minimum finite elements number.

A number of works present beam finite elements for the calculation of composite steel-concrete [33] and wood, in combination with a steel profile [34], structures. In papers, the comparison of solutions with experimental results was presented. The finite elemental analysis was also used for the design of laminated timber beams [35, 36]. The works examine the bending and shear stiffness of wooden beams with a composite cross-section. The tests of wooden samples and beams were carried out. A comparison was made between the experimental data and the finite element analysis results.

The purpose of current work is to perform comparative calculations of reinforced concrete beams using beam finite elements of two types: with three and five degrees of freedom at the node. The calculations must be performed both taking into account the physical nonlinearity of concrete and reinforcement, and without taking it into account. It assumes to evaluate the accuracy of calculating deformations and curvature of the beam axis depending on the number and finite elements type, as well as the accuracy of calculating stresses in reinforcing bars in the process of increasing the load until failure.

2. Methods

When solving structural mechanics problems using FEM, taking into account physical nonlinearity, the importance of determining deformations accuracy in the finite element region increases. The more accurately the deformations are calculated, the more accurately the stiffness finite elements parameters will be determined, and the more accurately the stresses and displacements will be determined.

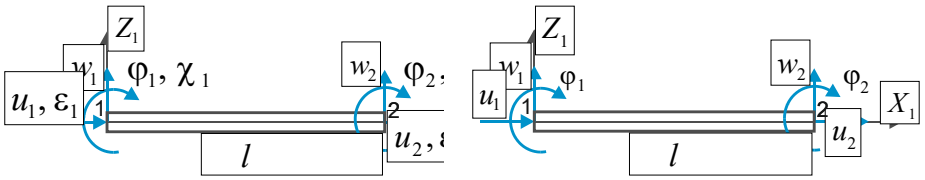

Figure 1. Variants of a rod finite element nodal unknowns.

In the standard rod finite element (Fig. 1a), the following polynomials are used to approximate the displacement fields:

$$\begin{aligned} &w(x)=N_1(x)w_1+N_2(x)\varphi_1+N_3(x)w_2+N_4(x)\varphi_2;\\ &u(x)=N_5(x)u_1+N_6(x)u_2;\\ &N_1(x)=1+2(x/l)^3-3(x/l)^2,\quad N_3(x)=3(x/l)^2-2(x/l)^3;\\ &N_2(x)=-x\left[(x/l)-1\right]^2,\quad N_4(x)=-x\left[(x/l)^2-x/l\right];\\ &N_5(x)=1-x/l,\quad N_6(x)=x/l. \end{aligned} \tag{1}$$

The deformations at any point in the finite element cross-section are determined by the deformation of the neutral axis ε_0 and the axis curvature value χ_0:

$$\begin{aligned} &\varepsilon_0(x)=\frac{du}{dx}=(-u_1+u_2)/l;\\ &\chi_0(x)=\frac{d^2w}{dx^2}=\frac{6}{l^2}\left[(2x/l)-1\right]w_1-\frac{2}{l}\left[(3x/l)-2\right]\varphi_1-\\ &\quad-\frac{6}{l^2}\left[(2x/l)-1\right]w_2-\frac{2}{l}\left[(3x/l)-1\right]\varphi_2. \end{aligned} \tag{2}$$

Thus, the neutral axis deformations are constant along the finite element length, and the axis curvature changes linearly. The axis curvature value at the beginning or end of an element depends on the displacement and rotation angle of the opposite node. Therefore, it is obvious that during the transition from one finite element to another, at the nodal point the deformations can undergo a discontinuity, both due to a jump in the axis deformation ε_0 and due to a discontinuity in the axis curvature value χ_0. Below we will give numerical examples illustrating discontinuities in the deformation fields at the nodal points of the finite element mesh.

In [32], to solve rod systems stability problems, a finite element with five degrees of nodal freedom was proposed (Fig. 1b). To approximate transverse displacements a fifth-degree polynomial was used, and for longitudinal displacements a third-degree polynomial was used. The deformation of the neutral axis and curvature were taken as additional unknowns at the nodes. Thus, if necessary, the deformations continuity at nodal points is ensured.

The functions of a finite element transverse and longitudinal displacements are determined by expressions (3–5):

$$\begin{aligned} &w(x)=H_1(x)w_1+H_2(x)\varphi_1+H_3(x)\chi_1+H_4(x)w_2+H_5(x)\varphi_2+H_6(x)\chi_2;\\ &u(x)=H_7(x)u_1+H_8(x)\varepsilon_1+H_9(x)u_2+H_{10}(x)\varepsilon_2. \end{aligned} \tag{3}$$

$$
\begin{aligned}
H_1(x) &= 1-10(x/l)^3+15(x/l)^4-6(x/l)^5;\\
H_2(x) &= l\left[x/l-6(x/l)^3+8(x/l)^4-3(x/l)^5\right];\\
H_3(x) &= \frac{l^2}{2}\left[(x/l)^2-3(x/l)^3+3(x/l)^4-(x/l)^5\right];\\
H_4(x) &= 10(x/l)^3-15(x/l)^4+6(x/l)^5;\\
H_5(x) &= l\left[-4(x/l)^3+7(x/l)^4-3(x/l)^5\right];\\
H_6(x) &= \frac{l^2}{2}\left[(x/l)^3-2(x/l)^4+(x/l)^5\right].
\end{aligned}
\tag{4}
$$

$$
\begin{aligned}
H_7(x) &= 1-3(x/l)^2+2(x/l)^3;\\
H_8(x) &= l\left[x/l-2(x/l)^2+(x/l)^3\right];\\
H_9(x) &= 3(x/l)^2-2(x/l)^3;\\
H_{10}(x) &= l\left[-(x/l)^2+(x/l)^3\right].
\end{aligned}
\tag{5}
$$

In this case, the neutral axis deformation varies along its length as a quadratic function, and the axis curvature varies according to a cubic polynomial:

$$
\begin{aligned}
\varepsilon_0(x) = \frac{du}{dx} = \frac{6}{l}\left[-(x/l)+(x/l)^2\right]u_1+\left[3(x/l)^2-4(x/l)+1\right]\varepsilon_1+\\
+\frac{6}{l}\left[(x/l)-(x/l)^2\right]u_2+\left[3(x/l)^2-2(x/l)\right]\varepsilon_2.
\end{aligned}
\tag{6}
$$

$$
\begin{aligned}
\chi_0(x) = \frac{d^2w}{dx^2} = \frac{60}{l^2}\left[-(x/l)+3(x/l)^2-2(x/l)^3\right]w_1+\\
+\frac{12}{l}\left[-3(x/l)+8(x/l)^2-5(x/l)^3\right]\varphi_1+\left[1-9(x/l)+18(x/l)^2-10(x/l)^3\right]\chi_1+\\
+\frac{60}{l^2}\left[(x/l)-3(x/l)^2+2(x/l)^3\right]w_2+\frac{12}{l}\left[-2(x/l)+7(x/l)^2-5(x/l)^3\right]\varphi_2+\\
+\left[3(x/l)-12(x/l)^2+10(x/l)^3\right]\chi_2.
\end{aligned}
\tag{7}
$$

In the future, we will agree to denote a finite element with three degrees of freedom as FE-3, and with five degrees of freedom as FE-5.

Let us obtain expressions for the secant stiffness matrix's elements of a reinforced concrete finite element, the cross section of which is shown in Fig. 2. A concrete and reinforcement can have arbitrary nonlinear dependencies $\sigma(\varepsilon)$. The number of reinforcement layers in a section is also arbitrary.

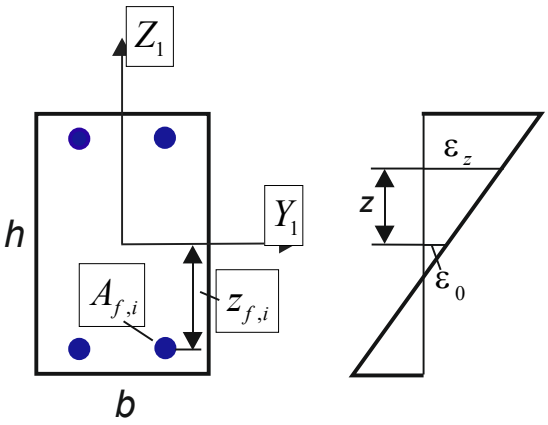

Figure 2. The beam cross section and deformations diagram.

$A_{f,i}$ is reinforcing bar cross-sectional area; $z_{f,i}$ is coordinate of the reinforcing bar position along Z_1 the axis; b, h are cross-sectional dimensions. We write the expressions for the median plane deformations and the axis curvature in the following vector form:

$$\varepsilon_0 = \mathbf{N}_{\mathrm{u}}^{\mathrm{T}}\mathbf{z}_{\mathrm{u}}, \quad \chi_0 = \mathbf{N}_{\mathrm{w}}^{\mathrm{T}}\mathbf{z}_{\mathrm{w}}. \tag{8}$$

For FE-3 with three nodal degrees of freedom, we obtain the following expressions:

$$\begin{aligned} \mathbf{N}_{\mathrm{u}}^{\mathrm{T}} &= \left[N_5'(x) \quad N_6'(x)\right]; \\ \mathbf{N}_{\mathrm{u}}^{\mathrm{T}} &= \left[N_1''(x) \quad N_2''(x) \quad N_3''(x) \quad N_4''(x)\right]. \end{aligned} \tag{9}$$

$$\mathbf{z}_{\mathrm{u}} = \begin{bmatrix} u_1 \\ u_2 \end{bmatrix}, \quad \mathbf{z}_{\mathrm{w}} = \begin{bmatrix} w_1 \\ \varphi_1 \\ w_2 \\ \varphi_2 \end{bmatrix}. \tag{10}$$

For FE-5 with five nodal degrees of freedom, the expressions will be as follows:

$$\begin{aligned} \mathbf{N}_{\mathrm{u}}^{\mathrm{T}} &= \left[N_7'(x) \quad N_8'(x) \quad N_9'(x) \quad N_{10}'(x)\right]; \\ \mathbf{N}_{\mathrm{u}}^{\mathrm{T}} &= \left[N_1''(x) \quad N_2''(x) \quad N_3''(x) \quad N_4''(x) \quad N_5''(x) \quad N_6''(x)\right]. \end{aligned} \tag{11}$$

$$\mathbf{z}_{\mathrm{u}} = \begin{bmatrix} u_1 \\ \varepsilon_1 \\ u_2 \\ \varepsilon_2 \end{bmatrix}, \quad \mathbf{z}_{\mathrm{w}} = \begin{bmatrix} w_1 \\ \varphi_1 \\ \chi_1 \\ w_2 \\ \varphi_2 \\ \chi_2 \end{bmatrix}. \tag{12}$$

Using the above notations, the strain energy expression of the finite element will have the following form:

$$E = \frac{1}{2}\int_{-h/2}^{h/2}\int_0^l bE_b^s\left(\varepsilon_0 - z\chi_0\right)^2 dxdz + \frac{1}{2}\sum_{i=1}^{n_f}\int_0^i E_{f,i}^s A_{f,i}\left(\varepsilon_0 - z_{f,i}\chi_0\right)^2 dx. \tag{13}$$

We take denotations for the cross-section rigidity parameters:

$$EI(x)=\int_{-h/2}^{h/2} z^2 bE_b^s dz+\sum_{i=1}^{n_f} E_f^s A_{f,i} z_{f,i}^2;$$

$$EA(x)=\int_{-h/2}^{h/2} bE_b^s dz+\sum_{i=1}^{n_f} E_f^s A_{f,i}; \tag{14}$$

$$ES(x)=\int_{-h/2}^{h/2} zbE_b^s dz+\sum_{i=1}^{n_f} E_f^s A_{f,i} z_{f,i}.$$

The expression (13) can be written in the following form:

$$E=\frac{1}{2}\int_0^l \left(EA(x)\varepsilon_0^2+EI(x)\chi_0^2-2ES(x)\varepsilon_0\chi_0 \right) dx. \tag{15}$$

Substituting (8) into (15), we get:

$$\begin{aligned} E=\frac{1}{2}\int_0^l \Big(& EI(x)\mathbf{z}_{\mathrm{w}}^{\mathrm{T}}\mathbf{N}_{\mathrm{w}}\mathbf{N}_{\mathrm{w}}^{\mathrm{T}}\mathbf{z}_{\mathrm{w}}+EA(x)\mathbf{z}_{\mathrm{u}}^{\mathrm{T}}\mathbf{N}_{\mathrm{u}}\mathbf{N}_{\mathrm{u}}^{\mathrm{T}}\mathbf{z}_{\mathrm{u}}- \\ & -ES(x)\mathbf{z}_{\mathrm{w}}^{\mathrm{T}}\mathbf{N}_{\mathrm{w}}\mathbf{N}_{\mathrm{u}}^{\mathrm{T}}\mathbf{z}_{\mathrm{u}}-ES(x)\mathbf{N}_{\mathrm{u}}^{\mathrm{T}}\mathbf{z}_{\mathrm{u}}\mathbf{N}_{\mathrm{w}}^{\mathrm{T}}\mathbf{z}_{\mathrm{w}} \Big) dx. \end{aligned} \tag{16}$$

Let us introduce the following notation:

$$\begin{gathered} \mathbf{K}_{\mathrm{ww}}=\int_0^l EI(x)\mathbf{N}_{\mathrm{w}}\mathbf{N}_{\mathrm{w}}^{\mathrm{T}}dx, \quad \mathbf{K}_{\mathrm{uu}}=\int_0^l EA(x)\mathbf{N}_{\mathrm{u}}\mathbf{N}_{\mathrm{u}}^{\mathrm{T}}dx, \\ \mathbf{K}_{\mathrm{uv}}=-\int_0^l ES(x)\mathbf{N}_{\mathrm{u}}\mathbf{N}_{\mathrm{w}}^{\mathrm{T}}dx. \end{gathered} \tag{17}$$

The finite element stiffness matrix in the local coordinate system will have the following simple form:

$$\mathbf{K}_{\mathrm{L}}=\begin{bmatrix} \mathbf{K}_{\mathrm{ww}} & \mathbf{K}_{\mathrm{uv}}^{\mathrm{T}} \\ \mathbf{K}_{\mathrm{uv}} & \mathbf{K}_{\mathrm{uu}} \end{bmatrix}. \tag{18}$$

For FE-5, the integrals (17) expressions will include the products of the third- and fifth-degrees polynomials. The stiffness parameters (14) for nonlinear problems will be variable along the length of the element. To calculate integrals (17), we apply the well-known Gauss-Legendre numerical integration procedure:

$$\mathbf{K}_{\mathrm{ww}}=\frac{l}{2}\sum_{i=1}^{n_g} G_i EI(x_i)\mathbf{N}_{\mathrm{w}}(x_i)\mathbf{N}_{\mathrm{w}}^{\mathrm{T}}(x_i);$$

$$\mathbf{K}_{\mathrm{uu}}=\frac{l}{2}\sum_{i=1}^{n_g} G_i EA(x_i)\mathbf{N}_{\mathrm{u}}(x_i)\mathbf{N}_{\mathrm{u}}^{\mathrm{T}}(x_i); \tag{19}$$

$$\mathbf{K}_{\mathrm{uv}}=\frac{l}{2}\sum_{i=1}^{n_g} G_i ES(x_i)\mathbf{N}_{\mathrm{u}}(x_i)\mathbf{N}_{\mathrm{w}}^{\mathrm{T}}(x_i), \quad x_i=\frac{l(\xi_i+1)}{2},$$

G_i, ξ_i are weight factor and integration point coordinate on the interval [–1, 1].

To calculate integrals (14) at points x_i corresponding to the Gauss-Legendre coordinates, we use the trapezoidal method:

$$EI(x_i)=\sum_{k=1}^{n+1} b\Delta h E_b^s z_k^2+\sum_{j=1}^{n_f} E_{f,j}^s A_{f,j} z_{f,j}^2;$$

$$EA(x_i)=\sum_{k=1}^{n+1} b\Delta h E_b^s+\sum_{j=1}^{n_f} E_{f,j}^s A_{f,j};\tag{20}$$

$$ES(x_i)=\sum_{k=1}^{n+1} b\Delta h E_b^s z_k+\sum_{j=1}^{n_f} E_{f,j}^s A_{f,j} z_{f,j}.$$

n is the sections number into which the section during numerical integration is divided by height. The elasticity secant modules E_b^s and $E_{f,j}^s$ are determined from specified dependencies $\sigma(\varepsilon)$ for concrete and reinforcement. In expressions (20), in accordance with the method of trapezoidal, the following parameters are used:

$$z_k=-\frac{h}{2}+\frac{h(k-1)}{n},\quad \Delta h=\begin{cases} h/2n, & k=1, k=n+1 \\ h/n, & 1<k<n+1 \end{cases}.\tag{21}$$

The stiffness matrix $\mathbf{K}_{\mathrm{L}}$ expression was obtained in the local coordinate system of the finite element X_1Z_1 (Fig. 1). The direction cosine matrices $\mathbf{C}$ for moving to the global coordinate system are given below:

$$\mathbf{C}=\begin{bmatrix} \cos\alpha & 0 & 0 & 0 & \sin\alpha & 0 \\ 0 & 1 & 0 & 0 & 0 & 0 \\ 0 & 0 & \cos\alpha & 0 & 0 & \sin\alpha \\ 0 & 0 & 0 & 1 & 0 & 0 \\ -\sin\alpha & 0 & 0 & 0 & \cos\alpha & 0 \\ 0 & 0 & -\sin\alpha & 0 & 0 & \cos\alpha \end{bmatrix};$$

$$\mathbf{C}=\begin{bmatrix} \cos\alpha & 0 & 0 & 0 & 0 & 0 & \sin\alpha & 0 & 0 & 0 \\ 0 & 1 & 0 & 0 & 0 & 0 & 0 & 0 & 0 & 0 \\ 0 & 0 & 1 & 0 & 0 & 0 & 0 & 0 & 0 & 0 \\ 0 & 0 & 0 & \cos\alpha & 0 & 0 & 0 & 0 & \sin\alpha & 0 \\ 0 & 0 & 0 & 0 & 1 & 0 & 0 & 0 & 0 & 0 \\ 0 & 0 & 0 & 0 & 0 & 1 & 0 & 0 & 0 & 0 \\ -\sin\alpha & 0 & 0 & 0 & 0 & 0 & \cos\alpha & 0 & 0 & 0 \\ 0 & 0 & 0 & 0 & 0 & 0 & 0 & 1 & 0 & 0 \\ 0 & 0 & 0 & -\sin\alpha & 0 & 0 & 0 & 0 & \cos\alpha & 0 \\ 0 & 0 & 0 & 0 & 0 & 0 & 0 & 0 & 0 & 1 \end{bmatrix}.\tag{22}$$

$$\cos\alpha=\frac{y_2-y_1}{l}.\tag{23}$$

y_1, y_2 are coordinates of the finite element start and end in the global coordinate system. Using (22), we obtain the stiffness matrix $\mathbf{K}_i$ expression for finite element i in the global coordinate system:

$$\mathbf{K}_i=\mathbf{C}^{\mathrm{T}}\mathbf{K}_{\mathrm{L}}\mathbf{C}.\tag{24}$$

Let us calculate the nodal forces vector from the action of uniformly distributed loads on FE-5 in the local coordinate system. The work of distributed loads will be expressed as follows:

$$A_q = \int_0^l \left[q_{z1} w(x) + q_{x1} u(x) \right] dx. \tag{25}$$

$$q_{z1} = q_z \cos\alpha - q_x \sin\alpha, \quad q_{x1} = q_z \sin\alpha + q_x \cos\alpha. \tag{26}$$

Substituting expressions (3–4) into (25), we will obtain:

$$A_q = \mathbf{z}_L^T \mathbf{B}_L, \quad \mathbf{z}_L = \begin{Bmatrix} \mathbf{z}_w \\ \mathbf{z}_u \end{Bmatrix};$$
$$\mathbf{B}_L^T = \left[\frac{q_{z_1} l}{2} \; \frac{q_{z_1} l^2}{10} \; \frac{q_{z_1} l^3}{120} \; \frac{q_{z_1} l}{2} \; \frac{-q_{z_1} l^2}{10} \; \frac{q_{z_1} l^3}{120} \; \frac{q_{x_1} l}{2} \; \frac{q_{x_1} l^2}{12} \; \frac{q_{x_1} l}{2} \; \frac{-q_{x_1} l^2}{12} \right]. \tag{27}$$

Vector $\mathbf{z}_L = \mathbf{C}^T \mathbf{z}$. Then we will get:

$$A_q = \mathbf{z}^T \mathbf{C} \mathbf{B}_L. \tag{28}$$

Calculating the derivative of work (28) with respect to the vector, we obtain the nodal forces vector from the action of uniformly distributed loads in the global coordinate system.

$$\mathbf{R}_q = \mathbf{C} \mathbf{B}_L. \tag{29}$$

For FE-3 vector:

$$\mathbf{B}_L^T = \left[\frac{q_{z_1} l}{2} \; \frac{-q_{z_1} l^2}{12} \; \frac{q_{z_1} l}{2} \; \frac{q_{z_1} l^2}{12} \; \frac{q_{x_1} l}{2} \; \frac{q_{x_1} l}{2} \right]. \tag{30}$$

From the vectors $\mathbf{R}_q$ formed for the finite elements, and the forces and moments concentrated in the nodes, the load vector $\mathbf{R}$ for the entire system is formed. The global stiffness matrix of the system is defined as the sum of finite element stiffness matrices

$$\mathbf{K} = \sum_i \mathbf{K}_i. \tag{31}$$

We write the system of the nonlinear algebraic equations in the following form:

$$\mathbf{K}(\mathbf{Z})\mathbf{Z} = \mathbf{R}. \tag{32}$$

$\mathbf{Z}$ is the nodal unknown's global vector for the entire system.

We will solve the nonlinear equations system (31) using the well-known method of variable elasticity parameters. The main stages of solving the nonlinear problem are presented in Fig. 3.

1. $k = 0, \; \mathbf{Z}_0 = 0$
2. $k = k + 1$
3. $\mathbf{Z}_k = \mathbf{K}^{-1}(\mathbf{Z}_{k-1})\mathbf{R} \pm$
4. $eps = \dfrac{\sum_j \left(Z_{k,j} - Z_{k-1,j} \right)^2}{\sum_j Z_{k,j}^2}$
5. If $eps > 0.005$ then go to 2
6. Exit

Figure 3. The method of elastic solutions algorithm.

3. Results and Discussion

The main aim of this study is to compare the values of curvature and axis deformation for various finite elements sections, obtained when using two options for approximating displacements. As a structure for comparing solutions obtained, using two variants of finite elements FE-3 and FE-5, we will use a single-span clamped horizontal and inclined reinforced concrete beams (Fig. 4). A uniformly distributed vertical load is applied to the beam. In reference sections, both displacements and rotation angles are excluded.

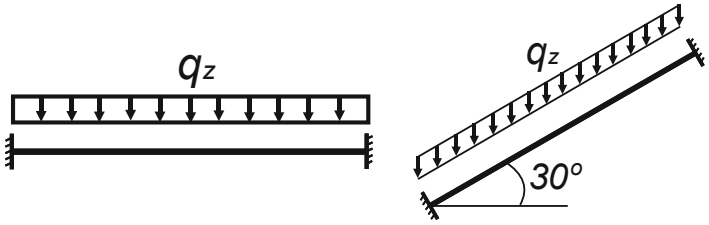

Figure 4. The horizontal and inclined beams.

The beam data are given in Table 1. Stress-strain diagrams for concrete and beam reinforcement are shown in Fig. 5.

Table 1. The clamped beam characteristics.

Beton	Reinforcement	Length, m	b, cm	h, cm	Bottom reinforcement		Top reinforcement	
					Diameter, mm	z_f, mm	Diameter, mm	z_f, mm
B30	A-III	6	20	40	2 d20	– 160	2 d20	160

Tables 2 and 3 present the characteristics of concrete and reinforcement necessary for constructing stress-strain diagrams.

Table 2. The characteristics of concrete.

R_b, MPa	R_{bt}, MPa	ε_{b1}	ε_{b0}	ε_{b2}	ε_{bt1}	ε_{bt0}	ε_{bt2}
17000	1150	– 0.000314	– 0.002	– 0.035	0.0000212	0.0001	0.00015

Table 3. The characteristics of reinforcement.

R_s, MPa	ε_{s0}	ε_{s2}	ε_{st0}	ε_{st2}
350000	– 0.00167	– 0.015	0.00167	0.0015

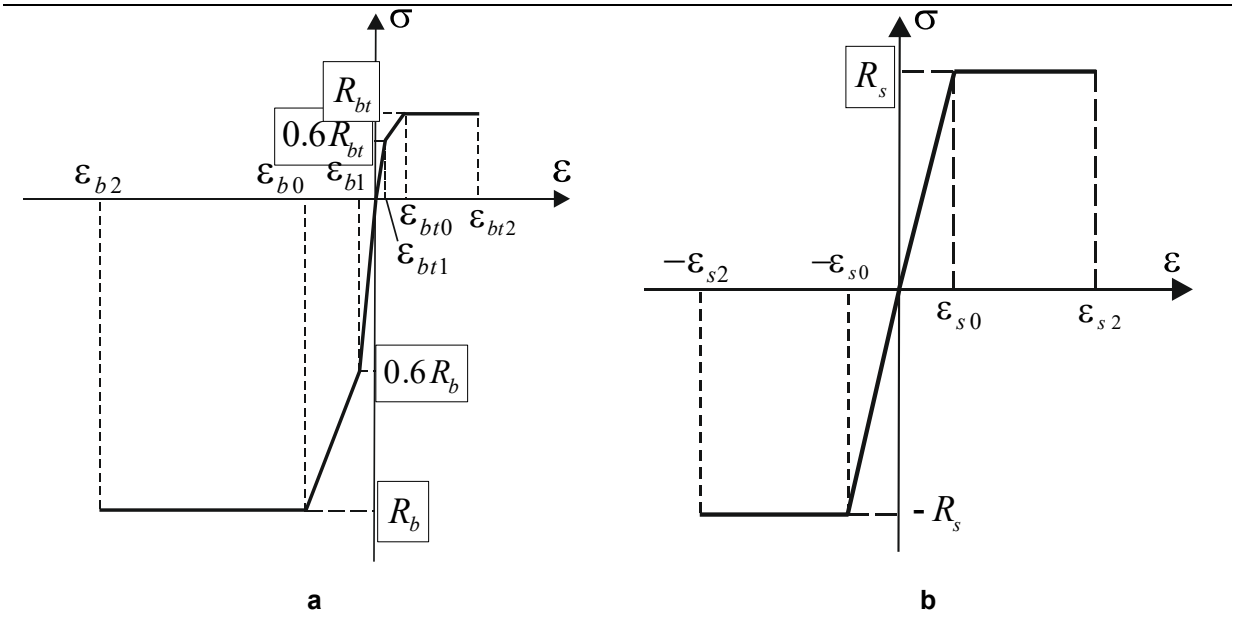

Figure 5. The stress-strain diagrams for concrete and reinforcement.

3.1. Linear Calculations

To compare solutions, beam calculations were performed (Fig. 4) when it was divided along the length into 2, 4, 8 and 16 finite elements. Calculations were performed in a linear formulation at the initial value of the concrete elastic modulus E = 30000 MPa. Reinforcement was not taken into account. The distributed load was assumed to be equal to q = 10 kN/m.

When calculating physically linear problems, it turned out that the bending moments and displacements in all beam nodal sections are the same for both versions of finite elements, regardless of the finite elements number. At the same time, we note that for the FE-5, the solution can also be obtained if the beam is represented by only one finite element. In this case, the only unknown parameters are the beam curvatures at the beginning and end. The solution even with this beam representation was exact.

Table 4. The beam sections axis curvature, q=10 kN/m (Fig. 4a).

A section coordinates along length, m	FE-3 [37]				FE-5	Bending moments, kN·m
	2 elements	4 elements	8 elements	16 elements	1 element	
0	– 0.000578	– 0.0007227	– 0.0007589	– 0.0007679	– 0.0007710	– 30
0.75	– 0.000289	– 0.0002891	– 0.0002530	– 0.0002620	– 0.0002650	– 10.313
1.5	0	0.0001445	0.0001084	0.0000994	0.0000960	3.75
2.25	0.000289	0.0002891	0.0003252	0.0003162	0.0003130	12.188
3.0	0.000578	0.0004336	0.0003975	0.0003885	0.0003850	15

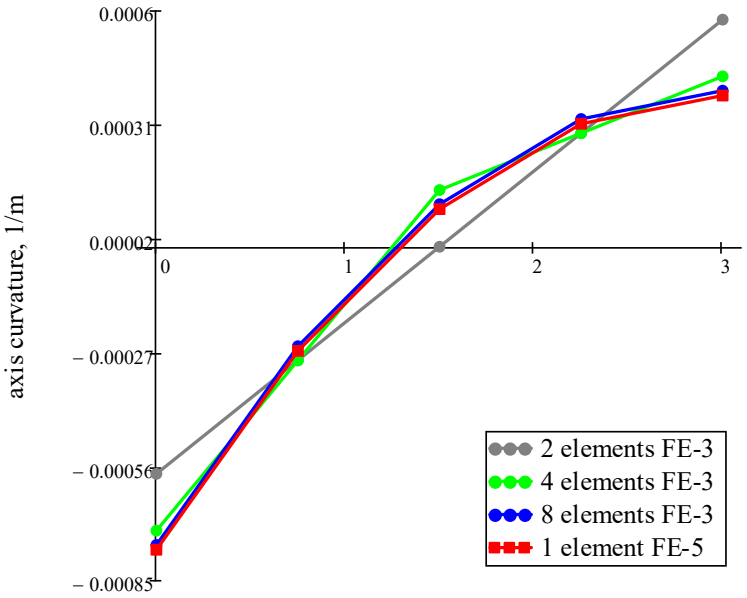

Figure 6. Axis curvature of the clamped beam (Fig. 4a).

Table 4 and Fig. 6 show the axis curvature values for various options for dividing the beam into finite elements under the action of a uniformly distributed load. For FE-5, the curvature values are the same for any elements number. Therefore, Table 4 presents the values for the case of the beam being represented by one FE-5. Using FE-3 [37], calculations were performed when the beam was divided into 2, 4, 8, and 16 finite elements. A comparison of the results shows that when the finite element mesh is refined, the axis curvature values in all beam sections tend to the values, which were obtained for one FE-5. The largest deviation in curvature values is observed in the pinched point. Therefore, when using two FE-3, the curvature value in the pinch point is 25 % less than the value obtained using FE-5. When using four elements, the deviation in this curvature values is 6 %. Therefore, the beam dividing into four FE-3 is not sufficient to obtain accurate curvature values in beam sections. We also note that the use of FE-3 gives underestimated curvature values in the extreme section where the bending moment has a maximum value by module.

Table 5. The vertical displacements of the clamped beam, q=10 kN/m (Fig. 4a).

A section coordinates along length, m	FE-3 [37]			FE-5
	2 elements	4 elements	8 elements	1 element
0	**0**	**0**	**0**	**0**
0.75	– 0.000164	– 0.000197	**– 0.000201**	– 0.000201
1.5	– 0.000525	**– 0.00059**	**– 0.00059**	– 0.00059
2.25	– 0.000885	– 0.000918	**– 0.000922**	– 0.000922
3.0	**– 0.001049**	**– 0.001049**	**– 0.001049**	– 0.001049

Table 5 shows the displacement values of beam sections for various finite element mesh options. The displacement values calculated at the finite element nodes are marked in bold, and the values in intermediate sections located between the finite element nodes are shown in regular font. It is interesting to note that the nodal points displacements when using FE-3 coincide with the values calculated when using one FE-5, and the values at the intermediate points of FE-3 differ from the exact ones.

Thus, for any mesh, the nodal displacements for FE-3 are calculated accurately, and the displacements of intermediate points between nodes approach the exact ones when the mesh is refined. The use of FE-5, due to additional degrees of freedom, leads to the displacement's refinement of intermediate sections between the finite element nodes, as well as to the refinement of axis curvature and deformations at the nodes and in the intermediate sections. In this case, for a clamped beam it is enough to use one FE-5.

Figs. 7–8 show the calculation results of an inclined beam under the uniformly distributed load action (Fig. 4b). In this case, in addition to curvature, longitudinal deformations also occur in the sections.

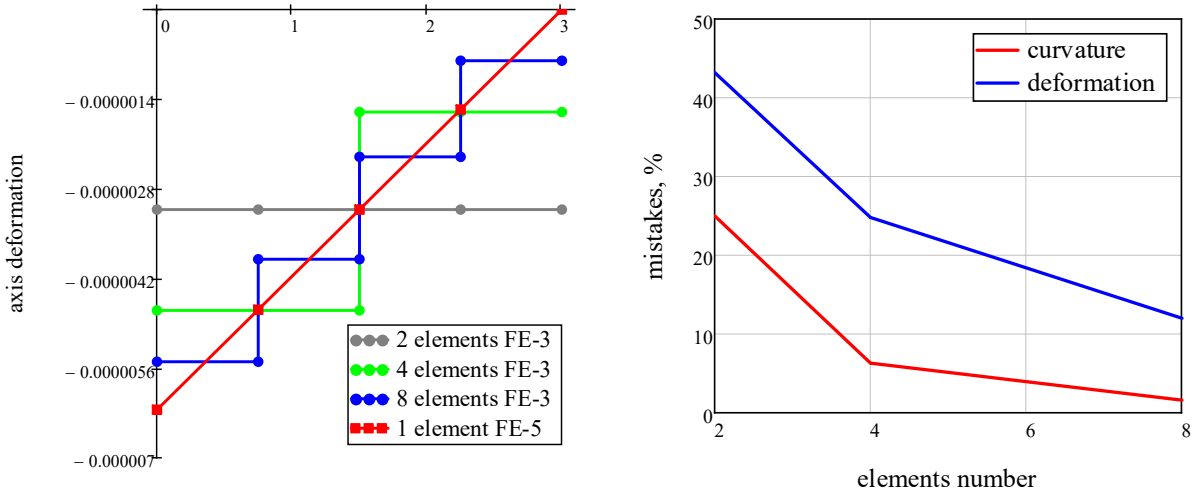

a **b**

Figure 7. The deformations of the inclined clamped beam (Fig. 4b) and errors in calculating curvatures and axis deformations for FE-3.

The graphs of changes in the inclined beam axis curvature, depending on the number and type of finite elements, coincide with the horizontal beam graph (Fig. 6). In this case, compressive forces and, corresponding to them, the beam axis longitudinal deformations arise too (Fig. 7a). When using FE-3, longitudinal deformations change stepwise along the beam length, and when using FE-5, the deformations change linearly, which corresponds to the law of longitudinal forces change. When FE-3 mesh is refined, the longitudinal deformation's values tend to the corresponding values obtained for FE-5. However, even if we use eight FE-3, the error in the longitudinal strains value is more than 10% (Fig. 7b). Fig. 7b also presents the errors in the axis curvature and axis deformation calculation for FE-3 depending on the finite elements number. Note that the error in calculating axis curvature is smaller but also significant when the FE-3 number is small.

3.2. Nonlinear Calculations

To determine the calculating accuracy of the stress-strain state parameters, taking into account the physical nonlinearity of concrete and reinforcement, the calculations were performed for an inclined beam

(Fig. 4b) with symmetrical reinforcement (Fig. 2). The calculations were performed both for different loading levels up to failure, and for different numbers of finite elements FE-3 and FE-5 at the same loading level q_z = 40 kN/m. To guarantee high numerical integration accuracy, during nonlinear calculations the section was divided in height into forty layers and nine Gauss-Legendre integration points were used along the length of the finite element. The nonlinear problem was solved iteratively using the elastic solutions method (Fig. 3). Fig. 8–10 show the calculation results of an inclined reinforced concrete beam (Fig. 4b) on the load action q_z = 40 kN/m.

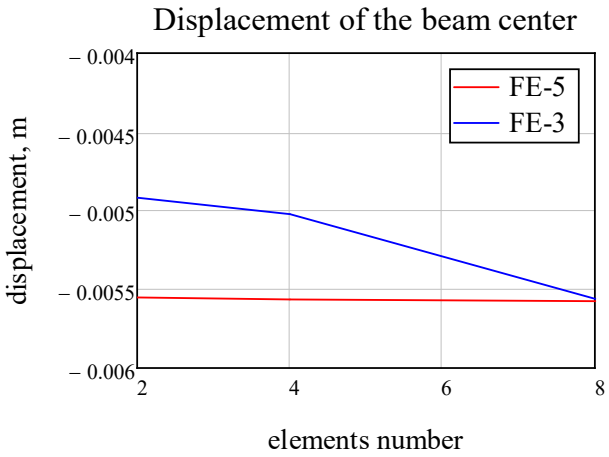

Figure 8. The vertical displacement of the beam center.

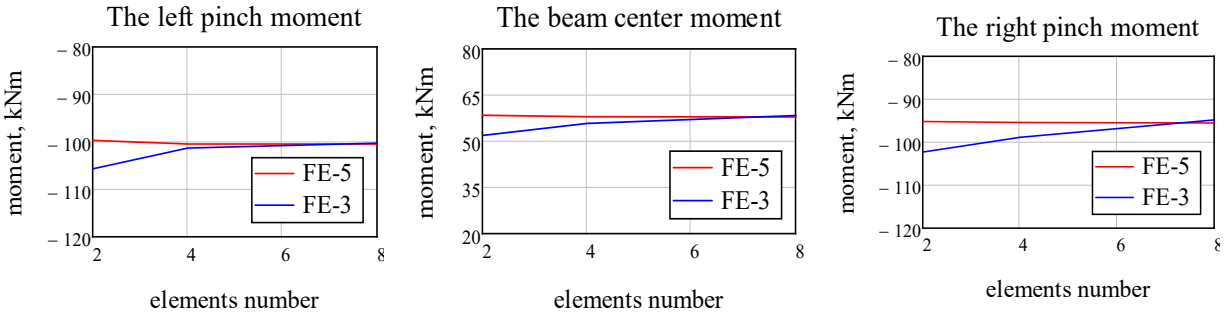

a **b** **c**

Figure 9. The bending moments in the inclined beam at q_z = 40 kN/m.

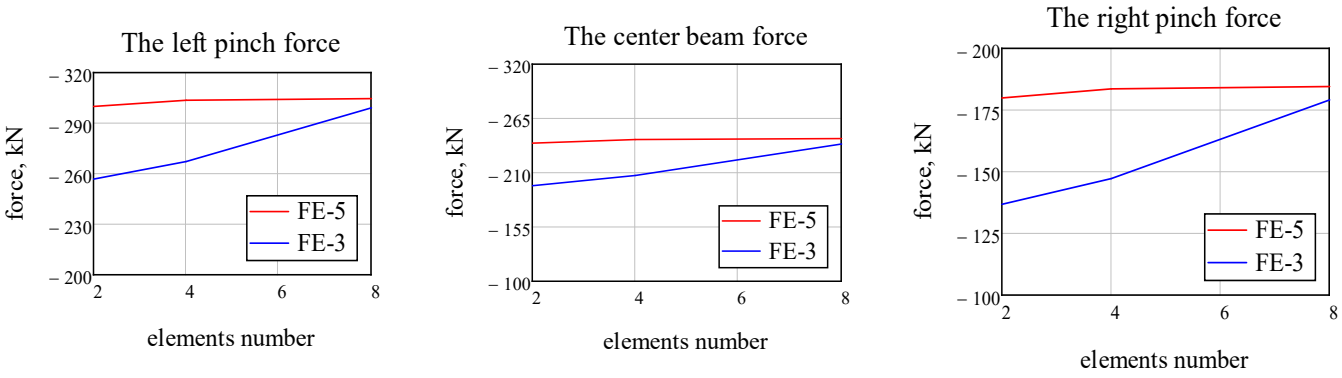

a **b** **c**

Figure 10. The longitudinal forces in the inclined beam at q_z = 40 kN/m.

Comparing the calculation results shown in Fig. 8–10, the following conclusions can be drawn:

- when using FE-5, the displacements magnitude, bending moments and longitudinal forces practically do not depend on the elements number into which the beam is divided;
- when refining the finite element mesh, the solutions obtained for FE-3 tend to the solutions obtained for FE-5;
- the greatest difference between the two solutions is observed for the longitudinal forces magnitudes; for a more accurate longitudinal forces calculation using FE-3, a mesh of at least eight elements is required;
- in contrast to the linear calculation, there is no coincidence of bending moments and displacements at nodal points obtained using finite elements FE-5 and FE-3;
- with four finite elements mesh, the differences in the bending moments values do not exceed 5 %, and for longitudinal forces they can be more than 15 %.

Next, we compare the reinforcing bars stress values. Fig. 11–13 show the reinforcing bars stress values for the support sections and the center of the inclined reinforced concrete beam for various options for beam dividing on the finite elements under the load action. It should be noted that the reinforcement stresses obtained for finite elements FE-3 and FE-5 differ more significantly, compared to the difference of the bending moments and longitudinal forces values. Bending moments and longitudinal forces differ little with the eight finite elements mesh, and the stresses in tensile reinforcement of the left and right support sections, in this case, differ by 27–28 % (Table 6). These calculation results are consistent with the results obtained from linear calculations, which showed that when we use FE-3, deformations and curvatures are calculated less accurately than moments and longitudinal forces.

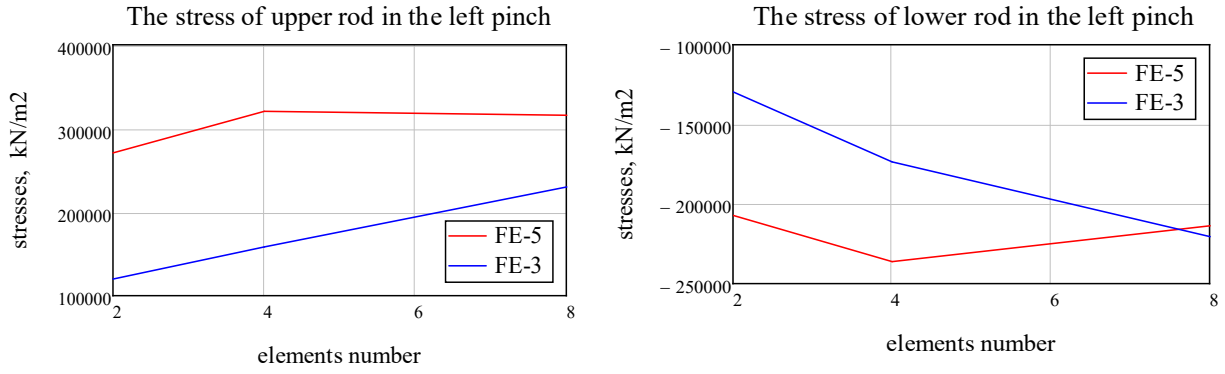

a **b**

Figure 11. The stresses of the reinforcement rods in the left pinch.

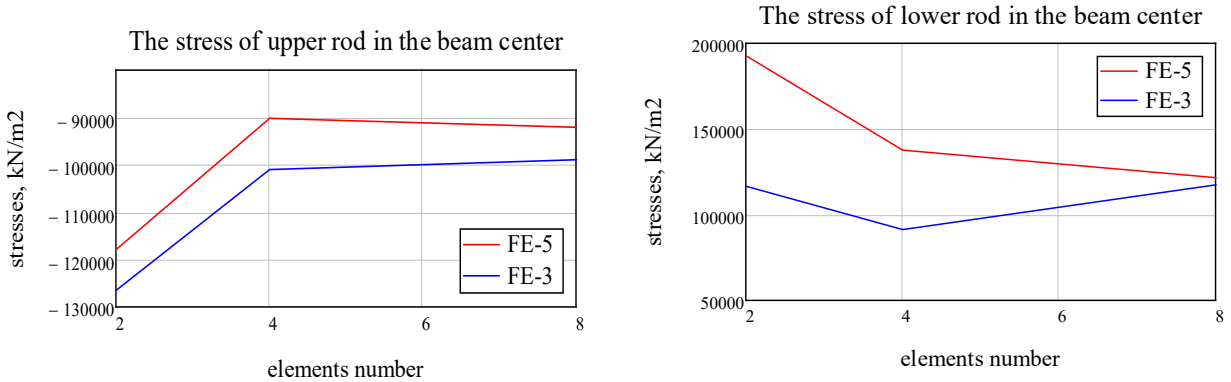

a **b**

Figure 12. The stresses of the reinforcement rods in the beam center.

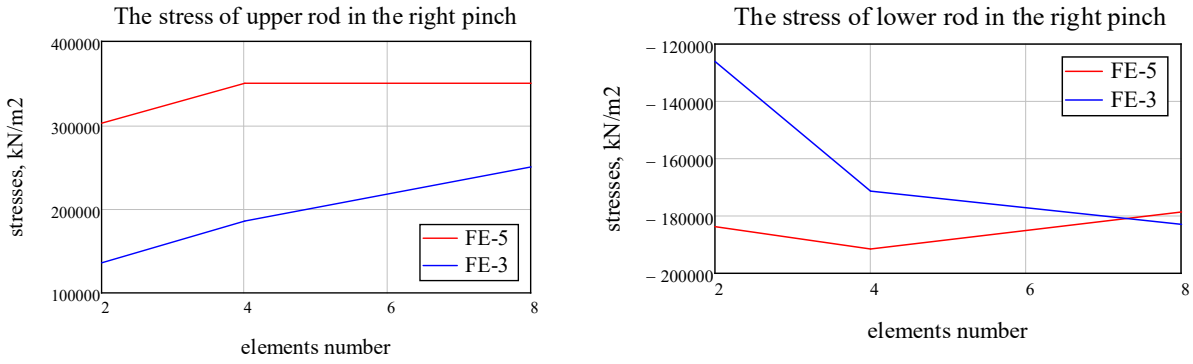

a **b**

Figure 13. The stresses of the reinforcement rods in the right pinch.

***Table 6. The upper reinforcing bars stresses of the support sections,* kN/m^2.**

Number of finite elements	The upper rod stress of the left pinch, kN/m^2			The upper rod stress of the right pinch, kN/m^2		
	FE-3	FE-5	Difference, %	FE-3	FE-5	Difference, %
2	119800	270700	55.7	135900	302400	55.1
4	158300	320400	50.6	185700	350000	46.9
8	230000	315700	27.1	250300	350000	28.5
16	280400	312665	10.3	313085	350000	10.5
32	297195	311805	4.7	337185	350000	3.7

Table 6 shows the tensile reinforcing bars stress values of support sections for various finite elements numbers. The values given in Table 6 show that to obtain a reasonably accurate value we must use four FE-5 or 32 FE-3. Obviously, the differences in stress are determined by the inaccuracy of calculating curvature and longitudinal strain when we use FE-3. FE-5 allows you to calculate more accurately strains of reinforcement and concrete, which is necessary to determine the level of load leading to failure. The stress values of the stretched reinforcement on the support and, therefore, the deformations obtained when we use FE-3 are less than the corresponding stresses calculated when we use FE-5. Therefore, the solution obtained on the basis of FE-3 will determine overestimated failure load values, which will be shown below.

The comparative inclined beam (Fig. 4b) calculations were performed with a gradual load increasing until the tensile reinforcement had reached the yield strength at the support and span sections. The beam was divided into 8 finite elements.

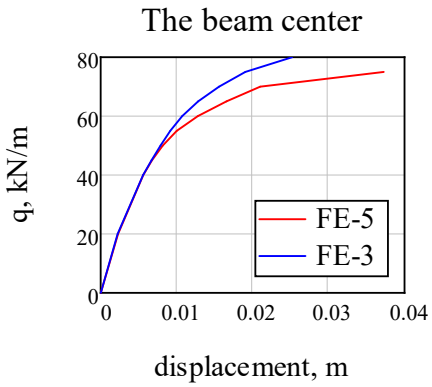

Figure 14. The vertical displacement of inclined beam center.

Fig. 14 shows the vertical displacement changes graph of the beam middle with load increasing. As is known, the system displacements obtained on the Lagrange functional basis when the mesh is refined tends to exact values from below. The approximation to exact values is achieved by increasing the total degrees of freedom number. FE-5 has a greater degrees of freedom number of the nodes compared to the FE-3, therefore, with the same finite element mesh, it gives a more pliable and closer to accurate solution. In addition, the ultimate load obtained using FE-5 is q_z = 75 kN/m, and that obtained using FE-3 is

q_z = 80 kN/m. The ultimate loads differ by about 7 %, and the displacements at the ultimate load differ by 30 %.

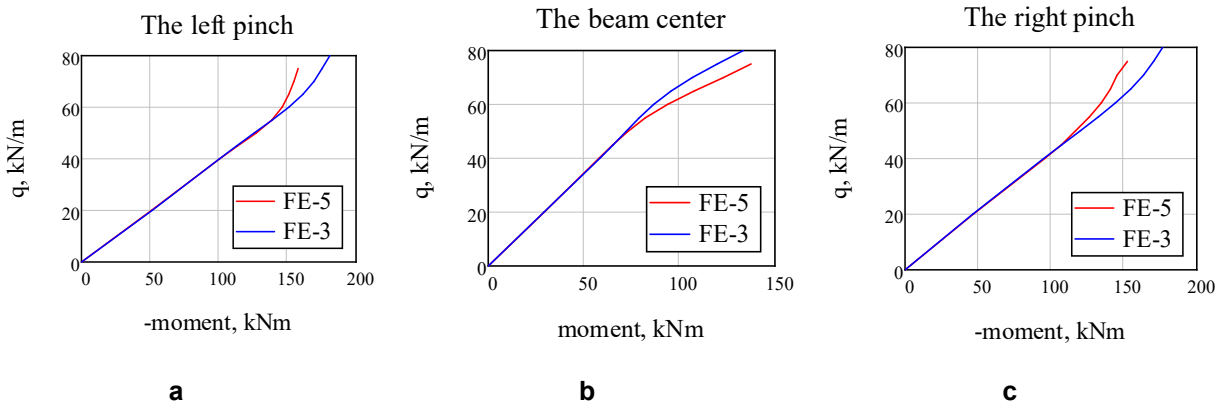

Figure 15. The moments in the inclined beam (Fig. 4b).

The bending moments of support sections that arise after the tensile reinforcement yielding onset when we calculated with FE-5 were less than the corresponding moments obtained when we used FE-3 (Fig. 15). Accordingly, the midspan bending moments (Fig. 15b) for FE-5 were larger than those for FE-3. Thus, after the plastic deformations formation, the bending moments' distribution along the beam length becomes different for the two finite elements types, in contrast to the elastic stage of the deformations.

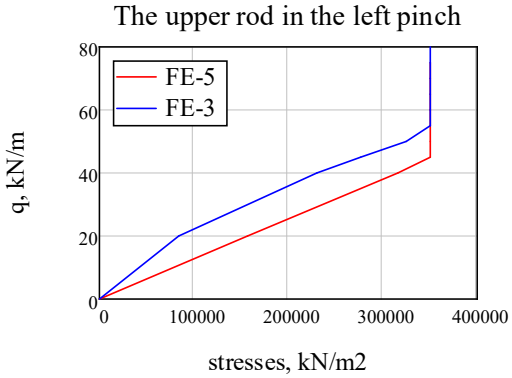

Figure 16. The stress of the upper rod in the left pinch.

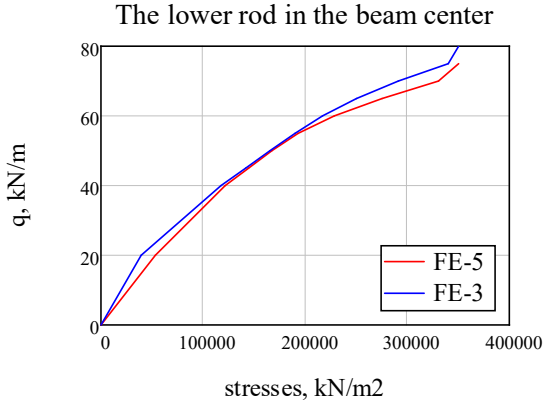

Figure 17. The stress of the lower rod in the beam center.

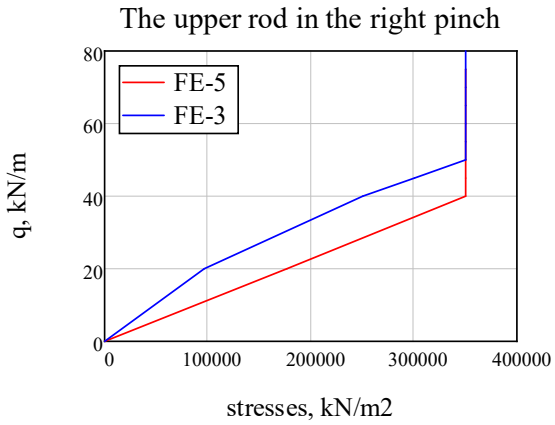

Figure 18. The stress of the upper rod in the right pinch.

Figs. 16–18 show the tensile reinforcement stresses change of the support sections and span middle with an increase of the distributed load to the maximum level. At the same load level, the reinforcing bars stresses of the reference section obtained using FE-5 are greater than the corresponding stresses calculated using FE-3. For example, under load the stresses difference was 21 %. Note that, accordingly, the tensile reinforcement plastic deformations for FE-5 began at a lower load.

4. Conclusions

1. When performing linear calculations, the bending moments, longitudinal forces and displacements do not depend on the number of FE-5 into which the clamped beam is divided. Only one element can be used. For any mesh, the nodal displacements when using FE-3 are calculated accurately, and the intermediate points displacements between nodes approach the exact ones when the mesh is refined. Using FE-5, due to additional degrees of freedom, leads to the displacement's, axis curvature and deformations refinements of the intermediate sections between the finite element nodes.
2. When solving physically nonlinear problems with refinement of the finite element mesh, the solutions obtained for FE-3 tend to the solutions obtained for FE-5. The greatest difference between the two solutions was observed for the longitudinal forces' magnitudes. To calculate more accurately longitudinal forces using FE-3, a mesh of at least eight elements was required. Unlike the linear calculation, there was no coincidence of bending moments and displacements at nodal points obtained using finite elements FE-5 and FE-3.
3. FE-5 allows more accurate calculation of deformations of the reinforcement and concrete, especially at the extreme points, which is necessary to determine the load level leading to failure. The stretched reinforcement stress values on the support and, therefore, the deformations when we used FE-3 were less than the corresponding stresses for FE-5. Therefore, the solution obtained on the basis of FE-3 will determine overestimated breaking load values.
4. The proposed beam finite element with five nodal degrees of freedom makes it possible to determine more accurately the axis curvatures and deformations, which is especially important when solving physically nonlinear problems.

References

1. Akhazhanov, S.B., Vatin, N.I., Akhmediyev, S., Akhazhanov, T., Khabidolda, O., Nurgoziyeva, A. Beam on a two-parameter elastic foundation: Simplified finite element model. Magazine of Civil Engineering. 2023. 121 (5). Article no. 12107. DOI: 10.34910/MCE.121.7
2. Apedo, K.L., Ronel, S., Jacquelin, E., Bennani, A., Massenzio, M. Nonlinear finite element analysis of inflatable beams made from orthotropic woven fabric. International Journal of Solids and Structures. 2010. 47 (16). Pp. 2017–2033. DOI: 10.1016/j.ijsolstr.2010.03.030
3. Arizou, R., Mohareb, M. Finite element formulation for distortional lateral buckling of I-beams. Engineering Structures. 2022. 262. Article no. 114265. DOI: 10.1016/j.engstruct.2022.114265
4. Basso Trujillo, P., Lagier, F., Jolin, M., Massicotte, B., Bissonnette, B. Finite element model of beam-end specimen with different qualities of reinforcing bar encapsulation. Engineering Structures. 2022. 269. Article no. 114789. DOI: 10.1016/j.engstruct.2022.114789
5. Zhu, S., Zhang, Y.X., Lee, C.K. A new finite element procedure for simulation of flexural fatigue behaviours of hybrid engineered cementitious composite beams. Engineering Structures. 2022. 269. Article no. 114839. DOI: 10.1016/j.engstruct.2022.114839

6. Bozorgmehri, B., Obrezkov, L.P., Harish, A.B., Mikkola, A., Matikainen, M.K. A contact description for continuum beams with deformable arbitrary cross-section. Finite Elements in Analysis and Design. 2023. 214. Article no. 103863. DOI: 10.1016/j.finel.2022.103863
7. Fortuna, B., Turk, G., Schnabl, S. A new locking-free finite element for N-layer composite beams with interlayer slips and finger joints. Finite Elements in Analysis and Design. 2023. 220. Article no. 103936. DOI: 10.1016/j.finel.2023.103936
8. Capdevielle, S., Grange, S., Dufour, F., Desprez, C. A shear warping kinematic enhancement for fiber beam elements with a damaging cross-section. Finite Elements in Analysis and Design. 2021. 195. Article no. 103559. DOI: 10.1016/j.finel.2021.103559
9. Čas, B., Saje, M., Planinc, I. Non-linear finite element analysis of composite planar frames with an interlayer slip. Computers & Structures. 2004. 82 (23–26). Pp. 1901–1912. DOI: 10.1016/j.compstruc.2004.03.070
10. Guo, A., Sun, Z., Satyavolu, J. Experimental and finite element analysis on flexural behavior of mortar beams with chemically modified kenaf fibers. Construction and Building Materials. 2021. 292. Article no. 123449. DOI: 10.1016/j.conbuildmat.2021.123449
11. Liao, Q., Yu, J.T., Su, Y.R., Yu, K.Q. Shear failure mechanism and parametric study for seawater sea-sand engineered cementitious composites beams reinforced by FRP bars: Finite element analysis. Construction and Building Materials. 2023. 407. Article no. 133497. DOI: 10.1016/j.conbuildmat.2023.133497
12. Lin, Y., Yan, J., Wang, Z., Zou, C. Experimental study, finite element simulation and theoretical analysis on failure mechanism of steel-concrete-steel (SCS) composite deep beams with UHPC. Engineering Structures. 2023. 286. Article no. 116124. DOI: 10.1016/j.engstruct.2023.116124
13. Nuguzhinov, Zh., Vatin, N., Bakirov, Zh., Khabidolda, O., Zholmagambetov, S., Kurokhtina, I. Stress-strain state of bending reinforced beams with cracks. Magazine of Civil Engineering. 2020. 97 (5). Article no. 9701. DOI: 10.18720/MCE.97.1
14. Kamiński, M., Supeł, Ł. Elastic critical moment for bisymmetric steel profiles and its sensitivity by the finite difference method. International Journal of Applied Mechanics and Engineering. 2016. 21 (1). Pp. 37–59. DOI: 10.1515/ijame-2016-0003
15. Mostafa, A.A.B., Razaqpur, A.G. Finite element model for predicting post delamination behaviour in FRP-retrofitted beams in flexure. Construction and Building Materials. 2017. 131. Pp. 195–204. DOI: 10.1016/j.conbuildmat.2016.11.066
16. Li, X., Li, L., Zhou, M., Wan, S., Chen, J., Kang, A. Refined beam finite element model for thin-walled multi-cell box girders considering distortion and secondary distortional moment deformation effect. Engineering Structures. 2024. 298. Article no. 117042. DOI: 10.1016/j.engstruct.2023.117042
17. Li, X., Wan, S., Zhang, Y., Zhou, M., Mo, Y. Beam finite element for thin-walled box girders considering shear lag and shear deformation effects. Engineering Structures. 2021. 233. Article no. 111867. DOI: 10.1016/j.engstruct.2021.111867
18. Zhu, L., Su, R.K.-L., Li, M.J. Finite beam element with 26 DOFs for curved composite box girders considering constrained torsion, distortion, shear lag and biaxial slip. Engineering Structures. 2021. 232. Article no. 111797. DOI: 10.1016/j.engstruct.2020.111797
19. Lolić, D., Zupan, D., Brojan, M. A consistent finite element formulation for laminated composites with nonlinear interlaminar constitutive law. Composite Structures. 2020. 247. Article no. 112445. DOI: 10.1016/j.compstruct.2020.112445
20. Harish, A.B., Matikainen, M.K. Alleviation techniques for volumetric locking in elements based on the absolute nodal coordinate formulation. Finite Elements in Analysis and Design. 2023. 224. Article no. 103990. DOI: 10.1016/j.finel.2023.103990
21. Hoffmeyer, D., Damanpack, A.R. Bending and torsion induced stresses in cylindrically orthotropic and inhomogeneous timber beams. Finite Elements in Analysis and Design. 2024. 229. Article no. 104072. DOI: 10.1016/j.finel.2023.104072
22. Hu, Y.J., Liu, M., Zhu, W., Jiang, C. An adaptive differential quadrature element method for large deformation contact problems involving curved beams with a finite number of contact points. International Journal of Solids and Structures. 2017. 115–116. Pp. 200–207. DOI: 10.1016/j.ijsolstr.2017.03.020
23. Lalin, V.V., Dmitriev, A.N., Diakov, S.F. Nonlinear deformation and stability of geometrically exact elastic arches. Magazine of Civil Engineering. 2019. 89 (5). Pp. 39–51. DOI: 10.18720/MCE.89.4
24. Murin, J., Aminbaghai, M., Hrabovsky, J., Gogola, R., Kugler, S. Beam finite element for modal analysis of FGM structures. Engineering Structures. 2016. 121. Pp. 1–18. DOI: 10.1016/j.engstruct.2016.04.042
25. Santos, H.A.F.A., Silberschmidt, V.V. Hybrid equilibrium finite element formulation for composite beams with partial interaction. Composite Structures. 2014. 108. Pp. 646–656. DOI: 10.1016/j.compstruct.2013.09.062
26. Schnabl, S., Saje, M., Turk, G., Planinc, I. Locking-free two-layer Timoshenko beam element with interlayer slip. Finite Elements in Analysis and Design. 2007. 43 (9). Pp. 705–714. DOI: 10.1016/j.finel.2007.03.002
27. Skrinar, M. Computational analysis of multi-stepped beams and beams with linearly-varying heights implementing closed-form finite element formulation for multi-cracked beam elements. International Journal of Solids and Structures. 2013. 50 (14–15). Pp. 2527–2541. DOI: 10.1016/j.ijsolstr.2013.04.005
28. Rybakov, V.A., Lalin, V.V., Ivanov, S.S., Azarov, A.A. Coordinate functions quadratic approximation in V.I. Slivker's semi-shear stability theory. Magazine of Civil Engineering. 2019. 89 (5). Pp. 115–128. DOI: 10.18720/MCE.89.10
29. Tyukalov, Yu.Ya. Calculation of circular plates with assuming shear deformations. IOP Conference Series: Materials Science and Engineering. 2019. 687 (3). Article no. 033004. DOI: 10.1088/1757-899X/687/3/033004
30. Tyukalov, Yu.Ya. Method of plates stability analysis based on the moments approximations. Magazine of Civil Engineering. 2020. 95 (3). Pp. 90–103. DOI: 10.18720/MCE.95.9
31. Tyukalov, Yu.Ya. Arbitrary quadrangular finite element for plates with shear deformations. Magazine of Civil Engineering. 2021. 107 (7). Article no. 10707. DOI: 10.34910/MCE.107.7
32. Tyukalov, Yu.Ya. Refined finite element of rods for stability calculation. Magazine of Civil Engineering. 2018. 79 (3). Pp. 54–65. DOI: 10.18720/MCE.79.6
33. Walls, R., Viljoen, C., de Clercq, H. A nonlinear, beam finite element with variable, eccentric neutral axis. Engineering Structures. 2019. 187. Pp. 341–351. DOI: 10.1016/j.engstruct.2019.02.056
34. Zhao, Y., Yuan, Y., Wang, C.L., Meng, S. Experimental and finite element analysis of flexural performance of steel-timber composite beams connected by hybrid-anchored screws. Engineering Structures. 2023. 292. Article No. 116503. DOI: 10.1016/j.engstruct.2023.116503

35. Zhang, X., Li, Z. Shear behaviour of stiffened hollow glulam beams: Experiments, analytical model, and finite element analysis. Construction and Building Materials. 2023. 392. Article Nno. 131826. DOI: 10.1016/j.conbuildmat.2023.131826
36. Zhang, X., Luo, L., Xie, X., Zhang, Y., Li, Z. Flexural bearing capacity and stiffness of stiffened hollow glulam beams: Experiments, finite element analysis and calculation theory. Construction and Building Materials. 2022. 345. Article no. 128407. DOI: 10.1016/j.conbuildmat.2022.128407
37. Gallagher, R.H. Finite element analysis: fundamentals. N.J.: Englewood Cliffs, 1975. 416 p.

Contacts:

Yury Tyukalov, *Doctor of Technical Sciences*
ORCID: https://orcid.org/0000-0001-6184-2365
E-mail: yutvgu@mail.ru

Received 23.11.2023. Approved after reviewing 11.06.2024. Accepted 11.06.2024.

Magazine of Civil Engineering

ISSN 2712-8172

journal homepage: http://engstroy.spbstu.ru/

Research article

UDC 624

DOI: 10.34910/MCE.128.3

Compressible soil thickness and settlement prediction using elastoviscoplastic models: a comprehensive method

A. Vasenin[1], ***M.M. Sabri***[2] ✉

[1] *PI Georekonstruktsiya, St. Petersburg, Russian Federation*

[2] *Peter the Great St. Petersburg Polytechnic University, St. Petersburg, Russian Federation*

✉ *mohanad.m.sabri@gmail.com*

Keywords: long-term settlements, soft soils, creep behavior, undrained shear strength, numerical analysis, elastoviscoplastic models, structural foundation design

Abstract. The paper is dedicated to developing a comprehensive analysis method of the criteria for defining the compressible thickness critical for estimating long-term settlements in buildings and structures situated on soft soils, focusing on their creep behavior. This study introduces an engineering method grounded on the criterion of soil's undrained condition within the mass, considering both elastic and residual deformations through equivalent creep deformations. Unlike previous methodologies, the proposed method facilitates the assessment of long-term settlements by incorporating creep effects over time, employing undrained shear strength for both normally consolidated and overconsolidated soils. The method enables settlement calculations based on static-sounding data, enhancing predictions' accuracy and reliability. This research endeavors to broaden the application of numerical and analytical calculations in real-world practices, employing elastoviscoplastic soil models to design structures on weak foundations.

Funding: This research was supported by the Russian Science Foundation grant No. 22-79-10021 “Strengthening foundations and waterproofing foundations of buildings and structures with self-healing injection materials”. Available online: https://rscf.ru/project/22-79-10021/.

Citation: Vasenin, A., Sabri, M.M. Compressible soil thickness and settlement prediction using elastoviscoplastic models: a comprehensive method. Magazine of Civil Engineering. 2024. 17(4). Article no. 12803. DOI: 10.34910/MCE.128.3

1. Introduction

Understanding the intricate behavior of soils and rocks in their natural state is significant in geotechnical engineering, as it aids in designing and implementing earth structures and foundations. A vital aspect of this comprehension is the ability to predict the long-term settlements of structures built on soft soils, which requires a sophisticated understanding of soil behavior under different loading conditions [1,2]. This research builds upon significant advancements in the elastoviscoplastic soil model, incorporating the viscoelastic and plastic deformation characteristics to improve settlement predictions. The model's capability to encapsulate the viscoelastic and plastic behavior of soils over time represents a pivotal advancement in geotechnical engineering, particularly for structures built on compressible soil layers [3].

The necessity of this study is underscored by the demand for accurate and reliable models during the design and construction phases of infrastructure projects on soft soils. Traditional models often fail to capture the intricate and time-dependent behavior of soils, which can result in inaccuracies in settlement predictions. This research aims to enhance the criteria for determining the thickness of compressible soils and apply an elastoviscoplastic model, thus establishing a more robust framework for predicting soil settlements. This effort is expected to contribute to developing safer and more durable infrastructure [4].

Supported by a broad spectrum of literature, the foundation of the proposed approach signifies the continuous evolution of soil modelling techniques and their application within geotechnical engineering. The calibration and validation of elastoviscoplastic soil models have been instrumental in providing critical insights into the behavior of Resedimented Boston Blue Clay under diverse loading conditions, serving as a benchmark for the model's development [3]. The work by Ter-Martirosyan [5] defining the parameters of such models further informs this research's methodology, emphasizing the importance of precise parameterization for accurate soil behavior representation.

Furthermore, research on probabilistic approaches to compressible soil thickness [6] and assessing liquefiable soil layers [7] have introduced a statistical perspective to understanding soil consolidation processes, offering a complementary viewpoint to this study. Studies on the behavior of deformable soil media under compaction [8] enhance the understanding of soil-structure interaction, particularly in road construction. Examination of soil-reinforcement interaction parameters [9] provides valuable context for evaluating the performance of structures built on compressible subgrades, thus significantly enriching the research framework.

Wroth's study [10] laid the groundwork for understanding the natural state of geotechnical materials under various conditions. This foundation is crucial for designing and implementing effective earth structures and foundation systems, enabling engineers to predict, how soil and rock will behave under different loads.

The introduction of a soft soil model by Vermeer and Neher [11], which accounts for creep, represents a significant advancement in computational geotechnics. This model allows for more precise simulations of time-dependent soil deformation, enhancing the ability to predict long-term settlements of structures on soft soils. Such a model is vital for designing and maintaining durable infrastructure on challenging ground conditions.

Schmidt's research [11] into earth pressures at rest and their relation to stress history has deepened the understanding of soil mechanics. By highlighting the influence of past stresses on current geostatic conditions, Schmidt's work aids in accurately assessing the stability and safety of geotechnical structures.

Perzyna's exploration [12] of fundamental problems in viscoplasticity laid the theoretical groundwork for analyzing materials that exhibit viscous and plastic behavior under stress. This theory is crucial for modelling the behavior of geotechnical materials under load, contributing to the design of structures that can withstand the complexities of real-world conditions.

The practical application of theoretical frameworks is exemplified by Khankelov [13] through their modelling of segmental excavator working tools for soil compaction. This work showcases integrating research findings into engineering practices, demonstrating, how theoretical models can be applied to solve practical engineering problems, thereby improving construction techniques and equipment.

Advancements in unified constitutive models have ultimately contributed to safer and more efficient infrastructure designs. These developments closely align with ongoing efforts to refine elastoviscoplastic models, which are crucial for enhancing the accuracy of settlement predictions in soft soils. As the field continues to evolve, these sophisticated models are becoming indispensable tools for geotechnical engineers, enabling them to address complex soil-structure interactions and ensure the stability and longevity of constructions built on challenging ground conditions [14-18].

The current study aims to develop an elastoviscoplastic soil model to refine settlement prediction accuracy.

2. Methods

2.1. Basic equations of the elastoviscoplastic model of the soil environment and the criterion of compressible thickness

The deformation components for elastoviscoplastic soil models are determined by the sum of elastic ε_{ij}^{e} and viscoplastic deformations ε_{ij}^{vp}:

$$\varepsilon_{ij} = \varepsilon_{ij}^{e} + \varepsilon_{ij}^{vp}. \quad (1)$$

Let us consider the criterion for limiting the compressible thickness under the conditions of a one-dimensional problem.

For the rate of viscoplastic deformation in the one-dimensional case, the general relation is valid:

$$\dot{\varepsilon}_{v,c} = \frac{\mu^*}{\tau}\left(\frac{p^{eq}}{p^{eq}_{p,new}}\right)^{\beta} = \dot{\varepsilon}_{NC}\left(\frac{p^{eq}}{p^{eq}_{p,new}}\right)^{\beta}; \quad (2)$$

$$\beta = \frac{\lambda^* - k^*}{\mu^*}. \quad (3)$$

By integrating equation (2), subject to constant effective stresses, we can obtain expressions for the increment of relative volumetric strain in the form:

$$\Delta\varepsilon_{vc} = \mu^* \ln\left(1 + \int_0^t \left(\frac{p^{eq}}{p^{eq}_{p,new}}\right)^{\beta} \frac{1}{\tau_{ref}} d\tau\right) = \mu^* \ln\left(1 + \frac{1}{\tau_{ref}}\left(\frac{p^{eq}}{p^{eq}_{p,new}}\right)^{\beta}\right). \quad (4)$$

By equating the logarithm of the second term to zero in equation (4), we can obtain a criterion for limiting the compressible thickness (hereinafter, $\tau_{ref} = \tau$):

$$\frac{t}{\tau}\left(\frac{p^{eq}}{p^{eq}_{p,new}}\right)^{\beta} = 1. \quad (5)$$

The value of the current equivalent volumetric pressure will be:

$$p^{eq} = p^{eq}_{p,new}\left(\frac{\tau}{t}\right)^{\frac{1}{\beta}}; \quad (6)$$

$$p^{eq}_{p,new} = p^{eq}_{p} \exp\left(\frac{\varepsilon^c_v}{\lambda^* - k^*}\right), \quad (7)$$

ε^c_v – volumetric plastic deformation at the loading step.

The resulting defining equation turns out to be expressed through a new value of over-consolidation pressure $p^{eq}_{p,new}$, which, according to (7), in turn, depends on the accumulated value of viscoplastic deformation. Meanwhile, the equation for the components of the viscoplastic deformation rate can be expressed through the reference value of the over-consolidation pressure p^{eq}_{p} (determined during standard compression tests) considering (31) in the form of the equation:

$$\dot{\varepsilon}_{v,c} = \frac{\mu^*}{\tau}\left(\frac{p^{eq}}{p^{eq}_{p,new}}\right)^{\beta} = \frac{\mu^*}{\tau}\left(\frac{p^{eq}}{p^{eq}_{p}}\right)^{\beta} \exp\left(\frac{-\varepsilon^c_v}{\mu^*}\right). \quad (8)$$

Since when deriving equation (6), it was assumed that the increments of creep strains should be reduced to zero, the indicated equation can be reduced to the form:

$$p^{eq} = p^{eq}_{p,t} = p^{eq}_{p}\left(\frac{\tau}{t}\right)^{\frac{1}{\beta}}. \quad (9)$$

The current value of the equivalent volume pressure during loading is determined by equation (9) since the loading vector (one-dimensional case) is located on the K_0 line:

$$p^{eq}_{p} = \frac{\left(1 + 2K_{0,NC}\right)\sigma_{zc}}{3}\left[1 + \left(\frac{\eta K_0}{M_{cs}}\right)^2\right]; \quad (10)$$

$$p^{eq}=\left(p_0+\Delta p\right)\left[1+\left(\frac{\eta K_0}{M_{cs}}\right)^2\right]=\frac{\left(1+2K_{0,NC}\right)\left(\sigma_{zg}+\sigma_{zp}\right)}{3}\left[1+\left(\frac{\eta K_0}{M_{cs}}\right)^2\right]; \tag{11}$$

$$\eta K_0=\frac{3\left(1-K_{0,NC}\right)}{1+2K_{0,NC}}; \tag{12}$$

$$OCR=\frac{\sigma_{zc}}{\sigma_{zg}}. \tag{13}$$

Substituting (10–13) into (9) express the known criterion for limiting the compressible thickness [19,20]:

$$\sigma_{zp}=\sigma_{zg}\left[OCR\left(\frac{\tau}{t}\right)^{\frac{1}{\beta}}-1\right]. \tag{14}$$

The criterion for limiting the compressible thickness, expressed by (14), makes it possible to calculate settlement in one-dimensional conditions in time at the stage of completion of consolidation as for an elastoplastic medium according to the relation:

$$S\left(t>t_{eop}\right)=$$

$$=\begin{vmatrix}\int_0^H\frac{C_r}{1+e_0}\lg\left(\frac{\sigma_{zp,i}+\sigma_{zg,i}}{\sigma_{zg,i}}\right) & \text{at} & \frac{\sigma_{zp,i}+\sigma_{zg,i}}{\sigma_{zc,ref}}\left(\frac{t}{\tau}\right)^{\frac{C_a}{C_c-C_r}}<1\\ \int_0^H\frac{C_r}{1+e_0}\lg\left(\frac{\sigma_{zc,ref}}{\sigma_{zg,i}}\left(\frac{t}{\tau}\right)^{\frac{C_a}{C_c-C_r}}\right)+\int_0^H\frac{C_c}{1+e_0}\lg\left(\frac{\sigma_{zp,i}+\sigma_{zg,i}}{\sigma_{zc,ref}}\left(\frac{t}{\tau}\right)^{\frac{C_a}{C_c-C_r}}\right) & \text{at} & \frac{\sigma_{zp,i}+\sigma_{zg,i}}{\sigma_{zc,ref}}\left(\frac{t}{\tau}\right)^{\frac{C_a}{C_c-C_r}}\geq 1\end{vmatrix}, \tag{15}$$

where H is the depth of the compressible thickness, assigned by equation (14).

2.2. Criterion for the undrained nature of soil action

Equation (8), in general form, allows evaluating the criterion for the undrained behavior of soil in a massif under the condition that the volumetric deformation is equal to zero:

$$\varepsilon_v=\varepsilon_v^e+\varepsilon_v^{vp}=0.$$

Accordingly, in this case, the magnitude of volumetric viscoplastic deformation is determined by the expression:

$$\varepsilon_v^{vp}=-\varepsilon_v^e=-k^*\ln\left(\frac{p^{eq}}{p_0^{eq}}\right). \tag{16}$$

Substituting equation (16) into (8) leads to obtaining, by analogy with (5), the criterion equation for the undrained state of a soil mass for the case of a one-dimensional problem in the form:

$$\begin{aligned}&\frac{t}{\tau}\left(\frac{p^{eq}}{p_p^{eq}}\right)^{\beta}\left(\frac{p^{eq}}{p_0^{eq}}\right)^{\frac{k^*}{\mu^*}}=\frac{t}{\tau}\left(\frac{\sigma_{zi}}{\sigma_{zc}}\right)^{\beta}\left(\frac{\sigma_{zi}}{\sigma_{zg}}\right)^{\frac{k^*}{\mu^*}}=\\&=\frac{t}{\tau}\left(\frac{\sigma_{zp}+\sigma_{zg}}{\sigma_{zc}}\right)^{\frac{\lambda^*-k^*}{\mu^*}}\left(\frac{\sigma_{zp}+\sigma_{zg}}{\sigma_{zg}}\right)^{\frac{k^*}{\mu^*}}=1.\end{aligned} \tag{17}$$

By analogy with equation (14), a criterion for the undrained nature of work in a soil massif could be obtained in the form of a relation:

$$\sigma_{zp} = \sigma_{zg}\left[OCR^{\frac{\lambda^* - k^*}{\lambda^*}} \left(\frac{\tau}{t}\right)^{\frac{\mu^*}{\lambda^*}} - 1 \right] = \sigma_{zg}\left[OCR^{\Lambda} \left(\frac{\tau}{t}\right)^{\frac{\mu^*}{\lambda^*}} - 1 \right]; \quad (18)$$

$$\Lambda = \frac{\lambda^* - k^*}{\lambda^*}. \quad (19)$$

The two-component equation (15) for calculating settlement is determined by the accepted relation (1), which expresses the volumetric deformation as the sum of elastic and creep deformation. In Fig. 1 the trajectory for calculating the settlement under the two-component expression (15) is shown in blue color.

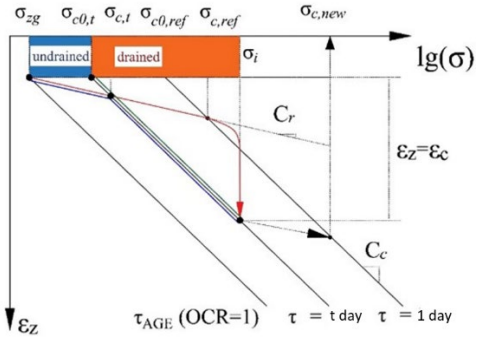

Figure 1. Scheme for determining settlement under one-dimensional conditions.

On the other hand, the total amount of strain can be expressed as a relation in which the equivalent amount of creep strain determines the total amount of strain:

$$\varepsilon_{ij} = \varepsilon_{ij}^{vp}. \quad (20)$$

In this case, the equation for calculating the settlement will take the form (the trajectory is shown in Fig. 1 in green):

$$S\left(t > teop\right) = \int_0^H \frac{C_c}{1+e_0} \lg\left(\frac{\sigma_{zp,i} + \sigma_{zg,i}}{\sigma_{c0,t}}\right) = \int_0^H \frac{C_c}{1+e_0} \lg\left(\frac{\sigma_i}{\sigma_{c0,t}}\right). \quad (21)$$

In equation (21), the symbol σ_i denotes the sum of household and additional effective stresses in the skeleton of the soil massive (Fig. 1).

In equation (21) the concept of the initial value of over-consolidation pressure is introduced, corresponding to the intersection of the household stress level (from its weight) with the line of standard compaction by a horizontal line:

$$\sigma_{c0,t} = \sigma_{c0,ref}\left(\frac{\tau}{t}\right)^{\frac{C_a}{C_c}} = \sigma_{zg} OCR^{\Lambda}\left(\frac{\tau}{t}\right)^{\frac{C_a}{C_c}}. \quad (22)$$

Considering relation (21), a one-component expression for calculating settlement is obtained:

$$S\left(t > teop\right) = \int_0^H \frac{C_c}{1+e_0} \lg\left(\frac{\sigma_i}{\sigma_{c0,ref}}\left(\frac{t}{\tau}\right)^{\frac{C_a}{C_c}}\right) = \int_0^H \frac{C_c}{1+e_0} \lg\left(\frac{\sigma_i}{\sigma_{zg} OCR^{\Lambda}}\left(\frac{t}{\tau}\right)^{\frac{C_a}{C_c}}\right), \quad (23)$$

where H is the depth of the compressible thickness, assigned in accordance with equation (18).

To perform verification procedures, determining the degree of plasticity (19) is possible based on the ratio of the logarithms of the initial value of the over-consolidation pressure $\left(OCR_{0,ref}\right)$ and the over-consolidation pressure, calculated, for example, by Terzaghi's method $\left(OCR_{ref}\right)$:

$$\Lambda = \frac{\lg\left(OCR_{0,ref}\right)}{\lg\left(OCR_{ref}\right)}. \quad (24)$$

Based on the processing of several experiments for the parameter of normalized undrained strength [21,22], the following ratio was suggested:

$$\left[\frac{s_u}{\sigma'_v}\right]_{oc} = \left[\frac{s_u}{\sigma'_v}\right]_{nc} OCR^{\Lambda} = mOCR^{\Lambda}. \quad (25)$$

Considering relation (25), the amount of settlement represented by (23) takes the form of an expression depending on the value of the undrained strength of the soil and the normalized coefficient of undrained strength *m* in a normally compacted state:

$$S\left(t > teop\right) = \int_0^H \frac{C_c}{1+e_0} \lg\left[\frac{\sigma_i}{\sigma_{zg,i}} \frac{s_{u,nc}}{s_{u,oc}} \left(\frac{t}{\tau}\right)^{\frac{C_a}{C_c}}\right] = \int_0^H \frac{C_c}{1+e_0} \lg\left[\frac{\sigma_i m}{s_{u,oc}} \left(\frac{t}{\tau}\right)^{\frac{C_a}{C_c}}\right]. \quad (26)$$

Accordingly, the criterion for limiting the compressible thickness can be expressed in the form of an equation depending on the ratio of the reference values of undrained strength in overconsolidated and normally compacted states (or their normalized values for a SHANSEP type structure, equation (25)):

$$\sigma_{zp} = \sigma_{zg}\left[\frac{\left[\frac{s_u}{\sigma'_v}\right]_{oc}}{\left[\frac{s_u}{\sigma'_v}\right]_{nc}} \left(\frac{\tau}{t}\right)^{\frac{C_a}{C_c}} - 1\right] = \sigma_{zg}\left[\frac{s_{u,oc}}{s_{u,nc}} \left(\frac{\tau}{t}\right)^{\frac{C_a}{C_c}} - 1\right] = \sigma_{zg} k_{u,i}\left(t\right), \quad (27)$$

where $k_{u,i}\left(t\right)$ – the coefficient of limitation of compressible thickness (undrained work) is variable in time.

Considering (27), it is possible to obtain a general one-component expression for calculating settlement over time using two criteria for limiting the compressible thickness:

$$S\left(t > t_{eop}\right) = \begin{cases} \int_0^H \frac{C_r}{1+e_0} \lg\left(\frac{\sigma_i}{\sigma_{zg,i}}\right) & \text{at} \quad \frac{\sigma_i}{\sigma_{zg,i}\left(1+k_i\left(t\right)\right)} < 1 \\ \int_0^H \frac{C_r}{1+e_0} \lg\left(\frac{\sigma_i}{\sigma_{zg,i}\left(1+k_{u,i}\left(t\right)\right)}\right) & \text{at} \quad \frac{\sigma_i}{\sigma_{zg,i}\left(1+k_i\left(t\right)\right)} \geq 1 \end{cases}. \quad (28)$$

Undrained shear strength relationship used in (26) can often be approximated from static-sounding results.

Mayne [23], based on a correlation analysis of over-consolidation pressure and resistance to penetration of the probe cone for 49 types of clays, proposed a simple relation:

$$OCR = k\frac{q_c}{\sigma'_v}. \quad (29)$$

Here k is the proportionality coefficient, which, according to the results of statistical processing, was 0.29.

By grouping the ratios (28) and (29), the equation (30) is obtained:

$$S\left(t>t_{eop}\right)=\begin{cases}\int_0^H \dfrac{C_r}{1+e_0}\lg\left(\dfrac{\sigma_i}{\sigma_{zg,i}}\right) & \text{at} \quad \dfrac{\sigma_i}{kq_c}\left(\dfrac{t}{\tau}\right)^{\frac{C_a}{C_c-C_r}}<1 \\ \int_0^H \dfrac{C_c}{1+e_0}\lg\left(\dfrac{\sigma_i}{\sigma_{zg,i}\left[k\dfrac{q_c}{\sigma'_v}\right]^{\Lambda}}\left(\dfrac{t}{\tau}\right)^{\frac{C_a}{C_c}}\right) & \text{at} \quad \dfrac{\sigma_i}{kq_c}\left(\dfrac{t}{\tau}\right)^{\frac{C_a}{C_c-C_r}}\geq 1\end{cases} \tag{30}$$

Equation (30) can be modified based on more complex relations between overconsolidation coefficients or undrained shear strength based on static-sounding results (considering the developing pore pressure in the massif).

3. Results and Discussion

3.1. Example of Settlement Calculation using Undrained Strength Parameters

An example of calculating the settlement over time is the administrative building in the central part of St. Petersburg, erected on a slab foundation on a weak foundation (dimensions 30×25 m in plan). Fig. 2 and 3 show the physical and compression properties of the clay soils composing the site.

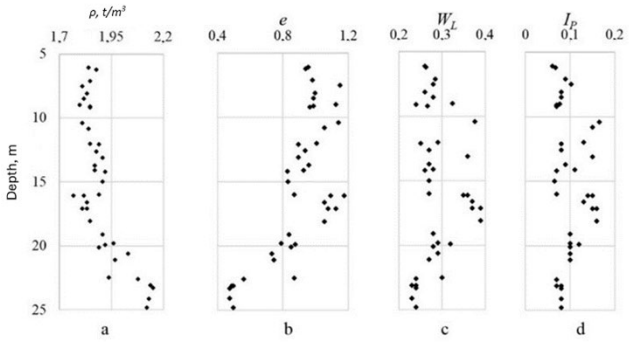

Figure 2. Physical properties of clay soils composing the site: a) density; b) porosity coefficient; c) is the moisture content at the yield boundary; d) plasticity index.

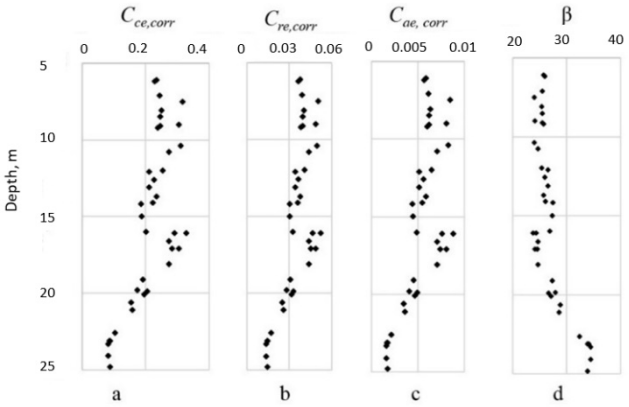

Figure 3. Properties of clay deposits according to empirical dependencies: a) compression index, b) unloading/ recompression index, c) secondary consolidation index, d) coefficient β (equation (3)).

The results of static sounding are shown in Fig. 4a.

Equations (27) and (28) for calculating settlement include the normalized parameter of undrained shear strength and the value of undrained strength in the over-consolidated state (in situ).

For approximate estimates of non-consolidated-undrained shear strength in St. Petersburg, a well-known relation can be used that uses the resistance value of the probe cone during static sounding with a constant coefficient $N_k \approx 19$:

$$C_{UUC} = \frac{q_c}{19}, \tag{31}$$

where q_c – resistance to penetration of the probe cone, kPa.

Relations (26) and (27) are valid for consolidated-undrained tests. Accordingly, it is necessary to convert non-consolidated-undrained characteristics into consolidated-undrained ones to use these equations. It can be done, for example, based on Chen's research [24], connecting isotopically unconsolidated-undrained and isotopically consolidated-undrained strengths by the ratio:

$$\frac{s_{UUC}}{s_{CIUC}} = 0.911 + 0.499\left[\frac{s_{UUC}}{\sigma'_v}\right]_{oc}. \tag{31}$$

The theoretical solution for the normalized parameter of isotropically consolidated-undrained strength in a normally compacted state will take the form:

$$m_{CIUC} = \left[\frac{s_{CIUC}}{\sigma'_v}\right]_{nc} = \frac{M}{2}\left[\frac{1}{2}\right]^{\Lambda} = \frac{3\sin(\varphi)}{3-\sin(\varphi)}\left[\frac{1}{2}\right]^{\Lambda}. \tag{32}$$

At angles of internal friction of the compressible mass of 28^0-32^0, the normalized parameter of the isotropically consolidated undrained strength will be 0.29–0.32 (Fig. 4b). Based on equation (31), the value of isotropically consolidated undrained strength can be calculated. The value of its normalized parameter is also shown in Fig. 4b.

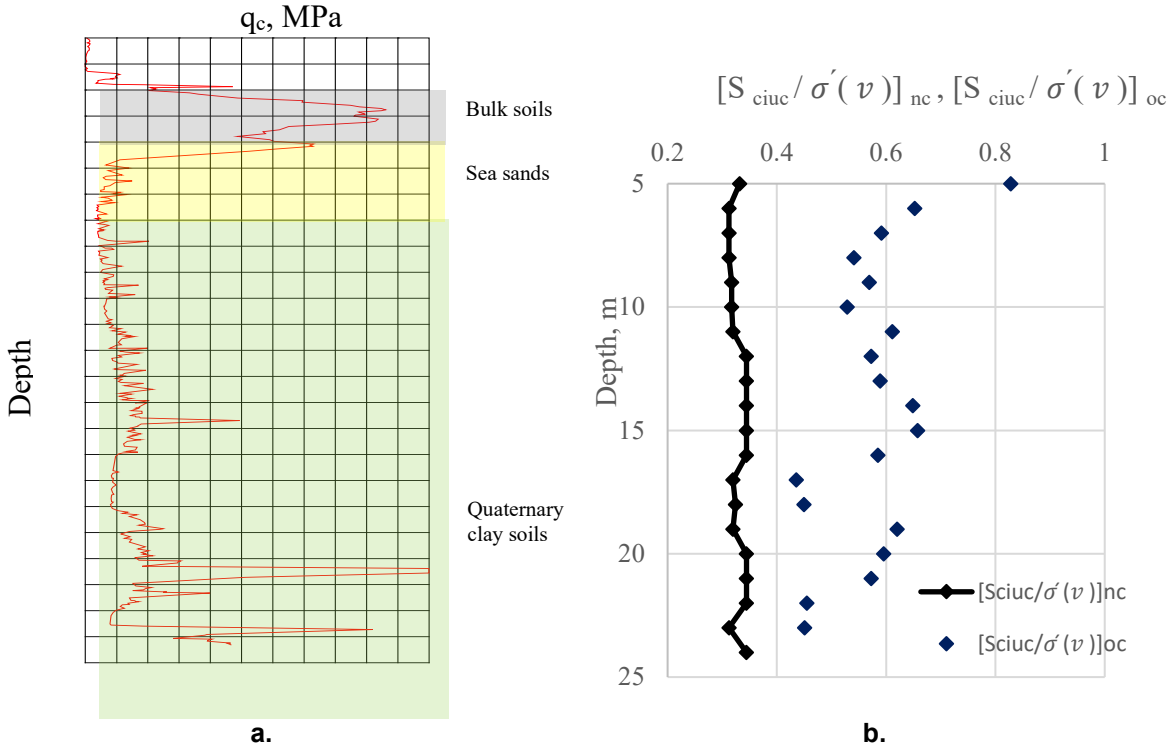

Figure 4. Engineering-geological conditions of the site: a) graph of penetration resistance to the probe cone during static sounding; b) determination of the normalized parameters of the undrained shear strength in a normally compacted and over-consolidated state (31), (32).

Using relation (25), the value of the soil mass over-consolidation coefficient can be approximated based on the ratios of the calculated normalized parameters of undrained shear strength. In general, the calculated value of the overconsolidation coefficient for the engineering-geological conditions of St. Petersburg is in reasonably good agreement with the determination based on the empirical relationship

(29) with a coefficient k = 0.28–0.29. Accordingly, the settlement of the soil mass can be calculated using equations (27) and (28), based on relation (30).

Fig. 5a and 5b show the results of calculating the total stresses in the soil mass, the reference value of the overconsolidation pressure and the value of vertical relative deformations in time (under the center of the loaded area of the slab – mainly under compression conditions).

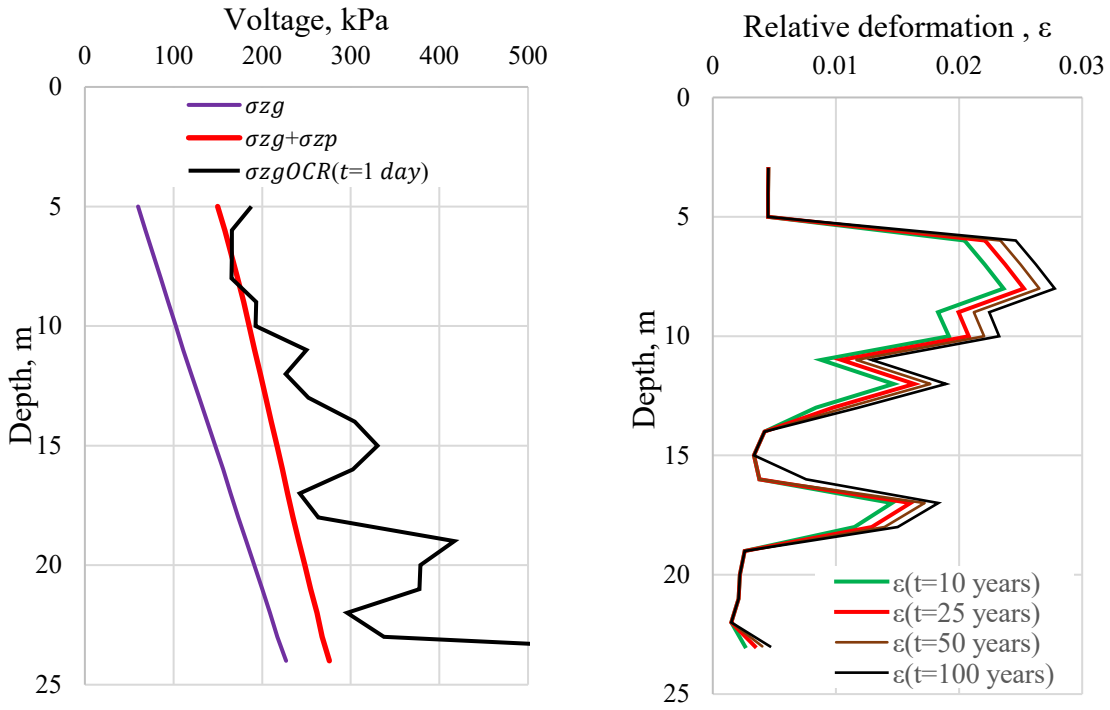

a. **b.**

Figure 5. Results of engineering calculations: a. distribution of stresses in the massif and the initial/reference value of over-consolidation pressure; b. relative vertical deformations of the massif at different times.

Fig. 6 compares observed and calculated settlements over time based on numerical solutions (soft soil creep, soft soil models) and the proposed engineering method using undrained shear strength parameters. According to the calculation results, the predicted precipitation values based on the engineering and numerical methods (according to the SSC model) are nearly 25–100 years. In the remaining (mainly initial) periods, the engineering calculation overestimates the development of settlement, which is explained by the failure to consider the phenomena of filtration consolidation (the solution was obtained at constant maximum effective stresses in the soil mass), as well as the failure to consider the construction time of the building.

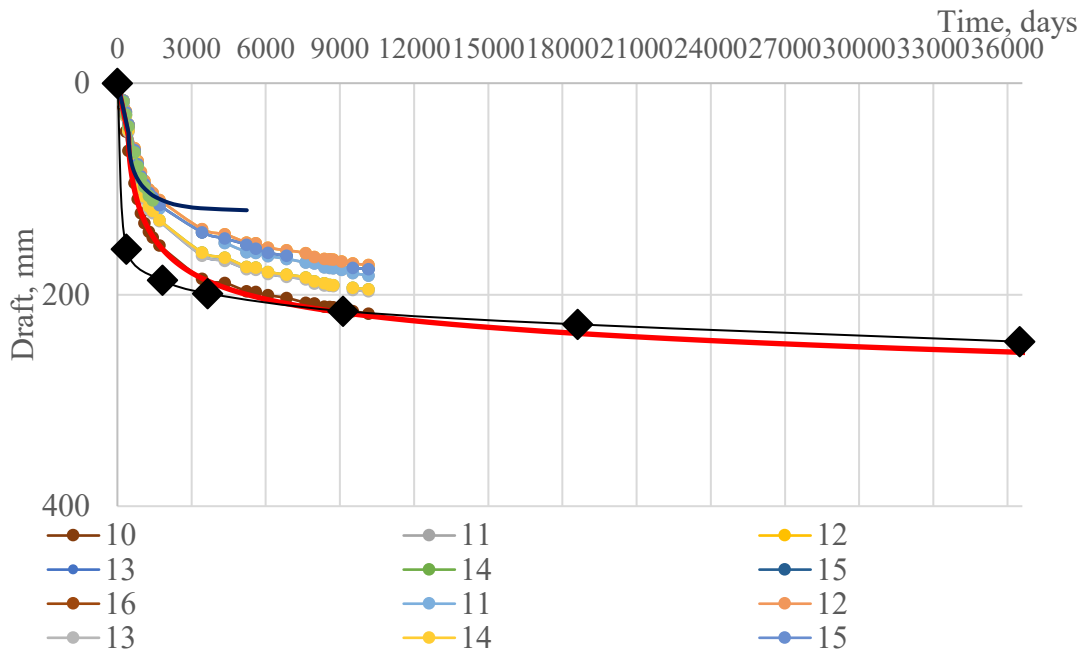

Figure 6. Comparison of calculation results based on numerical solutions (SSC, SS models) and the engineering method.

3.2. Discussion of Research Results

The presented work aims to develop an engineering method for calculating settlements of buildings and structures on weak soils. The obtained solutions make it possible to calculate long-term precipitation over time by modifying the layer-by-layer summation method.

For weak soils and additional loads comparable to the reference value of overconsolidation pressure, a one-component equation (23, 28) that already includes the elastic parts of deformations can be used to calculate settlement. The method's main advantages include the simplicity and speed of calculations and the ability to control the depth of the compressible soil mass at each calculated moment in time. The procedure for verifying the compressible layer limitation coefficients involves checking whether the calculated values are close to zero [19,20], which is especially important for thick layers of weak clayey deposits.

Considering the disturbance of natural structure of the samples, the calculated coefficients of limitation of the compressible thickness are often equal to zero or negative, leading to incorrect estimates of the degrees of deformation of the soil massif. The compressible layer limitation coefficients thus determined can be directly used to calculate settlement over time.

Values of consolidated undrained strength based on laboratory tests and indirect field methods, such as static probing, impeller testing, and dilatometric studies, can be used to perform calculations. It is possible to use a combination of these indirect field methods to calculate the settlement.

Also, an undoubted advantage of the one-component method is the possibility of using the concept of the ratio of secondary consolidation indices and compression indices in a power dependence (23, 26, 30) [25]. This approach for calculating settlement using field methods can be applied even at the soil classification level using appropriate regional correlations.

4. Conclusion

The paper provides method for calculating long-term settlements of buildings and structures on soft soils, considering their creep. Based on the results of this research, the derived conclusions are as follows:

1. A comprehensive framework (the results of which are expressed in Equations 28 - 30) has been established and validated for assessing the limit of compressible thickness in soft soils and for predicting long-term settlements through an elastoviscoplastic model (Equations 1-23), as detailed in this study.
2. The introduced elastoviscoplastic model provides a sophisticated understanding of soil mechanics under load, capturing both immediate and progressive deformations by incorporating viscoelastic and plastic characteristics of soil, thus offering an accurate representation of soil behavior under sustained loading conditions.

3. Criteria for determining the limiting compressible thickness have been developed. These criteria assist in identifying significant segments within the soil profile that are vital for settlement calculations, thereby enhancing the foundation design and evaluation processes on soft soils.
4. The precision of the model in predicting settlements has been illustrated through extensive numerical simulations. A conducted sensitivity analysis emphasizes the importance of accurate parameterization, highlighting the necessity of precise soil property determination for reliable results.
5. The practicality and reliability of the model and its criteria have been reinforced through empirical validation against real-world studies. The alignment of model predictions with observations from diverse engineering projects confirms the model's validity and potential to refine construction methodologies by enabling more informed foundational design decisions on soft soils.

This research marks a significant advancement in modelling soil behavior and predicting long-term settlements, enhancing the understanding of elastoviscoplastic soils.

References

1. Sabri, M.M., Shashkin, K.G. Soil-structure interaction: theoretical research, in-situ observations, and practical applications. Magazine of Civil Engineering. 2023. 120(4). Article no. 12005. DOI: 10.34910/MCE.120.5
2. Bezih, K., Chateauneuf, A., Demagh, R. Effect of long-term soil deformations on RC structures including soil-structure interaction. Civil Engineering Journal. 2020. 6. Pp. 2290–2311. DOI: 10.28991/cej-2020-03091618
3. Yuan, Y., Whittle, A.J. Calibration and validation of a new elastoviscoplastic soil model. International Journal for Numerical and Analytical Methods in Geomechanics. 2020. 45. Pp. 700–716. DOI: 10.1002/nag.3173
4. Desai, C.S., Sane, S.M. Rate dependent elastoviscoplastic model. Springer Series in Geomechanics and Geoengineering. 2013. Pp. 97–105. DOI: 10.1007/978-3-642-32814-5_8
5. Ter-Martirosyan, A., Manukyan, A., Ermoshina, L. Experience of determining the parameters of the elastoviscoplastic soil model. E3S Web of Conferences. 2021. 263. 02051. DOI: 10.1051/e3sconf/202126302051
6. Lee, S., Alam, M. Probabilistic compressible soil thickness from field settlement data. Proceedings of the GeoRisk. 2011. 2011/06/21.
7. Wang, Y., Fu, C., Huang, K. Probabilistic assessment of liquefiable soil thickness considering spatial variability and model and parameter uncertainties. Geotechnique. 2017. 67. Pp. 228–241.
8. Feng, S., Zhou, S., Li, H., Wei, L. A Nonlinear calculation approach of long-term settlement for pile groups in layered soft soils. Springer Series in Geomechanics and Geoengineering. 2018. Pp. 385–400. DOI: 10.1007/978-981-10-6632-0_30
9. Palmeira, E.M., Góngora, I.A.G. Assessing the influence of some soil–reinforcement interaction parameters on the performance of a low fill on compressible subgrade. Part I: Fill performance and relevance of interaction parameters. International Journal of Geosynthetics and Ground Engineering. 2015. 2. DOI: 10.1007/s40891-015-0041-3
10. Wroth, C.P. In situ measurement of initial stresses and deformation characteristics. International Journal of Rock Mechanics and Mining Sciences &amp, Geomechanics Abstracts. 1978. 15. 67. DOI: 10.1016/0148-9062(78)90214-0
11. Schmidt, B. Earth pressures at rest related to stress history. Canadian Geotechnical Journal. 1966. 3. Pp. 239–242. DOI: 10.1139/t66-028
12. Perzyna, P. Fundamental problems in viscoplasticity. Advances in Applied Mechanics. 1966. Pp. 243–377. DOI: 10.1016/s0065-2156(08)70009-7
13. Khankelov, T.K., Askarkhodzhaev, T.I., Aslanov, N.R. Modeling of segmental excavator working tool for soil compaction. E3S Web of Conferences. 2023. 401. 02052. DOI: 10.1051/e3sconf/202340102052
14. Zhu, Q.-Y., Yin, Z.-Y., Zhang, D.-M., Huang, H.-W. Numerical modeling of creep degradation of natural soft clays under one-dimensional condition. KSCE Journal of Civil Engineering. 2016. 21. Pp. 1668–1678. DOI: 10.1007/s12205-016-1026-z
15. Kimoto, S., Oka, F. An elasto-viscoplastic model for clay considering destructuralization and consolidation analysis of unstable behavior. Soils and Foundations. 2005. 45. Pp. 29–42. DOI: 10.3208/sandf.45.2_29
16. Staszewska, K., Cudny, M. Modelling the time-dependent behaviour of soft soils. Studia Geotechnica et Mechanica. 2020. 42. Pp. 97–110, DOI: 10.2478/sgem-2019-0034
17. Shu, X., Wang, Z., Peng, Y., Zhou, Z., Tian, Y. A novel elasto-viscoplastic constitutive model for predicting the embankment settlement on soft structured clay. Computers and Geotechnics. 2024. 167. DOI: 10.1016/j.compgeo.2024.106093
18. Ziotopoulou, T.J.O.R.W.B.K. A viscoplastic constitutive model for plastic silts and clays for static slope stability applications. Canadian Geotechnical Journal. 2024. DOI: 10.1139/cgj-2022-0479
19. Vasenin, V.A. Criteria for limiting the compressible thickness when calculating the settlement of foundations of buildings and structures. Part 2. Implementation of complex calculations in relation to engineering and geological conditions of St. Petersburg. Geotechnics. 2020. XII. Pp. 6–25. DOI: 10.25296/2221-5514-2020-12-3-6-25
20. Vasenin, V.A. Criteria for limiting the compressible thickness when calculating the settlement of foundations of buildings and structures. Part 1. Theoretical estimates taking into account secondary consolidation. Geotechnics. 2020. XII. Pp. 22–37. DOI: 10.25296/2221-5514-2020-12-2-22-37
21. Ladd, C.C., Germaine, J.T., Lancellotta, R., Jamiolkowski, M.B. New developments in field and laboratory testing of soils. Proceedings of the Proc. 11th ICSMFE. San Francisco, 1985. Pp. 57–153.
22. Ladd, C.C., Foott, R., Ishihara, K., Schlosser, F., Poulos, H.G. Stress deformations and strength characteristics: State of the art reports In Proceedings of the Proc. 9th ICSMFE. Tokyo, 1977. Pp. 421–494.
23. Kulhawy, F.H., Mayne, P.W. Manual on estimating soil properties for foundation designA. Publishing house of the Electric Power Research Institute, 1990.

24. Chen, Y.J., Kulhawy, F.H. Undrained strength interrelationships among CIUC , UU , and UC tests. Journal of Geotechnical Engineering. 1993. 119. Pp. 1732–1750.
25. Mesri, G., Castro, A. Cα/Cc Concept and K0 During Secondary Compression. Journal of Geotechnical Engineering. 1987. 113. Pp. 230–247. DOI: 10.1061/(asce)0733-9410(1987)113:3(230)

Information about the authors:

Vladislav Vasenin, *PhD in Technical Sciences*
E-mail: vavasenin@mail.ru

Mohanad Sabri, *PhD*
ORCID: https://orcid.org/0000-0003-3154-8207
E-mail: mohanad.m.sabri@gmail.com

Received: 26.02.2024. Approved after reviewing: 03.05.2024. Accepted: 10.06.2024.

Magazine of Civil Engineering

ISSN 2712-8172

journal homepage: http://engstroy.spbstu.ru/

Research article

UDC 622

DOI: 10.34910/MCE.128.4

Lightweight concrete containing recycled aggregates

A.A. Alani ✉

University of Anbar, Ramadi, Iraq

✉ *ahmed.anees@uoanbar.edu.iq*

Keywords: construction waste, recycled aggregate, green composites, lightweight concrete

Abstract. This study investigated the replacement of fine concrete aggregates with recycled aggregate. The results showed that the effect of recycled aggregate, so that, replacing 25, 50, 75 and 100 % of natural aggregate led to an 8, 23, 15 and 11 %, respectively, increase in the compressive strength of lightweight concrete samples. Based on these results, a microstructural analysis of the contact zone of the concrete using various types of aggregate was conducted. The shrinkage and expansion development of samples containing recycled aggregate formed from demolished waste differed from that of ordinary concrete, and the findings over 90 days indicated the impact of the substitution percentage in the recycled aggregates contained in the mixture. When 100 % fine natural aggregate was replaced with recycled aggregate, expansion increased by 15 % at 14 days and shrinkage increased by 45 % at 90 days as compared to references. Cement hydration in concrete mixes using different types of aggregates has been investigated by using an X-ray diffraction. The results showed that the sample without recycled aggregate from demolition waste LW-1 contained the maximum amount of C_3S and C_2S compared to the sample with recycled aggregate from demolition waste LW-5, which can harden when interacting with water. The concrete samples used to evaluate the abrasion resistance were first cured for 28 days. The results revealed that the abrasion Δh values for samples containing recycled aggregate were lower than that for the reference samples.

Funding: The research was financially supported by Shukhov Belgorod State Technological University (BSTU).

Acknowledgements: The author wishes to thank the College of Engineering, University of Anbar, for supplying materials to conduct the research work.

Citation: Alani, A. A. Lightweight concrete containing recycled aggregates. Magazine of Civil Engineering. 2024. 17(4). Article no. 12804. DOI: 10.34910/MCE.128.4

1. Introduction

Natural disasters and armed conflicts unfortunately can cause significant destruction to cities and infrastructure. In addition to the environmental effect and costs associated with obtaining and processing natural resources for the creation of new building materials, handling the waste from such disasters and reconstructing destroyed cities is undoubtedly a critical task. The traditional approach of using raw materials for construction can indeed have negative implications for sustainability and the principles of Green Building.

The high efficiency of using scrap concrete as a secondary concrete filler has been confirmed by numerous studies conducted in this direction. As reported in [1], the aggregates account for more than half of the material composition and up to 60–75 % of the total volume of concrete mix. Because of the increasing consumption for construction, which results in up to 48 billion tons of aggregates being used yearly for concrete production [2], the notion of using recycled concrete aggregate (RA) in the making of concrete was proposed. As compared to natural aggregate (NA), RA has 30 % lower embodied energy and

60 % lower CO_2 emissions, which makes it more environmentally friendly and promotes sustainable construction [3]. European nations have been striving to employ RA in brand-new concrete structures since the early 1980s. Several studies have been conducted that looked at recycled aggregate concrete (RC) and came to the conclusion that using RA is practical and widely acceptable [4]. Since up to 50 % of the materials used in the concrete for their contemporary constructions are recycled, Zurich, Switzerland, has been a leader in RC for more than 15 years. The percentage of non-concrete mineral components added to the concrete has been capped at 10 % in certain other nations, such as Finland and Germany [5]. In order to enhance RC's qualities and broaden its use as a respectable concrete in the building industry, numerous studies have been undertaken on the material. It is conceivable that the RC-built structures may be torn down once more at some point or for other causes, such as ongoing conflicts and natural disasters in specific regions [6–11].

According to [12], raising the strength from 30 to 40 MPa may decrease abrasion losses by approximately 17 %, while employing steel fibers with volumetric contents of 0.75 and 1.0 % can enhance abrasion resistance by over 23 %. As a multi-recycled aggregate (MRA), which is RA made from RC, will be employed in this instance, the created debris will be utilized. Concrete will be multi-recycled as a result of the application of MRA in its manufacture (MRC). There have not been many studies that have looked at the mechanical and other characteristics of MRC with various replacement amounts. By using MRA as an aggregate replacement for NA up to 100 % when studying the mechanical behavior of MRC [13, 14], it was discovered that the compressive strength was slightly decreased and that the third generation of MRC could outperform the necessary strength by at least 25 % replacement, demonstrating the beneficial influence of MRA.

Large amounts of concrete trash are created through the planned destruction of old buildings and structures, technical and natural disasters, and armed conflicts in different nations [15]. To address the seepage problem of recycled concrete, the effects of altering parent concrete strengths, the ratio of recycled aggregate, fly ash concentration, and water gel ratio were investigated using a design orthogonal experiment. Water gel ratio, matrix concrete strength, recycled aggregate replacement rate, and fly ash percentage were shown to have a significant to modest influence on the impermeability of recycled concrete [16]. According to [17–18], these wastes should primarily be used for new construction as well as repair and restoration work in their occurrence places. It is important to employ raw resources in this case, from demolished buildings and structures, to produce construction materials, including "green composites". Several papers, as is shown in [19], investigate the usefulness of recycling trash from destroyed buildings. Future research opportunities identified in [20] include:

1) detecting pollutant sources in construction and demolition waste generated by industrial structures;
2) creating complete pollution control strategies for construction waste;
3) improving construction and demolition waste recyclability;
4) creating enhanced assessment standards for debris and repurposed materials;
5) broadening the scope of demolition waste flows study;
6) establishing a demolition waste management fee scheme;
7) developing improved approaches for evaluating construction waste management performance;
8) investigating a better application of technology in demolition waste management;
9) minimizing construction waste from the beginning of the project;
10) minimizing waste from construction during the building process.

The results of this study are important not just for a better understanding of demolition waste research, but they may also help operators improve their waste management efficiency and reduce related pollutants.

The search for a more ecologically responsible strategy that has both economic and social benefits is aided, as described in [21], by the examination and use of foreign experiences in the processing of municipal solid waste and its secondary use. The rule of affinity of microstructures, which directs the selection of raw materials for composites with comparable physical and mechanical properties, is one part of this field. Composite binders with low water requirements have been developed. Their strength is roughly double that of the original cement, with 50–70 % of the crushed slag or quartz sand in its composition giving the same strength as Portland cement. It was proven that quartzite sand screening can be employed as filler in the production of fine-grained concretes [22, 23]. Based on the aforementioned, it can be concluded that the use of recycled materials from demolition waste aims to reduce costs associated with construction by making efficient use of resources and accounting for the complex influence of environmental and energy-saving factors, as well as the value of territories in urban planning [24].

The scientific innovation is that the nature of the processes of construction of samples based on recycled aggregate from fragments of demolished buildings has been conceptually established and empirically validated as a complicated polyfunctional system.

2. Materials and Methods

2.1. Materials

The binder utilized was Ordinary Portland cement (OPC) CEM I/42.5N (Belgorod cement, Russian Federation). Tables 1–2 show the chemical and mineralogical compositions, as well as the physical and mechanical properties of Portland cement. Portland cement has a specific surface area of 230–250 m^2/kg. NA from a nearby area in the Anbar governorate (Iraq) and an expanded clay fraction of 5–10 mm were used as raw materials (Fig. 1). Tables 3–5 show the characteristics of sand, gravel, and expanded clay.

Table 1. Mineralogical and chemical composition of Portland cement type CEM I/42.5N.

Chemical composition, % wt.							Mineralogical composition, % wt.			
SiO_2	CaO	MgO	Al_2O_3	Fe_2O_3	SO_3	Alkalis	C_3S	C_2S	C_3A	C_4AF
4.19	84.73	0.57	1.37	3.30	1.11	0.70	59.3	17.8	6.6	14.2

Table 2. Physical and mechanical properties of Portland cement type CEM I/42.5N.

Setting time, h:min		Flexural strength, MPa	Compressive strength, MPa		
start	end	3 d	start	end	3 d
2:25	3:28	6.2	2:25	3:28	6.2

Table 3. Characteristics of the sand used.

Characteristics	Value
Specific gravity, kg/m^3	2400
Fineness modulus	1.85
Content of dusty, clay and silt particles, % wt.	0.75
Bulk density, kg/m^3	1450
Absorption capacity, %	9.85

Table 4. Characteristics of expanded clay.

Characteristics	Value
Compressive strength, MPa	0.3–3.5
Water absorption, %	25
Freeze-thaw resistance, cycles	17
Bulk density, kg/m^3	350
Porosity, %	49

Figure 1. View of expanded clay.

The composition of the demolition and construction waste of buildings and structures in Iraq is shown in Table 5. According to the table, debris and cement concrete make up 99.88 % of the trash generated during building and demolition projects in Iraqi cities due to hostilities. In Fig. 2, the view of the crushed demolition waste is depicted.

Table 5. Demolition waste compositionю

Material	OPC	Crushed stone	Fiber	Wood	Metal	Plastic	Gypsum
Content, %	38.60	61.30	0.02	0.01	0.03	0.03	0.01

Table 6. Characteristics of the buildings and structures demolition and construction waste.

Density, kg/m^3	Bulk density, kg/m^3	Porosity, %	Water absorption, %
2560	1233	52	20

Figure 2. View of the crushed demolition waste.

After being crushed by a jaw crusher, the crushed stone from concrete waste reveals intermittent mortar component interlayers that are firmly clinging to the grains of the rock. Surfaces of crushed stone can have thin layers of hydrated phases when there is not a layer of cement-sand mortar. There is every reason to expect that this will increase the cement matrix's adherence in concrete. This notion is supported by the discovery that cement paste adheres to a wide range of materials, including quartz, granite, limestone, and clinker, with increasing consistency with time. These assumptions are supported by previous studies [22, 23].

2.2. Methods

Construction waste was processed with a jaw crusher laboratory (ECO building materials, Russian Federation) to produce aggregate (Fig. 3). Utilizing an average particle size of not greater than 5 mm. This material was utilized as a fine aggregate in compliance with the sieve analysis criteria.

Figure 3. Laboratory jaw crusher.

The microstructure features and properties of raw materials and the samples were investigated using both theoretical and empirical approaches. A scanning electron microscope with an accelerating voltage of 8.0 kV was used to analyze the morphology of raw materials and miniature concrete samples measuring 15 × 15 × 4 mm. The microstructure of materials was studied using a Tescan MIRA 3 LMU scanning electron microscope. The model is designed to operate under varying vacuum conditions (up to 150 Pa) in the sample chamber (Fig. 4). Working in a low vacuum, while maintaining all the advantages of a high vacuum, provides the opportunity to study non-conducting materials without first applying a layer of heat-conducting material. Scanning electron microscope allows the use of a raster method for imaging, which consists of sequential point-by-point scanning of the surface under study with a thin electron beam. In this case, the detector registers secondary electrons generated by the electron probe.

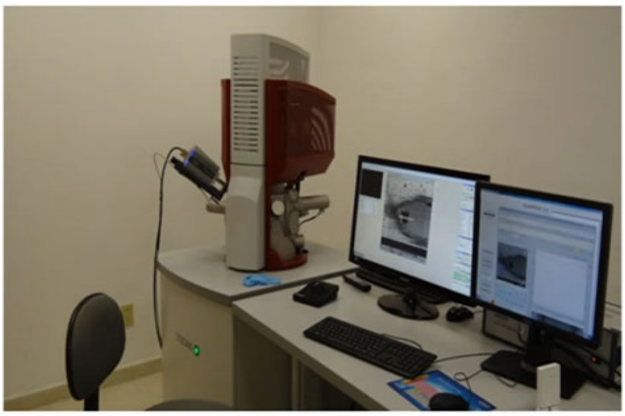

Figure 4. Electron microscope “Tescan MIRA 3 LMU”.

The results showed that the use of recycled aggregate has an effect on abrasion resistance. LKI-3 abrasion circles were used on cube samples measuring 70 × 70 × 70 mm to determine abrasion. Abrasion tests were performed on samples that had been dried to a consistent weight before assessment. Following drying, the samples were measured and weighed to an accuracy of 1 mm and 0.1 g. The sample was clamped with an applied pressure element and subjected to an axial load of 300 ± 1 N. The sample was rotated at 30 ± 1 rpm after applying 20 g of typical corundum powder to a steel disk. After each cycle, the disk and specimen's front surface were cleaned and rotated 90°. Between each test cycle, the specimen was weighed to within 0.1 g accuracy (Fig. 5).

Figure 5. LKI-3 abrasion device.

The chemical components of raw materials and microscopic concrete samples were evaluated using an X-ray spectrometer with an integrated diffraction system. The study of the mineralogical composition of raw materials and fragments of destroyed buildings and structures was carried out by X-ray phase analysis using an X-ray diffractometer model “ARL X’TRA. Thermo Fisher Scientific” with the use of which it is possible to determine the crystallographic, quantitative and qualitative parameters of materials, their phase composition, structural features and surface quality (Fig. 6).

Figure 6. X-ray diffractometer model "ARL X'TRA. Thermo Fisher Scientific".

The determination of the chemical and mineral composition of samples was carried out using an ARL 9900 WorkStation series spectrometer with a built-in diffraction system using the X-ray fluorescence (XRF) technique. The modular design and various additional options provide the ability to use this unit to solve a wide range of problems in a variety of production conditions (Fig. 7).

Figure 7. Spectrometer "ARL 9900 WorkStation".

Recognition of products of mineral composition and new formations was also carried out using differential thermal analysis and differential thermal device "NETZSCH STA 449F1" (Fig. 8).

Figure 8. Differential thermal device "NETZSCH STA 449F1".

The thermo gravimetric analyzer was used to conduct thermo gravimetric and differential thermal analyses (DTA). The amount of slump is measured after the liquid has been poured into a 30 cm high cone. The mean density of the material was determined using concrete cube samples of 100 × 100 × 100 mm. Six samples were obtained in each series to ensure acceptable results. A portion of the samples were hardened for 3 and 28 days under normal conditions, while another portion was hardened for one day while steaming using the "3 h + 8 h + cooling" technique (isothermal holding temperature 80 °C). The overall computed inaccuracy is less than 4 %.

3. Results and Discussion

3.1. Scanning Electron Microscope Images of Construction Waste

Fine aggregate was produced by grinding the demolition waste. Fig. 9 shows SEM images of the obtained aggregate. Table 7 provides the mineral composition of aggregate produced from demolition waste.

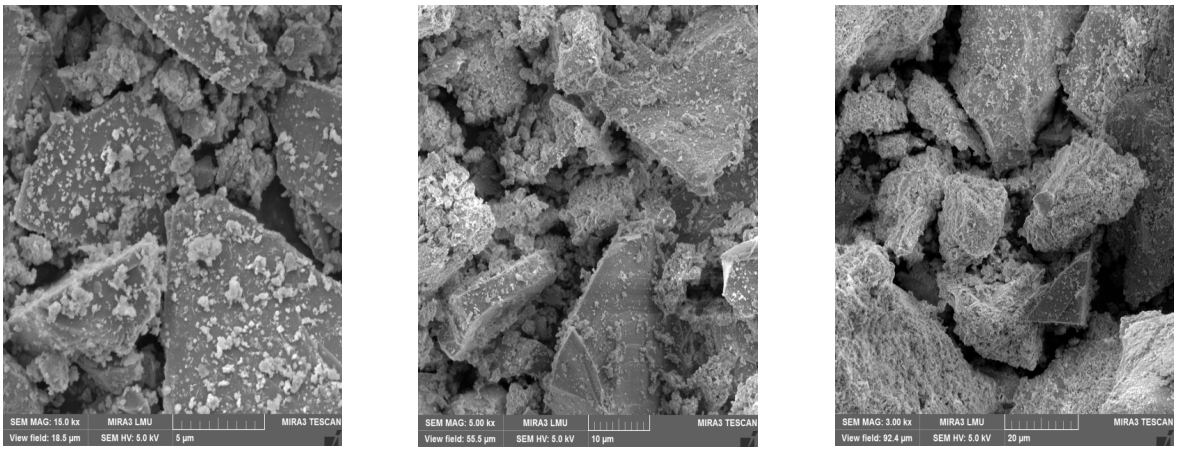

a) **b)** **c)**

Figure. 9. Micrographs of aggregate obtained from demolition waste: a) 5 mkm; b) 10 mkm; c) 20 mkm.

Table 7. The mineral composition of recycled aggregate from construction waste.

Sizes of particles, mm	Mineral content, %					
	$Ca(OH)_2$	SiO_2	$CaCO_3$	C-S-H	C_3S	C_2S
0.0–5	10.60	58.7	5.40	5.30	7.40	8

A considerable number of sharp particles may be seen in the aggregate from concrete waste as seen in SEM pictures, and this number increases as particle size decreases from 2.5 to 0–0.16 mm. This type of aggregate is the most sensible since it strengthens the interfacial transition zone by providing adhesion between the aggregate and cement matrix.

According to studies [25–29], the comminuted shape of the particles and their high silica and clinker mineral content will also contribute to their high activity. The particle form that has been crushed leads to a significant particular surface area, which interacts with the cement clinker's hydration byproducts. The reasonable reactivity of the particles of grinded concrete debris is also a result of the high silica content and previously unhydrated clinker minerals.

3.2. Compressive Strength

The C8/10 expanded clay concrete class experimented with substituting natural sand with synthetic crushed sand. The research investigations have been carried out using 1.8 mm demolition waste in place of sand, both partially and completely. Concrete mixes were created in this instance by using natural sand (control composition) and partial replacement artificial sand (25, 50, 75 and 100 %) (Table 8). According to the results of a study, the use of demolition waste increases the compressive strength of expanded clay concrete. This can be attributed to an increase in cement paste adhesion (Fig. 10).

Table 8. Lightweight concrete compositions and properties.

Mix ID	Materials content, kg/m^3					Slump test, cm	Density, kg/m^3	Compressive strength, MPa
	Portland cement	Natural sand	Demolition waste	Expanded clay	Water			
LW-1	475	600	–	410	240	3–4	1674	15.2
LW-2	475	450	150	410	243	4–5	1658	17.4
LW-3	475	300	300	410	249	3–4	1666	19.5
LW-4	475	150	450	410	255	3–4	1674	18.2
LW-5	475	–	600	410	270	3–4	1671	17.6

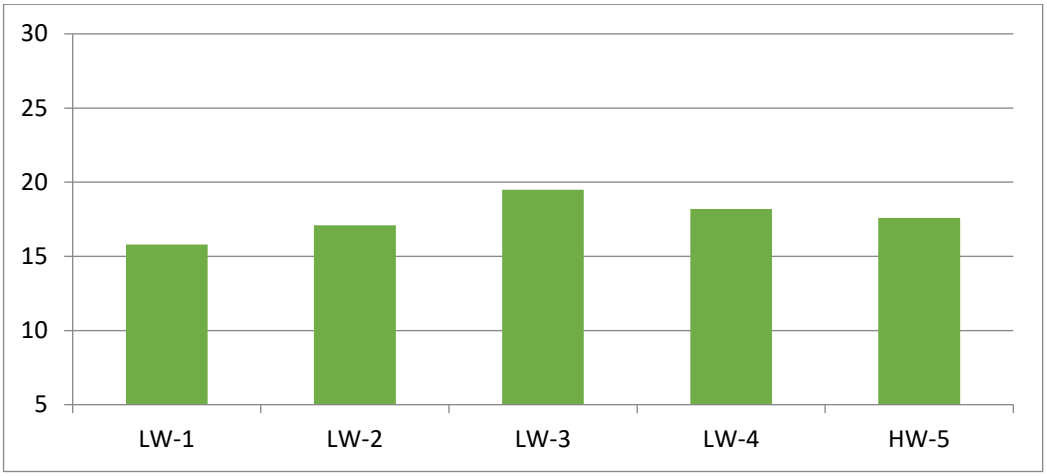

Figure 10. Compressive strength of lightweight concretes.

Experiments showed that when recycled aggregate replaces natural sand in lightweight concrete, the strength of the concrete increases rather than diminishes. Recycled aggregate was created by the classification of screening of crushed fragments of demolished waste, and it may be used as fine aggregate in concrete. The results of measured compressive strength for concrete samples surpassed those of previous authors by 12–35 % for lightweight concrete [30].

3.3. Microstructure Study

The interaction space of the paste of cement and the aggregate created from scrapped debris is shown in Fig. 11. The cement matrix's surface has a thick intergrowth and germination of concrete debris, and the two appear to be one cohesive unit.

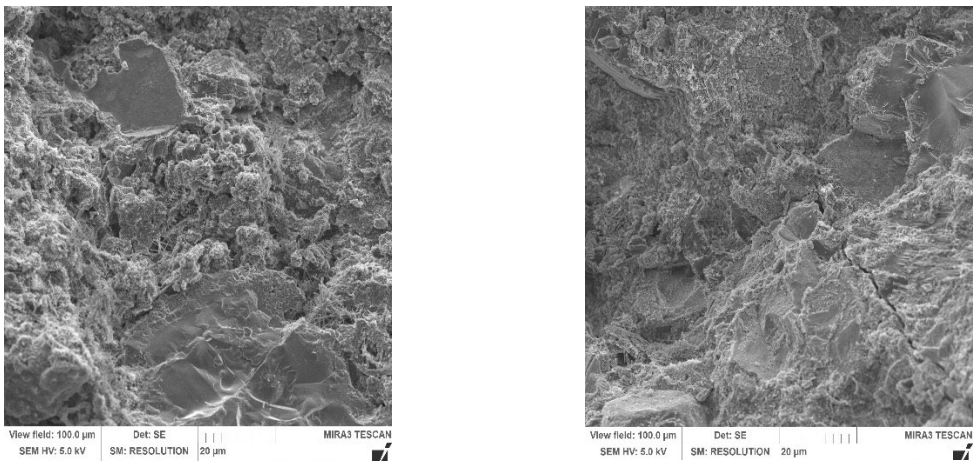

Figure 11. The zone of contact between the cement paste and the recycled aggregate.

The first phase in which the aggregate collects water from the concrete mix and the water retained in the pores, like in capsules, will offer an inflow of moisture for additional hydration of the binder, ensuring a thick contact zone. The water from the aggregate pores is drawn out by clinker minerals and new growths after the formation of a capillary-porous microstructure, increasing the rate of cement hydration without adversely influencing the workability of the concrete mix. Due to the presence of partially hydrated belite and portlandite particles, which make about up 15–25 % of fresh concrete, secondary (residual) cementitious characteristics may be present in concrete waste if it is small and has not undergone hydrothermal treatment.

The next step was to study the further hydration of concrete with the composition of cement and recycled aggregate from concrete scrap, at the age of 28 days. It can be seen that the microstructure of the samples is significantly compacted, the pores become smaller, they are gradually overgrown with cubic crystals of calcium hydro-alumoferrites, and partially or completely overgrown with calcium hydrosilicates (Fig. 11). The rough surface of semi-dissolved cubic crystals contributes to their better adhesion to calcium hydrosilicate crystals of a colloidal degree of dispersion. It is noted that the formation of the contact zone is so densely overgrown with neoplasm products that it is viewed with great difficulty.

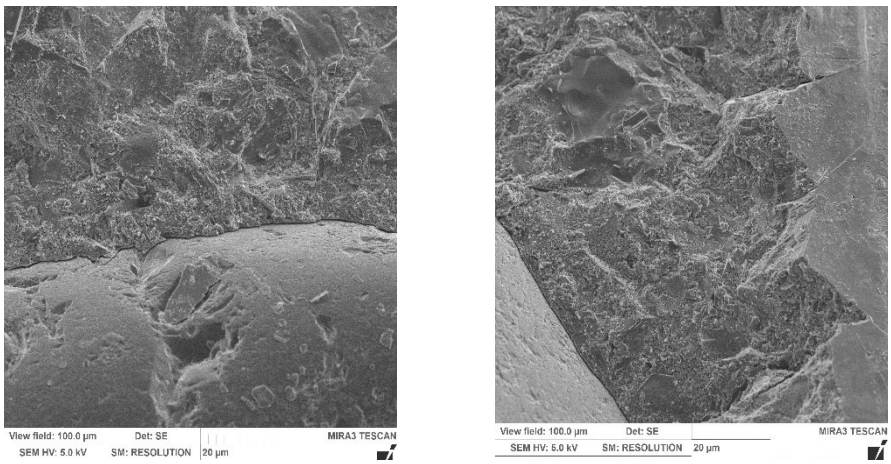

Figure 12. The zone of contact between the cement paste and natural sand.

Fig. 12 shows the contact zone of cement stone and grains of natural sand. The photo clearly shows the boundary, on the surface of which fine-grained calcium hydrosilicates form, forming a dense mesh layer of neoplasms that fills the entire space.

As a result, concretes made from waste concrete have greater cement matrix adhesion, which improves the eventual product's deformability, fracture resistance, dynamic load resistance, and other characteristics. These results have already been demonstrated in [22, 23], which are based on the rule of affinity of microstructures.

3.4. Shrinkage and Expansion Deformations

The impacts of alternating shrinkage and expansion of the material cause the development of destructive processes in concrete, which lead to permanent deformations and destruction of the material structure. Therefore, concrete shrinkage and expansion deformations are significant because they affect the basic qualities of structural elements. In this scenario, the acceptable concrete hardening regime is critical. As a result, after assessing shrinkage and expansion deformations for lightweight concrete, the samples were immediately placed in a typical hardening chamber with a relative humidity of up to 95 % and an air temperature 18–22 °C. Following two days of typical hardening, measurements were taken to assess sample deformations and moisture content changes. At the ages of 3, 7, 14, 28, 60, and 90 days, studies were conducted to detect sample deformations and changes in moisture content. Fig. 13 shows the test results.

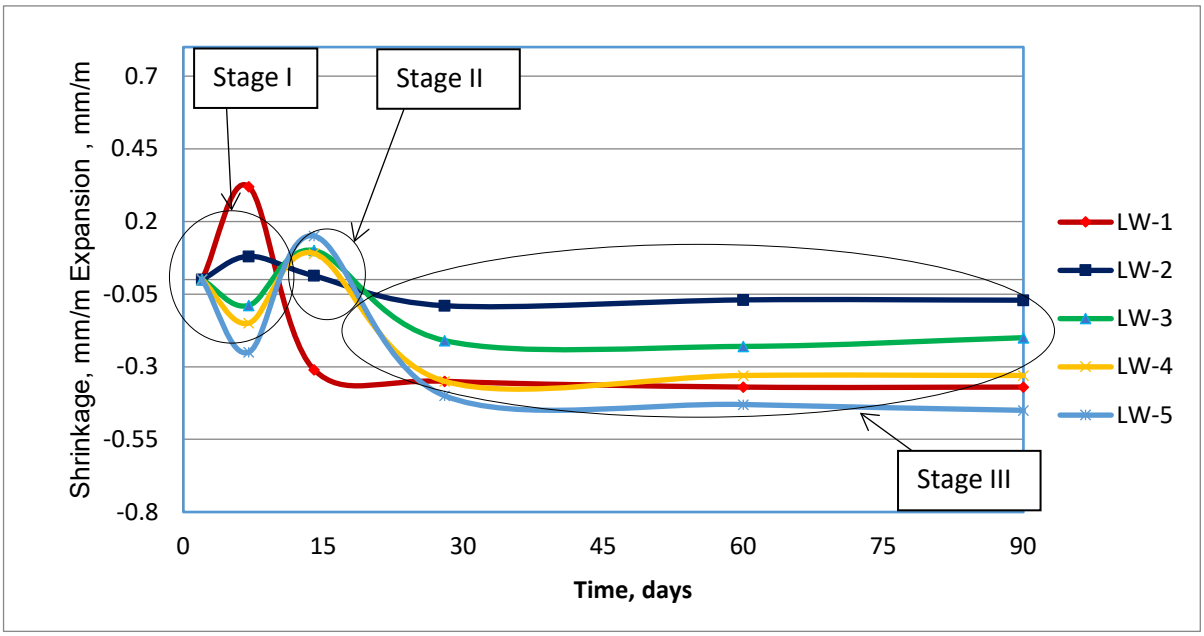

Figure 13. Shrinkage deformations of lightweight concrete.

Fig. 13 shows the evolution of autogenous shrinkage in mixtures containing various aggregates and water adsorptions. The results revealed three phases of hardened concrete growth, including fast shrinkage (Stage I), micro-expansion (Stage II), and continuous shrinkage (Stage III). Stage I lasts around 5 days

after “Time zero”, whereas Stage II lasts approximately 8–7 days. The autogenous shrinkage evolution of the performance of concrete built with various particles shows a significant difference. The autogenous shrinkage of the mixes made using recycled aggregate from demolition waste is almost insignificant for the first day before entering a shrinkage stage lasting around 9 days. This remarkable evolution pattern is characterized by little deformation and expansion lasting around 8 days.

Eventually, it is discovered that the commencement time of Stage III is uniform in all mixtures, and that variances in shrinkage growth during this stage are dependent on the amount of recycled aggregate. In addition, a temperature gradient distribution will be created within the matrix by the thermal energy produced by the hydration reaction of mixes with different aggregates, and thermal deformation will be a major element in how the samples behave when they gradually shrink on their own.

3.5. Cement Hydration in Concrete Mixes using Different Types of Aggregates

The benefits of reusing recycled aggregate from concrete scrap crushing were discovered using current X-ray phase analysis. An analysis of X-ray patterns of the samples showed that the intensity of C_3S and C_2S reflections decreases with the transition from a sample LW-1 to a sample LW-5. The sample LW-1 (without recycled aggregate from demolition waste) contains the maximum amount of C_3S and C_2S compared to sample LW-5 (with maximum amount of recycled aggregate), which can harden when interacting with water (Fig. 14).

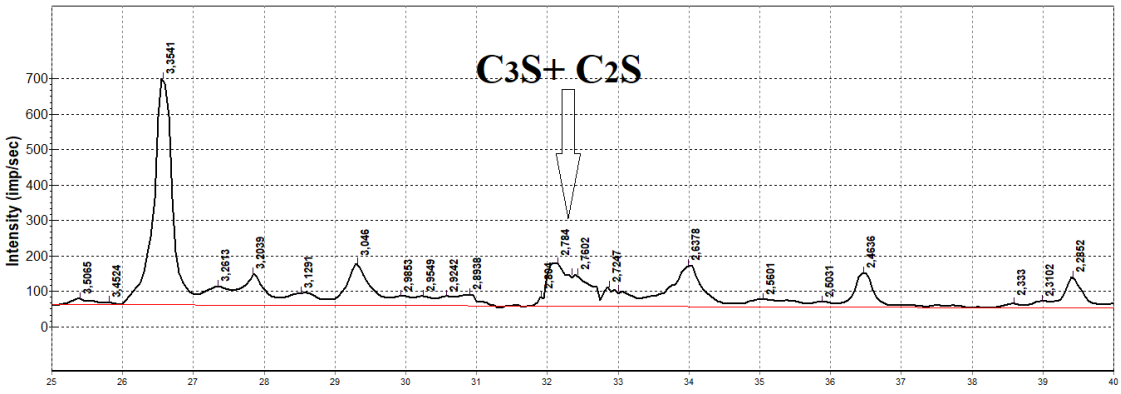

LW-1

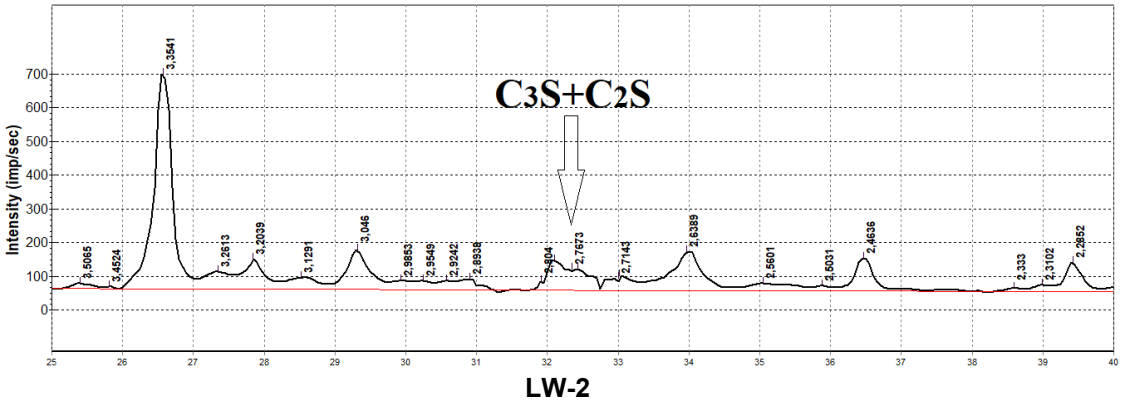

LW-2

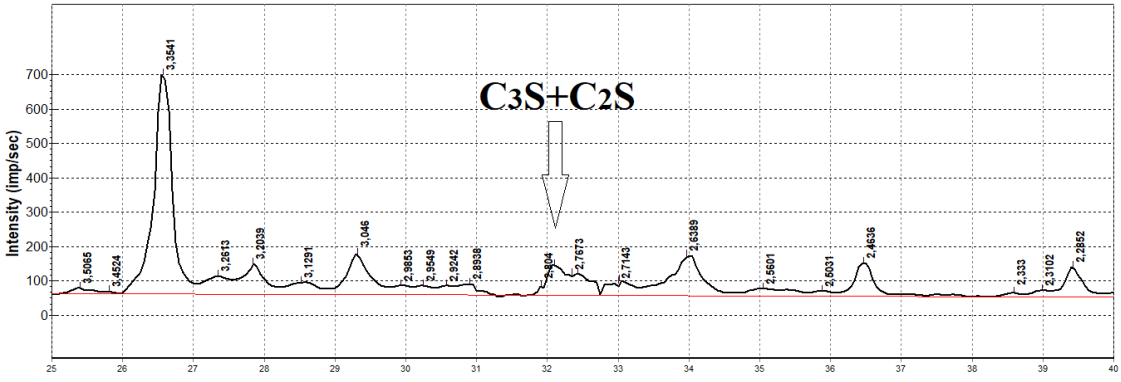

LW-3

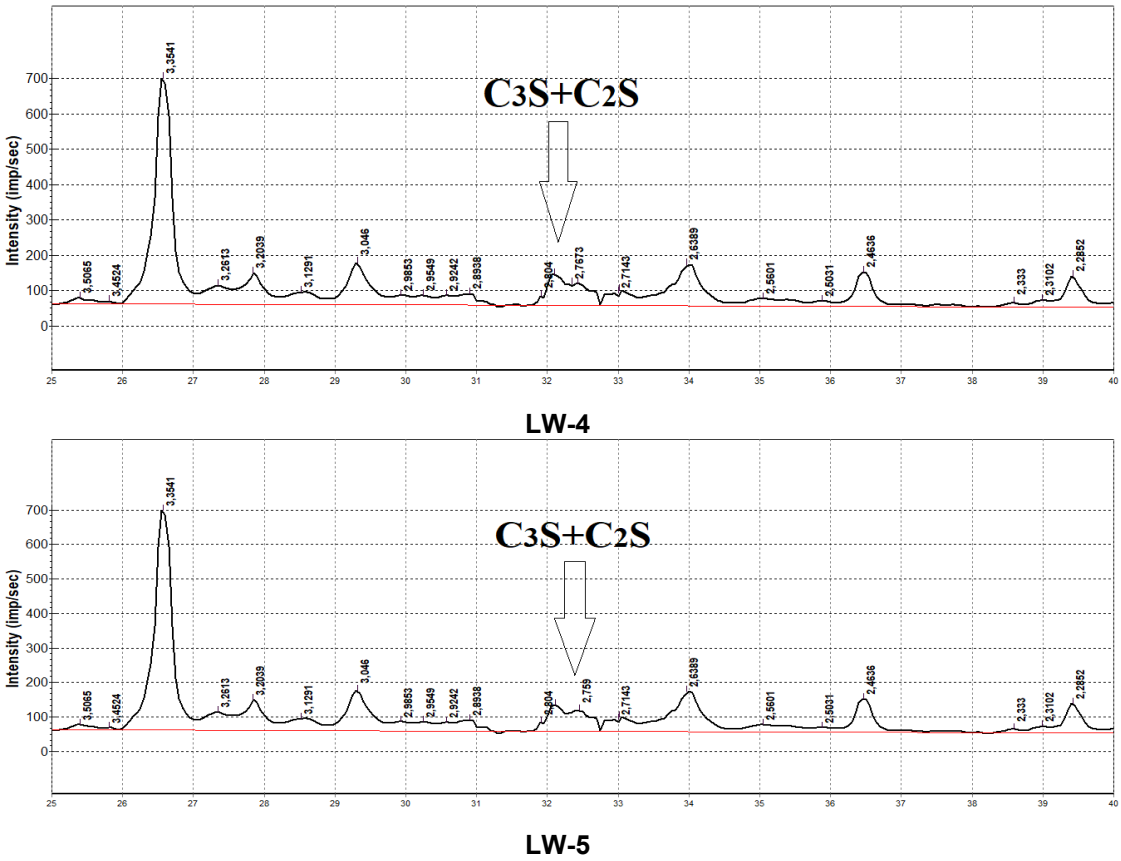

Figure 14. X-ray of cement paste, recycled aggregate and expanded clay.

It should be noted that the recycled aggregate from concrete scrap and expanded clay have certain porosity, which is clearly visible. The presence of porosity in the screening of concrete scrap crushing will certainly ensure an increase in the strength of the cement stone in the long term. Water trapped in the pores, as in capsules, will provide an influx of moisture for further hydration of the cement, which explains the increase in compressive strength.

3.6. Abrasion Resistance

In comparison to the reference samples, the abrasion testing results indicated that the samples containing recycled aggregate from demolition waste had a better resistance to abrasion. Table 9 shows results of the abrasion resistance test for lightweight concrete.

Table 9. Abrasion resistance test results for lightweight concrete.

Mix ID	Density, kg/m^3	Compressive strength, MPa	Abrasion, g/cm^2
LW-1	1674	15.2	0.8
LW-2	1658	17.4	0.7
LW-3	1666	19.5	0.6
LW-4	1674	18.2	0.6
LW-5	1671	17.6	0.7

It has been established that the samples LW-3 and LW-4 containing recycled aggregate allow for the production of lightweight concrete with up to 25 % lower abrasion than other samples. It is worth mentioning that the main reason for abrasion resistance is the presence of gravel in the recycled aggregate, which is inherently friction resistant.

4. Conclusions

This paper investigates the potential of reusing demolition waste to solve two problems: disposal of waste and concrete physic and mechanical characteristics. Its high activity is a result of its sharp shape, and high silica and clinker mineral concentration. Based on the results of the study, the following conclusions can be drawn:

1. The mechanical properties of lightweight concrete are produced in a manner similar to using natural sand when construction waste from buildings and other structures is used as a fine aggregate. These properties are the result of the dense development and sprouting of concrete debris onto the cement matrix's surface, which has given them the appearance of being a permanent fixture.

2. The additional cementitious material provides for higher compressive strength and a better contact zone of lightweight concrete when substituting recycled aggregate made from demolition waste. This is due to previously unreacted clinker mineral hydration products, which compact the microstructure of concrete waste. Because more hydration products are formed in a constant volume, the area of the matrix's interfacial transition of cement and aggregate can be compressed. Long-term strength of the cement stone would certainly increase with the existence of porosity, and water trapped in the pores, like in capsules, will give an input of moisture for further hydration of the cement, which explains the increase in compressive strength.

3. The water absorption of crushing screenings of fragments of destroyed buildings and expanded clay is 4 times higher than that of gravel. This explains the high consumption of water, which is absorbed and retained in the pores and microcracks of cement stone and aggregate grains. Lightweight concrete based on cement, recycled aggregate from demolition waste, and expanded clay (LW-2) shows the smallest shrinkage of 0.071 mm/m, which makes it possible to recommend this concrete for use in the construction of residential and civil facilities.

4. An increase in the strength of samples with demolition waste of concrete scrap is explained by the presence of aggregate porosity, which encapsulates a small fraction of water, which provides additional hydration in the absence of water in the surface layers. According to the studies carried out and the results obtained, it can be noted that in order to ensure a normal hydration process, it is necessary to create the essential moist conditions for gaining strength by covering the molded products with a film or tarpaulin with an exposure of up to 28 days.

5. Using recycled aggregate from building waste allows producing lightweight concrete with up to 25 % less abrasion than other samples. It is important to note that the primary reason for abrasion resistance is the presence of gravel in the recycled aggregate, which is naturally abrasion resistant.

In the future, research can be carried out to create completely cement-free binders, in which recycled aggregate and just grinded building waste are used as cement.

References

1. Rehman, M.U., Rashid, K., Haq, E.U., Hussain, M., Shehzad, N. Physico-mechanical performance and durability of artificial lightweight aggregates synthesized by cementing and geopolymerization. Construction and Building Materials. 2020. 232. Article no. 117290. DOI: 10.1016/j.conbuildmat.2019.117290
2. Silva, R.V., de Brito, J., Dhir, R.K. Properties and composition of recycled aggregates from construction and demolition waste suitable for concrete production. Construction and Building Materials. 2014. 65. Pp. 201–217. DOI: 10.1016/j.conbuildmat.2014.04.117
3. Verian, K.P., Ashraf, W., Cao, Y. Properties of recycled concrete aggregate and their influence in new concrete production. Resources, Conservation and Recycling. 2018. 133. Pp. 30–49. DOI: 10.1016/j.resconrec.2018.02.005
4. Behera, M., Bhattacharyya, S.K., Minocha, A.K., Deoliya, R., Maiti, S. Recycled aggregate from C&D waste & its use in concrete – A breakthrough towards sustainability in construction sector: a review. Construction and Building Materials. 2014. 68. Pp. 501–516. DOI: 10.1016/j.conbuildmat.2014.07.003
5. Land, P. The Swiss example: Using recycled concrete. Global Recycling. [Online] URL: https://global-recycling.info/archives/2956 (date of application: 01.06.2015).
6. Villoria Sáez, P., Osmani, M. A diagnosis of construction and demolition waste generation and recovery practice in the European Union. Journal of Cleaner Production. 2019. 241. Article no. 118400. DOI: 10.1016/j.jclepro.2019.118400
7. Al-Hadithi, A.I., Abbas, M.A. The effects of adding waste plastic fibers on the mechanical properties and shear strength of reinforced concrete beams. Iraqi Journal of Civil Engineering. 2018. 12 (1). Pp. 110–124. DOI: 10.37650/ijce.2018.142480
8. Shahzad Aslam, M., Huang, B., Cui, L. Review of construction and demolition waste management in China and USA. Journal of Environmental Management. 2020. 264. Article no. 110445. DOI: 10.1016/j.jenvman.2020.110445
9. Dilbas, H., Şimşek, M., Çakır, Ö. An investigation on mechanical and physical properties of recycled aggregate concrete (RAC) with and without silica fume. Construction and Building Materials. 2014. 61. Pp. 50–59. DOI: 10.1016/j.conbuildmat.2014.02.057
10. Corinaldesi, V., Moriconi, G. Influence of mineral additions on the performance of 100 % recycled aggregate concrete. Construction and Building Materials. 2009. 23(8). Pp. 2869–2876. DOI: 10.1016/j.conbuildmat.2009.02.004
11. Ismail, A.J., Younis, K.H., Maruf, S.M. Recycled aggregate concrete made with silica fume: experimental investigation. Civil Engineering and Architecture. 2020. 8 (5). Pp. 1136–1143. DOI: 10.13189/cea.2020.080540
12. Ayoob, N.S., Abid, S.R., Hilo, A.N., Daek, Y.H. Water-impact abrasion of self-compacting concrete. Magazine of Civil Engineering. 2020. 96 (4). Pp. 60–69. DOI: 10.18720/MCE.96.5
13. Amorim Beja, I., Motta, R., Bariani Bernucci, L. Application of recycled aggregates from construction and demolition waste with Portland cement and hydrated lime as pavement subbase in Brazil. Construction and Building Materials. 2020. 258. Article no. 119520. DOI: 10.1016/j.conbuildmat.2020.119520

14. Huda, S.B., Alam, M.S. Mechanical behavior of three generations of 100 % repeated recycled coarse aggregate concrete. Construction and Building Materials. 2014. 65. Pp. 574–582. DOI: 10.1016/j.conbuildmat.2014.05.010
15. Kharrufa, S. Reduction of building waste in Baghdad Iraq. Building and Environment. 2007. 42 (5). Pp. 2053–2061. DOI: 10.1016/j.buildenv.2006.03.011
16. Qiao, J., Zhang, L., Zhao, J., Zhou, Z. Test Study on Impermeability of Recycled Concrete. IOP Conference Series: Materials Science and Engineering. 2018. 423. Article no. 012010. DOI: 10.1088/1757-899X/423/1/012010
17. Sakai, Y. Relationship between water permeability and pore structure of cementitious materials. Magazine of Concrete Research. 2020. 72 (23). Pp. 1235–1242. DOI: 10.1680/jmacr.19.00135
18. Sharonova, O.M., Yumashev, V.V., Solovyov, L.A. Anshits, A.G. The fine high-calcium fly ash as the basis of composite cementing material. Magazine of Civil Engineering. 2019. 91 (7). Pp. 60–72. DOI: 10.18720/MCE.91.6
19. Wu, H., Zuo, J., Yuan, H., Zillante, G., Wang, J. A review of performance assessment methods for construction and demolition waste management. Resources, Conservation and Recycling. 2019. 150. Article no. 104407. DOI: 10.1016/j.resconrec.2019.104407
20. Huanyu, W., Jian, Z., Zillante, G., Wang, J., Hongping Y. Status quo and future directions of construction and demolition waste research: A critical review. Journal of Cleaner Production. 2019. 240. Article no. 118163. DOI: 10.1016/j.jclepro.2019.118163
21. Muzalev, S.V., Nikiforova, E.V., Petrova, O.A., Antonova, O.V., Melnikova, L.A. Recycling of municipal solid waste in construction. Construction Materials and Products. 2023. 6 (5). 7. DOI: 10.58224/2618-7183-2023-6-5-7
22. Lesovik, R.V., Tolypina, N.M., Alani, A.A., Al-bo-ali, W.S.J. Composite binder on the basis of concrete scrap. BUILDINTECH BIT 2020. Lecture Notes in Civil Engineering 95. 2021. Pp. 307–312. DOI: 10.1007/978-3-030-54652-6_46
23. Fediuk, R., Smoliakov, A., Muraviov, A. Mechanical properties of fiber-reinforced concrete using composite binders. Advances in Materials Science and Engineering. 2017. Article no. 2316347. DOI: 10.1155/2017/2316347
24. Zharov, A.N. Analysis of International Experience in the Construction of High-Rise Buildings and Justification of Organizational and Technological Solutions for High-Rise Construction. Construction materials and products. 2023. 6 (4.) P. 69 – 85. DOI: 10.58224/2618-7183- 2023-6-4-69-85
25. Lesovik, V.S., Volodchenko, A.A., Glagolev, E.S., Chernysheva, N.V., Lashina, I.V., Fediuk, R.S. Theoretical backgrounds of non-tempered materials production based on new raw materials. IOP Conference Series: Materials Science and Engineering. 2018. 327 (4). Article no. 042064. DOI: 10.1088/1757-899X/327/4/042064
26. Alani, A.A.A., Lesovik, R.V., Lesovik, V.S., Fediuk, R.S., Klyuev, S.V., Amran, M., Ali, M., de Azevedo, A.R.G., Vatin, N.I. Demolition Waste Potential for Completely Cement-Free Binders. Materials. 2022. 15 (17). Article no. 6018. DOI: 10.3390/ma15176018
27. Bassani, M., Riviera, P.P., Tefa, L. Short-Term and Long-Term Effects of Cement Kiln Dust Stabilization of Construction and Demolition Waste. Journal of Materials in Civil Engineering. 2017. 29 (5). DOI: 10.1061/(ASCE)MT.1943-5533.0001797
28. Sormunen, P., Kärki, T. Recycled construction and demolition waste as a possible source of materials for composite manufacturing. Journal of Building Engineering. 2019. 24. Article no. 100742. DOI: 10.1016/j.jobe.2019.100742
29. Arisha, A.M., Gabr, A.R., El-Badawy, S.M., Shwally, S.A. Performance Evaluation of Construction and Demolition Waste Materials for Pavement Construction in Egypt. Journal of Materials in Civil Engineering. 2018. 30 (2). DOI: 10.1061/(ASCE)MT.1943-5533.0002127
30. Mohammed, S.J., Al-Hadithi, A.I., Ahmed, S.K. Producing of eco-friendly lightweight concrete using waste polystyrene particles as aggregates with adding waste plastic. Iraqi Journal of Civil Engineering. 2018. 12 (1). Pp. 45–56. DOI: 10.37650/ijce.2018.142407

Information about the author:

Ahmed Anees Alani,
ORCID: https://orcid.org/0000-0003-2104-6457
E-mail: ahmed.anees@uoanbar.edu.iq

Received: 02.10.2023. Approved after reviewing: 28.06.2024. Accepted: 28.06.2024.

Magazine of Civil Engineering

journal homepage: http://engstroy.spbstu.ru/

ISSN 2712-8172

Research article

UDC 693.22

DOI: 10.34910/MCE.128.5

Numerical prediction of crack formation in historic masonry buildings

G.A. Iovlev ✉, ***N.V. Belov, A.G. Zileev***

Saint-Petersburg Mining University, St. Petersburg, Russian Federation
✉ *gregoriiovlev@gmail.com*

Keywords: constitutive modelling, masonry, brick, compression testing, numerical methods, PLAXIS, mortar, cracks

Abstract. This article investigated mechanical behavior of the masonry of historic buildings. It was assumed that reliable cracking processes can be obtained by modeling masonry as a continuous medium and using the Jointed Masonry Model (JMM). The paper gives an analytical review of JMM, identifying the input parameters required for its use. Laboratory tests of brick blocks and mortar for uniaxial compression were carried out and the results of these tests are presented. It is proposed to use the triaxial compression test methodology for rocks for cylindrical samples drilled from bricks. Based on the obtained laboratory data, a method for obtaining input parameters for JMM was proposed. To verify the obtained input parameters of JMM, the construction of a numerical model to predict the stress-strain state of historic masonry buildings was proposed. As an example, old workshop buildings located in the area near St. Petersburg were considered. The results of numerical calculations were compared with the results of building facades surveys for the presence of cracks and opening widths in them. It was found that the zones of the greatest shear deformations were formed mainly in the corners of window and door openings, mainly in the right and left parts of the model. Their position had a qualitative convergence with the results of surveys. The process of formation and qualitative change of zones of limiting compressive and tensile stresses that were formed in the walls of buildings was analyzed using different sets of input parameters of JMM. The influence of dilatancy effects on the stress-strain state was also considered. The study found that a reliable description of the mechanical condition of historic masonry can be obtained using JMM, whose input parameters should be based on the results of laboratory tests. The conducted work showed that along with classical methods of surveys it was possible to use methods of numerical modeling to predict areas where crack propagation occur for historic masonry buildings.

Citation: Iovlev, G.A., Belov, N.V., Zileev, A.G. Numerical prediction of crack formation in historical masonry buildings. Magazine of Civil Engineering. 2024. 17(4). Article no. 12805. DOI: 10.34910/MCE.128.5

1. Introduction

Nowadays the preservation of old historic buildings is an important task in the construction industry. Historic centers of modern cities are formed mainly by old brick buildings. In the conditions of rapid urban development, many new buildings and underground structures are being constructed in close proximity to historic buildings. It becomes relevant to assess the current state of historic buildings and the possibility of their reconstruction for further exploitation. The question arises about the ways to predict the fracturing accumulated in brick buildings during their existence.

Over many years of existence, accumulated deformations in foundation stone structures lead to emergence of cracks, brick falling out, and peeling of plaster. These are characteristic features of many historic buildings, because engineering methods of designing foundations at that time could not accurately predict the geomechanical processes occurring in the surrounding soils.

The object of the study is the masonry of historic buildings. The aim of the study is to obtain a reliable prediction of crack development in historic brick buildings. In the framework of continuum mechanics and solid mechanics approaches, when implemented by numerical methods, more sophisticated and complex constitutive models become one of the main ways to increase the reliability of the description of the mechanical state.

Researchers have developed a large number of nonlinear constitutive models aimed at determining the tensile strength of masonry and bricks [1, 2], which consider the anisotropy of properties caused by mortar joints [3, 4] and complex interaction between the masonry blocks [5–10]. However, most of these approaches are implemented under plane stress or plane strain conditions, which leads to negligible effects on the macroscopic elastic behavior [11], but significantly affects the nonlinear response [12]. More complex three-dimensional models have been proposed within the continuum [13] and discrete [14–16] approaches, for example, models that take into account the accumulation of material fracture provide a good representation of the post-fracture behavior [17, 18]. Only some of them consider the nonlinear behavior of both the soil mass and crack development phenomena in masonry for the two-dimensional [19–21] and three-dimensional [22–26] cases.

Italian researchers [27, 28] proposed a three-dimensional nonlinear model for the mechanical behavior of brick structures called Jointed Masonry Model (JMM). JMM is a modification of the better known Jointed Rock Model (JRM) [29, 30]. In the same studies, on verification tests, it is shown that JMM is able to reliably reproduce various mechanical tests of brick masonry units. The advantages of numerical modeling are demonstrated in the article [31], and the possibilities of PLAXIS for solving geotechnical problems are given in [32–34].

This study aimed to accurately describe the mechanical condition of historic masonry. However, the masonry of historic buildings is often characterized by heterogeneity of physical and mechanical properties [53]. Work [54] describes the causes of degradation of ceramic bricks and, consequently, justifies the combined effect of the aging process on the strength of the masonry. The presence of holes inside the bricks, caused by the production technology, is the cause of stress redistribution [35]. This factor increases the difficulty and possibility of data systematization from existing researches.

At the same time, when considering historic masonry, large-scale laboratory tests composed of assembled wall sections become difficult to achieve. This means that it is impossible to verify the correct operation of JMM based on these tests.

It can be assumed that for the mechanical behavior of historic brick masonry, the determination of the input parameters of JMM requires a set of mechanical laboratory tests. These tests should be performed separately for bricks and masonry. Taking into account the variety of influencing factors, the input parameters thus obtained will describe the mechanical behavior of a particular object. To verify the obtained parameters, it is possible to compare the crack development pattern in the numerical model with that obtained from the survey results.

Under these conditions, the development of a methodology for obtaining input parameters for JMM of historic masonry buildings with their further verification with the results of surveys becomes an urgent task.

2. Methods

The paper describes the process of deformation and crack formation in historic masonry building structures using a user-defined JMM in the PLAXIS 3D software package.

In order to determine the input parameters of the model, an analytical review of JMM is performed. To determine some of the input parameters for JMM, a set of laboratory tests is performed. For finding the cohesion and internal friction angle of bricks and mortar, either uniaxial tensile (UT) or triaxial tests (TXT) must be performed. Since masonry structures are under volumetric stress conditions, TXT is more preferable.

The tests performed for masonry structures are not enough to specify all parameters for JMM. To determine the remaining parameters, additional lab tests were carried out and data from tests on bricks and mortar from published researches results was used [38–40]. For example, the paper [41] summarizes the information about the deformation parameters of bricks and mortar.

There are also investigations aimed to determine the strength properties of bricks and mortar. In [42–45] results from tests on brick masonry under different types of stress-strain state are presented. A number of works [46–51] investigates the bond strength between mortar and brick as well as the mechanical parameters of masonry mortar. Articles [52–54] provide data on mortar tests in triaxial compression tools. The obtained input parameters are summarized and given in the table below.

It is also necessary to verify the obtained input parameters. For this purpose, a numerical model of the building under consideration is built. The mechanical state of the numerical model is reduced to the mechanical state of the building by loading the building model with the given precipitation accumulated over the period of the building existence[1].

2.1. Constructive Design of the Workshop Building

One building of the 17 forts and batteries erected on the Kronstadt roadstead is considered as an example of historic masonry. The fort was originally built of wood in 1724. After a major flood in 1824, the structures were rebuilt in stone in 1833. There are 12 buildings on the fort's territory. It lost its military significance by the beginning of the 20th century, but it was still used in the defense of Leningrad (St. Petersburg) during the World War II. The right-flank curtain building (workshops) was built in 1914 and is located in the southwestern part of the fort. Fig. 1 shows a general view of the central and inner facades of the building.

Figure 1. General view of the workshops[2].

The workshops are located between the horseshoe shaped tower (on the right in fig. 1) and the half circular tower (on the left in fig. 1). Fig. 2 shows a first-floor plan of the building.

Building foundation is a strip, with a heterogeneous structure, which include different components, such as granite blocks 10–50 cm in height, ceramic bricks and limestone. Lime-sand and cement-sand mortar was used as a binder. The depth of the foundations reaches 6.4 m from the first-floor level.

[1] Forty Kronshtadskoĭ kreposti – shedevry rossiĭskogo inzhenernogo dela pervoĭ poloviny XIX v. [The forts of the Kronstadt Fortress are masterpieces of Russian engineering in the first half of the 19th century]. [Online] URL: https://youtu.be/vjlP8JxezHk?si=W-f2NJ3NrvxOagfw (reference date: 24.06.2024); Yandex Maps [Online]. URL: https://yandex.ru/maps/-/CDGOI-LS (reference date: 24.06.2024).

[2] Forty Kronshtadskoĭ kreposti – shedevry rossiĭskogo inzhenernogo dela pervoĭ poloviny XIX v. [The forts of the Kronstadt Fortress are masterpieces of Russian engineering in the first half of the 19th century]. [Online] URL: https://youtu.be/vjlP8JxezHk?si=W-f2NJ3NrvxOagfw (reference date: 24.06.2024); Yandex Maps [Online]. URL: https://yandex.ru/maps/-/CDGOI-LS (reference date: 24.06.2024).

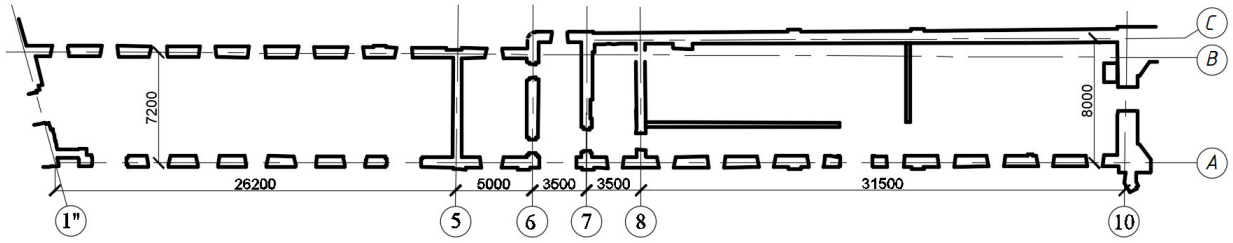

Figure 2. First floor plan of the workshops[3].

The walls are made of ceramic solid bricks using a complex lime-sand mortar. The outer walls are 2.5 bricks thick, with a total width of 640–705 mm. The walls from "C" axis to 10-axis reach at least 850 mm wide. The internal walls in the middle (near the stairwells) are 2.5 bricks thick, with a total width of 600–700 mm.

The ceilings are mainly in the form of concrete arches supported on metal beams. Fig. 3 shows their general view. As a coarse filler for the slabs crushed bricks are used. The average height of the slabs is 25 cm.

Figure 3. General view of the slab structures[4].

2.2. Jointed Masonry Model

2.2.1. Strength parameters of the model

To analyze mechanical behavior of masonry structures, JMM was used [27, 28]. As it was mentioned above, this model is a modification of the better known JRM implemented in PLAXIS 3D. JRM is an anisotropic elastoplastic model designed to simulate the behavior of stratified and fractured rock mass.

JRM assumes that there is rock mass with a definite layering direction and preferential crack orientations. A total of three such orientations can be specified. Each i-th direction has its own normal and shear stresses (Fig. 4). Shear stresses are limited according to Mohr-Coulomb failure criterion. When the maximum shear stress on one of the directions is achieved, plastic flow occurs and both associated and unassociated flow rules can be used.

In addition to the shearing along the crack planes, the tensile stresses are limited by a specified value according to Rankine's criterion. The Mohr-Coulomb yield function and the tensile yield limit are defined by equations (1) and (2):

$$f_i^C = \left|\tau_{s,i}\right| + \sigma_{n,i}\tan\varphi_i - c_{n,i}, \text{ where } i = 1,..,n_{p0}; \quad (1)$$

$$f_i^t = \sigma_{n,i} - \sigma_{t0,i}, \text{ where } i = 1,..,n_{p0}, \quad (2)$$

where $n_{p0} \le 3$ is the specific orientation considered;

[3] Forty Kronshtadskoĭ kreposti – shedevry rossiĭskogo inzhenernogo dela pervoĭ poloviny XIX v. [The forts of the Kronstadt Fortress are masterpieces of Russian engineering in the first half of the 19th century]. [Online] URL: https://youtu.be/vjlP8JxezHk?si=W-f2NJ3NrvxOagfw (reference date: 24.06.2024).

[4] Яндекс.Карты [Online]. URL: https://yandex.ru/maps/-/CDGOI-LS (reference date: 24.06.2024).

i – crack orientation number;

$\tau_{s,i}$ – shear stresses, acting along i-th direction;

$\sigma_{n,t}$ – normal stresses, acting perpendicular to i-th direction;

φ_i – friction angle in the i-th direction;

$c_{0,i}$ – cohesion in the i-th direction;

$\sigma_{t0,i}$ – tensile strength in the i-th direction,

where $\sigma_{t0,i} < c_{0,i} \cot \varphi_i$.

Similarly, it is possible to describe the behavior of masonry structures composed by solid blocks (bricks) and weakening surfaces (mortar joints). JRM well describes the behavior of masonry in the horizontal joint plane orientation (direction 2) (Fig. 5). However, unlike the rock mass, masonry tends to have a well-defined, chessboard structure. Thus, in the vertical direction (direction 1) (Fig. 5) there is an additional grip between the surfaces of the blocks. As a result, the tensile and shear strength of the masonry increases along the interconnected section (interlocking effect).

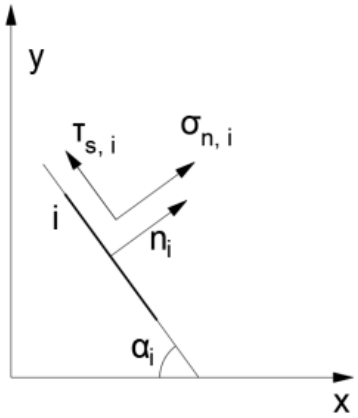

Figure 4. Global and local coordinate systems in 2D conditions [27].

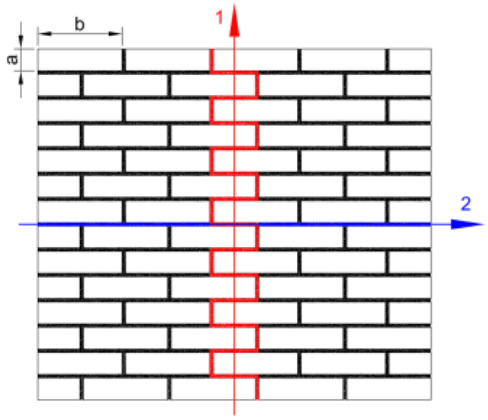

Figure 5. Definition of plane 1 and plane 2 in JMM [27].

Considering masonry in general, it is worth noting its heterogeneity, which is that the material of bricks and mortar are characterized by different deformation properties. The lateral extension of a brick blocks is much smaller than that of mortar for the same stress acting values. As a result, during the deformation of the masonry, the more intense lateral expansion of the mortar will cause additional tensile stresses in the bricks due to the strong cohesion between the brick block and the mortar. This effect increases with a decrease of the mortar grade [55, 56].

On Fig. 6*a* the section of wall made of bricks with height a and length b is shown. As the stress σ_2 increases, the fragment of the wall sustains longitudinal strains, most of which are realized by deformations of the mortar due to its high deformability. The longitudinal mortar strains are accompanied with lateral strains, which are constrained by the bricks above and below (more precisely by cohesion and internal frictional forces between the mortar and the bricks). As a result, tensile stresses σ_1 will arise in the bricks. This effect is increased because of the different values of the lateral extension.

Each brick is under compression stress $\sigma_{n,2} = \sigma_2$, acting perpendicularly to the plane of the horizontal mortar joints, also the bricks are under tensile stress $\sigma_{n,1} \leq \sigma_1$ acting perpendicularly to the plane of the vertical joints and tangential stress $\tau_{s,2}$ acting in the plane of the horizontal joints, as shown in Fig. 6*b*. The stress $\tau_{s,2}$ is due to friction between the bricks and mortar and has an opposite sign relative to the central vertical axis.

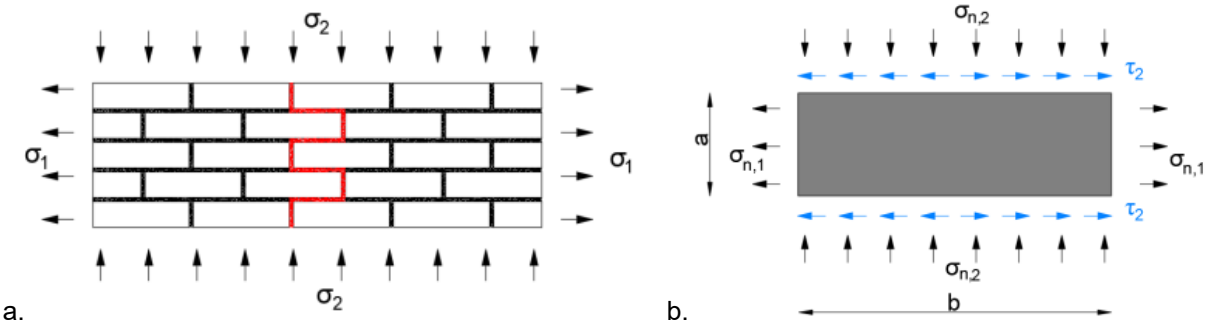

Figure 6. Stress state acting on: a) a part of the masonry wall [27]; b) the single block [27].

To consider the effect of grip between the brick halves, see Fig. 6*a*. Using the failure criteria described in equations (1) and (2), the tensile strength $\sigma_{t,1}$ in plane 1 can be rewritten as:

$$\sigma_{t,1} = \sigma_{t0,1} + \frac{n}{h}(c_{0,2} - \sigma_{n,2}\tan\varphi_2)\frac{b}{2}, \tag{3}$$

where h is the height of the part of the wall, while n is the corresponding number of bed joints.

The height of the block joint can be written as:

$$a = \frac{h}{n}. \tag{4}$$

Using equation (4), equation (3) can be rewritten in the following form:

$$\sigma_{t,1} = \sigma_{t0,1} + \frac{b}{2a}c_{0,2} - \frac{b}{2a}\sigma_{n,2}\tan\varphi_2. \tag{5}$$

The first term of equation (5) is the contribution of the tensile strength $\sigma_{t0,1}$ in plane 1, the second term includes the contribution of cohesion $c_{0,2}$ between the joints in plane 2, and the third term represents the contribution of frictional forces $\tan\varphi_2$ along horizontal joints under the action of compressive stresses $\sigma_{n,2}$.

If we abandon the effect of grip between the bricks in plane 2, i.e., remove the modification of the original JRM, then the tensile stresses will be equal:

$$\sigma_{t,1} = \sigma_{t0,1}. \tag{6}$$

Thus, it follows from equation (6) that the tensile stresses will be the same as the tensile strength $\sigma_{t0,1}$ along the vertical joints.

In turn, the grip effect between the bricks leads to an expansion of the yield surface and an increase in tensile strength. The increase in tensile strength in plane 1 involves a corresponding increase in the existing cohesion (Fig. 7).

$$c_1 = c_{0,1} - \left(\frac{b}{2a}\sigma_{n,2}\tan\varphi_2 - \frac{b}{2a}c_{0,2}\right)\tan\varphi_1. \tag{7}$$

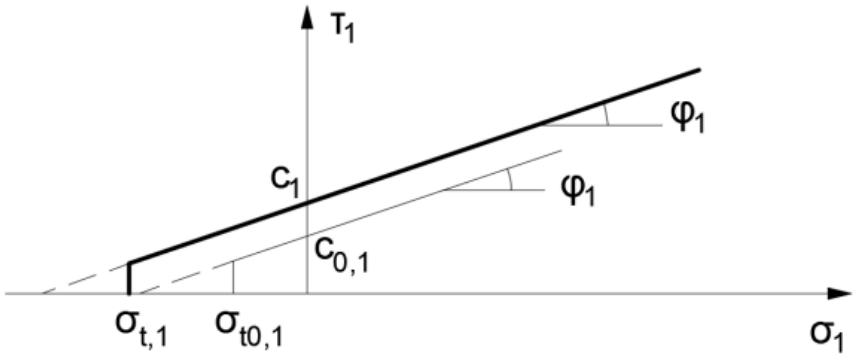

Figure 7. Modified Mohr-Coulomb criterion [27].

Thus, in the formulation of JMM for cohesion forces (7), the effect of interlocking blocks is considered by a new parameter defined as follows:

$$\beta = \tan\varphi_2 \frac{b}{2a}. \tag{8}$$

That coefficient (8) is a function of the dimension ratio of the bricks, while the ratio between the tensile and shear strength is constant.

Equations (5) and (7) can be rewritten as:

$$\sigma_{t,1} = \sigma_{t0,1} - \beta\sigma_{n,2} + c_{0,2}\frac{\beta}{\tan\varphi_2}; \tag{9}$$

$$c_1 = c_{0,1} - \left(\beta\sigma_{n,2} - c_{0,2}\frac{\beta}{\tan\varphi_2}\right)\tan\varphi_1. \tag{10}$$

It should be noted that in JMM, masonry is considered as a continuous medium, so material failure can occur at any point in the area of interest.

Modern masonry structures are characterized by higher tensile strength and cohesion at vertical joints, while old masonry has weak strength and cohesion, near to zero, as a result of mortar degradation at joints. Under such conditions, it is possible to ignore the strength components related to tearing and cohesion.

Then equations (9) and (10) can be rewritten as:

$$\sigma_{t,1} = -\beta\sigma_{n,2}; \tag{11}$$

$$c_1 = -\beta\sigma_{n,2}\tan\varphi_1. \tag{12}$$

Thus, equations (11) and (12) describe the case of complete mortar degradation in masonry. Since in the horizontal direction (direction 2) there is no grip effect between the bricks, the strength parameters in JMM, relative to JRM, are unchanged. As a result, direction 2 is the weakest when loads are applied.

As mentioned previously, JMM can specify up to three sliding directions. Two of them are typically used to specify the masonry pattern. The direction of the sliding surface is described by the angle of incidence α_1 and the angle of rotation α_2. The angle α_1 is defined by turning the sliding plane around the x-axis clockwise; the angle α_2 is defined by turning the sliding plane around the z-axis, counterclockwise. For masonry, a properly defined pattern is set according to the scheme in Fig. 8.

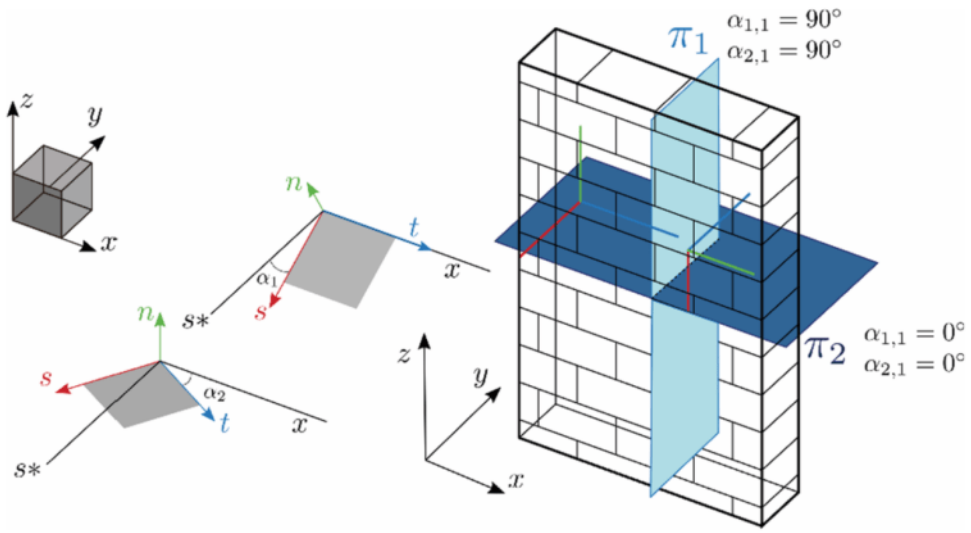

Figure 8. JMM bed and head joint plane orientation [27].

Thus, to describe the strength parameters of the masonry using JMM, it is necessary to find the following set of strength parameters:

c_b – cohesion of the brick block;

φ_b – friction angle of the brick block;

ψ_b – dilatancy angle of the brick block;

$\sigma_{b,t}$ – tensile strength of the brick block;

c_m – shear cohesion of the mortar;

φ_m – friction angle of the mortar;

ψ_m – dilatancy angle of the mortar;

$\sigma_{m,t}$ – normal cohesion of the mortar;

a – block height;

b – block width.

2.2.2. Elastic parameters of the model

It is assumed that the macroscopic structure of the masonry is a homogeneous anisotropic medium where the movement of blocks is replaced by the average movement of the homogenized medium. The general behavior of the medium is calculated with adequate accuracy without considering the motion of each individual block.

In addition to the strength parameters, JMM also considers the isotropic elasticity of the masonry due to the shear modulus G and Poisson's ratio ν. When the deformation parameters of bricks and mortar are available separately, the homogenization procedure of the parameters [57] converts to the equivalent parameters of the masonry. These parameters describe the general behavior of the masonry in the elastic zone.

The shear modulus is given by equation (13), and the Poisson's ratio ν is calculated as an average between ν_{12} and ν_{21}, calculated from equation (14):

$$\frac{1}{G}=\frac{1}{aK_t}+\frac{4a}{b^2K_n+4abK_t}+\frac{1}{\mu_b}; \quad (13)$$

$$\frac{\nu_{12}}{E_1}=\frac{\nu_{21}}{E_2}+\frac{\lambda_b}{2(3\mu_b\lambda_b+\mu_b^2)}. \quad (14)$$

The normal joint stiffness K_n is given by equation (15), the shear joint stiffness K_t – by equation (16),

$$K_n=\frac{E_bE_m}{t_m(E_b-E_m)}; \quad (15)$$

$$K_t=\mu_b\mu_m\frac{1}{t_m}\frac{1}{\mu_b-\mu_m}. \quad (16)$$

The Lame's coefficients are calculated by equations (17) and (18),

$$\mu_b=\frac{E_b}{2(1+\nu_b)}; \quad (17)$$

$$\lambda_b=\frac{\nu_bE_b}{(1-2\nu_b)(1+\nu_b)}. \quad (18)$$

The Young's moduli of masonry are calculated as arithmetic mean of Young's moduli values head E_1 and bed E_2 (19), (20):

$$\frac{1}{E_1}=\frac{1}{aK_n}+\frac{1}{4\mu_b}+\frac{\lambda_b+2\mu_b}{4(3\mu_b\lambda_b+2\mu_b^2)}; \quad (19)$$

$$\frac{1}{E_2}=\frac{4a}{4abK_n+b^2K_t}+\frac{1}{4\mu_b}+\frac{\lambda_b+2\mu_b}{4(3\mu_b\lambda_b+2\mu_b^2)}. \quad (20)$$

Thus, to specify the elastic parameters of the masonry as a homogeneous continuum medium, the following set of parameters should be determined:

E_b – Young's modulus of brick;

E_m – Young's modulus of mortar;

ν_b – Poisson's ratio of brick;

ν_m – Poisson's ratio of mortar.

2.3. Getting Input Model Parameters according to the Results of Laboratory Tests

The program of mechanical compression tests is standard for similar materials and is described in the Russian regulatory literature (GOST R 58767-2019 "Mortars. Test methods using reference specimens" and GOST R 58527-2019 "Wall materials. Methods for determination of ultimate compressive and bending strength"). Based on the uniaxial compression tests performed, the peak strength of bricks and mortar are defined. Obtained data is used to calculate the average parameters of the masonry. Then, in accordance with the Russian regulatory documents, the values of normal and shear cohesion of the mortar are determined.

Tests were also performed on cylindrical specimens drilled out of bricks for uniaxial and triaxial compression tools (TXT) using techniques similar to those used for laboratory rock testing.

For this purpose, samples of brick and masonry mortar were taken from the walls of the workshop buildings. The extraction of masonry fragments was carried out in three sites on each floor of the building (Fig. 11). 15 brick samples were collected. During sampling, it was found that during construction, bricks

from several manufacturers were used. A large textural heterogeneity of the samples was observed. This phenomenon is directly related to the features of the ceramic brick production in the 19th century, namely the imperfection of the technology of forming bricks, which led to the formation of imperfect texture.

The rest of load-bearing elements: floor beams, slab floor, foundations – were specified by a linear-elastic model. To specify the slab material, concrete samples were extracted from cemented crushed bricks and used for uniaxial compression test (UCT).

2.3.1. Laboratory methodology for brick material

UCT were carried out in accordance with prescribing displacements, with loading speed not exceeding 0.5 mm/min, full mythology described in Russian State Standard GOST 21153.2-84 “Rocks. Methods for determination of axial compression strength”, and TXT – in accordance with GOST 21153.2-84 “Rocks. Method for determination of triaxial compressive strength”. All tests were carried out on SPGU, Toni Hendrick and MTS 816 Rock Test System presses.

Selected bricks were dried for two months at room temperature in a non-ventilated dry room. After drying, some of the bricks were prepared for testing. According to the methodology, the selected bricks were divided into two halves. The beds of each brick were smoothed with gypsum mortar with grade G5 (Fig. 9) and laid bedded on top of each other.

Figure 9. Brick samples prepared for UCT, compiled by the authors.

For extra alignment, cardboard sheets of up to 1 cm thick were placed between the brick beds.

From the stretcher faces of the rest bricks, cylindrical core samples were drilled for UCT and TXT. The result of drilling and the final look of the specimens are shown in Fig. 10.

Figure 10. Cylindrical samples prepared for TXT and UCT, compiled by the authors.

The surfaces of the cylinder specimens were grinded, and visual defects on the surface were “cured” with plasticine.

To construct failure line of the bricks, in addition to UCT, 3 series of tests with different values of lateral compression were performed. Lateral compression varied in the range from 2 to 6 MPa with step of 2 MPa.

2.3.2. Laboratory methodology for mortar material

The test program for mortar joint material included testing cubic samples of 20–40 mm under uniaxial compression according to the methodology described earlier. To make the mortar samples of the desired size, large pieces were removed from the masonry and cut into 20–40 mm square plates. Then two plates were cemented together with a layer of gypsum paste 1–2 mm thick and G5 grade. Top and bottom surfaces were also smoothed with a thin layer of gypsum. Fig. 12 shows the final views of the specimens before testing.

Figure 11. Samples of wall and floor materials, compiled by the authors.

Figure 12. Mortar samples prepared for testing, compiled by the authors.

2.4. Creating numerical model for verification

As a part of the restoration work of this object, measurements of cumulative unequal settlements and building tilt were made. Fig. 13 shows a profile of measuring the cumulative unequal settlements of the building. The largest differential settlement is i_{max} = 0.015. Everywhere the vertical walls deviation is observed. The largest detected wall decline is j_{max} = 0.028. In general, the wall along A-axis deviates to the "island" side by up to 108 mm. Cross walls also have tilt towards the island, which is demonstrated by the existence of inclined through cracks in them. At the same time, the wall on B-axis (sea facade) remains stable.

Figure 13. Diagram of the accumulated settlements across wall A. The values are given in millimeters[5].

In PLAXIS 3D software package, the numerical simulation of the whole workshop building was performed. In current research, the interaction between soils and foundations of the building is not considered directly. The available results of the survey allow to model in-situ settlements of the foundation footing by specified displacements along it. Fig. 14 represents the general view of the numerical model. To achieve adequate results, the building walls were modeled with mesh coarsners factor equal to 0.07. Thus, the numercial model contains 324675 finite elements. In "staged construction" section three steps were performed sequentially:

1. All building structures were modeled. Displacements along the footings of all foundations in all directions were forbidden.

[5] Forty Kronshtadskoĭ kreposti – shedevry rossiĭskogo inzhenernogo dela pervoĭ poloviny XIX v. [The forts of the Kronstadt Fortress are masterpieces of Russian engineering in the first half of the 19th century]. [Online] URL: https://youtu.be/vjlP8JxezHk?si=W-f2NJ3NrvxOagfw (reference date: 24.06.2024).

2. The computational step required to reach the equilibrium state and set the accumulated strains to zero.

3. The accumulated strains were repeatedly set to zero again, and the diagram of vertical settlements along the base of the foundation of wall A was created.

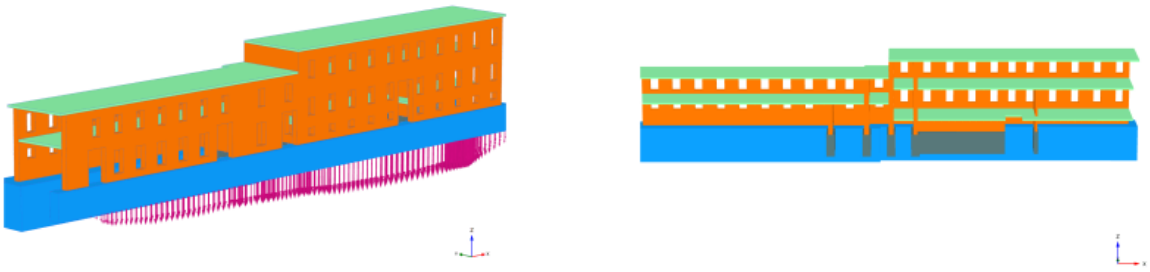

a) b)

Figure 14. Design scheme of the workshop building: a) general view of the design scheme with given displacements; b) sectional drawing of the building, compiled by the authors.

3. Results and Discussion

3.1. Laboratory Tests Results

3.1.1. Obtained mechanical parameters of brick samples

Fig. 15 shows a typical failure mechanism of the half's brick samples. When processing test results, test results that strongly deviated from the sample mean were discarded. Table 1 shows the obtained deformation moduli and uniaxial compression stress of masonry bricks. Fig. 16 shows the obtained stress-strain curves of bricks under uniaxial loading.

Figure 15. General view of the brick samples at failure, compiled by the authors.

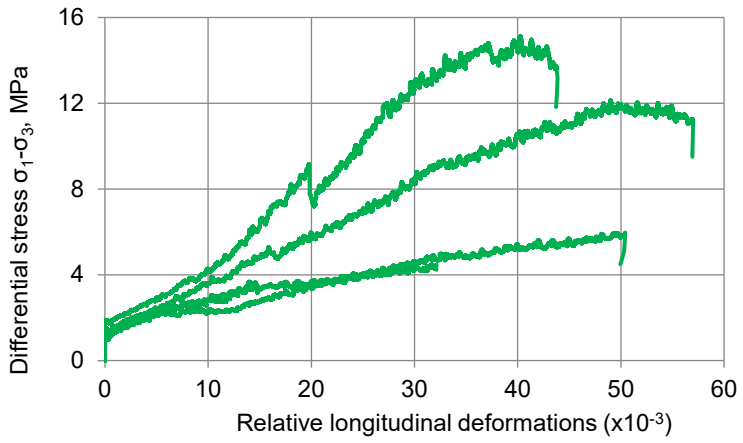

Figure 16. Stress-strain relations curves for brick samples, compiled by the authors.

Table 1. Geometrical properties of brick specimens and test results.

No.	Block length a, mm	Block width b, mm	Block height h, mm	Mass m, g	UCS σ, MPa	Young's modulus E, GPa
1	125	135	147	4675	3.7	0.4
2	115	105	120	2605	4.5	0.3
3	120	100	140	4400	15.1	0.5
4	120	118	155	4640	12.2	0.2
5	125	125	130	4002	6.0	0.1

The failure mechanism of the drilled brick specimens after UCT and TXT shown in Fig. 17, 18.

Figure 17. General view of cylindrical samples at failure after TXT, compiled by the authors.

Figure 18. General view of cylindrical samples at failure after UCT, compiled by the authors.

The received results are characterized by high heterogeneity, therefore, they should be processed with a certain safety factor.

Heterogeneity is probably caused by various manufacturing technology of tested bricks and different sampling sites. Moreover, heterogeneity was observed even in speciments drilled from the same brick, which may reflect the influence of the historical distribution in stress-strain state applying to the brick surfaces and therefore lead to different microfracture formation. In the future, more sophisticated statistical procedures, such as the use of artificial neural networks, should be applied to samples with such heterogeneity [58, 59].

Obtained results allow identifying the dependence between increasing strength limit of bricks with growing lateral compression. Fig. 19 shows the final set of stress-strain curves.

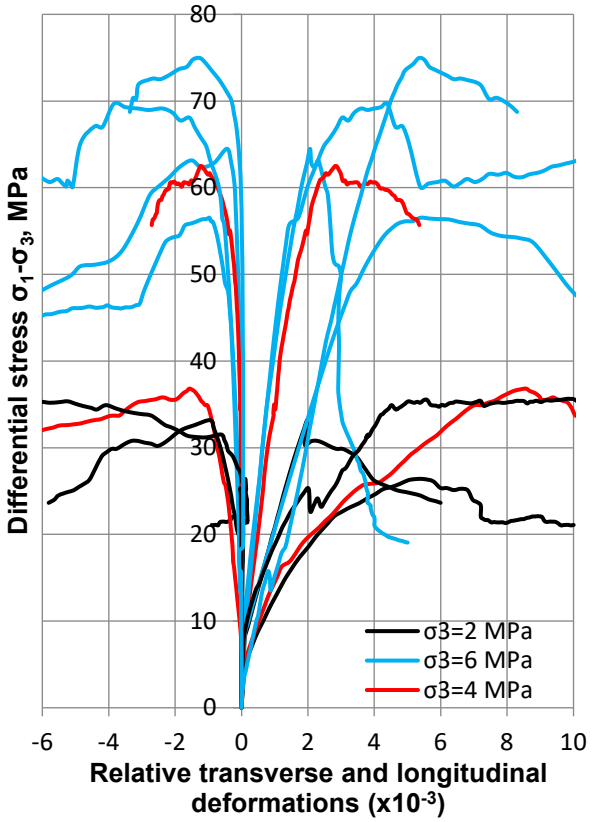

Figure 19. Stress-strain relations curves for brick cylindrical samples, compiled by the authors.

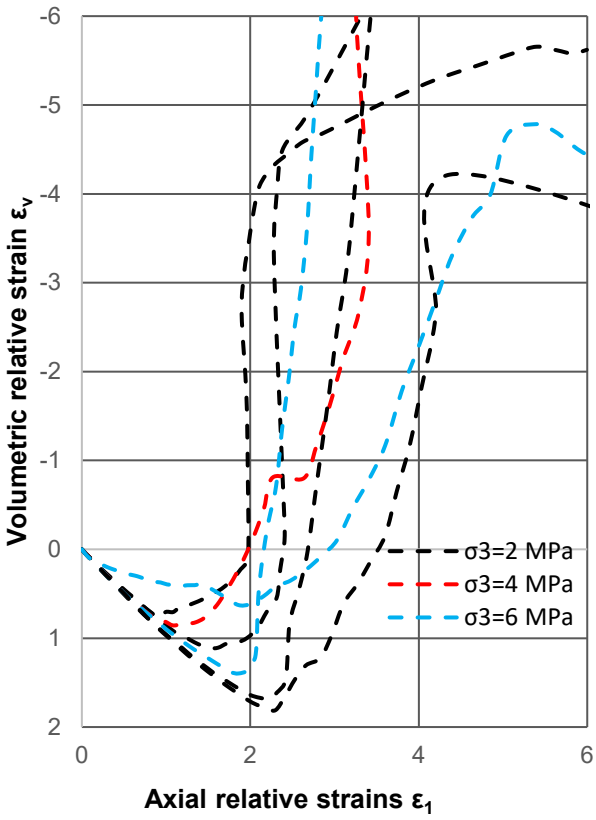

Figure 20. Curves representing the dependence of volumetric strains versus axial strains, compiled by the authors.

Analysis the obtained data shows the influence of the scale effect on the test results [60], because uniaxial compression stress (UCS) of brick parts is much lower than that USC of cylindric samples. The average UCS of bricks parts is 8.28 MPa, while the average UCS of cylinder specimens is 18.77 MPa. Thus, the ratio of these values may give a scale factor k equal to 0.44. The indicates and influence of the scale effect on the test results for bricks is given in [61, 62]. The coefficient k is used in further to reduce the strength limits and deformation moduli. The resulting parameters are presented in Table 2.

Table 2. Geometrical properties of brick cylindrical specimens and test results decreases by k.

Site location	Sample number	Diameter d, mm	Height h, mm	Mass m, g	Lateral pressure σ_3, MPa	Volume strength $k \cdot \sigma_v$, MPa	Young's modulus $k \cdot E$, GPa	Poisson's ratio ν
1	1	39.9	93.4	196.8	2	12.52	3.54	–
	2	39.9	93.3	201.9	4	17.99	3.42	0.274
	3	39.8	82.5	192.1	2	15.51	7.44	0.136
	4	39.9	94.8	224.3	6	27.57	6.07	0.254
2	5	39.8	94.8	266.7	6	31.07	15.98	0.080
	6	39.8	93.0	243.1	0	8.93	2.27	–
3	7	39.9	87.8	246.9	4	29.30	14.75	0.104
	8	39.8	87.4	249.2	6	33.37	18.42	0.310
	9	39.8	85.2	249.8	2	16.59	5.89	0.008
	10	39.9	93.2	256.4	6	35.68	6.76	–
	11	40.0	92.8	191.4	0	9.25	1.35	–
	12	39.6	92.1	189.6	0	7.71	1.79	–
	13	39.9	69.5	145.1	0	9.82	1.70	–
	14	39.1	91.3	210.3	0	5.67	1.50	–

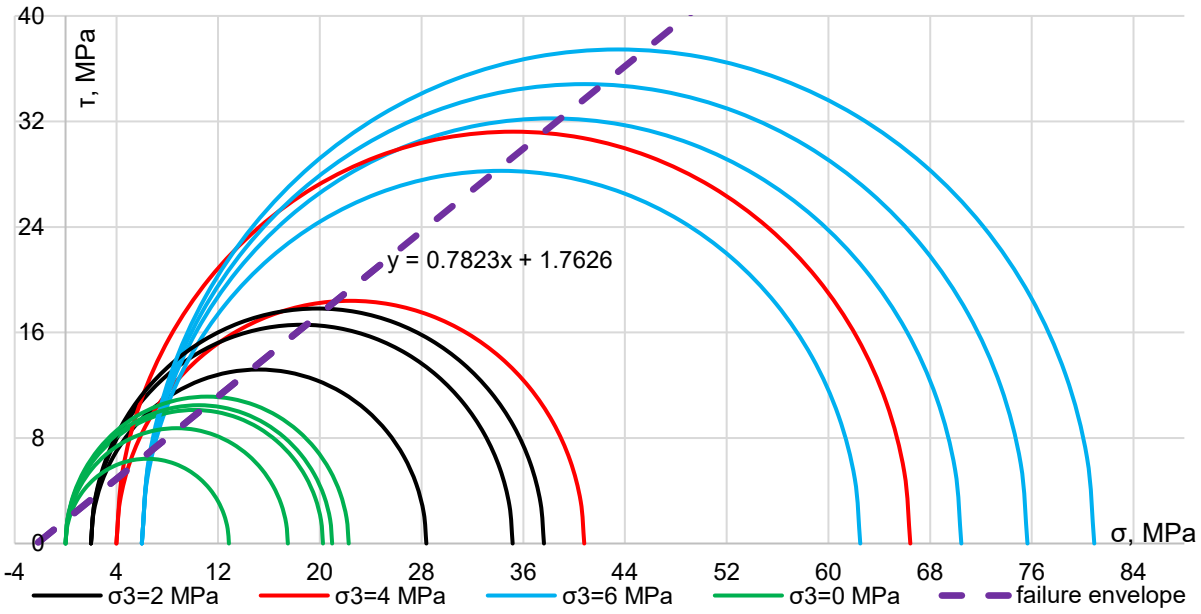

Figure 21. Mohr's circles for UCT and TXT and Mohr-Coulomb failure envelope, compiled by the authors.

From the obtained failure line of the brick (Fig. 21) the value of the internal friction angle of the material $\varphi_b = 38°$, cohesion $c_b = 1.17$ MPa were defined.

From TXT curves for dependency volume strain versus axial strain $\varepsilon_1 - \varepsilon_2$ are plotted. This graph is shown in Fig. 20.

The obtained data illustrates changing signs of volumetric deformations, which means the dilatancy existence with an attenuated character. Using equation (21) proposed by Vermeer and De Borst [63], the average value of the dilatancy angle for each sample are calculated.

$$\psi = \arcsin\left(\frac{\Delta\varepsilon_v}{\Delta\varepsilon_v - 2\Delta\varepsilon_1}\right), \quad (21)$$

where $\Delta\varepsilon_v$ – volumetric strain increment; $\Delta\varepsilon_1$ – axial strain increment.

Depending on the chosen range for any curves, the dilatancy angle takes values differing from the angle of internal friction by $\pm 5°$ in both directions. Therefore, the dilatancy angle was taken to be equal to the angle of internal friction $\psi_b = 38°$. In this case, an associated law of plastic flow rule is valid for the brick material.

The tensile strength was defined by two methods. First one is geometrical, by plotting the Mohr-Coulomb failure line in the tensile zone. The second method from tabulated data in Russian regulatory documents, according to which $\sigma_{t,mc}$ equals 200 or 180 KH/m^2, depending or brick grade. Grades where defining during building survey.

In the homogenization procedure of elastic parameters for masonry, the average value of the deformation modulus from results of UCT equal to $E_b = 1722$ MPa, was used. The lateral stain coefficient (Poisson's ratio) based on TXT defined as $\nu_b = 0.17$.

3.1.2. Obtained mechanical parameters of mortar material

Table 3 shows the deformation modules and UCS for masonry mortar and the stress-strain curves of the mortar under uniaxial loading.

Table 3. Geometrical properties of mortar specimens and test results and stress-strain relations curves for mortar samples, compiled by the authors.

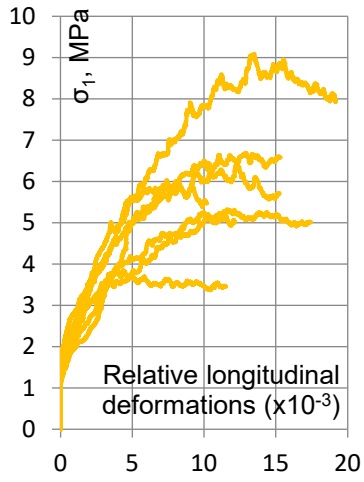

S. num.	Length, a, mm	Width b, mm	Height h, mm	Mass m, g	Volume strength σ_v, MPa	Young's modulus E, GPa
1	29.0	36.0	42.0	95.3	9.09	0.56
2	35.0	40.0	33.0	95.3	6.69	0.62
3	38.0	40.0	44.0	150.8	6.25	0.75
4	37.0	40.0	56.0	187.0	5.35	0.37
5	35.3	40.0	38.0	108.6	6.41	0.61
6	40.0	36.0	53.0	158.6	3.93	0.66
7	40.0	40.0	37.5	125.0	5.45	0.49

In the homogenization procedure of elastic parameters for masonry, the average value of the deformation modulus equal to $E_m = 556.1$ MPa, was used. The lateral strain coefficient, based on data from [39, 40], was assumed to be $\nu_m = 0.25$ with the ratio $\frac{\sigma}{R} = 0.6$, where R is the ultimate compressive strength of the mortar.

3.2. Summurised Input Parameters for JMM and Numerical Simulation

The structures of the foundation, walls and slabs are implemented as three-dimensional elements. The slab beams are made in the form of ideal-elastic wire elements. For the walls, 2 sets of input parameters were considered (see w.1 and w.2 in Table 4). First set included lab test data and scientific research materials. Second set was based on tabulate data in Russian regulatory documents. The input JMM

parameters are presented in Tables 4, 5. An elastic model was adopted for the floor beams, with the input parameters in Table 6.

Within the framework of scientific and educational work, it was not possible to obtain all necessary parameters of adhesion and the angle of internal friction of the solution; the results of studies were used to set them [46–49]. The dilatancy angle was taken to be equal to the angle of internal friction. In this case, an associated law of plastic flow rule is valid for the mortar material.

Table 4. Input parameters of masonry walls for JMM.

Material	w.1	w.2	
	a, b	*a*	*b*
γ, kH/m^3	19.7	19.7	19.7
G, kH/m^2	4.58E05	8.00E05	6.18E05
ν	0.19	0.2	
c_{mc}, kH/m^2	1760	800	650
φ_{mc}, °		38.04	
ψ_{mc}, °		38.04	
$\sigma_{t,mc}$, kH/m^2	1350	200	180
SF_{beta}		1.07	
$a_{1,1}$, °		90	
$a_{1,2}$, °		90	
c_i, kH/m^2	160	160	
φ_i, °		30	
ψ_i, °		30	
$\sigma_{t,i}$, kH/m^2	140	80	
$a_{2,1}$, °		0	
$a_{2,2}$, °		0	

Table 5. Input parameters of foundations and slabs for Linear Elastic model.

Material	Foundation	Foundation of internal walls	Floor
γ, kH/m^3	20	20	20
E_{ref}, kH/m^2	13.00E6	0.80E6	8.826E6
ν		0.2	

Table 6. Input parameters of flor beams for Linear Elastic model.

Material	I-beam profile N18	I-beam profile N26
γ, kH/m^3	78	78
A, m^2	2.790E-3	5.340E-3
I_2, m^4	0.01450E-3	0.05740E-3
I_3, m^4	0.8730E-6	2.880E-6
E_{ref}, kH/m^2	210.0E6	210.0E6

3.3. Numerical Simulation Results and Comprasion with Survey Data

In PLAXIS 3D two calculation situations were considered, namely (a, b) by used sets of masonry materials (Table 4, 8). In addition, two more calculation scenarios were considered, so in models *a* and *c* masonry materials were used considering the associated plastic flow rule. In models *b* and *d* materials without regard to dilatancy were used (Table 8). Thus, 4 calculations with different sets of input parameters to JMM were performed. The results of a set of laboratory tests on bricks correlate with the results obtained by other authors [36, 38]. The obtained parameters of JMM adequately correlate with the input parameters accepted by other researchers [27, 64].

Fig. 22 shows the results of the building survey with the defects applied to wall A. The numerical modeling results are shown in Fig. 23–25. It can be noted that the shear strains presented in Fig. 23 with a good reliability are formed in the same places as observed wall defects. Cracks are concentrated at the lintels above the window and door openings in the left and right parts of the facade. There is also a detachment of the cornice under the building's roof. The nature of the distribution, the angle of inclination, and the direction of development indicate the sedimentary nature of their occurrence, which is confirmed by the results of numerical calculations.The similarity of the survey and numerical results indicates that there is a visual qualitative convergence between the behavior of real masonry structures and those predicted by the numerical model based on JMM.

It may be concluded that mostly cracks in the building facade are formed as a result of irregular settlement of the building foundations. The obtained result demonstrated the effectiveness of JMM for predicting the development of cracks in historic masonry buildings.

It should be noted that a set of tools PC PLAXIS 3D can not fully describe the interaction of different structural elements of the building, which leads to distorted simulation results.

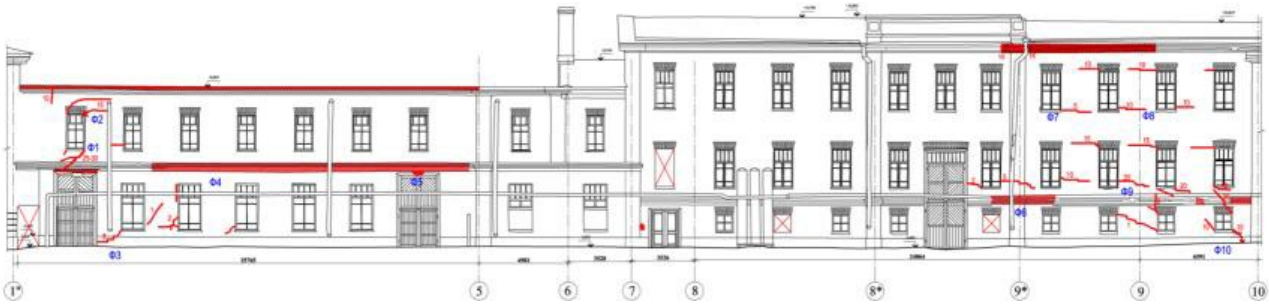

Figure 22. Scheme of building facade defects[6].

Comparing calculation results for two input parameters set indicates the observed qualitative similarity of deforming processes in the masonry. Second input parameters set (calculations *c* and *d*), which used tabulated data in Russian regulatory documents, show widespread development of tension zones (Fig. 24), due to lower (almost two times) tensile strength of normal cohesion of mortar and lower (seven times) tensile strength of bricks. The tensile strength of the bricks was intentionally decreased to demonstrate a further failure process in the tensile stress zones. At the same time, for *c* and *d* input parameters set an additional increase of plastic strains in the compression zones was also observed. In the right and left lower corners of the building, the compressive loads have such magnitude that reaching the strength limit and material failure occurs (red points in Fig. 24*c*), which is practically not observed in the scenario *a*.

Numerical results derived with input parameters for JMM based on tabulated data lead to a more conservative solution and include relatively large fracture zones. Thus, the parameters according to the scenario c enable to consider the worst-case scenario for this problem conditions.

The dilatancy angle determines the direction of the plastic potential vector with respect to the Mohr-Coulomb yield surface. As a consequence, dilatancy is responsible for the proportional relation between plastic volume strains and plastic shear strains. Thus, if $\psi = 0^\circ$, as it was assumed in calculations (*b, d*), volumetric strains occur only under the volume compression stress paths, see Fig. 25 (*b, d*), while shear strains develop more intensively, see Fig. 23 (*b, d*). For cases where $\psi = \varphi$, extra volumetric deformations occur in zones where stresses level exceed Mohr-Coulomb failure criterion, as is shown in Fig. 25 (*a, c*) and Fig. 23 (*a, c*).

The presence of dilatancy affects the angle of inclination of the formed zones of shear deformations (or zones of crack development) from window openings, in relation to the horizon, which is especially evident in the right side of the building (Fig. 23). Also, the location of cap and hardening points is changed (Fig. 24).

Both cases of flow rule, associated and no-associated, are presented in the paper.

[6] Forty Kronshtadskoĭ kreposti – shedevry rossiĭskogo inzhenernogo dela pervoĭ poloviny XIX v. [The forts of the Kronstadt Fortress are masterpieces of Russian engineering in the first half of the 19th century]. [Online] URL: https://youtu.be/vjlP8JxezHk?si=W-f2NJ3NrvxOagfw (reference date: 24.06.2024).

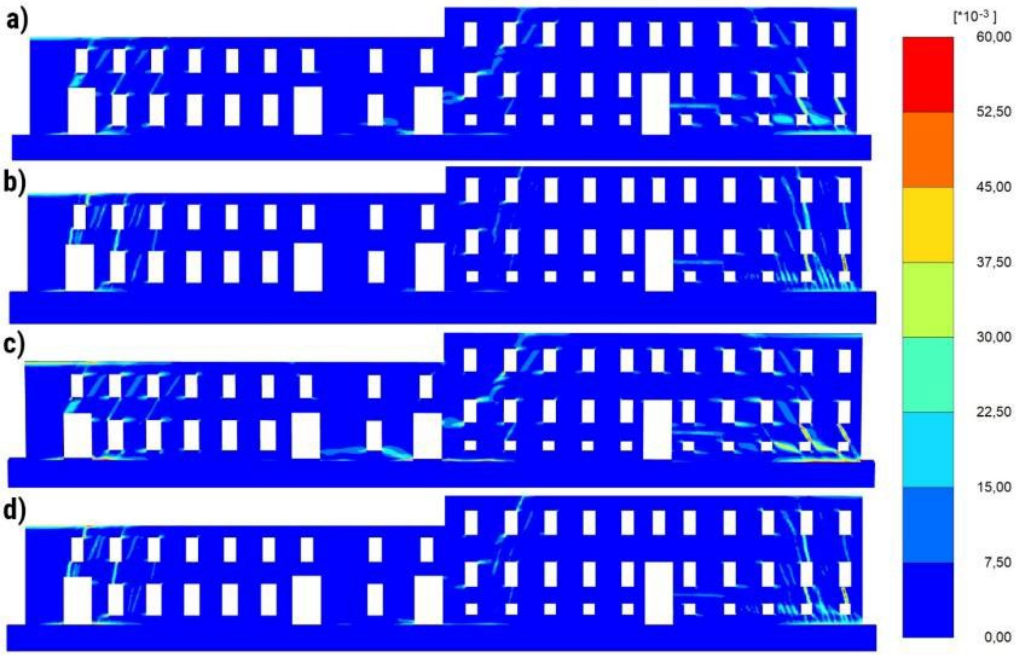

Figure 23. Achieved shear strains after applying defined displacements, compiled by the authors.

The diagrams showing the zones of crack formation and development during nonuniform building settlement correlate with the diagrams obtained by the model developers [27, 28], other researchers [8] and by comparing the simulation results with discrete [64] and other [14] approaches.

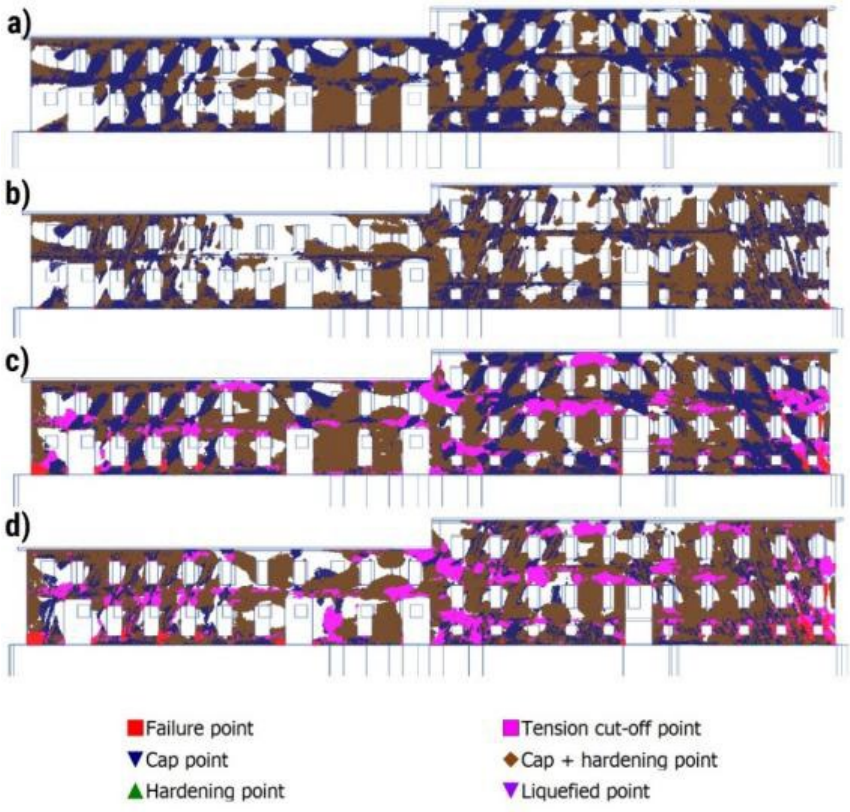

Table 8. Considered calculation scenarios.

Case	Input parameters by:	Dilatancy
a	laboratory	$\psi = \varphi$
b	laboratory	$\psi = 0°$
c	tablulated data	$\psi = \varphi$
d	tablulated data	$\psi = 0°$

Figure 24. Achieved plastic points after applying defined displacements, compiled by the authors.

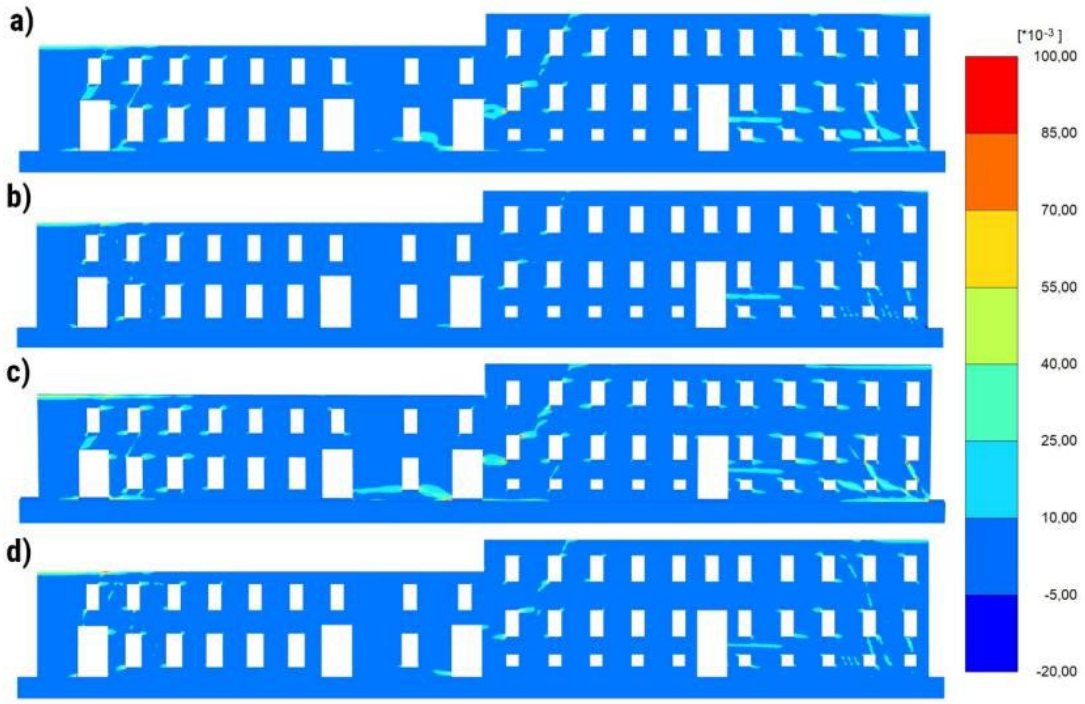

Figure 25. Achieved volume strains after applying defined displacements, compiled by the authors.

4. Conclusions

A set of laboratory tests was carried out, strength and deformation properties of historic bricks and masonry were obtained. To determine the mechanical behavior of bricks under triaxial stress state, a new method of laboratory testing was proposed - by drilling cylindrical specimens from the brick body. A method for obtaining JMM input parameters based on uniaxial tests of mortar and bricks and triaxial tests of bricks was proposed.

It was found that the parameters thus obtained were sufficient to determine the mechanical behavior of historic brick masonry using JMM. The principle of JMM operation was demonstrated on the example of a historic brick building constructed in the beginning of the 20th century. Numerical modeling of the main load-bearing structures of the building was carried out, considering the subsidence of its foundation part. Based on the results of the study, the following conclusions were obtained:

1) The JMM qualitatively described the processes of crack formation with a high degree of reliability, which indicated the possibility of verifying the obtained input parameters of JMM in a similar way.

2) The parameters of brickwork obtained as a result of tests adequately described the process of deformation of a real structure. Further refinement of the test methodology is required. Emphasis should be placed on the scale effect that occurs when testing brick samples. This phenomenon significantly affects the resulting masonry input parameters.

3) A large heterogeneity of the mechanical properties of the tested samples should be noted, which leads to a distortion of the final values of the parameters. More extensive research is required in this direction.

4) When modeling masonry with parameters from tabulated data, more conservative solution was obtained. The formation of zones with excess tensile strength was observed, which was related to the tensile strength of the brick material.

5) Relatively closer agreement with the survey results was achieved when the input parameters for JMM were obtained from lab tests of the bricks, in this way it is possible to verify the input parameters of the JMM model.

6) Calculations considering dilatancy better present the distribution of volumetric deformations in the zones of crack initiation. Based on the received results, it was difficult to conclude which version of flow rule better describe survey findings.

The results allow to conclude that numerical simulation of historic brick buildings can be used as well as their surveys, which will make it possible to clarify the positions of crack development zones in hard-to-reach places and/or in places which was missed during the surveys.

The methodology for determining JMM input parameters is particularly relevant for cases where large-scale testing with sections of old masonry structures is not possible. The considered approach has the prospect of being used to describe the further state of the brickwork during aging by setting an increased differential settlement of the walls of the building.

References

1. Angelillo, M. Constitutive relations for no-tension materials. Meccanica. 1993. 28(3). Pp. 195–202. DOI: 10.1007/bf00989121
2. Nazir, S., Dhanasekar, M. Modelling the failure of thin layered mortar joints in masonry. Engineering Structures. 2013. 49. Pp. 615–627. DOI: 10.1016/j.engstruct.2012.12.017
3. Nazir, S., Dhanasekar, M. A non-linear interface element model for thin layer high adhesive mortared masonry. Computers & Structures. 2014. 144. Pp. 23–39. DOI: 10.1016/j.compstruc.2014.07.023
4. de Buhan, P., de Felice, G. A homogenization approach to the ultimate strength of brick masonry. Journal of the Mechanics and Physics of Solids.1997. 45(7). Pp. 1085–1104. DOI: 10.1016/S0022-5096(97)00002-1
5. Cecchi, A., Sab, K. A multi-parameter homogenization study for modeling elastic masonry. European Journal of Mechanics – A/Solids. 2002. 21(2). Pp. 249–268. DOI: 10.1016/S0997-7538(01)01195-0
6. Zucchini, A., Lourenço, P.B. A micro-mechanical model for the homogenisation of masonry. International Journal of Solids and Structures. 2002. 39(12). Pp. 3233–3255. DOI: 10.1016/S0020-7683(02)00230-5
7. Marfia, S., Sacco, E. Multiscale damage contact-friction model for periodic masonry walls. Computer Methods in Applied Mechanics and Engineering. 2012. 205–208. Pp. 189–203. DOI: 10.1016/j.cma.2010.12.024
8. de Felice, G., Malena, M. Failure pattern prediction in masonry. Journal of Mechanics of Materials and Structures. 2019. 14(5). Pp. 663–682. DOI: 10.2140/jomms.2019.14.663
9. Kapustin, S.A., Likhacheva, S.lu. Modelirovanie protsessov deformirovaniia i razrusheniia materialov s periodicheski povtoriaiushcheĭsia strukturoĭ [Modeling the processes of deformation and destruction of materials with a periodically repeating structure]. Nizhniy Novgorod: NNGASU, 2012. 96 p.
10. Anthoine, A. Homogenization of periodic masonry: plane stress, generalized plane strain or 3D modelling? Communications in numerical methods in engineering. 1997. 13(5). Pp. 319–326. DOI: 10.1002/(sici)1099-0887(199705)13:5<319::aid-cnm55>3.0.co;2-s
11. Massart, T., Peerlings, R., Geers M., Gottcheiner, S. Mesoscopic modeling of failure in brick masonry accounting for three-dimensional effects. Engineering Fracture Mechanics. 2005. 72(8). Pp. 1238–1253. DOI: 10.1016/j.engfracmech.2004.09.007
12. Milani, G., Lourenço, P.B., Tralli, A. Homogenised limit analysis of masonry walls. Part I: failure surfaces. Computers & Structures. 2006. 84(3). Pp. 166–180. DOI: 10.1016/j.compstruc.2005.09.005
13. Livesley, R.K. Limit analysis of structures formed from rigid blocks. International Journal for Numerical Methods in Engineering. 1978. 12(12). Pp. 1853–1871. DOI: 10.1002/nme.1620121207
14. Portioli, F., Casapulla, C., Gilbert, M., Cascini, L. Limit analysis of 3D masonry block structures with non-associative frictional joints using cone programming. Computers & Structures. 2014. 143. Pp. 108–121. DOI: 10.1016/j.compstruc.2014.07.010
15. Malena, M., Portioli, F., Gagliardo, R., Tomaselli, G., Cascini, L., de Felice, G. Collapse mechanism analysis of historic masonry structures subjected to lateral loads: a comparison between continuous and discrete models. Computers & Structures. 2019. 220. Pp. 14–31. DOI: 10.1016/j.compstruc.2019.04.005
16. Karasev M.A., Petrushin V.V., Rysin A.I. The hybrid finite/discrete element method in description of macrostructural behavior of salt rocks. MIAB – Mining Informational and Analytical Bulletin. 2023. 4. Pp. 48–66. DOI: 10.25018/0236_1493_2023_4_0_48
17. Belyakov, N., Smirnova, O., Alekseev, A., Tan, H. Numerical Simulation of the Mechanical Behavior of Fiber-Reinforced Cement Composites Subjected Dynamic Loading. Applied Sciences. 2021. 11(3). Article no. 1112. DOI: 10.3390/app11031112
18. Verbilo, P., Karasev, M., Belyakov, N., Iovlev, G. Experimental and numerical research of jointed rock mass anisotropy in a three-dimensional stress field. Rudarsko-geološko-naftni zbornik. 2022. 37(2). Pp. 109–122. DOI: 10.17794/rgn.2022.2.10
19. Liu, G., Houlsby, G.T., Augarde, C.E. 2-dimensional analysis of settlement damage to masonry buildings caused by tunnelling. The Structural Engineer. 2000. 79(1). Pp. 19–25.
20. Amorosi, A., Boldini, D., de Felice, G., Malena, M. Tunnelling-induced deformation on a masonry structure: a numerical approach. Geotechnical aspects of underground construction in soft ground. 2012. Pp. 353–359. DOI: 10.1201/b12748-48
21. Giardina, G., van de Graaf, A.V., Hendriks, M.A.N., Rots, J.G., Marini, A. Numerical analysis of a masonry façade subject to tunnelling-induced settlements. Engineering Structures. 2013. 54. Pp. 234–247. DOI: 10.1016/j.engstruct.2013.03.055
22. Burd, H.J., Houlsby, G.T., Augarde, C.E., Liu, G. Modelling tunnelling-induced settlement of masonry buildings. Proceedings of the Institution of Civil Engineers – Geotechnical Engineering. 2000. 143(1). Pp. 17–29. DOI: 10.1680/geng.2000.143.1.17
23. Pickhaver, J.A., Burd, H.J., Houlsby, G.T. An equivalent beam method to model masonry buildings in 3D finite element analysis. Computers & Structures. 2010. 88(19–20). Pp. 1049–1063. DOI: 10.1016/j.compstruc.2010.05.006
24. Giardina, G., Ritter, S., DeJong, M.J., Mair, R.J. Modelling the 3D brittle response of masonry buildings to tunnelling. Structural analysis of Historical Constructions: Anamnesis, diagnosis, therapy, controls. 2016. Pp. 481–488. DOI: 10.1201/9781315616995-64
25. Burd, H.J., Yiu, W.N., Acikgoz, S., Martin, C.M. Soil-foundation interaction model for the assessment of tunnelling-induced damage to masonry buildings. Tunnelling and Underground Space Technology. 2022. 119. Article no. 104208. DOI: 10.1016/j.tust.2021.104208
26. Yiu, W.N, Burd, H.J., Martin, C.M. Finite-element modelling for the assessment of tunnel-induced damage to a masonry building. Géotechnique. 2017. 67(9). Pp. 780–794. DOI: 10.1680/jgeot.sip17.P.249
27. Lasciarrea, W.G., Amorosi, A., Boldini, D., de Felice, G., Malena, M. Jointed Masonry Model: A constitutive law for 3D soil-structure interaction analysis. Engineering Structures. 2019. 201. Article no. 109803. DOI: 10.1016/j.engstruct.2019.109803

28. Amorosi, A., Sangirardi, M. Coupled three-dimensional analysis of the progressive tunnelling-induced damage to masonry buildings: is it always worth it? Tunnelling and Underground Space Technology. 2021. 118. Article no. 104173. DOI: 10.1016/j.tust.2021.104173
29. Godman, R.E., Taylor, R.L., Brekke, T.L. A model for the mechanics of jointed rock. Journal of the Soil Mechanics and Foundations Division. 1968. 94(3). Pp. 637–659. DOI: 10.1061/JSFEAQ.0001133
30. Amorosi, A., Boldini, D., de Felice, G., Lasciarrea, W.G., Malena, M. Analisi geotecnica e strutturale del Ninfeo di Genazzano. Rivista Italiana di Geotecnica. 2015. 1. Pp. 29–44.
31. Baryakh, A.A., Devyatkov, S.Yu., Denkevich, E.T. Mathematical modelling of displacement during the potash ores mining by longwall faces. Journal of Mining Institute. 2023. 259. Pp. 13–20. DOI: 10.31897/PMI.2023.11
32. Protosenya, A.G., Alekseev, A.V., Verbilo, P.E. Prediction of the stress-strain state and stability of tunnel face at the intersection of disturbed zones of the soil mass. Journal of Mining Institute. 2022. 254. Pp. 252–260. DOI: 10.31897/PMI.2022.26
33. Karasev, M.A., Nguyen, T.T. Method for predicting the stress state of the lining of underground structures of quasi-rectangular and arched forms. Journal of Mining Institute. 2022. 257. Pp. 807–821. DOI: 10.31897/PMI.2022.17
34. Demenkov, P.A., Komolov, V.V. Study of influence of the deep pit construction on soil mass in flat and spatial formulation. MIAB – Mining Informational and Analytical Bulletin. 2023. 6. Pp. 97–110. DOI: 10.25018/0236_1493_2023_6_0_97
35. Perunov, A.S. On the issue of heterogeneity of structural bricks of buildings of historical development. Engineering journal of Don. 2021. 5(77). Pp. 32–44.
36. Chumachenko, N.G., Chmarkova, S.V. To the question of brick laying restoration of old construction buildings. Problemy gradostroitel'noĭ rekonstruktsii [Problems of urban reconstruction]. 2019. Pp. 148–153.
37. Gospodarikov, A.P., Trofimov, A.V., Kirkin A.P. Evaluation of deformation characteristics of brittle rocks beyond the limit of strength in the mode of uniaxial servohydraulic loading. Journal of Mining Institute. 2022. 256. Pp. 539–548. DOI: 10.31897/PMI.2022.87
38. Moayedian, S.M., Hejazi, M. Effect of scale on compressive strength of brick masonry with gypsum mortar. Measurement. 2021. 172. Article no. 108932. DOI: 10.1016/j.measurement.2020.108932
39. Soleymani, A., Najafgholipour, M.A., Johari, A. An experimental study on the mechanical properties of solid clay brick masonry with traditional mortars. Journal of Building Engineering. 2022. 58. Article no. 105057. DOI: 10.1016/j.jobe.2022.105057
40. Kaldar-ool, A-Kh.B., Opbul, E.K. Stress condition of orthotropic vault structure with cylindrical anisotropy. Magazine of Civil Engineering. 2022. 116(8). Article no. 11605. DOI: 10.34910/MCE.116.5
41. Kabantsev, O.V. Deformation properties of masonry as a piecewise homogeneous medium for elastoplastic strain. Earthquake engineering. Constructions safety. 2013. 4. Pp. 36–40.
42. Smirnova, O.M., Menendez Pidal, I., Alekseev, A.V., Petrov, D.N., Popov, M.G. Strain Hardening of Polypropylene Microfiber Reinforced Composite Based on Alkali-Activated Slag Matrix. Materials. 2022. 15(4). Article no. 1607. DOI: 10.3390/ma15041607
43. Calderón, S., Sandoval, C., Araya-Letelier, G., Aguilar, V. A detailed experimental mechanical characterization of multi-perforated clay brick masonry. Journal of Building Engineering. 2023. 63(B). Article no. 105505. DOI: 10.1016/j.jobe.2022.105505
44. Donnini, J., Maracchini, G., Lenci, S., Corinaldesi, V., Quagliarini, E. TRM reinforced tuff and fired clay brick masonry: Experimental and analytical investigation on their in-plane and out-of-plane behavior. Construction and Building Materials. 2021. 272. Article no. 121643. DOI: 10.1016/j.conbuildmat.2020.121643
45. Laskov, N.N., Laskov, A.N., Artucshin, D.V. The influence of the thickness brick sewer on toughness under joint action vertical and horizontal power. Ėffektivnye stroitel'nye konstruktsii: teoriia i praktika [Efficient building structures: theory and practice]. 2019. Pp. 78–82.
46. Derkach, V.N. Tangential adhesion strength of cement mortars in masonry. Magazine of Civil Engineering. 2012. 29(3). Pp. 19–28. DOI: 10.5862/MCE.29.2
47. Demchuk, I.E., Derkach, V.N. Research of the bonding strength of mortar in masonry. Vestnik of Brest State Technical University. 2012. 1(73). Pp. 70–75.
48. Derkach, V.N. Normal cohesive strength of cement mortar in the masonry. Magazine of Civil Engineering. 2012. 33(7). Pp. 6–13. DOI: 10.5862/MCE.33.1
49. Üçer Erduran, D., Elias-Ozkan, S.T., Ulybin, A. Assessing potential environmental impact and construction cost of reclaimed masonry walls. International Journal of Life Cycle Assessment. 2020. 25(2). Pp. 1–16. DOI: 10.1007/s11367-019-01662-2
50. Pelà, L., Canella, E., Aprile, A., Roca, P. Compression test of masonry core samples extracted from existing brickwork. Construction and Building Materials. 2016. 119. Pp. 230–240. DOI: 10.1016/j.conbuildmat.2016.05.057
51. Pelà, L., Kasioumi, K., Roca, P. Experimental evaluation of the shear strength of aerial lime mortar brickwork by standard tests on triplets and non-standard tests on core samples. Engineering Structures. 2017. 136. Pp. 441–453. DOI: 10.1016/j.engstruct.2017.01.028
52. Ghimire, A., Noor-E-Khuda, S., Ullah, S.N. et al. Determination of Mohr–Coulomb failure envelope, mechanical properties and UPV of commercial cement-lime mortar. Materials and Structures. 2022. 55(4). Pp. 1–19. DOI: 10.1617/s11527-022-01959-z
53. Hayen, R., Schueremans, L., Van Balen, K., Van Gemert, D. Triaxial testing of historic masonry, test set-up and first results. WIT Transactions on the Built Environment. 2001. 55. Pp. 151–160.
54. Hayen, R., Van Balen, K., Van Gemert, D. Triaxial interaction of natural stone, brick and mortar in masonry constructions. Building Materials and Building Technology to Preserve the Built Heritage. 2009. Pp. 333–352.
55. 55. Onishchik, L.I. Kamennye konstrukcii [Stone constructions]. Moscow: Strojizdat, 1939. 412 p.
56. Onishchik, L.I. Prochnost' i ustojchivost' kamennyh konstrukcij [Strength and stability of stone structures]. Moscow: ONTI, 1937. 276 p.
57. de Felice, G., Amorosi, A., Malena, M. Elasto-plastic analysis of block structures through a homogenization method. International Journal for Numerical and Analytical Methods in Geomechanics. 2010. 34(3). Pp. 221–247. DOI: 10.1002/nag.799
58. Heyman, J. The stone skeleton. International Journal of Solids and Structures. 1966. 2(2). Pp. 249–279. DOI: 10.1016/0020-7683(66)90018-7
59. Ofrikhter, I.V., Ponomaryov, A.B., Zakharov, A.V., Shenkman, R.I. Estimation of soil properties by an artificial neural network. Magazine of Civil Engineering. 2022. 110(2). Article No. 11011. DOI: 10.34910/MCE.110.11

60. Verbilo, P.E., Vilner, M.A. Study of the jointed rock mass uniaxial compression strength anisotropy and scale effect. MIAB – Mining Informational and Analytical Bulletin. 2022. 6−2. Pp. 47–59. DOI: 10.25018/0236_1493_2022_62_0_47
61. Ulybin, A.V., Zubkov, S.V. Control methods for strength of ceramic bricks in the inspection of buildings. Magazine of Civil Engineering. 2012. 3(29). Pp. 29–34. DOI: 10.5862/MCE.29.3
62. Belentsov, Yu.A., Kharitonov, A.M., Leykin, A.P. Evaluation of the bearing capacity of the historical buildings' masonry. Bulletin of civil engineers. 2021. 4(87). Pp. 79–85. DOI: 10.23968/1999-5571-2021-18-4-79-85
63. Vermeer P.A., De Borst, R. Non-associated plasticity for soils, concrete and rock. Heron. 1984. 29(3). Pp. 5–64.
64. Pepe, M., Sangirardi, M., Reccia, E., Pingaro, M., Trovalusci, P., de Felice, G. Discrete and Continuous Approaches for the Failure Analysis of Masonry. Frontiers in Built Environment. 2020. 6. Article no. 43. DOI: 10.3389/fbuil.2020.00043

Information about the authors:

Gregorii Iovlev, *PhD of Technical Sciences*
ORCID: https://orcid.org/0000-0002-8615-390X
E-mail: gregoriiovlev@gmail.com

Nikita Belov
E-mail: nikita_belov23@mail.ru

Aleksandr Zileev, *PhD of Technical Sciences*
ORCID: https://orcid.org/0000-0001-9586-8379
E-mail: Zileev_AG@pers.spmi.ru

Received: 28.03.2023. Approved after reviewing: 05.06.2024. Accepted: 06.06.2024.

Magazine of Civil Engineering

ISSN 2712-8172

journal homepage: http://engstroy.spbstu.ru/

Research article

UDC 69

DOI: 10.34910/MCE.128.6

Fire flame effect on some properties of hybrid fiber reinforced LECA lightweight self-compacting concrete

W.H. Al-Kabi ✉ **, *H.K. Awad***

University of Baghdad, Baghdad, Iraq

✉ *fhussein555@gmail.com*

Keywords: lightweight self-compacting concrete, LECA, fire flame, steel fiber, polypropylene fiber, hybrid fiber

Abstract. This research aims to produce lightweight self-compacting concrete (LWSCC) using lightweight expanded clay aggregate (LECA) as coarse aggregate. The additional aim is to study the influence of steel fiber and hybrid fibers (steel and polypropylene (PP)) on the properties of LWSCC in fresh and hardened state. Furthermore, compressive, tensile, and flexural strengths of LWSCC specimens (with and without fibers) are tested after being subjected to the fire exposure. In this study, four LWSCC mixtures with different fiber percentages (0 % fiber, 1 % steel, 0.75 % steel + 0.25 % PP, and 0.5 % steel + 0.5 % PP) are prepared and tested. The specimens were burned at temperatures 25, 300, 400, and 600 °C. The results show that all mixtures have excellent resistance to segregation and high ability to filling and passing. The presence of fibers slightly reduced the workability of LWSCC. The mechanical properties of LWSSC decrease with increasing temperature. The results show that mixtures containing fibers have good mechanical qualities and spalling resistance compared to mixtures without fibers when exposed to fire.

Acknowledgments: The experiments mentioned in this paper were conducted at the Building Materials Laboratory, College of Engineering, Baghdad University.

Citation: Al-Kabi, W.H, Awad, H.K. Fire flame effect on some properties of hybrid fiber reinforced LECA lightweight self-compacting concrete. Magazine of Civil Engineering. 2024. 17(4). Article no. 12806. DOI: 10.34910/MCE.128.6

1. Introduction

Self-compacting concrete (SCC) was first invented in 1986 in Japan by Prof. Okumara. This type of concrete is extremely fluid and does not require vibration or tamping after pouring, it can fill the space between the reinforcement and the corners of the molds [1]. Superior deformability and segregation resistance characterize this type of concrete. Advantages of using SCC include reduced construction time, labor costs, and noise pollution, as well as the ability to fill crowded and thin portions with ease [2].One of the drawbacks of SCC is its large cost, which is due to the usage of large amount of Portland cement and chemical additives. The SCC cost can be lowered if the mineral additions replace a portion of the Portland cement [3]. Mineral additives used in SCC production also have positive economical and environmental effects [4].

Many modern architectural projects are using increasingly structural lightweight concrete (LWC) due to its low density [5]. LWC has good heat insulation due to low thermal conductivity as well as superior sound insulation [6, 7]. Since the forces of earthquakes that influence civil engineering buildings and structures are proportional to the mass of those buildings and structures, it is essential to reduce their mass for earthquake sustainability [8]. Lightweight concrete can be produced in three ways:

1) by substituting the conventional mineral aggregate with lightweight aggregate (this type of concrete is known as lightweight aggregate concrete);

2) by incorporating gas or air bubbles into concrete (air-entrained concrete);

3) by excluding sand from the aggregate (no fines concrete).

Lightweight aggregate concrete is the most common type [9]. Despite its many benefits, LWC has some disadvantages due to the low density of lightweight aggregates, which causes the segregation of aggregate from the mixture [7]. Unsuitable vibration of LWC can cause inefficient distribution of lightweight aggregates, i.e. particles float to the surface of concrete, resulting in forming of a weak layer [10]. Since SCC does not require vibration, using lightweight particles in SCC can help to overcome this problem. Lightweight self-compacting concrete (LWSCC) is a novel concrete that combines the benefits of both SCC and LWC. Inclusion of lightweight aggregates in SCC helps to achieve better strength-to-weight ratio, thermal properties, and fire resistance when subjected to high temperature. Using lightweight aggregates also helps to reduce the dead load of buildings [11, 12]. LWSCC needs no external vibration and can spread into place, fill the formwork and encapsulate reinforcement without any bleeding or segregation [13]. When concrete is exposed to extreme temperatures, a common phenomenon known as spalling can occur, significantly reducing the stability and affecting the structural safety of concrete. Incorporating polypropylene (PP) or steel fibers into concrete is an effective method of preventing spalling [15]. The spalling resistance of concrete containing steel fiber has been shown to be lower than concrete containing PP fiber [16]. Al-Obaidey conducted research [32] to study the effect of steel fibers on fresh and some mechanical properties of LWSCC. According to the findings, using of steel fibers led to negative effects on fresh properties. The steel fibers had the marginal effect on compressive strength, while for both splitting and flexural tensile strengths significant increase was obtained with increasing of steel fibers content. Hachim and Fawzi studied the effect of the type of lightweight aggregate (Thermostone and Porcelinite) in production of LWSCC, the effect of using silica fume (SF) and high reactivity metakaoline (HRM), and the effect of using different ratios of w/cm ratio (0.32 and 0.35) on the properties of LWSCC in the fresh and hardened state. The results indicate that the air dry density for LWSSC of Porcelinite aggregate is 1964 kg/m^3 and the compressive strength is 29.57 MPa after 28 days for w/cm ratio 0.32. The air dry density for LWSCC of Thermostone aggregate is 1820 kg/m^3 and the compressive strength is 25.75 MPa after 28 days for w/cm ratio 0.32. The results demonstrated that the HRM performance, which is locally available, is better than SF in production of LWSCC [33]. Wu et al. in [15] studied the effects of PP fiber on the spalling characteristics and mechanical properties of LWSCC at elevated temperature. The results indicate that the addition of PP fibers greatly reduces the risk of LWSCC spalling. The thermal damage and the loss in residual mechanical properties of LWSCC with PP fibers are smaller compared with that without PP fibers. AL-Radi et al. investigate in [2] mechanical properties of SCC with PP, steel, and hybrid fibers at high temperatures. At temperatures below 200 °C, SCC reinforced with steel fiber shows significant improvement in mechanical properties; at temperatures over 200 °C, these properties begin to drop. Mechanical properties of SCC reinforced with PP fiber dropped at 200 °C. Occurrence of explosive spalling was reduced by using SCC reinforced with steel and PP fibers.

The purpose of this study was to evaluate the properties of LWSCC in fresh and hardened state employing light expanded clay aggregate (LECA) as coarse aggregate. This study also investigated the influence of hybrid fibers on the aforementioned properties. In addition, it evaluated the compressive, flexural, and splitting strengths of LWSCC specimens after being subjected to fire exposure at various temperatures (300, 400, and 600 °C).

2. Methods and Materials

2.1. Materials

2.1.1. Cement

Ordinary Portland Cement (OPC) was used in this research (CEM I-42.5R). The physical and chemical requirements were in accordance with the specifications of IOS.5 [17]. Tables 1 and 2 show the properties of OPC.

Table 1. Chemical properties of OPC.

Oxides	Test results (% by weight)	Limit of IOS.5 [17]
CaO	62.8	----
SiO_2	20.57	----
Al_2O_3	5.56	----
Fe_2O_3	3.32	----
MgO	2.91	5.0 (max)
SO_3	2.23	≤ 2.8 % for C_3A > 3.5 %
I.R	1.00	1.5 (max)
L.O.I	1.94	4.0 (max)
Main compounds of OPC		
C_3S	50.79	---------
C_2S	20.74	---------
C_3A	9.12	---------
C_4AF	10.10	---------

Table 2. Physical properties of OPC.

Physical properties	Test results	Limits of IQS.5 [17]
Specific surface area m^2/kg (Blain method)	381	≥ 280
Setting time (Vicat apparatus)		
Initial setting, min	165	≥ 45 min
Final setting, hr : min	4 : 30	≤ 10 hr
Soundness (Autoclave method), %	0.14	≤ 0.8
Comp. strength at 2 day, MPa	23	≥ 20
Comp. strength at 28 day, MPa	44	≥ 42.5

2.1.2. Fine Aggregate

In this research, natural sand from the region of Al-Ukhaidir was used as fine aggregate in accordance with IOS.45 specifications [18].

2.1.3. Lightweight Expanded Clay Aggregate (LECA)

In this study, LECA was used as lightweight coarse aggregate with maximum size 10 mm. Fig. 1 shows the dry LECA that was soaked in water for one day before being added to the concrete to obtain saturated surface dry LECA particles.

Figure 1. Lightweight expanded clay aggregate (LECA).

Table 3 shows properties of LECA.

Table 3. Properties of LECA.

Property	Results	Limits of IOS.45/1984
Specific gravity	0.65	----
Absorption, %	21	----
Bulk density (loose), kg/m^3	320	----
SO_3	0.07	≤ 0.1

2.1.4. Silica Fume (SF)

In this study, Sika SF with an activity index of 122 % was used. The chemical and physical properties, as well as the activity index, all meet the requirements of ASTM C1240-14 standard [19].

2.1.5. Limestone Powder (LP)

LP was used as an inert mineral filler to enhance the workability and resistance to segregation.

2.1.6. Superplasticizer

In this research, BETONAC®1030, a very effective polycarboxylate-based plasticizer, was used. It was designed to enhance workability and improve slump flow. As a result, the concrete has superior workability without segregation. The superplasticizer used in this study meets the requirements of ASTM C494 standard [20].

2.1.7. Water

The mixing and curing water used in this study was clean and free of impurities, in accordance with IOS.1703 specifications [21].

2.1.8. Steel Fiber

Hook-end steel fibers 35 mm in length and 0.55 mm in diameter with an aspect ratio of 64 were used in this research. This fiber was produced by Bundrex (South Korea). The properties of steel fiber are shown in Table 4.

Table 4. Properties of steel fiber.

Appearance	Hook
Length	35 mm
Diameter	0.55 mm
Aspect ratio “L/D”	64
Density	7800 kg/m^3
Tensile strength	2200 MPa

2.1.9. Polypropylene Fiber

Sika PP fiber used in this research was 12 mm in length, 18 μm in diameter and had density 910 kg/m^3. Table 5 shows the properties of PP fiber.

Table 5. Properties of PP fiber.

Shape	Straight
Color	White
Length	12mm
Diameter	18 μm
Modulus of elasticity	4000 N/mm^2
Specific gravity	0.91 g/cm^2

2.2. Mixture Proportion

In this research, LWSCC mixtures were designed to produce structural lightweight concrete that would meet the requirements of the European guidelines for self-compacting concrete [22] and ACI 213R-03 guide [5]. Therefore, several experimental mixtures were conducted to produce this type of concrete. In this study, four LWSCC mixtures were made with different fiber volume fractions (0 fibers, 1 % steel, 0.75 % steel + 0.25 % PP, and 0.5 % steel + 0.5 % PP). The properties of all four mixtures are shown in Table 6.

Table 6. The concrete mixes.

Mixtures	Binder content		LP, kg/m³	Water, kg/m³	w/b ratio	Sand, kg/m³	LECA, kg/m³	High range water reducing admixtures (HRWRA), % by wt. of binder content	Steel fiber, kg/m³	PP fiber, kg/m³
	Cement, kg/m³	SF, kg/m³								
MR	480	80	30	195	0.34	800	150	1.6	0	0
M S	480	80	30	195	0.34	800	150	1.65	78	0
M SP1	480	80	30	195	0.34	800	150	1.71	58.5	2.275
M SP2	480	80	30	195	0.34	800	150	1.77	39	4.55

Where MR is the reference mix, MS is the mix containing steel fiber only, MSP1 is the mix containing hybrid fiber (0.75% steel + 0.25% PP), and MSP2 is the mix containing hybrid fiber (0.5% steel + 0.5% PP).

2.3. Mixing Procedure

Since LECA has a high capacity for water absorption, it was soaked in water for 24 h before being added to the mixture, and then spread out in the laboratory for an adequate period of time to obtain a state of dry saturated surface. LECA was treated in this way to keep it from absorbing excess mixing water. The process for mixing was as follows:

4) sand and LECA were mixed in the mixer for 1 min;
5) dry ingredients (SF, cement, and LP) were added;
6) water with superplasticizer was added to dry ingredients, and the mixture was mixed for another 5 min;
7) finally, steel and PP fibers were gradually mixed into the mixture until a consistent distribution was achieved.

2.4. Burning and Cooling

The day after making, the concrete samples were removed from the molds and stored in water for up to 28 days. They were then stored in the laboratory at about 23 °C for up to 56 days (28 day in water and 28 day in air). The LWSCC samples were subjected to fire exposure at 300, 400, and 600 °C according to ASTM E119-00a [31] in a furnace specifically designed for this purpose. The temperatures in this study were chosen based on the results of some previous studies [2, 14]. A digital thermometer, as shown in Fig. 3, was used to record the temperature. After reaching the desired temperature, the samples were kept in the furnace for another hour. After that, the samples were taken out and gradually cooled down to room temperature.

Figure 2. Burning furnace.

Figure 3. Digital thermometer.

3. Results and Discussion

3.1. Fresh Properties Results

3.1.1. Slump Flow Tests and T_{500mm} Value

The flow ability of fresh concrete can be evaluated by slump flow tests with Abrams cone. Table 7 and Fig. 4a show the results of slump flow tests. All of the mixtures showed a diameter of slump flow between 650 and 760 mm. All mixture were in accordance with the European guidelines for self-compacting concrete [22] requirements. The slump flow diameter of LWSCC reduced significantly with added fibers in comparison to the mixture without it. The addition of fibers increased flow resistance and decreased flow ability as a result of increased adhesion and friction between the fibers and aggregate.

T_{500mm} values represent the time necessary for the concrete to reach a diameter of 500 mm during slump flow test (i.e. viscosity). The values varied between 2.1 and 3.7 sec. The addition of fibers to LWSCC mixtures increased T_{500mm} values. This was attributed to the increase in flow resistance and the decrease in flow ability as a result of increased adhesion and friction between the fibers and the aggregate [29]. As has been demonstrated in similar studies [27].

3.1.2. V-Funnel Time

The V-Funnel test was used to determine the viscosity and filling ability of SCC [22]. The findings of the V-Funnel test are shown in Table 7 and Fig. 4b. The values ranged between 7 and 10.5 sec. This indicated an increase in the V-Funnel flow time when fibers were included in the LWSCC mixture. This was due to an increase in the viscosity factor of the mixtures, which resulted in concrete with greater cohesion and adhesion. As a result, the exit velocity of fresh concrete through the tab door of the V-Funnel device was slowed down. As has been shown in similar studies [26].

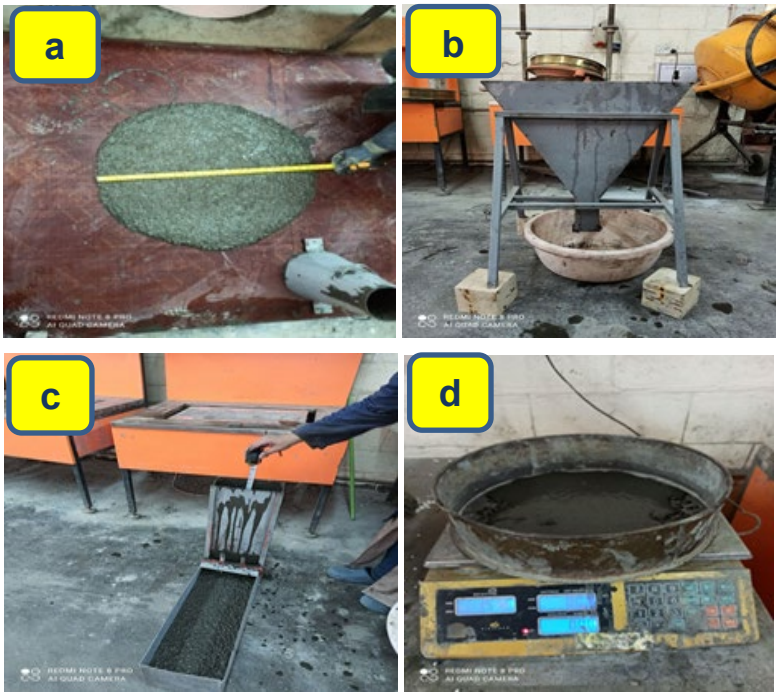

Figure 4. Testing of fresh properties.

Table 7. Fresh properties tests results.

Mixtures	Slump flow, mm	T_{500mm}	V-Funnel, sec	L-Box	Segregation resistance (SR), %
MR	760	2.1	7.0	0.98	18.3
M S	690	2.7	8.5	0.90	12.5
M SP1	675	3.2	9.7	0.85	9.2
M SP2	650	3.7	10.5	0.80	7.7

3.1.3. L-Box Test

In this study, the L-Box with two bars was used to evaluate the passing ability of LWSCC. The findings of the blocking ratio (BR = H2/H1) tests are shown in Table 7 and Fig. 4c. The results ranged between 0.8 and 0.98. This indicated that the addition of fibers into the LWSCC mixture lead to a decrease in blocking ratio (BR). The addition of fiber had a negative effect on passing ability because it increased flow resistance

and decreased flow ability as a result of increased adhesion and friction between fibers and aggregate, as has been demonstrated in similar studies [26].

3.1.4. Sieve Segregation Tests

Sieve segregation was used to measure segregation resistance, as shown in Fig. 4d. Table 7 shows the segregation values for all LWSCC mixtures. According to the results, mixes with added fibers showed lower values when compared to mixtures without fibers. This is due to the distribution of fibers in concrete, which resulted in formation of a network that could effectively prevent aggregate particles from becoming separated from one another. This is why LWSCC with fibers had a higher resistance to segregation. The segregation values for all LWSCC mixtures were within the limits set by the European guidelines for self-compacting concrete [22].

3.2. Hardened Properties Results

3.2.1. Compressive Strength

Compressive strength test for LWSCC was conducted using 100 × 100 × 100 mm cube in accordance with BS EN 12390-3 standard [23]. Table 8 shows the compressive strength values at 28 and 56 days. Compressive strength of LWSCC with fibers specimens (MS, MSP1, and MSP2) increased by approximately 19, 14, and 7 % compared with the reference mixture (without fiber). The fibers enhanced mechanical bonding, which slowed the formation of micro-cracks, limited their further spread, and thus increased compressive strength. Fig. 5 shows the compressive strength of LWSCC mixture after exposure to burning at different temperature. The results showed that compressive strength decreased with increasing temperature in both the specimen with and without fibers. The compressive strength of specimen without fibers decreased by approximately 22, 35, and 55 % at 300, 400, and 600 °C, respectively, due to incompatible changes in the volume of cement paste and aggregate during heating and cooling, leading to dissolution of the interfacial bond [28]. Compressive strength of LWSCC specimen containing steel fibers decreased by approximately 14, 22, and 41 %. Compressive strength of specimen containing hybrid fibers (0.75 % steel + 0.25 % PP) decreased by approximately 16, 30, and 46 %. Compressive strength of specimen containing hybrid fibers (0.5 % St + 0.5 % PP) decreased by approximately 19, 32, and 48 % at 300, 400, and 600 °C, respectively. Heating negatively affected all mechanical properties of LWSCC. However, steel fibers prevented cracking and mitigated damage caused by increased temperatures. The melting of PP fibers resulted in the formation of a large number of small holes between concrete materials, which contributed to the decrease in compressive strength in specimens containing PP fiber. This agrees with other research findings [2].

Table 8. Hardened properties tests results.

Mixtures	Compressive strength, MPa		Splitting strength, MPa		Flexural strength, MPa		Density, kg/m^3
	28 days	56 days	28 days	56 days	28 days	56 days	
MR	25.6	27.2	2.5	2.8	3.9	4.1	1710
MS	30.5	33.1	3.6	4.1	6.2	6.5	1850
MSP1	29.2	31.8	3.4	3.8	5.8	6.1	1800
MSP2	27.6	29.2	3.1	3.5	5.3	5.6	1740

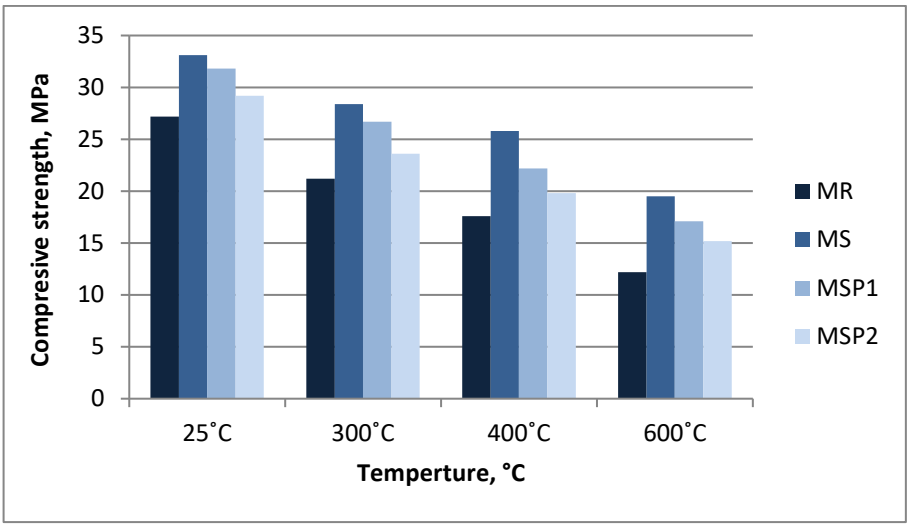

Figure 5. The compressive strength of LWSCC after exposure to different burning temperature.

3.2.2. Splitting Strength

Splitting strength test was conducted using 100 × 200 mm cylinder in accordance with ASTM C496 standard [24]. Table 8 shows the splitting strength values at 28 and 56 days. LWSCC mixtures with fibers (MS, MSP1, and MSP2) had a higher splitting strength than those without fibers by approximately 45, 38, and 25 %, respectively. This was because fibers prevented the formation of micro-cracks in the concrete, thus the tensile strength increased [29]. Fig. 6 shows the splitting strength of LWSCC mixture after exposure to burning at different temperature. The results showed that the splitting strength decreased with increasing temperature in both the specimen with and without fibers. Splitting strength of LWSCC specimen without fibers decreased by approximately 30, 48, and 73 % at 300, 400, and 600 °C, respectively. Splitting strength of specimens with steel fibers decreased by approximately 14, 31, and 51 %. Splitting strength of specimens with hybrid fiber (0.75 % steel + 0.25 % PP) decreased by approximately 18, 34, and 57 %. Splitting strength of specimens with hybrid fiber (0.5 % steel + 0.5 % PP) decreased by approximately 20, 42, and 64 %, respectively. Loss of strength could be caused by a number of factors, including the difference in thermal expansion between the aggregates and cement paste, the degree of drying of the cement paste, and the disintegration of the aggregates.

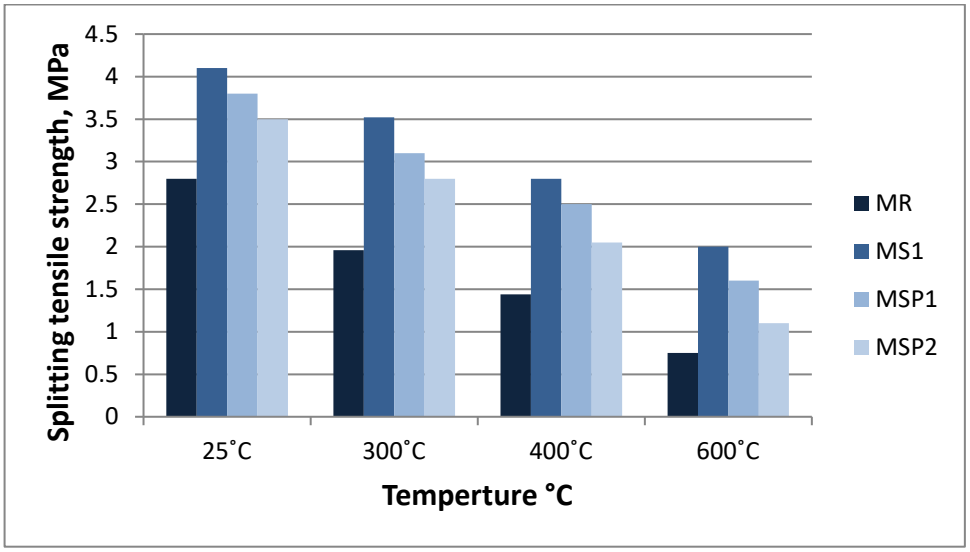

Figure 6. The splitting strength of LWSCC after exposure to different burning temperature.

3.2.3. Flexural Strength

Flexural strength test was conducted using 80 × 80 × 380 mm prism in accordance with ASTM C293-08 standard [25].Table 8 shows the flexural strengths values at 28 and 56 days. In comparison to reference mixtures without fibers, the flexural strength of LWSCC mixtures containing fibers (MS, MSP1, and MSP2) increased by approximately 58 %, 48 %, and 36 %, respectively. This was due to the presence of fibers that prevented the appearance of micro-cracks in the concrete. These results were similar with those obtained by other researchers [2, 30]. Fig. 7 shows the result of flexural strength of LWSCC mixture after exposure to burning at different temperature. The results showed that the flexural strength of LWSCC with and without fibers decreased with increasing temperature. At temperatures 300, 400, and 600 °C, the flexural strength of LWSCC specimen without fibers decreased by approximately 25, 40, and 73 %. Flexural strength of specimens with steel fibers decreased by approximately 14, 25, and 55 %. Flexural strength of specimens with hybrid fiber (0.75 % steel + 0.25 % PP) decreased by approximately 19, 32, and 65 %. Flexural strength of specimens with hybrid fiber (0.5 % steel + 0.5 % PP) decreased by approximately 22, 37, and 69 %, respectively. The reason is that the high temperature had altered the properties of the concrete. Since calcium hydroxide dehydrates at high temperatures, the cement paste contracted. When flexural strength decreased, many micro- and macro-cracks appeared in the specimens due to the thermal incompatibility of the cement used in the paste and the aggregates.

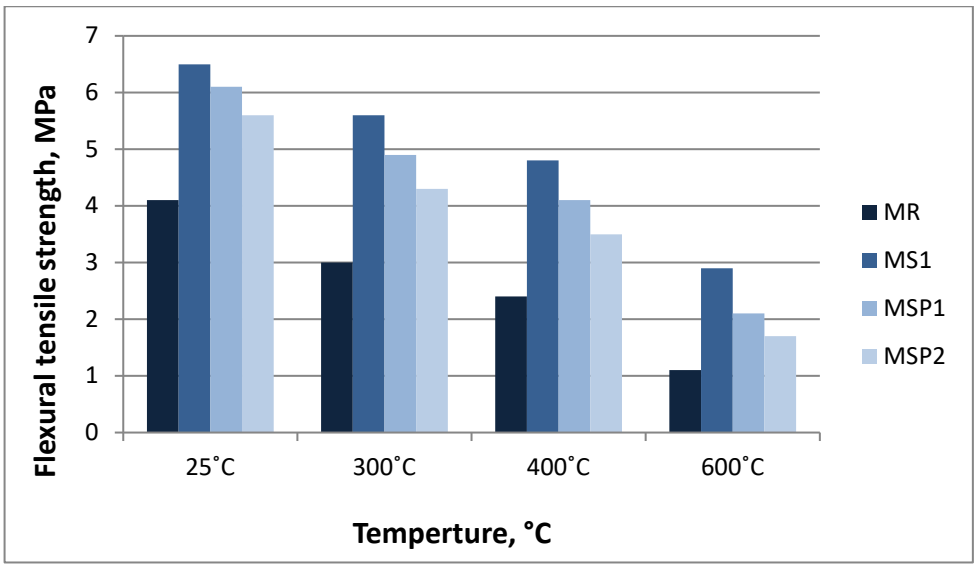

Figure 7. The flexural strength of LWSCC after exposure to different burning temperature.

4. Conclusion

In this study, we conducted a set of experiments to determine the impact of fire exposure on the mechanical properties of LWSCC specimens at different temperatures, as well as to study the effect of using steel and hybrid fibers on same parameters. Based on the discussed results, the following can be concluded:

- All mixtures met the SCC limitations recommended by the European guidelines for self-compacting concrete [22]. Thus, all mixtures had high filling capacity and segregation resistance. The addition of fiber to the mixtures decreased the workability of LWSCC, but the mixtures still met the requirements of the European guidelines for self-compacting concrete [22].
- When compared mixtures without fibers (MR) to mixtures with steel fiber (MS) and hybrid fibers (MSP1, MSP2), slump flow diameter decreased by approximately 9, 11, and 14 %. T_{500mm} increased by approximately 28, 52, and 76 %. V-Funnel increased by approximately 21, 38, and 50 %. L-Box decreased by approximately 8, 13, and 18 %. Sieve segregation resistance decreased by approximately 25, 31, and 40 %. For this reason, large amount of superplasticizer was added to these mixtures in order to preserve their workability.
- The incorporation of steel fibers increased the mechanical properties significantly.
- When specimens were subjected to fire, the compressive strength, tensile strength, and flexural strength decreased.
- When compared to the reference mixture, mixtures with steel and hybrid fibers improved the concrete's residual mechanical qualities at temperatures between 300 and 600 °C.

References

1. Aslani, F., Ma, G. Normal and high-strength lightweight self-compacting concrete incorporating perlite, scoria, and polystyrene aggregates at elevated temperatures. Journal of Materials in Civil Engineering. 2018. 30(12). Article no. 04018328. DOI: 10.1061/(ASCE)MT.1943-5533.0002538
2. AL-Radi, H.H.Y., Dejian, S., Sultan, H.K. Performance of Fiber Self Compacting Concrete at High Temperatures. Civil Engineering Journal. 2021. 7(12). Pp. 2083–2098. DOI: 10.28991/cej-2021-03091779
3. Abd, J., Ahmed, I.K. The Effect of Low Velocity Impact Loading on Self-Compacting Concrete Reinforced with Carbon Fiber Reinforced Polymers. Engineering, Technology & Applied Science Research. 2021. 11(5). Pp. 7689–7694. DOI: 10.48084/etasr.4419
4. Ramanathan, P., Baskar, I., Muthupriya, P. et al. Performance of self-compacting concrete containing different mineral admixtures. KSCE journal of Civil Engineering. 2013. 17(2). Pp. 465–472. DOI: 10.1007/s12205-013-1882-8
5. Robinson, H.C., Spamer, A.B. ACI 213R-87. Guide for Structural Lightweight Aggregate Concrete. Reported by ACI Committee 213. American Concrete Institute. 1987.
6. Maghsoudi, A.A., Mohamadpour, Sh., Maghsoudi, M. Mix design and mechanical properties of self compacting light weight concrete. International Journal of Civil Engineering. 2011. 9(3). Pp. 230–236.
7. Almawla, S.A., Mohammed, M.K., Al-hadithi, A.I. Fresh and mechanical properties of self-compacting lightweight concrete containing Ponza aggregates. 12th International Conference on Developments in eSystems Engineering (DeSE). 2019. Pp. 100–104. DOI: 10.1109/DeSE.2019.00028
8. Sajedi, F., Shafigh, P. High-strength lightweight concrete using leca, silica fume, and limestone. Arabian Journal for Science and Engineering. 2012. 37(7). Pp. 1885–1893. DOI: 10.1007/s13369-012-0285-3

9. Singh, N.T. Effective uses of light weight concrete. Journal of Civil Engineering and Environmental Technology. 2016. 3(3). Pp. 208–211.
10. Madandoust, R., Ranjbar, M.M., Mousavi, S.Y. An investigation on the fresh properties of self-compacted lightweight concrete containing expanded polystyrene. Construction and Building Materials. 2011. 25(9). Pp. 3721–3731. DOI: 10.1016/j.conbuildmat.2011.04.018
11. Abdelaziz, G.E. A study on the performance of lightweight self-consolidated concrete. Magazine of Concrete Research. 2010. 62(1). Pp. 39–49. DOI: 10.1680/macr.2008.62.1.39
12. Medher, A.H., Al-Hadithi, A.I., Hilal, N. The possibility of producing self-compacting lightweight concrete by using expanded polystyrene beads as coarse aggregate. Arabian Journal for Science and Engineering. 2021. 46(5). Pp. 4253–4270. DOI: 10.1007/s13369-020-04886-9
13. Wu, Z., Zhang, Y., Zheng, J., Ding, Y. An experimental study on the workability of self-compacting lightweight concrete. Construction and Building Materials. 2009. 23(5). Pp. 2087–2092. DOI: 10.1016/j.conbuildmat.2008.08.023
14. Tang, C.-W. Residual mechanical properties of fiber-reinforced lightweight aggregate concrete after exposure to elevated temperatures. Applied Sciences. 2020. 10(10). Article no. 3519. DOI: 10.3390/app10103519
15. Wu, X., Wu, Z.-m., Zheng, J.-j., Ueda, T., Yi, S.-h. An experimental study on the performance of self-compacting lightweight concrete exposed to elevated temperature. Magazine of Concrete Research. 2013. 65(13). Pp. 780–786. DOI: 10.1680/macr.12.00218
16. Aydın, S., Yazıcı, H., Baradan, B. High temperature resistance of normal strength and autoclaved high strength mortars incorporated polypropylene and steel fibers. Construction and Building Materials. 2008. 22(4). Pp. 504–512. DOI: 10.1016/j.conbuildmat.2006.11.003
17. Iraqi Organization of Standards (IOS). Portland Cement. IOS.5. National Centre for Construction Laboratories and Researches. 2019.
18. Iraqi Organization of Standards (IOS). Aggregates from Natural Sources for Concrete and Construction. IOS.45/1984. National Centre for Construction Laboratories and Researches. 1984.
19. American Society for Testing and Materials (ASTM). Standard specification for silica fume used in cementitious mixtures. ASTM C1240-14. 2014. 7 p. DOI: 10.1520/C1240-14
20. American Society for Testing and Materials (ASTM). Standard specification for silica fume used in cementitious mixtures. ASTM C494. 2013. 10 p. DOI: 10.1520/C0494_C0494M-17
21. Iraqi Organization of Standards (IOS). Water Used in Concrete. IOS.1703. National Centre for Construction Laboratories and Researches. 1992.
22. The European guidelines for self-compacting concrete: Specification, production and use. 2005. 68 p.
23. British Standards Institution (BSI). Testing hardened concrete – Compressive strength of test specimens. BS EN 12390-3. 2019.
24. American Society for Testing and Materials (ASTM). Standard test method for splitting tensile strength of cylindrical concrete specimens. ASTM C496. 2011. 4 p. DOI: 10.1520/C0496-96
25. American Society for Testing and Materials (ASTM). Standard test method for flexural strength of concrete (using simple beam with center-point loading), ASTM C293-08. 2008. 4 p. DOI: 10.1520/C0293_C0293M-16
26. Ibrahim, H.A., Abbas, B.J. Influence of hybrid fibers on the fresh and hardened properties of structural light weight self-compacting concrete. IOP Conference Series: Materials Science and Engineering. 2019. 518(2). Article no. 022022. DOI: 10.1088/1757-899X/518/2/022022
27. Ali, A.S., Hasan, T.M. Flexural behavior of fiber reinforced self-compacting rubberized concrete beams. Journal of Engineering. 2020. 26(2). Pp. 111–128. DOI: 10.31026/j.eng.2020.02.09
28. Sadrmomtazi, A., Gashti, S.H., Tahmouresi, B. Residual strength and microstructure of fiber reinforced self-compacting concrete exposed to high temperatures. Construction and Building Materials. 2020.230. Article no. 116969. DOI: 10.1016/j.conbuildmat.2019.116969
29. AL-Ameeri, A. The effect of steel fiber on some mechanical properties of self compacting concrete. American Journal of Civil Engineering. 2013. 1(3). Pp. 102–110. DOI: 10.11648/j.ajce.20130103.14
30. Ahmad, S., Umar, A., Masood, A. Properties of Normal Concrete, Self-Compacting Concrete and Glass Fibre-Reinforced Self-Compacting Concrete: An Experimental Study. Procedia Engineering. 2017. 173. Pp. 807–813. DOI: 10.1016/j.proeng.2016.12.106
31. American Society for Testing and Materials (ASTM). Standard test methods for fire tests of building construction and materials. ASTM E119-00a. 2000. 36 p. DOI: 10.1520/E0119-24
32. Al-Obaidey, S.J.K. The Effects of Maximum Attapulgite Aggregate Size and Steel Fibers Content on Fresh and Some Mechanical Properties of Lightweight Self Compacting Concrete. Journal of Engineering. 2020. 26(5). Pp. 172–190. DOI: 10.31026/j.eng.2020.05.12
33. Hachim, Q.J.-A., Fawzi, N.M. The effect of different types of aggregate and additives on the properties of self-compacting lightweight concrete. Journal of Engineering. 2012. 18(8). Pp. 875–888.

Information about authors:

Wafaa Hussein Al-Kabi,
E-mail: fhussein555@gmail.com

Hadeel Khalid Awad,
E-mail: hadeel.kalid@coeng.uobaghdad.edu.iq

Received 07.01.2023. Approved after reviewing 28.05.2024. Accepted 29.05.2024.

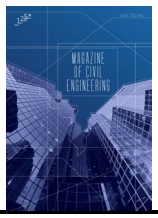

Magazine of Civil Engineering

ISSN 2712-8172

journal homepage: http://engstroy.spbstu.ru/

Research article

UDC 624

DOI: 10.34910/MCE.128.7

Suitability of earthen materials for rammed earth in arid region

E.L. Hasan, M.A. Al-Sharrad ✉

University of Anbar, Ramadi, Iraq

✉ *muayad.alsharrad@uoanbar.edu.iq*

Keywords: earthen materials, rammed earth, sustainable buildings, dynamic adsorption

Abstract. This study investigated the suitability of two engineered earthen materials manufactured by mixing different proportions of sand, silt, and clay for rammed earth constructions under dry conditions. The first mix contained 30 % fine material, whereas the second mix contained 50 % fine material. Test specimens were prepared by static compaction to 4.5, 25, 50, and 100 MPa, equilibrated at relative humidity values of RH = 35 % and RH = 55 % and tested in the lab to characterize plasticity, mechanical, hydric, and thermal behavior. The materials showed a drying shrinkage of no more than 4 %, depending on the initial water content and the unit weight of the material. The results indicated a remarkable increase in materials elastic stiffness and strength of 50 % to 120 % and 10 % to 70 %, respectively, with increasing dry unit weight or compaction energy. The increase in soil suction led to a profound improvement in stiffness and strength, owing to an increase in capillary bonding. In addition, the increase in finer content from 30 % to 50 % significantly enhanced the mechanical behavior. If a minimum compressive strength of 2 MPa is considered, then compacting the earthen material to 50 MPa or greater would provide sufficient strength under the operational humidity RH=55 %. For the mix with 50 % finer content, a compressive strength of almost 5.75 MPa was achieved when the material was compacted to 100 MPa and equalized to RH = 55 %. As relative humidity increased, materials strength decreased where the amount of reduction was found to be inversely proportional to the compaction level and the maximum dry unit weight. The dynamic adsorption behavior was, largely, independent of the amount of compaction energy or finer content. The dynamic adsorption test indicated that the tested materials exchange a considerable amount of moisture with the atmosphere. Compared to traditional brick and concrete blocks, the materials showed good insulation characteristics. It was observed that the increase in finer content yielded slightly higher thermal conductivity values. Overall, the engineered material examined in this work can be potentially used for rammed earth under dry conditions.

Acknowledgments: The authors would like to thank the staff of the soil mechanics lab at the University of Anbar for making lab equipment available for the experimental work of this paper.

Citation: Hasan, E.L., Al-Sharrad, M.A. Suitability of earthen materials for rammed earth in arid region. Magazine of Civil Engineering. 2024. 17(4). Article no. 12807. DOI: 10.34910/MCE.128.7

1. Introduction

The exceptional environmental and energy challenges, particularly in arid regions, have mandated a rebirth of sustainable construction materials and building technologies. One of the major differences between modern and ancient earthen constructions recounts to the ability to engineer a material with preferential properties, such as high strength and excellent durability. Modern earth building techniques have been developed with the objective of optimizing quality control, increasing construction efficiency and reducing labor and material costs.

As a sustainable replacement for conventional building materials like concrete or fired bricks, rammed earth provides a number of advantages. The embodied energy and carbon dioxide footprints of a rammed earth construction can be much lower than that of an identical structure composed of more

traditional materials, such as concrete or masonry [1–3]. In addition, rammed earth buildings outperform traditional buildings in terms of the energy consumed during buildings operation, thanks to the outstanding hygrothermal properties [4, 5]. Moreover, raw rammed earth is eco-friendly and can be fully recyclable.

Despite the numerous advantages of rammed earth regarding sustainability, various limitations restrict its extensive use for constructions. Because of the profound effect of water on the raw rammed earth, the mechanical behavior is always disputable. The admission of moisture into the wall can decrease material strength significantly as a consequence to suction decrease. These concerns have been emerging over the last few decades, see for example [6, 7]. Moreover, rammed earth constructions are quite sensitive to rain and wind erosion and to the effect of aggressive environments, so they frequently need a protection against weathering [8–10].

According to [11], the soil should generally contain a high proportion of sand and gravel, along with silt and just enough clay to serve as a binder, which is also able to provide acceptable hygroscopic and thermal characteristics. According to [12], rammed earth should have a clay fraction of 5 % to 15 %, a silt fraction of 15 % to 30 %, and a sand with fine gravel fraction of 50 % to 70 %.

An interesting statistical analysis of numerous plasticity data on compressed earth blocks (CEB) and adobe was performed in [13]. The analysis indicated significant variation in the liquid limit (LL) and the plastic limit (PL) values for both the CEB and adobe. Nevertheless, according to the researchers, three quarters of the LL values of the CEB material were between 25 % and 45 %, whereas more than half of these values were between 20 % and 40 % for the adobe material. The analysis of the PL values showed that the majority of the PL values were between 15 % and 29 % for both, the CEB and adobe materials.

Having knowledge of the shrinkage factors such as shrinkage limit, linear and volumetric shrinkage is essential to regulate swelling and shrinkage and to avoid serviceability problems such as crack generation and material disintegration in rammed earth buildings. The occurrence of these problems depends on the type and percentage of clay, the materials gradation, and the amount of moisture. Maniatidis and Walker in [11] cited few examples of maximum permissible linear shrinkage values, ranging from 0.05 % to 3 %. According to numerous studies e.g. [14–16], shrinkage and plasticity of the earthen material can be regulated partly by controlling sand proportion.

Durability in the context of earth construction means the ability of the structure and all its elements to withstand the destructive action of weathering and other actions without degradation to the expected service life [11]. The German standard DIN 18945 [17] classified earth bricks with respect to their resistance to water penetration into three classes. The first class should possess sufficient resistance under partial or complete exposure to water without weather protection. The second class should possess sufficient resistance under weather protection condition. The third class is not water resistant and can be specified to only dry applications such as stacked walls. In the present work, the researchers utilized local soils to engineer a sustainable building material favorable for sustainable constructions in arid climate regions with the best use of the passive energy from the atmosphere.

2. Methods and Materials

2.1. Materials

For the present work, local soils brought from two borrow sites near Ramadi city, Iraq, were collected. Two soil types were selected; Soil 1 was a fine material, while Soil 2 was sand. The mineral composition of these soils was examined by performing X-ray fluorescence (XRF) with a Spectro XLab Pro analyzer. Table 1 shows the main minerals comprising these soils.

Table 1. Mineral composition of Soil 1 and Soil 2.

Element	(%) by weight	
	Soil 1	Soil 2
Sodium	1.61	0.09
Magnesium	4.02	0.36
Aluminum	10.61	1.21
Silicon	41.98	71.07
Sulfur	2.39	0.35
Potassium	2.74	0.08
Calcium	15.58	2.57
Titanium	0.83	0.16
Iron	6.00	1.07

2.2. Mixtures and Experimental Procedures

2.2.1. Grain size distribution (GSD)

The grain size distribution was determined according to the ASTM Standard D422 [18] by dry sieving for the material larger than 75 μm and a hydrometer for the material smaller than 75 μm. Soil 1 comprised of 50 % silt and 50 % clay, whereas Soil 2 comprised of 100 % sand.

Neither Soil 1 nor Soil 2 complies with the gradation requirements for earthen building materials suggested in the literature e.g. [19]. Therefore, two new soils were fabricated, namely: Mix 1 with 70 % sand, 15 % silt, and 15 % clay, and Mix 2 with 50 % sand, 25 % silt, and 25 % clay. The gradation curves of Mix 1 and Mix 2 are shown in Fig. 1.

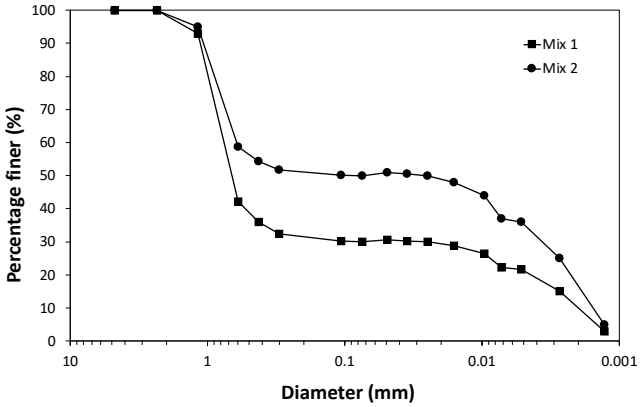

Figure 1. Grain size distribution of Mix 1 and Mix 2.

2.2.2. Plasticity

The liquid limit and plastic limit tests were performed on materials finer than 0.425 mm (sieve No. 40), according to the ASTM Standard D4318 [20]. The plasticity index (PI) was determined as the difference between the liquid limit and the plastic limit of the soil. The shrinkage factors test was performed by the water submersion method of the ASTM Standard D4943 [21] on materials finer than 0.425 mm, taken from Mix 1 and Mix 2. Initially, the samples were mixed thoroughly with water to form a paste with a water content higher than the liquid limit by 10 %. In this test the shrinkage limit (SL), shrinkage ratio (R), volumetric shrinkage (Vs), and linear shrinkage (Ls) are determined. The values of the plasticity factors for Mix 1 and Mix 2 are summarized in Table 2.

Table 2. Plasticity factors of the mixes.

	Liquid limit	Plastic limit	Plasticity index	Shrinkage limit	Shrinkage ratio	Volumetric shrinkage	Linear shrinkage
	LL	PL	PI	SL	R	Vs	Ls
	(%)	(%)	(%)	(%)		(%)	(%)
Mix 1	48.4	23.62	24.8	20.3	1.78	59.7	79.1
Mix 2	54.3	24.2	30.1	14.6	1.82	90.5	82.5

2.2.3. Specimen preparation

Test specimens with 100 mm height and 50 mm in diameter were fabricated by static compaction. A compaction rig was manufactured, as shown schematically in Fig. 2, following the proposal of [22, 23]. This method targets increasing material density, hence providing higher compressive strength, by applying a static compressive force on a laterally confined soil specimen. Specimens were prepared by thoroughly mixing predetermined proportions of the materials in a dry state, then the required amount of water was introduced. Specimen compaction was achieved by pouring one-third of the wet material, each time, inside the mold, then applying constant displacement compression (0.1 mm/min) until a target compressive pressure of 4.5, 25, 50, and 100 MPa was reached. The specimen was unloaded then extruded and taken for weight-volume measurements before being properly stored inside a plastic bag until the next stage. The static compaction pressure 4.5 MPa was relatively small and was only taken as a reference, equivalent to the standard Proctor compaction.

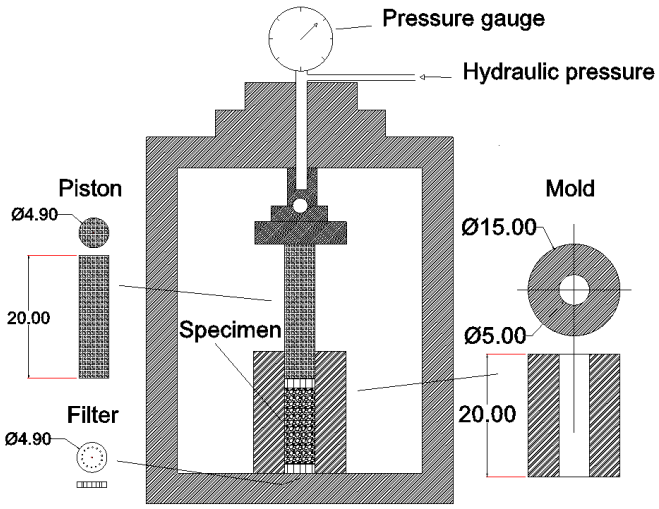

Figure 2. Schematic diagram of the compaction rig.

2.2.4. Compressive strength test

The material stiffness and compressive strength were investigated by performing unconfined compression tests on specimens with different initial unit weight values and moisture states, according to the ASTM Standard D2166 [24]. The test was performed at a constant loading/unloading rate of 1 mm/min. Young's modulus was obtained by performing loading-unloading cycles, between one-ninth and one-third of the estimated compressive strength. The elastic modulus was determined as the average slope of the lines best fitting the unloading branches of these cycles. It is assumed that material behavior is elastoplastic during loading but mainly elastic during unloading. The specimens were subsequently loaded to failure to measure the unconfined compressive strength.

2.2.5. Soil suction test

In this work, the matric and total suctions of the materials were measured indirectly with the filter paper technique, in which the filter paper has a predefined water retention curve. Under vapor equilibrium condition inside a closed system, the soil suction is inferred from the water content of the contact filter paper for matric suction and non-contact filter paper for total suction. Three identical specimens with 20 mm height and 50 mm in diameter were initially prepared at each compaction pressure of the two mixes at the target optimum water content and maximum dry unit weight. Two of these specimens were equalized at a constant temperature of 20 ± 2 °C to a constant mass at relative humidity values of RH = 55 ± 2 % and RH = 35 ± 2 %. These values correspond to the prevailing winter and summer humidity values in Ramadi, respectively. Matric and total suction of these samples were measured with the filter paper technique by the ASTM Standard D5298 [25], using Whatman No. 42 filter papers. Alternatively, for a given constant temperature and relative humidity, the value of total suction can be obtained by using the Kelvin equation [26]:

$$\psi = -\frac{RT}{V_m}\ln\left(RH\right), \tag{1}$$

where R is the universal gas constant (8.31 J mol^{-1} K^{-1}), T is the absolute temperature (K) and V_m is the molar volume of water (18*10^{-6} m^3/mol). The containers were kept closed for 10 days in order to achieve vapor pressure equilibrium of the water in the filter papers, the specimen and the air inside the container.

2.2.6. Moisture buffering

The absorptive behavior of the material was evaluated by measuring the moisture buffering value (MBV) following the NORDTEST project method described in [27]. The practical MBV is calculated as follows:

$$MBV_{practical} = \frac{\Delta m}{S\Delta\%RH}, \tag{2}$$

where $MBV_{practical}$ quantifies the amount of moisture $\left(\Delta m\right)$ gained or released per exposed surface area (S) over a given time interval as a result of a variety of relative humidity $\left(\Delta\%RH\right)$. For each mix, four

samples with 100 mm height and 50 mm in diameter were prepared at the optimum water content and dry unit weight corresponding to 4.5, 25, 50, and 100 MPa compaction pressure. These specimens were then conditioned inside a humidity room to the same relative humidity of RH=55 %. The specimens were mounted in an upright position in such a manner that the top and the curved faces were the only ones exposed to RH variation. Subsequently, the samples were subjected to a step cyclic increase/decrease of RH between 75 ± 2 % and 50 ± 2 % until a virtually constant mass of water was absorbed/released over the last few cycles. The step increase/decrease was performed every 12 hours. Meanwhile, the specimen weight was frequently recorded.

2.2.7. Thermal conductivity

The steady-state coefficient of thermal conductivity of the earthen material was tested using WL373 thermal conductivity meter, as shown in Fig. 3. Soil specimens with 30 mm height and 21 mm in diameter were compacted to predefined moisture and unit weight values inside a HDPE tube, which was placed inside the compaction mold. A set of three specimens were prepared at the maximum dry unit weight of each compaction pressure. Then two of each set were equalized at a relative humidity of RH = 55 ± 2 % and RH = 35 ± 2 %, under a constant temperature of 20 ± 2 °C. The test specimen is mounted between a heat source and a heat sink. A steady-state heat flux (Q) was applied, while the temperature drop across the specimen (ΔT) was monitored and measured by thermocouples installed close to the specimen faces. The coefficient of thermal conductivity (k) was calculated under steady-state temperature distribution as [28]:

$$k = \frac{QL}{A\Delta T}, \tag{4}$$

where L and A are the length and the cross-sectional area of the sample, respectively.

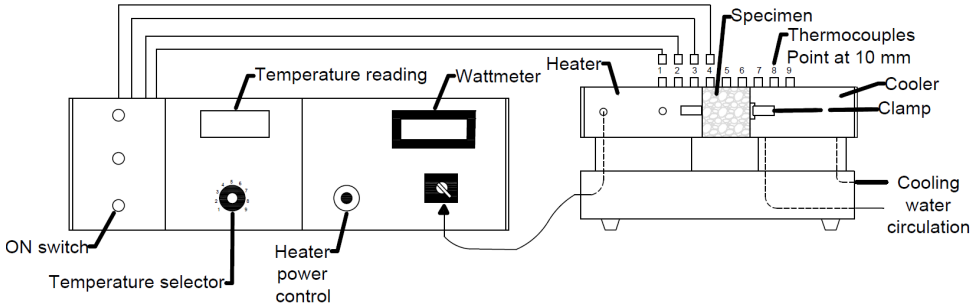

Figure 3. Thermal conductivity meter model WL373.

3. Results and Discussion

3.1. Compaction Characteristics

The compaction curves of Mix 1 and Mix 2 for 4.5, 25, 50, and 100 MPa compaction pressures are shown in Fig. 4. The maximum dry unit weight increased and the optimum water content decreased with increasing compaction energy. For Mix 1, the maximum dry unit weight increased from 19.94 kN/m^3 to 21.91 kN/m^3, while the corresponding optimum moisture content decreased from 10 % to 4.2 % when compaction pressure increased from 4.5 to 100 MPa. Similarly, for Mix 2, the maximum dry unit weight increased from 19.02 kN/m^3 to 21.51 kN/m^3, while the corresponding optimum moisture content decreased from 12.5 % to 5.8 %.

The variation of dry unit weight with compaction energy, as shown in Fig. 5, follows a nonlinear pattern, in which the former tends toward an ultimate virtual value corresponding to zero porosity. Therefore, the higher the compaction pressure, effectively up to 75 MPa, the lower the porosity. Mix 2 always showed lower unit weights compared to Mix 1, despite its high finer content. This is probably attributed to the higher suction values attained by Mix 2 specimens. In addition, the corresponding decrease in porosity was found to be from 22.1 % to 14.4 % and from 25.7 % to 16.0 % for Mix 1 and Mix 2, respectively. These observations are in good agreement with those reported by many researchers, e.g. [22, 29].

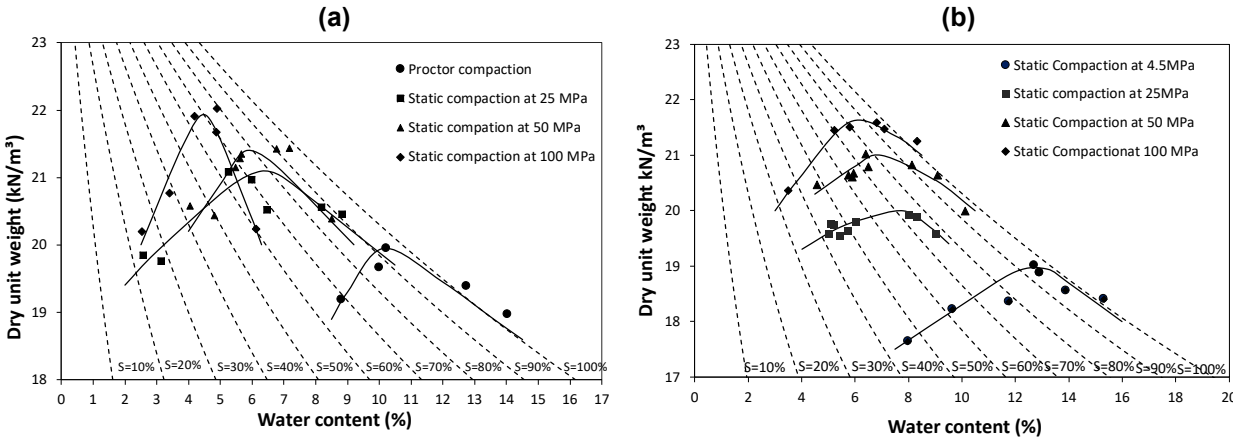

Figure 4. Compaction characteristics for: (a) Mix 1, (b) Mix 2.

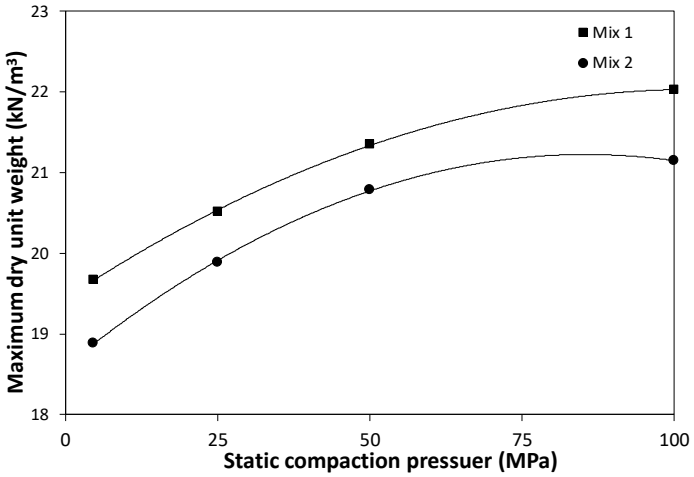

Figure 5. Variation of as-compacted maximum dry unit weight with compaction pressure.

3.2. Moisture Equalization

The moisture equalization was performed under the constant temperature 20 ± 2 °C and the relative humidity RH = 55 ± 2 % and RH = 35 ± 2 %. Over the equalization period, specimen's water content was decaying exponentially. Moisture equilibrium was practically achieved, under a given constant RH, when the mass of the specimens varied by less than 0.1 % during a minimum of one week. On average, moisture equilibrium was achieved after at least one month. In theory, the rate of evaporation of pore water is affected by the difference in relative humidity of the pore air and that of the adjacent air outside the specimen. In principle, the drying process continues until a particular vapor pressure satisfying equilibrium condition is achieved. Fig. 6 illustrates that a modest increase in the dry unit weight took place due to moisture equalization of Mix 1 and Mix 2 specimens originally compacted at the optimum moisture content to 4.5, 25, 50, and 100 MPa.

The amount of shrinkage that occurs due to drying from the as-compacted state to the state at RH=35 % was calculated based on the specimen volume before and after the equalization. A general trend emerged that the higher the initial water content, the higher the drying shrinkage will be. Conversely, the higher the dry unit weight, the lower the drying shrinkage will be. The maximum amount of drying shrinkage, which was nearly 4 %, is considerably lower than the volumetric shrinkage (see Table 2). Thanks to the compaction technique that allows production of dense material at rather low optimum moisture content (4–7 %). By the end of the equalization stage, no shrinkage cracks or discontinuities were observed in the specimens. This promotes the selected material for the next level of the investigation, as illustrated in the following sections.

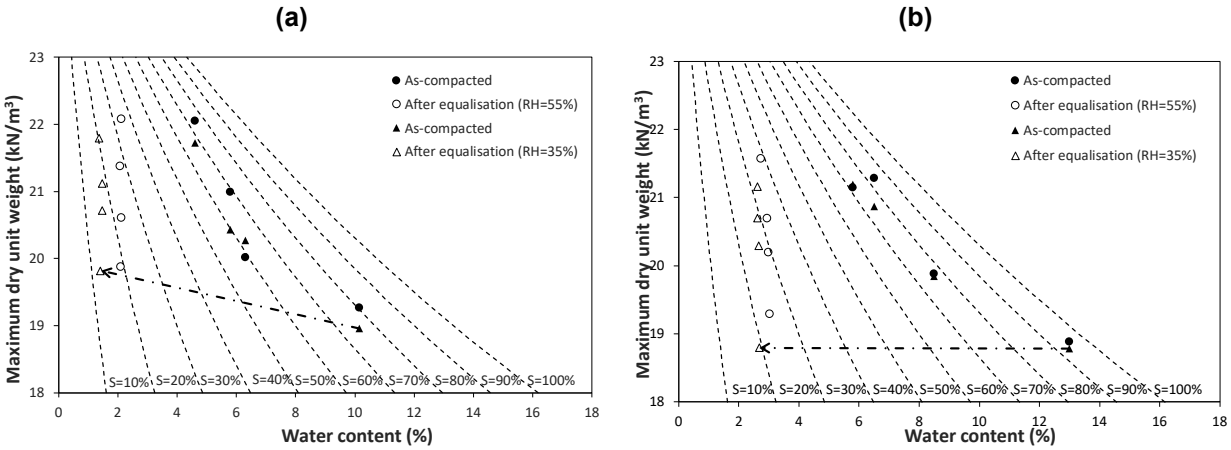

Figure 6. Changes in dry unit weight and water content during equalization for: (a) Mix 1, (b) Mix 2.

3.3. Soil Suction

Fig. 7 presents the variation of total and matric suction with degree of saturation, measured after achieving moisture equilibrium at RH=55 % and RH=35 % as well as at the as-compacted states. Both total and matric suction values were progressively increasing with saturation decreasing. For a given water content, Mix 2 expectedly showed higher suction values than Mix 1, owing to the higher clay content, which in turn resulted in smaller pore sizes and higher adsorption. It appears that the moisture equilibrium brought the saturation and the suction to a residual state. At the residual water content region, most likely at water contents less than 2 %, the residual total and matric suction became the same. This is anticipated where the capillary effect ceases and the available water forms a thin layer surrounding the solid particles. The variation of suction with saturation, i.e. with RH, has several consequences on earthen material strength and the hygrothermal response, as will be explained later in this paper. It was noticed that the higher the dry unit weight of the soil, the more slowly the saturation declines when suction is increased (i.e. when the RH was set to 55 % and 35 %). The soil specimen's smaller, interconnecting pores most likely caused this.

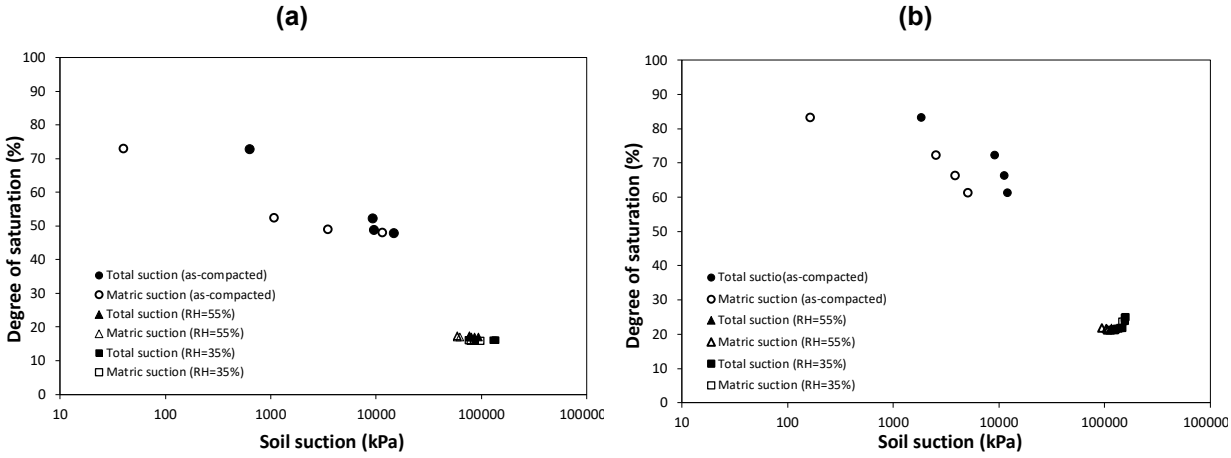

Figure 7. Variation of total and matric suction with degree of saturation for: (a) Mix 1, (b) Mix 2.

3.4. Mechanical Behavior

Three identical specimens initially compacted to 4.5, 25, 50, and 100 MPa for each mix. The main objective was to determine the effect of the compaction pressure (hence the dry unit weight), moisture variation, and finer content, on the stiffness and strength of the unstabilized earth. To imitate the effect of materials moisture variation triggered by ambient humidity variation, two of each three identical compacted specimens were brought to moisture equilibrium at RH = 55 % and RH = 35 % inside the humidity room. Fig. 8 presents typical stress-strain response for specimens compacted to 100 MPa. Fig. 9 captures the effect of dry unit weight increase on earthen material stiffness and compressive strength for Mix 2. These material variables increased substantially, in a nonlinear fashion, with increasing dry unit weight as a result of frictional resistance increase.

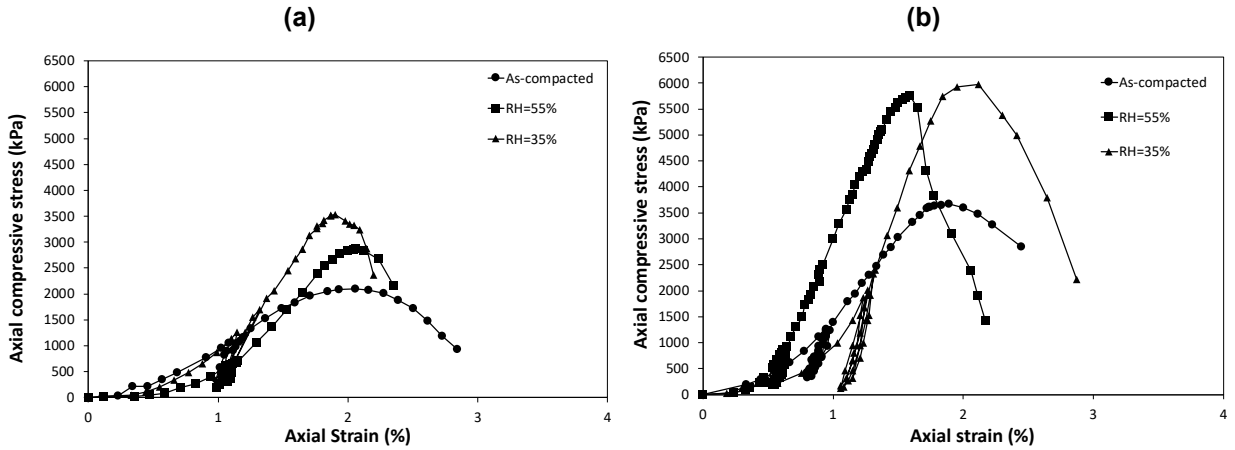

Figure 8. Typical stress-strain behavior for specimens compacted at 100 MPa: (a) Mix 1, (b) Mix 2.

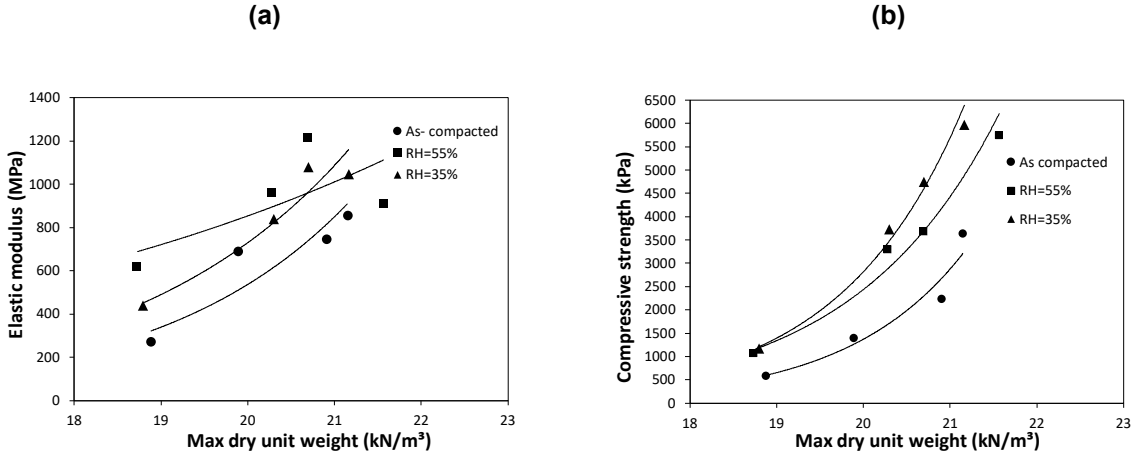

Figure 9. Variation of Young's modulus and the compressive strength with dry unit weight for Mix 2.

3.5. Effect of the Relative Humidity Variation

The effect of relative humidity variation, expressed in terms of total suction, on the stiffness and compressive strength of Mix 2 specimens is shown in Fig. 10. The total suction appears to have a profound effect on the stiffness and strength of the earthen material. A similar observation can be found in [30]. The increase of suction produced a remarkable increase in Young's modulus and compressive strength. For instance, compressive strength of specimens compacted to 50 MPa increased from just about 1400 kPa to slightly less than 2600 kPa for Mix 1 and from 2200 kPa to 4750 kPa for Mix 2, over suction variation from the as-compacted state to that corresponding to RH=35 %. As the earthen material dries, capillary suction increases leading to an increase in stiffness and strength.

Raw earth is characterized by the presence of meniscus water bridges between particles, which generate capillary bonding thereby increasing the overall strength and stiffness of the material. In other words, the mechanical properties of compacted earth improve, as degree of saturation decreases with decreasing ambient humidity. At the same time, the material becomes more brittle as the ability of the material to undergo substantial plastic straining before failure decreases with drying, see for example Fig. 8.

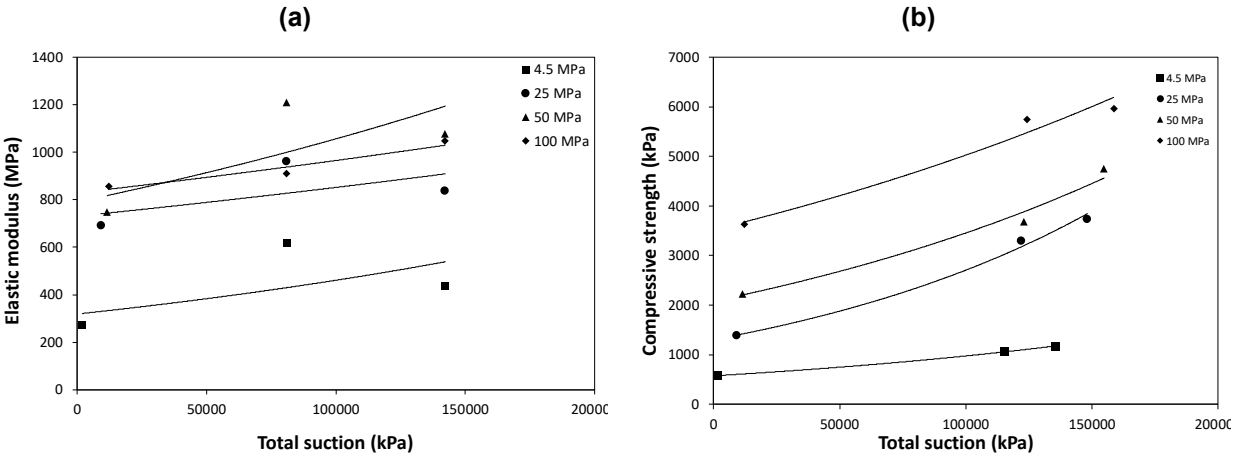

Figure 10. Variation of strength and Young's modulus with suction for Mix 2.

Results analysis indicated that Mix 1 could provide a minimum compressive strength of 1300 to 2900 kPa and provide a maximum compressive strength of 2300 to 3500 kPa when the material statically compacted to pressure level between 25 and 100 MPa, as shown in Table 3. Instead, Mix 2 could provide a minimum compressive strength of 3300 to 5750 kPa and provide a maximum compressive strength of 3700 to 6000 kPa when the material statically compacted between 25 and 100 MPa. The minimum and the maximum figures above correspond to the RH = 55 % and RH = 35 %, respectively. For a given compaction condition, the compressive strength decreases with increase in relative humidity as per Table 3. The reduction in strength appears to show a dependency on the compaction level where specimens compacted at 100 MPa preserved more strength upon wetting than those compacted at 50 and 25 MPa. That suggests that material mechanical behavior is more controlled by variables, such as pore size and pore size distribution, than by the effect of suction.

Table 3. Reduction in strength produced by an increase of RH from 35 % to 55 %.

Mix	Compaction pressure (MPa)	Compressive strength (kPa)		Reduction in strength (%)
		RH = 35 %	RH = 55 %	
Mix 1	25	2300	1300	43
	50	2600	2000	23
	100	3500	2900	17
Mix 2	25	3700	3300	11
	50	4750	3700	22
	100	6000	5750	4

3.6. Moisture Buffering

Each specimen was subjected to seven cycles of a relative humidity step change between RH = 50 % and RH = 75 %. The moisture buffering value (MBV) was calculated from Equation 1, see a typical variation of the MBV in Fig. 14 for Mix 2. During the first few cycles, the MBV tended to be greater for moisture absorption than for moisture release. The last few cycles indicated that the tested material has a moisture buffering values of about 1.50 and 1.55 (g/ (m^2%RH)) for Mix 1 and Mix 2, respectively. The increase in finer content does not appear to improve the moisture exchange between the material and the atmosphere. Further investigation is therefore required on the materials sorption capacity and materials vapor permeability. It can be seen that the hygroscopic behavior of the specimens is essentially the same regardless of the differences in initial unit weight.

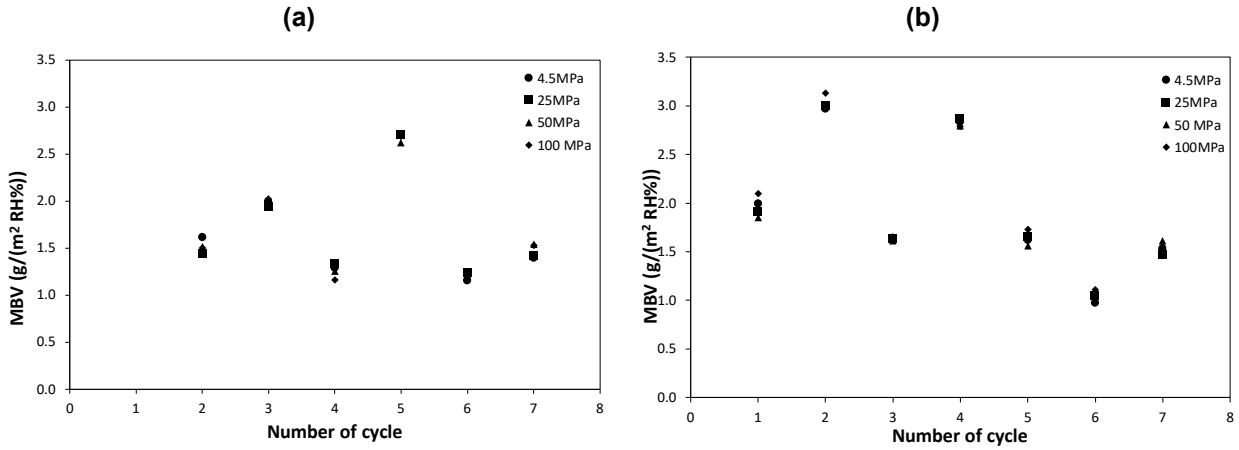

Figure 11. Typical moisture buffering variation for Mix 2 for: (a) moisture adsorption, (b) moisture release.

3.7. Thermal conductivity

Fig. 12 shows typical variation of the coefficient of thermal conductivity (k) with bulk unit weight and degree of saturation for Mix 2. Inspection of this figure suggests that k generally decreased with increasing material's bulk unit weight but tend to increase slightly with increasing saturation. As saturation increases, pore air is gradually replaced by water, which possesses significantly higher thermal conductivity. It is believed that under a residual state, which may occur at saturation degrees less than 15 % for Mix 1 and 30 % for Mix 2, the water mainly exists as a thin film surrounding the particles. This residual water is not expected to contribute much to the thermal conductivity. At higher saturation degrees, the water menisci are formed at the inter-particles contacts, leading to an increase in the thermal conductivity. Over the examined range of unit weight and degree of saturation values, the thermal conductivity *k* varied from 1.10 to 1.35 W/(m.K) for Mix 1 and from 1.2 to 1.3 W/(m.K) for Mix 2. These figures of the current earthen material are comparable to those of other construction materials, such as adobe blocks and fired bricks, see [31].

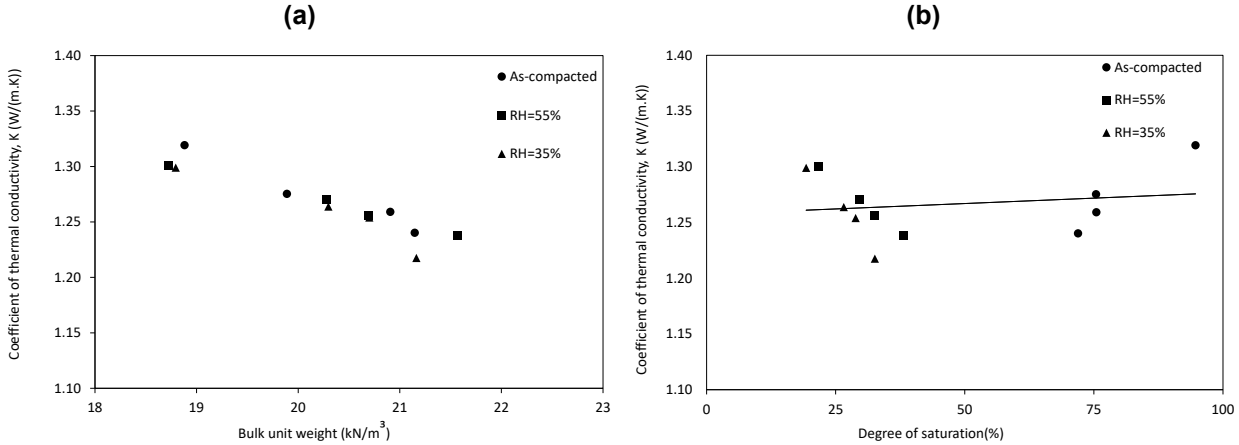

Figure 12. Variation of the thermal conductivity of Mix 2 with: (a) bulk unit weight, (b) degree of saturation.

3.8. Microstructural Characteristics

Fig. 13 shows SEM images taken at 7000× magnification of samples taken from Mix 1 and Mix 2, compacted to 25 MPa or to 100 MPa. Comparison of Fig. 13a and 13b indicates that the Mix 1 sample exhibited larger pore sizes compared to the Mix 2 sample. These pores became very small for the compaction pressure 100 MPa, as can be seen in Fig. 13c and 13d. In addition, aggregations of fine particles can be observed very clearly on the samples compacted to 25 MPa. These aggregations are an inherited feature of compacted materials, formed when water is introduced during the compaction process. A dual-porosity structure, characterized by macro pores between the aggregates and micro pores between the particles, can be observed. As the compaction pressure proceeds to100 MPa, the macro pores became progressively smaller.

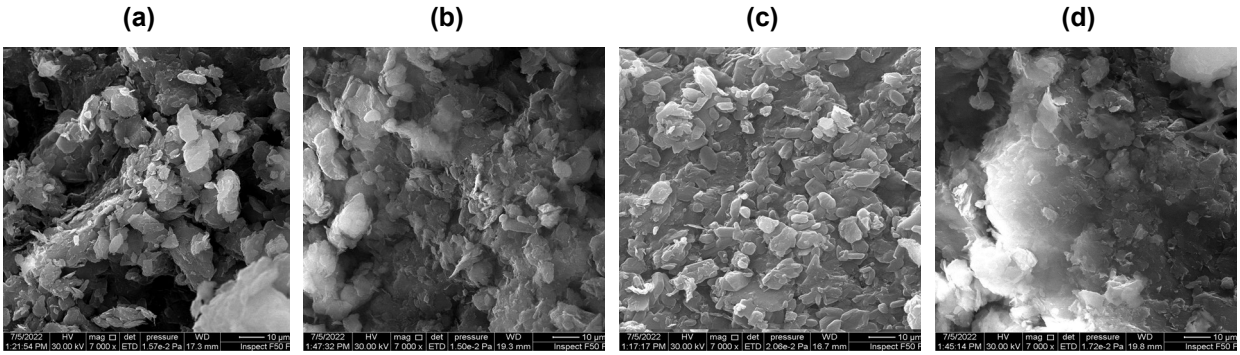

Figure 13. SEM images of: (a) Mix 1, 25 MPa; (b) Mix 2, 25 MPa; (c) Mix 1, 100 MPa; (d) Mix 2, 100 MPa.

3.9. Effect of Fine Content on the Earthen Material Behavior

A quantitative comparison on the effect of increasing finer content on soil suction, stiffness, compressive strength, moisture buffering, and thermal conductivity is presented in Fig. 14–18. Structurally, Mix 2 outperforms Mix 1 with respect to stiffness, provided that failure occurred at rather the same strain level (about 1–2 %). Mix 2 showed also a superior response, with respect to compressive strength, compared to Mix 1 at almost all the compaction pressure levels. The compressive strength increased remarkably by 60–150 % as the finer content increased from 30 % to 50 %. This improvement cause the increase of binder content and the increase of capillary suction, as shown in Fig.16. Mix 2, unlike Mix 1, showed a marginal increase in the moisture buffering value with increasing compaction pressure. In terms of thermal conductivity, Mix 2 tended to generally show marginally higher k values than Mix 1, with few exceptions, as shown in Fig. 18. These comparisons suggest that increasing finer content to certain levels can improve earthen material behavior, particularly stiffness and strength.

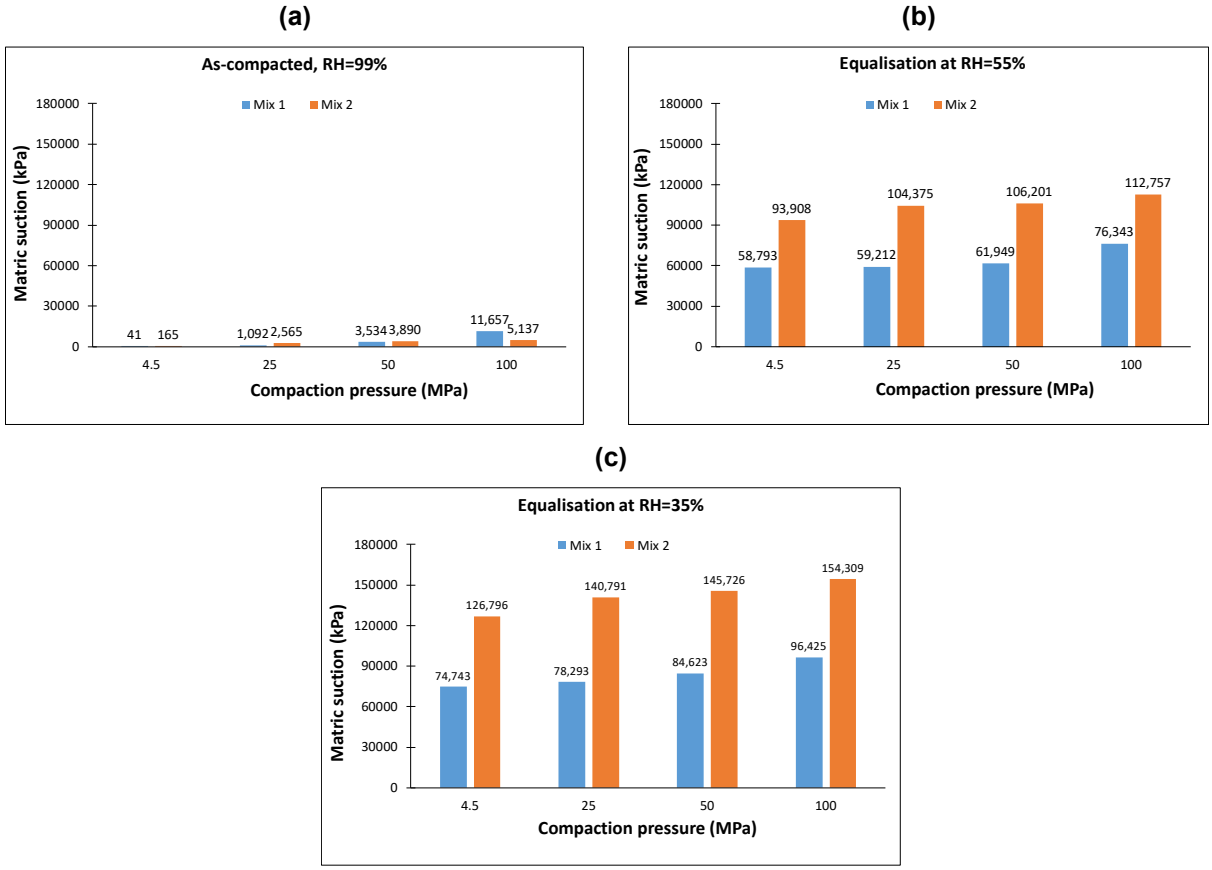

Figure 14. Comparison of matric suction values for Mix 1 and Mix 2: (a) at as-compacted state, (b) at RH = 55 %, (c) at RH = 35 %.

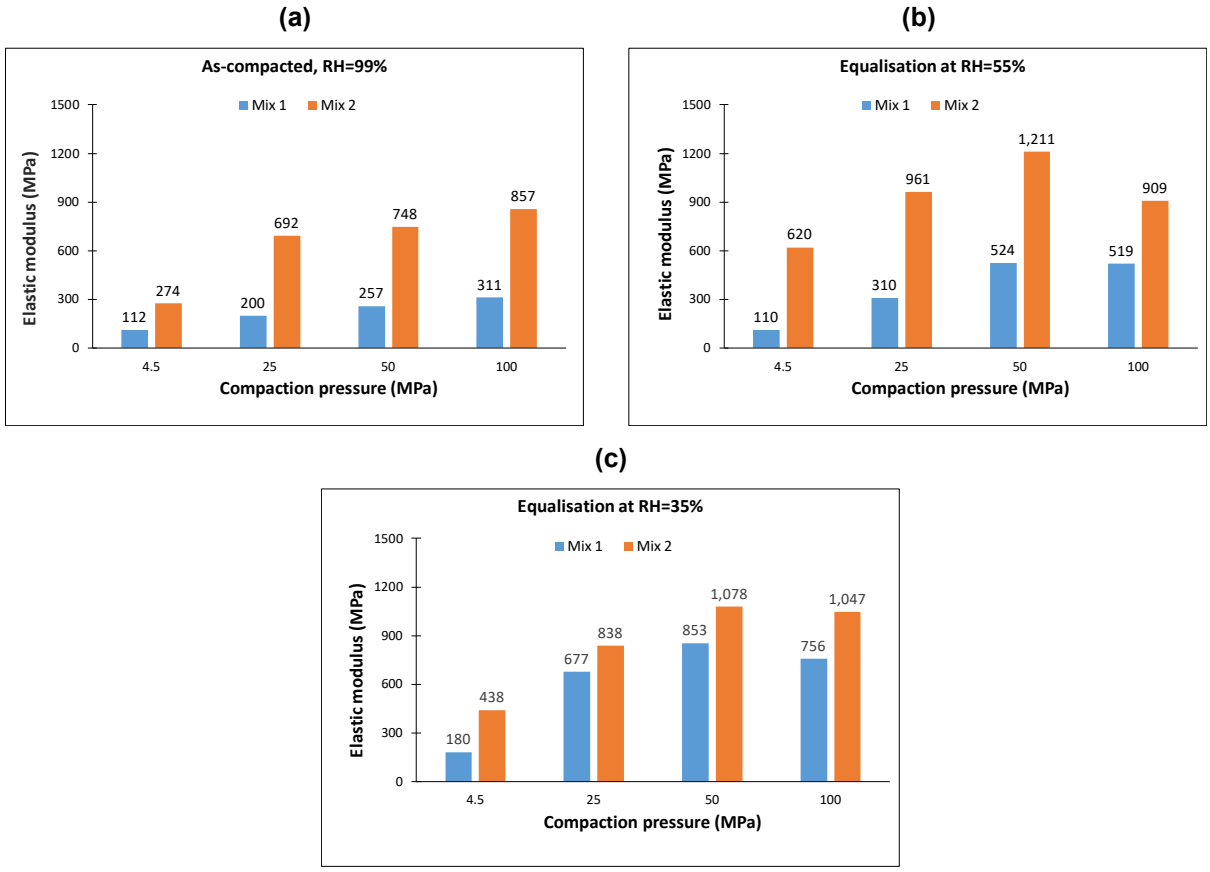

Figure 15. Comparison of Young's modulus values for Mix 1 and Mix 2: (a) at as-compacted state, (b) at RH = 55 %, (c) at RH = 35 %.

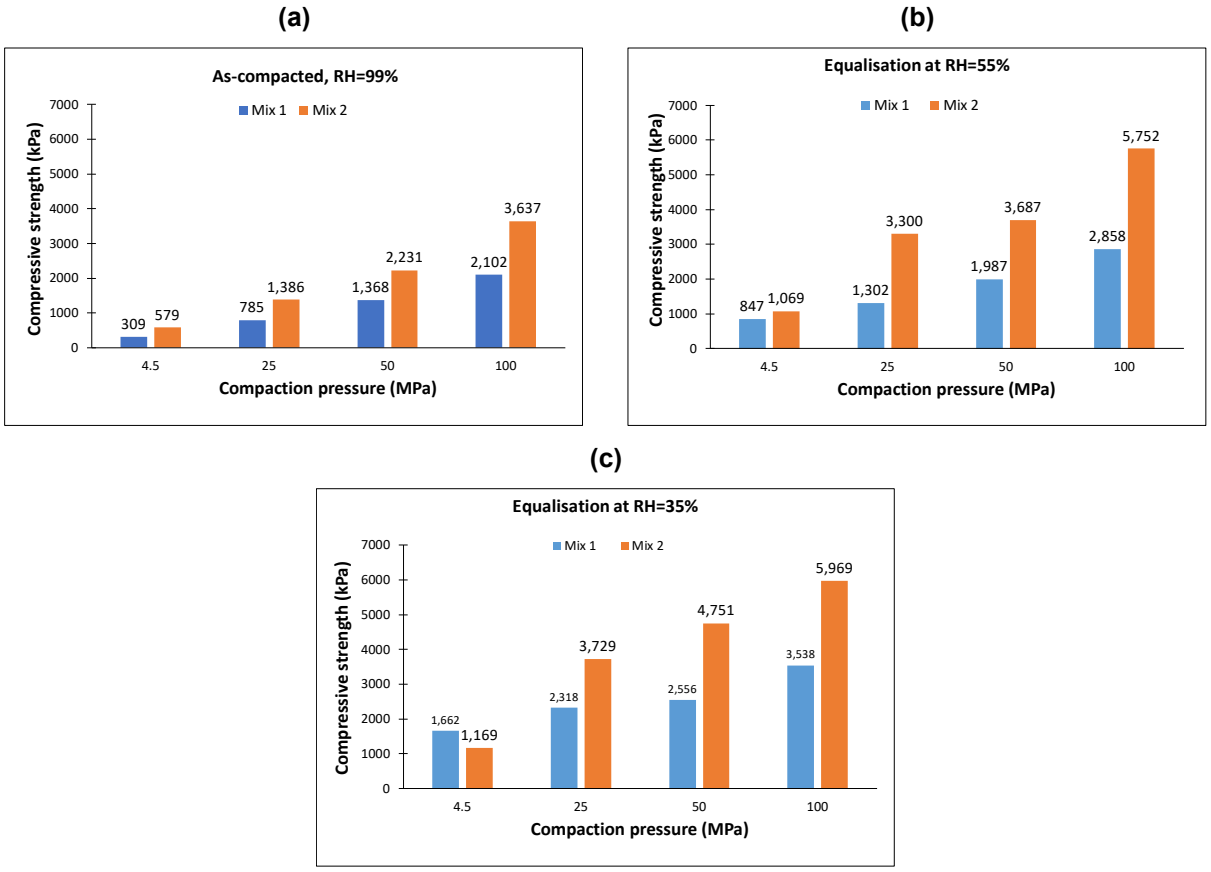

Figure 16. Comparison of compressive strength values for Mix 1 and Mix 2: (a) at as-compacted state, (b) at RH = 55 %, (c) at RH = 35 %.

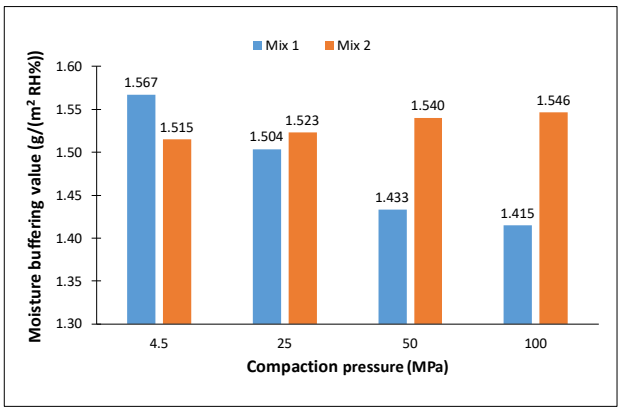

Figure 17. Comparison of moisture buffering values for Mix 1 and Mix 2.

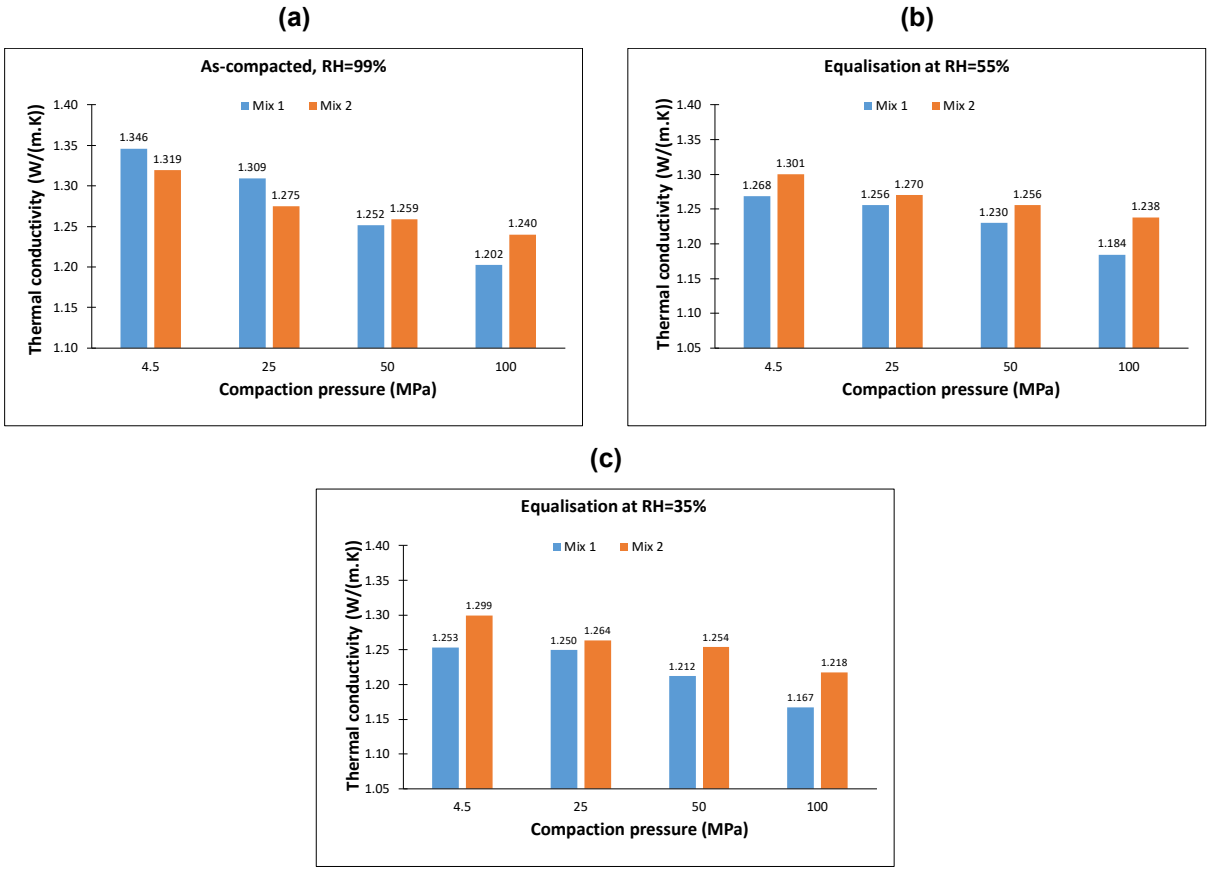

Figure 18. Comparison of thermal conductivity coefficient values for Mix 1 and Mix 2: (a) at as-compacted state, (b) at RH = 55 %, (c) at RH = 35 %.

4. Conclusions

The current work studied suitability of two raw earthen materials for unstabilized rammed earth buildings, based on their physical properties. Two mixes made of different proportions of sand, silt, and clay were prepared. A set of laboratory tests was performed on specimens compacted statically to 4.5, 25, 50, and 100 MPa to characterize mechanical, hydric, and thermal behavior of these materials. Upon drying from the as-compacted moisture to the moisture states corresponding to RH=35 %, the material showed a drying shrinkage between 0 % and 4 %, depending on the initial water content and the unit weight of the material. In addition, the compacted materials were found free of shrinkage cracks even under a completely dry state.

With increasing dry unit weight, frictional resistance increased and produced a noticeable increase in materials stiffness and strength. Likewise, with increasing soil suction, i.e. when relative humidity decreases, a remarkable increase in the elastic modulus and compressive strength was observed. The stiffness and strength were found to increase with increasing finer content from 30 % to 50 %. If a threshold compressive strength of 2 MPa is considered, then compacting the earthen material to at least 50 MPa

would provide sufficient strength under the operational high humidity RH = 55 %. A significant gain in strength was achieved by increasing the compaction pressure to 100 MPa. For example, the mixture with 50 % finer content, achieved a compressive strength of almost 6 MPa when compacted to 100 MPa. In addition, the reduction in strength due to relative humidity increase appeared to show a dependency on the compaction level where specimens compacted at 100 MPa preserved more strength upon wetting than those compacted at 50 and 25 MPa.

Interestingly, the dynamic adsorption behavior appeared to be rather independent of the mount of compaction energy or finer content. The increase in finer content showed a minor increase in the dynamic adsorption with increasing compaction pressure. Nevertheless, the moisture buffering test indicated that both materials exchange sufficient amount of moisture with the atmosphere. On the thermal conductivity front, the increase in finer content yielded slightly higher thermal conductivity values. Despite that, the materials exhibited good insulation characteristics, compared to traditional brick and concrete blocks. Finally, it is concluded that the engineered material examined in this work can be potentially used for rammed earth for dry applications. When comparing both the mixtures, Mix 2 is considered to be preferable due to its higher strength and stiffness, compared to Mix 1.

References

1. Morel, J.C., Mesbah, A., Oggero, M., Walker, P. Building houses with local materials: means to drastically reduce the environmental impact of construction. Building and Environment. 2001. 36(10). Pp. 1119–1126. DOI: 10.1016/S0360-1323(00)00054-8
2. Venkatarama Reddy, B.V., Jagadish, K.S. Embodied energy of common and alternative building materials and technologies. Energy and Buildings. 2003. 35(2). Pp. 129–37. DOI: 10.1016/S0378-7788(01)00141-4
3. Ciancio, D., Boulter, M. Stabilised rammed earth: a case study in Western Australia. Proceedings of the Institution of Civil Engineers – Engineering Sustainability. 2012. 165(2). Pp. 141–154. DOI: 10.1680/ensu.10.00003
4. Beckett, C., Augarde, C. The Effect of Relative Humidity and Temperature on the Unconfined Compressive Strength of Rammed Earth. Unsaturated Soils: Research and Applications. Berlin, Heidelberg: Springer. 2012. Pp. 287–292. DOI: 10.1007/978-3-642-31116-1_39
5. Gallipoli, D., Bruno, A.W., Perlot, C., Salmon, N. Raw earth construction: Is there a role for unsaturated soil mechanics? Unsaturated Soils: Research & Applications. Sydney: CRC Press. 2014. Pp. 55–62. DOI: 10.1201/b17034
6. Jaquin, P.A., Augarde, C.E., Gallipoli, D., Toll, D.G. The strength of unstabilised rammed earth materials. Géotechnique. 2009. 59(5). Pp. 487–490. DOI: 10.1680/geot.2007.00129
7. Bui, T.T., Bui, Q.-B., Limam, A., Maximilien, S. Failure of rammed earth walls: From observations to quantifications. Construction and Building Materials. 2014. 51. Pp. 295–302. DOI: 10.1016/j.conbuildmat.2013.10.053
8. Ghasemalizadeh, S., Toufigh, V. Durability of rammed earth materials. International Journal of Geomechanics. 2020. 20(11). DOI: 10.1061/(ASCE)GM.1943-5622.0001829
9. Arrigoni, A., Beckett, C., Ciancio, D., Dotelli, G. Life cycle analysis of environmental impact vs. durability of stabilised rammed earth. Construction and Building Materials. 2017. 142. Pp. 128–136. DOI: 10.1016/j.conbuildmat.2017.03.066
10. Luo, Y., Yang, M., Ni, P., Peng, X., Yuan, X. Degradation of rammed earth under wind-driven rain: The case of Fujian Tulou, China. Construction and Building Materials. 2020. 261. Article no. 119989. DOI: 10.1016/j.conbuildmat.2020.119989
11. Maniatidis, V., Walker, P. A Review of rammed earth construction. 2003. Paper presented at DTI Project Report, Bath. [Online]. URL: https://people.bath.ac.uk/abspw/rammedearth/review.pdf (accessed: 28.05.2024).
12. Standard SADC ZW HS 983: Rammed earth structures – Code of practice. [Online]. URL: https://www.rammedearthconsulting.com/library/african-rammed-earth-harmonised-standard-en.pdf (accessed: 28.05.2024)
13. Aubert, J.E., Faria, P., Maillard, P., Ouedraogo, K.A.J., Ouellet-Plamondon, C., Prud'homme, E. Characterization of Earth Used in Earth Construction Materials. Testing and Characterisation of Earth-based Building Materials and Elements. RILEM State-of-the-Art Reports. 35. Springer, Cham, 2022. Pp. 17–81. DOI: 10.1007/978-3-030-83297-1_2
14. Walker, P.J. Strength, durability and shrinkage characteristics of cement stabilised soil blocks. Cement and Concrete Composites. 1995. 17(4). Pp. 301–310. DOI: 10.1016/0958-9465(95)00019-9
15. Walker, P. Bond characteristics of earth block masonry. Journal of Materials in Civil Engineering. 1999. 11(3). Pp. 249–256. DOI: 10.1061/(ASCE)0899-1561(1999)11:3(249)
16. Guettala, A., Mezghiche, B., Chebili, R., Houari, H. Durability of lime stabilised earth blocks. Challenges of Concrete Construction. 2002. 5. Pp. 645–654. DOI: 10.1680/scc.31777.0064
17. Deutsches Institut für Normung (DIN). Earth blocks – Terms and definitions, requirements, test methods. DIN 18945. 2013.
18. American Society of Testing and Materials (ASTM). Standard test method for particle-size analysis of soils. ASTM D422. West Conshohocken PA: ASTM International, 2007. 8 p.
19. Ciancio, D., Jaquin, P., Walker, P. Advances on the assessment of soil suitability for rammed earth. Construction and Building Materials. 2013. 42. Pp. 40–47. DOI: 10.1016/j.conbuildmat.2012.12.049
20. American Society of Testing and Materials (ASTM). Standard test methods for liquid limit, plastic limit, and plasticity index of soils. ASTM D4318. West Conshohocken PA: ASTM International, 2017. 20 p.
21. American Society of Testing and Materials (ASTM). Standard test method for shrinkage factors of cohesive soils by the water submersion method. ASTM D4943. West Conshohocken PA: ASTM International, 2018. 7 p.
22. Bruno, A.W., Gallipoli, D., Perlot, C., Mendes, J. Effect of very high compaction pressures on the physical and mechanical properties of earthen materials. E3S Web of Conferences. 2016. 9. Article no. 14004. DOI: 10.1051/e3sconf/20160914004
23. Gallipoli, D., Bruno, A.W., Perlot, C., Mendes, J. A geotechnical perspective of raw earth building. Acta Geotechnica. 2017. 12. Pp. 463–478. DOI: 10.1007/s11440-016-0521-1

24. American Society of Testing and Materials (ASTM). Standard test method for unconfined compressive strength of cohesive soil. ASTM D2166. West Conshohocken PA: ASTM International, 2016. 6 p.
25. American Society of Testing and Materials (ASTM). Standard test method for measurement of soil potential (suction) using filter paper. ASTM D5298. West Conshohocken PA: ASTM International, 2016. 6 p.
26. Likos, W.J., Lu, N. Filter Paper Technique for Measuring Total Soil Suction. Transportation Research Record: Journal of the Transportation Research Board. 2002. 1786(1). Pp. 120–128. DOI: 10.3141/1786-14
27. Rode, C. et al. Moisture Buffering of Building Materials. Technical University of Denmark, Department of Civil Engineering. 2005. BYG Report No. R-127. [Online]. URL: https://backend.orbit.dtu.dk/ws/portalfiles/portal/2415500/byg-r126.pdf (accessed: 28.05.2024)
28. Zhao, D., Qian, X., Gu, X., Jajja, S.A., Yang, R. Measurement techniques for thermal conductivity and interfacial thermal conductance of bulk and thin film materials. Journal of Electronic Packaging. 2016. 138(4). Article no. 040802. DOI: 10.1115/1.4034605
29. Kouakou, C.H., Morel, J.C. Strength and elasto-plastic properties of non-industrial building materials manufactured with clay as a natural binder. Applied Clay Science. 2009. 44(1–2). Pp. 27–34. DOI: 10.1016/j.clay.2008.12.019
30. Xu, L., Wong, K.K., Fabbri, A., Champiré, F., Branque, D. Loading-unloading shear behavior of rammed earth upon varying clay content and relative humidity conditions. Soils and Foundations. 2018. 58(4). Pp. 1001–15. DOI: 10.1016/j.sandf.2018.05.005
31. Bruno, A.W., Gallipoli, D., Perlot, C., Kallel, H. Thermal performance of fired and unfired earth bricks walls. Journal of Building Engineering. 2020. 28. Article no. 101017. DOI: 10.1016/j.jobe.2019.101017

Information about the authors:

Eanas Hasan,
E-mail: ean20e1010@uoanbar.edu.iq

Muayad Al-Sharrad,
ORCID: https://orcid.org/0000-0001-6180-8837
E-mail: muayad.alsharrad@uoanbar.edu.iq

Received 06.12.2022. Approved after reviewing 15.09.2023. Accepted 15.09.2023.

Magazine of Civil Engineering

ISSN 2712-8172

journal homepage: http://engstroy.spbstu.ru/

Research article

UDC 69

DOI: 10.34910/MCE.128.8

Influence of silica fume addition on enhancing the autoclaved aerated concrete properties

R. Shabbar ✉, ***L.A.M. Alasadi, J.K. Taher***

University of Kufa, Najaf, Iraq

✉ *rana.shubber@uokufa.edu.iq*

Keywords: autoclaved aerated concrete, modified AAC mix, waste material, water absorption coefficient

Abstract. The demand for lightweight concrete has increased because of its low density, fire resistance and good thermal insulation. Autoclaved aerated concrete (AAC) is the combination of cement, fine-grained sand, lime and water with aluminium powder. This study aims to investigate the influence of adding silica fume (SF) on improving the properties of AAC. The response was studied in terms of testing the mechanical and physical properties including compressive, splitting tensile, flexural strength, density, porosity and coefficient of water absorption. Different mixes have been proposed by incorporating the SF with contents of 10 %, 20 % and 30 % by cement weight, which is compared with the AAC sample that is used in practical applications. The results indicated that there was a significant improvement in the compressive and flexural strength of AAC, which increased by six and three times, respectively, when 30 % of SF was used with an acceptable dry density. Furthermore, the microstructural analysis revealed that SF had a positive effect on the development of calcium silicate hydrate and it can be used in AAC masonry block productions.

Acknowledgements: The authors are grateful to MSc. Abbas Diwan, a researcher at the Nanotechnology and advanced Materials Research Unit, and to MSc. Mohammed Madlool, Materials Engineering Department, Faculty of Engineering, University of Kufa, for their support in preparing the tests.

Citation: Shabbar, R., Alasadi, L.A.M., Taher, J.K. Influence of silica fume addition on enhancing the autoclaved aerated concrete properties. Magazine of Civil Engineering. 2024. 17(4). Article no. 12808. DOI: 10.34910/MCE.128.8

1. Introduction

In the last two decades, much attention has been paid to the production of lightweight concrete (LWC) due to its low density, good thermal insulation and fire resistance, lower thermal conductivity and shrinkage with a fast construction process [1, 2]. In addition, the use of LWC increases the building's resistance to seismic loads and decreases operating and construction costs. Thus, it is used in a number of applications over normal concretes [3, 4]. Generally, LWC is divided into lightweight aggregate concrete (LWAC), in which light coarse aggregate is used, and aerated concrete (AC), which is produced using cement mortar with some foaming agent or void-forming materials without coarse aggregate [5, 6].

Several researchers have investigated the physical and mechanical characteristics of AC with using an autoclave. Sufficient autoclave curing results in the crystallization of calcium silicate hydrate (CSH) and neutral tobermorite-11, the main structural minerals of autoclaved aerated concrete (AAC). The tobermorite phase begins after 2 h of autoclaving and lasts up to 8 h. Wang et al. [7] realised that an extreme prolongation of autoclaving did not affect the formation of tobermorite. In contrast, Mostafa [8] observed that compressive strength enhanced during the first 6 h of autoclaving, and then the gain in strength declined at 12 h and 24 h. Kunchariyakun et al. [9] reported that the compressive strength in the range of 20–60 % was lower than the strength of the control samples, while the unit weight loss was in the range of 16–45 % for the samples that were subject to autoclave curing. In addition, the highly reactive silica in rice

husk ash (RHA) affected the transformation of tobermorite and the increasing the autoclaving time to 18 h had no major effect on the properties of AAC. Cai et al. [10] studied the effect of iron tailings content and fineness on mechanical properties of AAC. The mass ratio of iron tailing to silicon sand (MSIS) were 0 %, 20 %, 40 %, 50 %, 60 %, 80 % and 100 % with a grinding time prolonged from 10 to 30 mins. It is indicated that the compressive strength reduced by 21 % with the increase of MSIS up to 50 %, while it dropped by 48 % with the increase of MSIS up to 100 %. It was reported that the optimal grinding time was 20 min. Cai et al. [11] investigated the influence of waste materials on high content solid-wastes autoclaved aerated concrete (HCS-AAC) performance. The results exhibited that the grinding process had a significant influence on the powder particle size and the compressive strength obtained from mix grinding increased by 3–6 %.

Wongkeo et al. [12] studied the flexural strength, compressive strength and thermal conductivity of AAC by replacing cement with bottom ash (BA) up to 30 % by weight. The results exhibited that the flexural strength, compressive strength and thermal conductivity increased with increasing BA content. The 20 % increase in both compressive and flexural strengths was found for mixes with 30 % BA content compared to the mixes without BA content, whereas the thermal conductivity improved only by 6 %. Różycka and Pichór [13] utilized perlite waste as a quartz sand replacement in conventional AAC mixtures at 5 %, 10 %, 20 %, 30 % and 40 % by weight. The results showed that the bulk density decreased by 12 %, compressive strength by 9 % and thermal conductivity by 10 % with 5 % of perlite waste. Gunasekaran et al. [14] studied the effect of natural sand replacement by flash ash (FA) up to 100 %. The results indicated that compressive strength, dry density and water absorption declined with adding FA. The maximum values were with 0 % FA that was greater than with 100 % FA by 53 %, 33 % and 22 % respectively. Furthermore, Qin and Gao [15] used the recycling of waste autoclaved aerated concrete (WAAC) powder with cement by accelerated carbonation. Carbonation curing was achieved on a cement paste containing up to 50 % of WAAC powder. The result revealed the highest compressive strength was obtained with the optimal dosage of WAAC of 20 % that was enhanced by 2 %.

However, Li et al. [16] used the municipal solid waste incineration (MSWI) bottom ash as a sand replacement in AAC. The results showed that MSWI caused a reduction in compressive strength, density and thermal conductivity with increasing its content. The lowest value was with 100 % replacement, which caused a decrease in compressive strength, density and thermal conductivity by 71 %, 9 % and 17 % respectively. Kunchariyakun et al. [17] studied the impact of black rice husk ash (BRHA) and bagasse ash (BA) on the dry density and compressive strength of AAC at 180 °C for 4, 8 and 12 h. Sand with the range of 0 %, 30 % and 50 % by weight was replaced with BRHA and BA. The results showed that an increase in curing time has an obvious effect on the compressive strength of AAC which improved by 46.59 % and 26.97 % in samples containing 30 % of BA and 30 % of BRHA respectively. However, no significant effect on the dry density developed by 9 % and 10 % with the optimum time of 12 h has been reported. In addition, Zafar et al. [18] used waste granite dust (WGD) as a sand replacement for up to 20 %. The results revealed that the maximum increase in the hardened density, thermal conductivity, compressive and flexural strength is higher with 20 % of WGD than 0 % of WGD by 13.45 %, 36 %, 42 % and 38 % respectively, while the minimum water absorption was lower with 20 % by 26.7 %.

The influence of pozzolanic materials such as silica fume (SF), granulated blast furnace slag (GBFS) and fly ash (FA) on the AAC properties considers an essential issue on its behavior analysis [19]. Pehlivanlı et al. [20, 21] investigated the impact of four different types of fibers (polypropylene, carbon, basalt and glass fiber) on the compressive and flexural strength of AAC. The results indicated that carbon fiber-reinforced AAC, as opposed to other types of fibers, provided the greatest compressive and flexural strength, which increased by 31 % and 61 % respectively. In Güçlüer et al. [22] siliceous aggregate was replaced by fly ash and silica fume was added with the range of 3 %, 6 %, 9 % and 12 % to the cement. Results showed that curing under 177 °C had a greater compressive strength than at 156 °C, which improved by 78 % with SF of 3 %.

Chen et al. [19] studied the effects of silica-lime-cement composition on the density and compressive strength. Lime (L) and cement (C) were used with a range between 5 % and 30 %, while SF was from 60 % to 70 % and aluminium powder from 0.25 % to 1 %. It was revealed that samples with 70 % of SF, 25 % of L and 5 % of C had the highest strength and density. The increase in the compressive strength was related not only to the progress of hydration reactions, but also to pores filling with the hydration products. On the other hand, the effects of SF and steel slag additions on compressive strength and thermal properties of lime-fly ash pastes were studied by Zhao et al. [23]. Curing conditions of 180 °C for 8 h and SF content of 8 % and 15 % of SF was adopted. SF caused a significant development in compressive strength, which raised by 59.6 % with 15 % of SF. Leonteva et al. [24] considered the influence of ultra- and nanodisperse size of silica gel content in the range between 4 % and10 % additives on the structure and mechanical-and-physical properties of heat insulating AAC. The results showed that the compressive strength increased 5 times, when using silica up to 10 % with a slightly improved dry density of 6.5 %. Pachideh et al. [25] adopted SF with 7 %, 14 % and 21 % of cement weight. They confirmed that the compressive and

tensile strength enhanced by 63 % and 23 % when 21 % and 7 % of SF respectively were used, while water absorption decreased with increasing SF content up to 21 % which decreased 2 times at 10 and 30 and 21 % at 90 min. Almajeed and Turki [26] used SF with a maximum value of 16 %. They observed that the compressive strength developed up to 23 % with 12 % of SF.

Lashari et al. [27] studied the effect of SF and FA as cementitious materials on the properties of the AAC. SF was substituted up to 20 %. Then FA was replaced with cement up to 30 % after selecting the optimum contain of the SF. It is indicated that the greatest split tensile and compressive strength of the AAC was when cement was replaced by 15 % of SF and 30 % of FA.

It is known that the use of AAC blocks has increased dramatically throughout the world due to several advantages of such blocks, including their light weight, thermal insulation and cost-effectiveness. However, low mechanical properties and problems with the durability of such blocks limit their use, for example, for filling the walls of internal partitions of multi-story buildings. This study aims to improve the mechanical properties (compressive, tensile and flexural strengths) of the non-structural AAC blocks to be used in the construction of load-bearing walls and reduce the cracking shrinkage resulting from dimensional changes caused by environmental humidity. A modified mix with different contents of SF (10 %, 20 % and 30 %) and reduced sand and water content was proposed to reduce the size of voids in the mix.

2. Methods and Materials

2.1. Material Properties for the AAC Mix Design

The ACC mixture prepared during this study consists of the following components:

- Ordinary Portland Cement CEM I/42.5N that satisfies the requirements of the Iraqi Organization of Standards (IOS.5/1984 [28]);
- sand with particle size distribution between 1 and 3 mm [29];
- ECA MICROSILICA-D [30] with an average diameter of 0.15 μ;
- lime (CaO), approximately 90 % of which can pass through the sieve 90 μm [31].

To produce AAC samples, aluminium powder with a purity of 90 % was used. The chemical, physical and mechanical properties of the OPC are revealed in Tables 1, 2 and 3. Whereas, the properties of lime and silica fume which were used in the mixtures are shown in Tables 4 and 5 respectively.

Table 1. Chemical properties of Ordinary Portland Cement.

Component	Test result, %	IOS.5/1984
SiO_2	20.35	-
Al_2O_3	5.71	-
Fe_2O_3	3.46	-
CaO	61.93	-
MgO	3.78	Max. 5.0
SO_3	2.39	Max. 2.8
Loss on ignition	1.51	Max. 4.0
Insoluble residue	0.52	Max. 1.5

Table 2. Physical properties of Ordinary Portland Cement.

		Test result	IOS.5/1984
Setting time	Initial (min)	110	Min. 45
	Final (hr)	2.76	Min. 10
Fineness		2795	Min. 2300

Table 3. Mechanical properties of Ordinary Portland Cement.

Mechanical	Compressive strength	3 days	22.3 MPa	Min. 15
		7 days	32.3 MPa	Min. 23
Soundness, %		0.31	0.32	
Residue, %	90	6.08	6.08	
	180	0.58	0.58	

Table 4. Lime properties.

Properties	Test result	IOS.807/1988
Extinguishing time (min)	13	5-15
Activity CaO, %	91.97	Min. 85
CO_2	1.46	Max. 5
Fineness (remaining on sieve 90 μ), %	1	Max. 10

Table 5. ECA MICROSILICA-D Silica Fume properties [30]

Properties	Test result	ACI 234R-96 [32]
Specific Gravity	2.25±15 % at 20°C	2.2 %
Sulphate Content	1.0 % as SO_3	≤ 4 %
Bulk Density	≥550 kg/m^3	480–720 kg/m^3
SiO_2 Content	90 %	84–91 %

2.2. Preparation of Samples

To produce a slurry, sand was mixed with one-third of water for nearly 1.5 min. Then, cement and lime were added to the slurry and mixed for 100 sec. The remaining water was mixed with silica fume and aluminium powder for 80 sec. Then, all materials were mixed and the mixing process was completed within 50–60 sec. After that, the molds were heated to 42 °C and filled with fresh AAC. The samples were demolded for approximately 24 h, as shown in Fig. 1 [18]. The samples were cured under high-pressure steam conditions of 12 bars for 10 h at 190 °C and were left in the open air for 7 days. Then the AAC samples were tested for physical and mechanical properties with microstructural fracture surface.

(a) Samples after casting **(b) Samples volume after expansion**

Figure 1. AAC samples with different silica fume content: cubes, beams and cylinders.

2.3. Mechanical and Physical Tests

The compression test was achieved using 100 mm cubes according to BS EN 679 [33], whereas the splitting test has been conducted using a cylinder of 100 mm diameter and 200 mm height according to BS EN 1881-117 [34], as indicated in Fig. 2 and 3. Flexural strength has been measured by using a prism with dimensions of 100 × 100 × 400 mm according to BS EN 1351 [35], as indicated in Fig. 4. However, bulk density was measured using a cylinder of 100 mm diameter and 70±5 mm height according to BS EN 678 [36]. Four values of SF (%) have been considered. Three samples were tested and the average value was adopted. For the industrial (control) and AAC, three samples were prepared.

As for porosity, it is defined as the ratio of the pore volume filled following a 30-min soak. After the samples had been dried to a constant weight, they were weighed (W_d). Then the samples were immersed in water for 30±0.5 min and the amount of water absorbed was weighted (W_s). The porosity was calculated using (1) [37].

$$P = \frac{(W_s - W_d)}{W_d} \times 100. \quad (1)$$

Figure 2. AAC cube for compressive strength test.

Figure 3. AAC cylinder for tensile strength test.

Figure 4. AAC prism for flexural strength test.

However, the coefficient of water absorption C_w detects the capability of material absorbing water through a cross-section area in the stated time according to BS EN 772-11 [38]. After the dry mass of the samples had been recorded, the samples were immersed in water (t_{so}) to a depth of 5±1 mm for 10, 30 and 90 min. Then each sample has been weighed as a mass of saturated surface. The water absorption coefficient was calculated using (2) [39].

$$C_w = \frac{W_{sat} - W_{dry}}{A_s \sqrt{t_{so}}} \times 10^6 \left[g \Big/ \left(mm^2 \times t^{0.5} \right) \right]. \quad (2)$$

2.4. Mix design

The mix proportion of the AAC containing different percentages of SF is shown in Table 6. For the industrial AAC, two parts of sand screened (0–3 mm) to one part of cement and 33 % lime with 0.32 % aluminium powder were used. However, for the proposed AAC, 2.6 of sand to 52 % lime with 0.21 % of aluminium powder were used. SF was inserted with 10 %, 20 % and 30 % by cement weight.

Table 6. Mix proportions for industrial and proposed AAC (kg/m³).

Material, kg/m³	Industrial (Control) sample	0 % SFAAC	10 % SFAAC	20 % SFAAC	30 % SFAAC
Cement	139	145	145	145	145
Sand	278	387	387	387	387
Water	463	220	220	220	220
Lime	46	75	75	75	75
AL powder	0.45	0.31	0.31	0.31	0.31
Silica fume (SF)	-	0	14.5	29	43.5

2.5. Optical microscope observations

The cross-section images of the AAC sample were captured by using an advanced metallurgical microscope, as shown in Fig. 5. It is a manual microscope, which is manufactured by KJ Group. Model EQ-MM500T-USB with 5.0 MP resolution was used to disclose the detailed microstructure of the samples. AAC with greater SF content exposed the lower number and non-uniform shapes of pores.

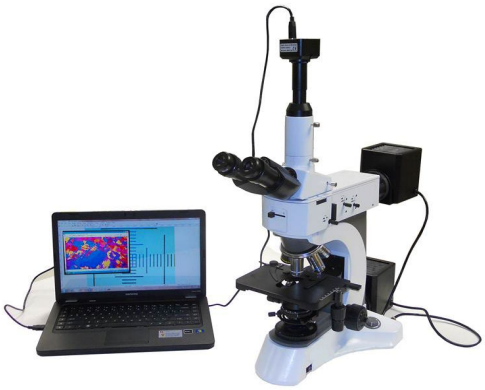

Figure 5. Advanced Metallurgical Microscope [40].

3. Results and Discussion

3.1. Compressive Strength

The compressive strength of AAC containing different SF percentages is shown in Fig. 6. The results indicated that compressive strength of the industrial (control) samples was lower than the experimental AAC without SF by 123 %, which may be due to its high water/cement ratio and aluminium powder content. Moreover, the space occupied by the hydration product improved due to an increase in water content, while the hydration volume remained constant regardless of the mixture's water content at a certain degree of hydration. It is unsure that an increase in water to water-to-cement ratio causes a rise in capillary voids and gel pores which was agreed with Naik [41].

The results showed that the strength of AAC increased with an increase in the proportion of SF. For the samples with 10 % and 20 % of SF, the compressive strength was higher than that of the control sample. However, the maximum strength was obtained at 30 % of SF, which was six times higher than that of the control sample. This behavior may be due to the effects of fine particle size of silica and large surface area consisting mainly of amorphous silicon dioxide. In addition, the formation of non-crystalline and crystalline CSH under autoclaving conditions was due to the reactions between reactive silica and lime [42], as shown in (3) and (4) [1]. The compressive strengths of the AAC samples were within the requirements of ASTM-C1693, which specifies the compressive strength of AACs from 2 to 6 MPa [43].

$$SiO_2 + CaO \xrightarrow{\text{Slag}} \alpha - C_2SH + C - S - H \longrightarrow \text{Tobermorite} \quad (3)$$

$$SiO_2 + CaO \xrightarrow{\text{Silica Fume}} C - S - H \longrightarrow \text{Tobermorite} \quad (4)$$

It was noted that the increase in the amount of waste materials resulted in an increase in the AAC strength, which is consistent with the other researches. Similar behaviors were reported in [18, 26, 44, 45]. Additional CSH gels occurred due to the reactions between free cement (created from cement hydration) and waste materials such as sawing mud, silica fume, granulated blast-furnace slag and WGD respectively, which caused a high compressive strength. It is expected that adding excess SF to AAC could increase the strength and durability of cementitious material with a slight increase in its weight.

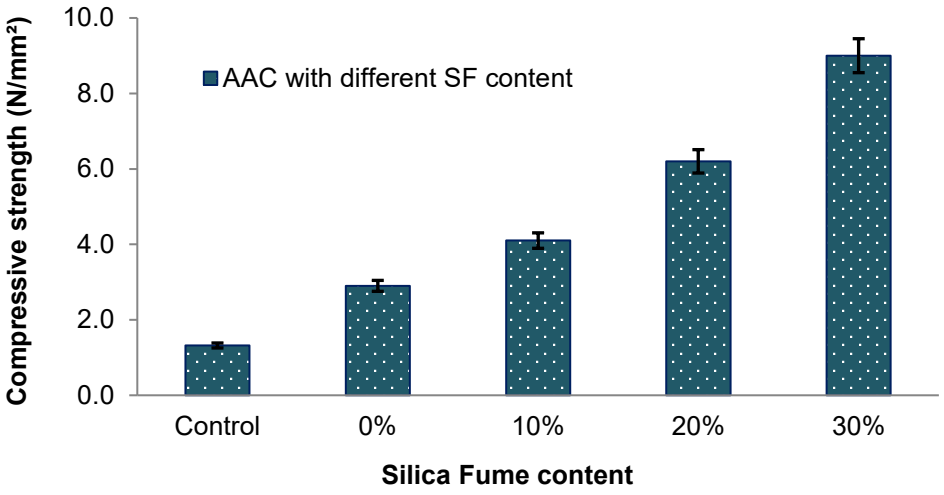

Figure 6. Compressive strength for the control and experimental AAC samples.

3.2. Tensile Strength

The tensile strength test results with different SF content are shown in Figure 7. The tensile strength of the control sample was higher than that with SF by up to 20 %. It was observed that the strength of the control sample was higher than that with 0 % SFAAC by 44 %. It could be referred to its high cement/sand ratio, which was ½ that appears to be adequate in providing a good tensile strength. However, the strength of the laboratory AAC mix increased with increasing SF content. At 10 % of SF, tensile strength increased by 38 % over 0 % of SF, followed by 52 % for 20 % of SF and the highest strength was achieved at 92 % by increasing SF to 30 % by weight. Based on the above results, when the addition of SF exceeds this limit, it is expected that higher tensile strength may be obtained. In addition, the tensile strength of 30 % SFAAC was slightly higher than that of the control sample by 7 %. This is in contrast with Toutanji et al. and Pachideh and Gholhaki results [25, 46], where SF was used in the range of (8-25) % and (7-21) % respectively. The results showed that the tensile strength increased slightly by 3 % when up to 8 % of SF was added, then it declined with increasing SF content, also the tensile strength increased by 23 %, when 7 % of SF was used [44, 46].

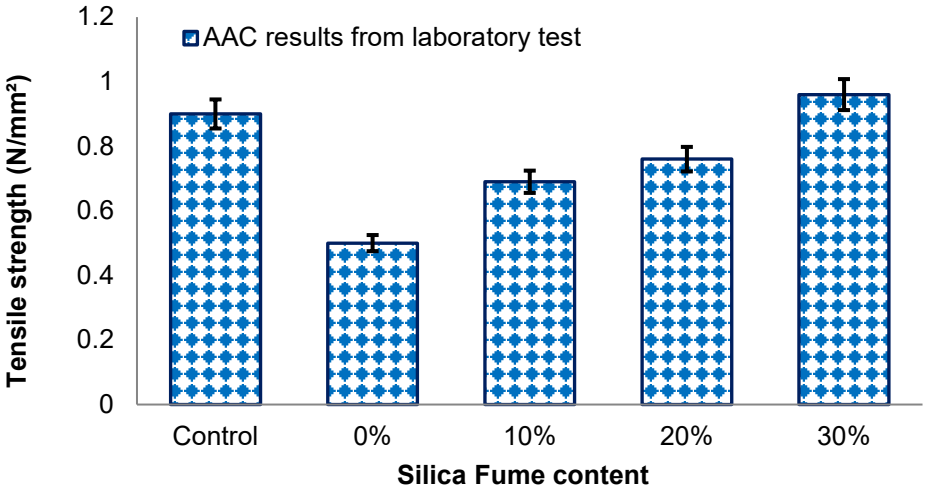

Figure 7. Tensile strength for the control and experimental AAC samples.

3.3. Flexural Strength

The results showed that all values of the AAC with SF were higher than that of the control sample, as shown in Fig. 8. In addition, the SF had a more prominent effect on flexural strength than on the splitting tensile strength, and for a high percentage significantly improved in strength, which agrees with [44]. The lowest value of the flexural strength was for control sample, which increased significantly by 122 % for 0 % SFAAC due to its high water/cement ratio. The presence of SF increased the flexural strength of AAC at 10 %, 20 % and 30 % of SF content by 1.6, 2 and 2.7 times, respectively. This behavior may refer to the further reaction of SF with $Ca(OH)_2$ obtained during Portland Cement hydration and create more CSH gels, which increase the strength of AAC. The optimal strength of mixes with SF was obtained for 30 % SFAAC.

In [12] similar behavior was observed, when BA was used as cement replacement in the range of 10–30 %. The flexural strength improved with increasing BA replacement and approximately 20 % increase in strength was obtained for mix with 30 % BA. However, in [40] SF with a range of up to 25 % was used. The result showed that maximum strength was obtained by replacing cement with 15 % of SF.

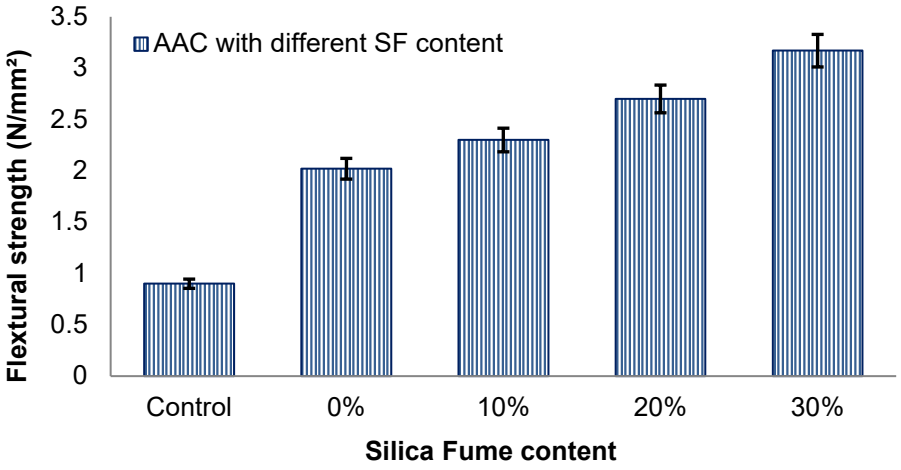

Figure 8. Flexural strength for the control and experimental AAC samples.

3.4. Bulk Density

Bulk density is one of the most important properties of AAC, and the mechanical and physical properties of AAC depend on their density and materials properties [13]. Fig. 9 shows the density of AAC with different SF content. The results showed that the density of AAC samples increased with the addition of SF, and the lowest value was for control sample, which improved by 28 % for 0 % SFAAC. With 10 % of SF, the bulk density increased by 44 %, followed by 46 % and 54 % for 20 % SFAAC and 30 % SFAAC, respectively. It could be due to the reactivity of the finer SF grain size, resulting in hardening AAC density. Moreover, the hydration process was accelerated by siliceous properties of waste materials by increasing the CSH content, resulting in a denser microstructure, which is consistent with [18, 47], where SF and WGD were used, respectively. The results showed that high density tobermorite crystals were formed with increasing waste materials content. In [26] it was observed that the dry density of AAC was not affected by the addition of SF due to its low content compared to the total amount of the mix.

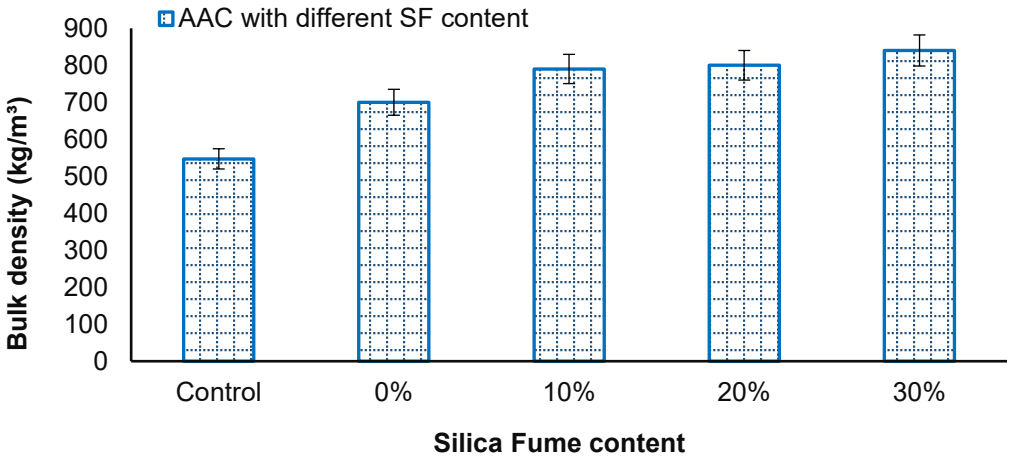

Figure 9. Dry density for the control and experimental AAC samples.

3.5. Porosity Measurement

AAC has a high porosity of more than 70 % of hardened material/volume, which leads to low compressive strength and density compared to conventional concrete [48].

The pore size distribution and porosity of AC are different and depend on the method of curing and materials composition. An increase in the volume of macropores led to an increase in porosity, which leads to thinning of the pore walls, thereby reducing the micropore volume of AC [49]. The results of the porosity of the control and proposed AAC samples with different SF content are shown in Fig. 10. The decrease in porosity with increasing SF content is neglected. The highest value was for control sample, which was

higher than 0 % SFAAC by 8 %, followed by 4.5 % and 2 %, when SF increased up to 30 %, which is consistent with [50]. When lightweight concrete (LWC) with different nanosilica content had similar porosity and NS1 (with 1 % cement replacement) showed lower porosity, which was reduced by 15 % compared to the control sample.

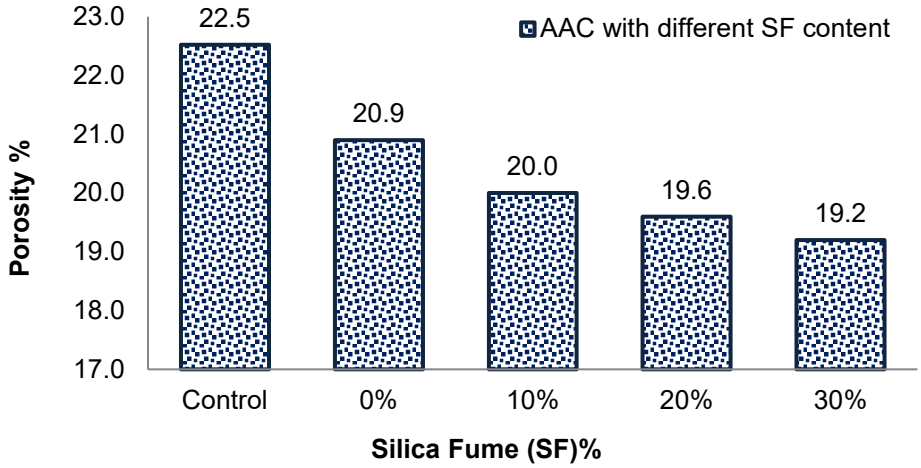

Figure 10. Porosity for the control and experimental AAC samples.

3.6. Coefficient of Water Absorption

Aerated concrete blocks have high water absorption and this problem needs to be solved. Fig. 11 shows the water absorption coefficients of the control and proposed AAC mixes at different times, including different SF content. It can be observed that all samples showed an increase in water absorption after 10, 30 and 90 min. After 10 min, the water absorption of the modified AAC samples with modified SF content was negligible. The highest value had the control sample, which may be due to its high aluminium content that caused a large number of voids.

After 30 min the water absorption for all experimental samples was the same, whereas after 90 min it was greater than that without silica and 30 % SF. Water absorption decreased with the addition of more SF content, which may be due to the fineness of void-filling particles and the cellular structure of AAC. This could be attributed to the plugging of connected pores by the microstructure densification due to the tobermorite formation and nano-micro-filling of voids. The capillary absorption mechanism of AAC is still unclear and its behavior depends on the features of the surrounding mortar, aggregate type and test conditions.

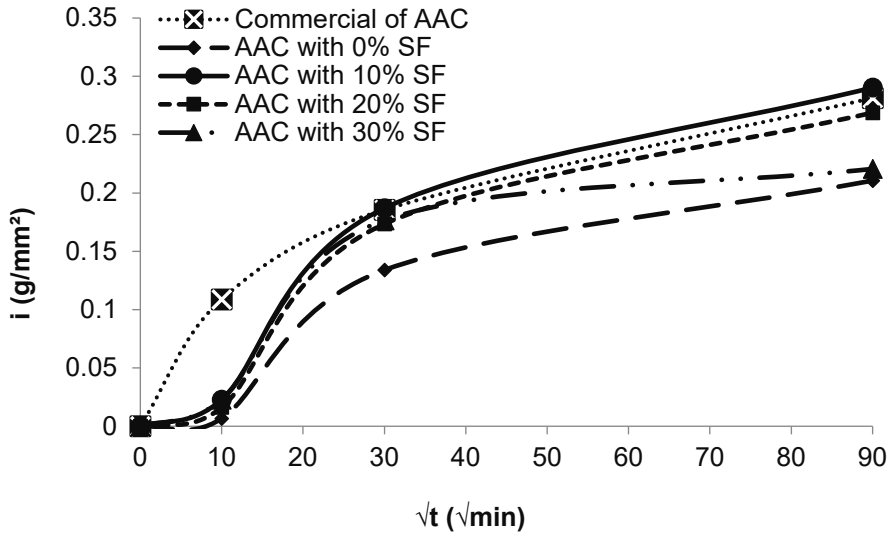

Figure 11. Water absorption for the control and experimental AAC samples.

3.7. Microstructural analysis

The microstructure of the AAC depends on many factors such as materials composition, type and amount, hydration rate and type of reaction produced and their distribution [9, 13]. However, the distribution of the micropore is more sensitive to the hydrothermal reaction [50]. The microstructures of the SFAAC and

the control samples were examined using advanced metallurgical microscope, and the results of this examination are shown in Fig. 12. Fig. 12a shows the high rate of macro- and micropores and subsequent tobermorite due to its high water/cement ratio. It resulted in an improvement in the hydration products formed and caused swells in the CSH gel and pore size became less than before. 0 % SFAAC had a higher rate of macropore volume, which tend to remain isolated as shown in Fig. 12b. This behavior may be due to intense reaction of silica with calcium hydroxide to form calcium silicate hydrates as indicated in (5) [51].

$$(C3S + C2S) + S \rightarrow CSH + CH + S\ (silica) \rightarrow CSH \rightarrow tobermorite \quad (5)$$

AAC with 10 %SF was more stable to conglomerate than to stay isolated because it had high pore volumes (Fig. 12c) and more tobermorite platelets were created, when there was enough silica in the mix. Moreover, an increase in SF to 20 % led to strength development of the AAC, but part of Al powder and lime did not react properly, because all mixes had the same water content (Fig. 12d). For AAC with 30 %SF, the CSH phase's improvement may be observed, as fibrous groups are surrounded by aggregate particles (Fig. 12e) and its porosity decreases with the addition of more SF.

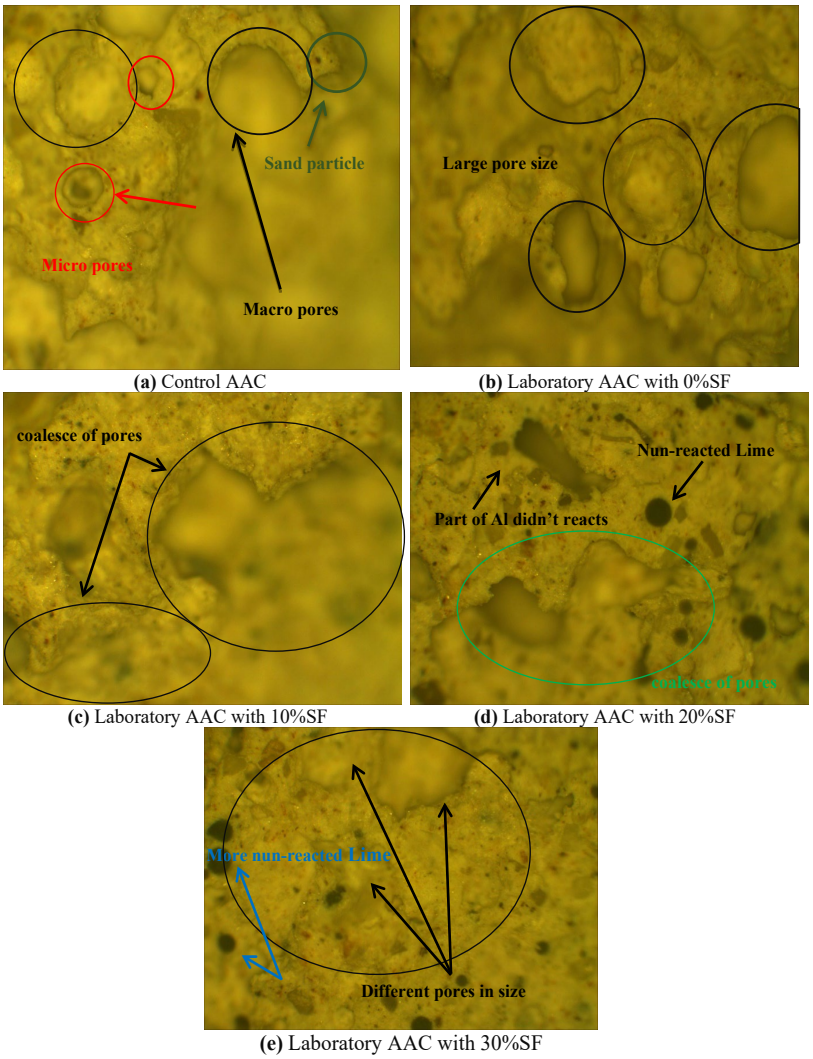

(a) Control AAC **(b)** Laboratory AAC with 0%SF

(c) Laboratory AAC with 10%SF **(d)** Laboratory AAC with 20%SF

(e) Laboratory AAC with 30%SF

Figure 12. Fracture surface micrographs for the control and experimental AAC samples with varying SF content.

4. Conclusion

The use of SF in autoclaved aerated concrete (AAC) has an eco-friendly effect in reducing the amount of waste material, and significantly influencing the physical and mechanical properties of AAC by improving the microstructure of the paste matrix. A series of AAC mixes with different content of SF (0–30 %) was created. At the end of the tests, the following results were obtained:

1. The effect of both lime to cement and sand to cement ratios was small, whereas the water to cement ratio had a considerable influence on the bulk density and compressive strength of AAC.

2. The compressive strength increased up to 6 times for the mixture containing up to 30 % of SF. The result showed that the progress of hydration reactions effects not only AAC strength but also pores filling with the hydration products.
3. It was indicated that an increase in pozzolanic materials resulted in increasing the tensile strength of the AAC sample. At the ratios of 10, 20 and 30 % SF, it was observed that the addition of SF up to 30 % slightly improved its tensile strength (approximately by 7 %). In addition, the brittleness of AAC was reduced by the addition of SF to increase strength. However, a considerable improvement in flexural strengths of AAC was obtained by using SF. 30 % of SF demonstrated high strength values of an adopted AAC sample, 3 times compared with that used in practical applications.
4. The maximum hardened density was with 30 % of SF, which was 54 % higher than that of the control sample, as it was affected by hardened density and its microstructure. The addition of SF resulted in improvement in tobermorite crystals and the pore structure of the AAC. Most of the air voids are unconnected voids, which were significantly affected by the introduction of SF. Due to the close relations between material properties and mix proportions, optimization of its proportions had great importance for the load-bearing strength of AAC.
5. SF caused a reduction in surface water absorption of AAC. The lowest water absorption was with 0 % SF that was reduced by 94 %, 28 % and 25 % respectively after 10, 30 and 90 min. However, the maximum water absorption of the proposed AAC was with 10 % of SF. It is recommended to use cementitious systems (SF + cement) to enhance the desired properties of AAC containing a high silica percentage. Moreover, additional research may be required on the influence of silica when taking into consideration the use of industrial wastes as adding/replacement materials in AAC production with varying percentages.

References

1. Qu, X., Zhao, X. Previous and present investigations on the components, microstructure and main properties of autoclaved aerated concrete – A review. Construction and Building Materials. 2017. 135. Pp. 505–516. DOI: 10.1016/j.conbuildmat.2016.12.208
2. Thienel, K.-C., Haller, T., Beuntner, N. Lightweight Concrete—From Basics to Innovations. Materials. 2020. 13(5). 1120. DOI: 10.3390/ma13051120
3. Sari, K., Sani, A.R. Applications of Foamed Lightweight Concrete. MATEC Web of Conferences. 2017. 97. 01097. DOI: 10.1051/matecconf/20179701097
4. Junaid, M.F., Rehman, Z.ur., Kuruc, M., Medveď, I., Bačinskas, D., Čurpek, J., et al. Lightweight concrete from a perspective of sustainable reuse of waste byproducts. Construction and Building Materials. 2022. 319. 126061. DOI: 10.1016/j.conbuildmat.2021.126061
5. Kalpana, M., Mohith, S. Study on autoclaved aerated concrete: Review. Materials Today: Proceedings. 2020. 22. Pp. 894–896. DOI: 10.1016/j.matpr.2019.11.099
6. Cai, Q., Ma, B., Jiang, J., Wang, J., Shao, Z., Hu, Y., et al. Utilization of waste red gypsum in autoclaved aerated concrete preparation. Construction and Building Materials. 2021. 291. 123376. DOI: 10.1016/j.conbuildmat.2021.123376
7. Wang, C.-l., Ni, W., Zhang, S.-Q., Wang, S., Gai, G.-S., Wang, W.-K. Preparation and properties of autoclaved aerated concrete using coal gangue and iron ore tailings. Construction and Building Materials. 2016. 104. Pp. 109–115. DOI: 10.1016/j.conbuildmat.2015.12.041
8. Mostafa, N.Y. Influence of air-cooled slag on physicochemical properties of autoclaved aerated concrete. Cement and Concrete Research. 2005. 35(7). Pp. 1349–1357. DOI: 10.1016/j.cemconres.2004.10.011
9. Kunchariyakun, K., Asavapisit, S., Sombatsompop, K. Properties of autoclaved aerated concrete incorporating rice husk ash as partial replacement for fine aggregate. Cement and Concrete Composites. 2015. 55. Pp. 11–16. DOI: 10.1016/j.cemconcomp.2014.07.021
10. Cai, L., Ma, B., Li, X., Lv, Y., Liu, Z., Jian, S. Mechanical and hydration characteristics of autoclaved aerated concrete (AAC) containing iron-tailings: Effect of content and fineness. Construction and Building Materials. 2016. 128. Pp. 361–372. DOI: 10.1016/j.conbuildmat.2016.10.031
11. Cai, L., Li, X., Liu, W., Ma, B., Lv, Y. The slurry and physical-mechanical performance of autoclaved aerated concrete with high content solid wastes: Effect of grinding process. Construction and Building Materials. 2019. 218. Pp. 28–39. DOI: 10.1016/j.conbuildmat.2019.05.107
12. Wongkeo, W., Thongsanitgarn, P., Pimraksa, K., Chaipanich, A. Compressive strength, flexural strength and thermal conductivity of autoclaved concrete block made using bottom ash as cement replacement materials. Materials & Design. 2012. 35. Pp. 434-439. DOI: 10.1016/j.matdes.2011.08.046
13. Różycka, A., Pichór, W. Effect of perlite waste addition on the properties of autoclaved aerated concrete. Construction and Building Materials. 2016. 120. Pp. 65–71. DOI: 10.1016/j.conbuildmat.2016.05.019
14. Gunasekaran, M., Elamaran, L., Suresh, P., Sakthivel, P., Saranya, G. Development of Light Weight Concrete by using Autoclaved Aerated Concrete. International Journal for Innovative Research in Science & Technology. 2016. 11(2). 5. Pp. 518–522.
15. Qin, L., Gao, X. Recycling of waste autoclaved aerated concrete powder in Portland cement by accelerated carbonation. Waste Management. 2019. 89. Pp. 254–264. DOI: 10.1016/j.wasman.2019.04.018
16. Li, X., Liu, Z., Lv, Y., Cai, L., Jiang, D., Jiang, W., et al. Utilization of municipal solid waste incineration bottom ash in autoclaved aerated concrete. Construction and Building Materials. 2018. 178. Pp. 175-182. DOI: 10.1016/j.conbuildmat.2018.05.147

17. Kunchariyakun, K., Asavapisit, S., Sinyoung, S. Influence of partial sand replacement by black rice husk ash and bagasse ash on properties of autoclaved aerated concrete under different temperatures and times. Construction and Building Materials. 2018. 173. Pp. 220–227. DOI: 10.1016/j.conbuildmat.2018.04.043
18. Zafar, M.S., Javed, U., Khushnood, R.A., Nawaz, A., Zafar, T. Sustainable incorporation of waste granite dust as partial replacement of sand in autoclave aerated concrete. Construction and Building Materials. 2020. 250. 118878. DOI: 10.1016/j.conbuildmat.2020.118878
19. Chen, Y.-L., Chang, J.-E., Lai, Y.-C., Chou, M.-I. A comprehensive study on the production of autoclaved aerated concrete: Effects of silica-lime-cement composition and autoclaving conditions. Construction and Building Materials. 2017. 153. Pp. 622–629. DOI: 10.1016/j.conbuildmat.2017.07.116
20. Pehlivanlı, Z.O., Uzun, İ., Demir, İ. Mechanical and microstructural features of autoclaved aerated concrete reinforced with autoclaved polypropylene, carbon, basalt and glass fiber. Construction and Building Materials. 2015. 96. Pp. 428–433. DOI: 10.1016/j.conbuildmat.2015.08.104
21. Pehlivanlı, Z.O., Uzun, İ., Yücel, Z.P., Demir, İ. The effect of different fiber reinforcement on the thermal and mechanical properties of autoclaved aerated concrete. Construction and Building Materials. 2016. 112. Pp. 325–330. DOI: 10.1016/j.conbuildmat.2016.02.223
22. Güçlüer, K., Ünal, O., Demir, İ., Başpınar, M.S. An Investigation of Steam Curing Pressure Effect on Pozzolan Additive Autoclaved Aerated Concrete. TEM Journal. 2015. 4. Pp. 78–82.
23. Zhao, Z., Qu, X., Li, F., Wei, J. Effects of steel slag and silica fume additions on compressive strength and thermal properties of lime-fly ash pastes. Construction and Building Materials. 2018. 183. Pp. 439–450. DOI: 10.1016/j.conbuildmat.2018.05.220
24. Leontev, S., Saraykina, K., Golubev, V., Yakovlev, G., Rakhimova, N., Shamanov, V., et al. Research into Influence of Ultra- and Nanodisperse Size Additives on the Structure and Properties of Heat Insulating Autoclaved Aerated Concrete. Procedia Engineering. 2018. 172. Pp. 649–656. DOI: 10.1016/j.proeng.2017.02.076
25. Pachideh, G., Gholhaki, M., Moshtagh, A. On the post-heat performance of cement mortar containing silica fume or Granulated Blast- Furnace Slag. Journal of Building Engineering. 2019. 24. 100757. DOI: 10.1016/j.jobe.2019.100757
26. Almajeed, I., Turki, S. Enhance Properties of Autoclaved Aerated Concrete by Adding Silica Fume. International Journal of Recent Technology and Engineering. 2019. 7(6). Pp. 11–15.
27. Lashari, A.R., Kumar, A., Kumar, R., Rizvi, S.H. Combined effect of silica fume and fly ash as cementitious material on strength characteristics, embodied carbon, and cost of autoclave aerated concrete. Environmental Science and Pollution Research. 2023. 30(10). Pp. 27875–27883. DOI: 10.1007/s11356-022-24217-9
28. IOS. Iraqi Organization of Standards, 5: Portland Cement. National Centre for Construction Laboratories and Researches, 2019.
29. IOS. Iraqi Organization of Standards, 45-84 (Reapproved 2016): Aggregates from Natural Sources for Concrete and Construction. . National Centre for Construction Laboratories and Researches, 2016.
30. ECA. ECA® MICROSILICA-D. Amman - Jordan: Europen concrete additives, 2010.
31. IOS. Iraqi Organization of Standards, 807: Lime Using in Construction. National Centre for Construction Laboratories and Researches, 1988.
32. ACI-Committee. ACI-2349: Guide for the use of silica fume in concrete. USA: American Concrete Institute, 2000. Pp. 1-63.
33. BS-EN. BS EN 679: Determination of the compressive strength of autoclaved aerated concrete, 2005.
34. BS-EN. BS EN 1881-117: Testing concrete. Method for determination of tensile splitting strength, 1983.
35. BS-EN. BS EN 1351: Determination of flexural strength of autoclaved aerated concrete, 1997.
36. BS-EN. BS EN 678: Determination of the dry density of autoclaved aerated concrete. 94th ed2017 1 June 2017.
37. Al-Defai, N. The consequences of the dewatering of freshly-mixed wet mortars by the capillary suction of brick masonary. University of Manchester, 2013.
38. BS-EN. BS EN 772-11: Methods of test for masonry units. Determination of water absorption of aggregate concrete, autoclaved aerated concrete, manufactured stone and natural stone masonry units due to capillary action and the initial rate of water absorption of clay masonry units: British Standards Institution (BSI), 2011.
39. ASTM. ASTM C1639: Standard specification for fabrication of cellular glass pipe and tubing insulation. The American Society for Testing and Materials, 2019. 4 p.
40. Link to the Figure 5 https://www.mtixtl.com/advancedmetallurgicalmicroscopewithpolarizingdarkfieldandduallights30mpdigitalcamera40x-1600x-eq-mm500t-usb.aspx.
41. Naik, T.R. Concrete durability as influenced by density and/or porosity. Cement and Concrete Institute of Mexico Symposium "World of Concrete - Mexico": Milwaukee DoCEaMCoEaASTUOW; 1997.
42. Rathod, S., Akbari, Y. Performance evaluation of aerated autoclaved concrete blocks using silica fume. Journal of Emerging Technologies and Innovative Research (JETIR). 2017. 4(4). Pp. 220-225.
43. ASTM. ASTM C1693-11: Standard Specification for Autoclaved Aerated Concrete (AAC). The American Society for Testing and Materials, 2017.
44. Pachideh, G., Gholhaki, M. Effect of pozzolanic materials on mechanical properties and water absorption of autoclaved aerated concrete. Journal of Building Engineering. 2019. 26. 100856. DOI: 10.1016/j.jobe.2019.100856
45. Wan, H., Hu, Y., Liu, G., Qu, Y. Study on the structure and properties of autoclaved aerated concrete produced with the stone-sawing mud. Construction and Building Materials. 2018. 184. Pp. 20–26.
46. Toutanji, H.A., Liu, L., El-Korchi, T. The role of silica fume in the direct tensile strength of cement-based materials. Materials and Structure. 1999. 32. 7. DOI: 10.1007/BF02481516
47. Baspinar, M., Demir, I., Kahraman, E., Gorhan, G. Utilization Potential of Fly Ash together with Silica Fume in Autoclaved Aerated Concrete Production. KSCE Journal of Civil Engineering. 2014. 18(1). Pp. 47–52. DOI: 10.1007/s12205-014-0392-7
48. Thongtha, A., Maneewan, S., Punlek, C., Ungkoon, Y. Investigation of the compressive strength, time lags and decrement factors of AAC-lightweight concrete containing sugar sediment waste. Energy and Buildings. 2014. 84. Pp. 516–525. DOI: 10.1016/j.enbuild.2014.08.026

49. Narayanan, N., Ramamurthy, K. Structure and properties of aerated concrete: a review. Cement and Concrete Composites. 2000. 22(5). Pp. 321–329. DOI: 10.1016/s0958-9465(00)00016-0
50. Elrahman, M.A., Chung, S.-Y., Sikora, P., Rucinska, T., Stephan, D. Influence of Nanosilica on Mechanical Properties, Sorptivity, and Microstructure of Lightweight Concrete. Materials. 2019. 12(19). 3078. DOI: 10.3390/ma12193078
51. Mindess, S., Young, J., Darwin, D. Concrete. 2nd ed. U.S.A.: Prentice Hall, Pearson Education, Inc. Upper Saddle River, NJ 07458, 2003.

Information about the author:

Rana Shabbar
ORCID: https://orcid.org/0000-0003-3087-0333
E-mail: rana.shubber@uokufa.edu.iq

Layth Abdulrasool Mahdi Alasadi,

ORCID: https://orcid.org/0000-0001-6244-7965

E-mail: laitha.alasadi@uokufa.edu.iq

Jaber Kadhim Taher,

Received: 14.02.2023. Approved after reviewing: 14.11.2023. Accepted: 17.11.2023.

Magazine of Civil Engineering

ISSN 2712-8172

journal homepage: http://engstroy.spbstu.ru/

Research article

UDC 625.068.2

DOI: 10.34910/MCE.128.9

Structure of clay minerals of road soil-cement during complex modification

E.A. Vdovin[1], ***P.E. Bulanov***[1] ✉, ***V.F. Stroganov***[1], ***V.P. Morozov***[2]

[1] *Kazan State University of Architecture and Engineering, Kazan, Russian Federation*

[2] *Kazan (Volga region) Federal University, Kazan, Russian Federation*

✉ *pavel.bulanov1991@yandex.ru*

Keywords: kaolinite, montmorillonite, dodecyltriethoxysilane, complex modification, polycarboxylate ester, intercalation, splitting, chemisorption, soil-cement

Abstract. Previously obtained positive results of studies of physical, mechanical, technological and operational properties of road soil-cement at their complex multifunctional modification with organosilicon compounds and polycarboxylate superplasticizers have shown the effectiveness of the use of *strengthened* soils in the construction of roads. However, the influence of complex modification on changes in the structure of clay minerals of strengthened soils in road construction remains insufficiently studied. Using X-ray phase analysis, comprehensive studies of the structure of modified clay minerals were carried out to reveal intercalation processes and changes in the size of their particles as a result of splitting processes. Chemical structure of the studied modifiers, nature of their interaction with clay minerals and organomineral bonds were confirmed using IR spectroscopy. The combined influence of modifying effect of dodecyltriethoxysilane and polycarboxylate ester on kaolinite and montmorillonite clays was established, which led to the manifestation of synergistic mechanism at strengthening of clay soils. During the modification, a multifunctional effect was noted, characterized by an increase of integral intensity of diffraction maxima on the diffraction patterns of modified clay soils, associated with an increase of interplanar distances in their structure as a result of intercalation processes. The positive effect of complex modification of clays is associated with splitting and reduction of mineral particle sizes. It has been established that the consequence of complex modification is chemical interaction (chemisorption) with the formation of organosilane bonds, which provide increased efficiency in strengthening of clay soils in road construction.

Citation: Vdovin, E.A., Bulanov, P.E., Stroganov, V.F., Morozov, V.P. Structure of clay minerals of road soil-cement during complex modification. Magazine of Civil Engineering. 2024. 17(5). Article no. 12809. DOI: 10.34910/MCE.128.9

1. Introduction

It is known that soil-cements are the building material type obtained by mixing and subsequent compaction of soils, Portland cement and water (modifiers as necessary) [1, 2]. Their demand is ensured by a number of advantages: cost-effectiveness, reduction of negative load on the environment and workability during construction [3].

In road bases and surfaces construction various types of soils and local materials are used, especially in areas with a lack of durable stone materials [4, 5]. However, these materials (especially clay soils strengthened by Portland cement) in humid conditions [6] are susceptible to the climatic factors effects, which contributes to development of damage processes the road pavements structural layers and the roads service life reduction [7].

Clay soils have a wide range of mineralogical composition and consist mainly of small particles – hydrous aluminosilicates and other minerals. Clays are mainly inorganic materials [8, 9]. Clay minerals are a diverse group of hydrous aluminosilicates that usually display layered or fibrous structures encompassing polymeric sheets of silica tetrahedra linked with octahedral sheets [10, 11]. Clay minerals with silica tetrahedral and alumina octahedral sheets are called 1:1 clays. Similarly, clay minerals with one octahedral aluminate sheet sandwiched by two silica tetrahedral are called 2:1 layer clays [12].

The most common clay minerals in soils are kaolinite and montmorillonite. Kaolinite is a relatively stable mineral found in fairly large quantities in many clay soils (Al_2O_3•$2SiO_2$•$2H_2O$). The second, most common clay mineral, montmorillonite ($2Al_2O_3$•$2SiO_2$•$4H_2O$), is formed under alkaline conditions in continental and marine sediments and in the weathering crust. It belongs to the layered silicates subclass and has the ability to swell strongly [13]. According to their mineral composition, clay soils are usually divided into monomineral (kaolinite, montmorillonite, illite, etc.) and polymineral, consisting of various clay and relict minerals [14, 15].

It is known that one of the methods for improving the soil-cement quality and durability is hydrophobization, which gives the mineral particles and their aggregates surfaces the ability not to be wetted by water [16, 17]. The most effective modifiers for reducing water absorption and increasing frost resistance of strengthened soils are organosilicon compounds (silanes, siloxanes, etc.) [18, 19].

Molecules of organosilicon compounds consist of two parts, opposite in nature and properties. At one end of the molecules there are hydrophilic (polar) groups (OH, CHO, COOH, NH_2, etc.), which are a source of strong molecular interaction and therefore are highly soluble in water. At the other end of the molecules, there are hydrophobic parts formed by one or several rather long chains saturated with hydrocarbon radicals (C_nH_{2n+2}), incapable of hydration and insoluble in water [20–22].

Hydrocarbon chains of hydrophobic molecules tend to repel each other, causing them to form a brush-like structure on the absorbent surfaces (Langmuir palisade). Such structures presence promotes the adjacent particles separation and reduces friction between them, which contributes to the soils mixing and compaction processes when they are treated by surfactants. It has been established that the hydrophobic films effect can manifest itself in different ways: they prevent the water molecules penetration to the mineral particles contact points [23]. In addition, the enveloping process the soil capillaries walls contributes to the reverse curvature menisci formation in them, which prevent the movement of capillary and gravitational moisture. The process of mineral particles enveloping with hydrophobic films protects them from swelling, dissolution and destruction [24].

The greatest effect of hydrophobization processes is shown, as noted above, by organosilicon compounds, in the molecules of which silicon atoms are connected to alkyl (methyl, ethyl) and aryl radicals (phenyl) [25, 26].

Another effective direction of increasing operational and technological (workability) characteristics is the soil-cement plasticization [28, 29]. The most promising modifiers among plasticizing substances are polycarboxylate esters, which, unlike known superplasticizers, according to [30], contribute to a positive change in the hydrate new formations morphology and the ettringite crystals size decrease. The possibility of the stable organomineral phases formation due to the polymer modifier incorporation into the calcium hydroaluminate lamellar structure is also noted [31].

The previously obtained positive results of modified soil-cement by polycarboxylate plasticizers [28] are explained by the influence processes on both the soil clay minerals and the cement system. Theoretically, the existence of two main interactions between clay minerals and polycarboxylates is assumed [29, 30]:

- electrostatic interaction between positively charged clay surface areas and negatively charged plasticizer groups;
- plasticizer side chains intercalation between clay minerals aluminosilicate layers as a result of deprotonation processes.

The action mechanism when modified by substances described above was previously considered mainly on cement systems. It is known that plasticizers and water repellents are used mainly in the modification of cement concrete mixtures, in which inert material is used as a filler. However, in strengthened clay soils there is a diverse minerals amount, including clay minerals, which have high cation exchange and specific surface area [12, 32]. These minerals presence in strengthened soils causes their strength and frost resistance decrease [33]. Previously carried out studies on the strengthened clay soils modification made it possible to identify the most effective modifiers for increasing the soil-cement strength and frost resistance: polycarboxylate superplasticizers [27, 33, 34] and water repellents – dodecyltriethoxysilane and others [35, 36]. However, in the works carried out there are no studies of these modifiers influence on the clay minerals structure.

In connection with the above, the purpose of the work is to study the joint modification mechanisms of soil-cement with a polycarboxylate superplasticizer and an organosilicon water repellent (dodecyltriethoxysilane), the structural characteristics change, and, as a consequence, the level of clay minerals properties in road construction:

- to study the modifiers intercalation processes in clay minerals using X-ray phase analysis;
- to determine the chemisorption possibility of the studied modifiers with clay minerals using IR spectroscopy;
- to determine the magnitude of the region of clay minerals particles coherent scattering after modification by X-ray phase analysis;
- to identify the influence mechanisms of complex modification on structural changes that ensure an increase the indicators level of soil-cement compositions properties in road construction.

2. Materials and Methods

For the research, kaolinite clay produced by NPP Industrial Minerals LLC (Samara Region, Russia) with kaolinite mineral content of up to 95 % and montmorillonite clay from the Biklyansky quarry of the Tukaevsky district of the Republic of Tatarstan with a montmorillonite mineral content of up to 70 % were used.

The following modifiers were used:

- dodecyltriethoxysilane $C_{18}H_{40}O_3Si(OC_2H_5)_3$. Hubei Co-Formula Material Tech Co., Ltd. (China);
- Ready-Mix 304 – plasticizing additive based on a composition of polycarboxylate ethers. JSC TechnoNIKOL (Russia).

X-ray diffraction analysis was used to determine the interplanar spacing of clay minerals during modification. Experiments were carried out on a Bruker D2 Phaser automatic X-ray diffractometer with a linear coordinate detector. CuKα radiation, monochromatic (λ(Cu-K) = 1.54184 Å), X-ray tube operating mode 40 kV, 40 mA were used. Experiments were performed at room temperature in Bragg-Brentano geometry with a flat sample. Construction and analysis of diffraction patterns to determine the mineral composition were performed using the DIFFRACplusEvaluationPackage – EVA, Search/Match, Bruker Diffrac Eva program. The degree of crystallinity was assessed (determining the size of the coherent scattering region) based on the width of the diagnostic diffraction maxima using the Scherer formula.

IR spectroscopy was used to determine the chemical structure of modifiers and their nature of interaction with clay minerals, as well as to determine the covalent bonds between clay minerals and additives. Data were collected using a Bruker Vertex 70 FTIR spectrometer with a single reflection, germanium crystal ATR accessory (MIRacle, PIKE Technologies) purged under dry air to remove atmospheric water vapor. Background spectra of 64 scans at a resolution of 2 cm^{-1} were subtracted from sample spectra.

3. Results and Discussion

In accordance with the set goals and objectives, a set of studies was carried out to establish the mechanisms and features of the modification processes influence on the interaction between polycarboxylate ester and dodecyltriethoxysilane and soils clayey components.

In the presented diffraction patterns (Fig. 1), there is an integral intensity increase of the diffraction maxima by 29 % (for montmorillonite clay modified by polycarboxylate ether) and 5.8 % (for montmorillonite clay modified by dodecyltriethoxysilane). This is explained by an increase of clay mineral interplanar distance as a result of the polymer radicals intercalation with montmorillonite [30]. A multifunctional effect was noted, characterized by an increase of diffraction maxima integral intensity on modified clay soils diffraction patterns, associated with an interplanar distances increase in their structure as a result of intercalation processes. When kaolinite clay was modified by polycarboxylate ether and dodecyltriethoxysilane, no changes was observed in the interplanar distance.

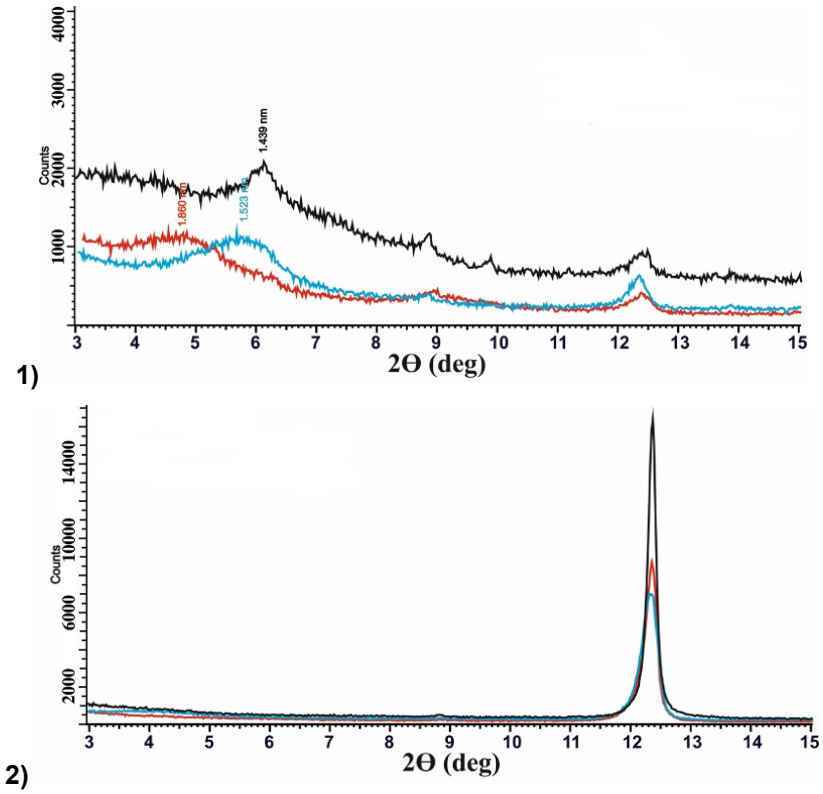

Figure 1. X-ray diffraction patterns of studied clays: —— – unmodified clay; —— – clay modified with polycarboxylate ether; —— – clay modified with dodecyltriethoxysilane: 1 – montmorillonite clay; 2 – kaolinite clay.

Table 1. Results of determining the region of clay mineral particles coherent scattering.

Name of materials studied	LVol-IB, nm
Kaolinite clay	37.72
Kaolinite clay modified by polycarboxylate ester	25.85
Kaolinite clay modified by dodecyltriethoxysilane	22.62
Montmorillonite clay	18.89
Montmorillonite clay modified by polycarboxylate ester	9.65
Montmorillonite clay modified by dodecyltriethoxysilane	8.47

Using the X-ray phase analysis method, the values of coherent scattering region (CSR) of clay minerals particles were calculated (Table 1). The studies performed suggest that modifiers cause the minerals shape and size changes (as a result of their splitting). The positive effect of complex clays modification is associated with a decrease in size of kaolinite clay mineral particles by 31.5 % and 40.0 %, and in montmorillonite clay by 48.9 % and 55.2 %, respectively.

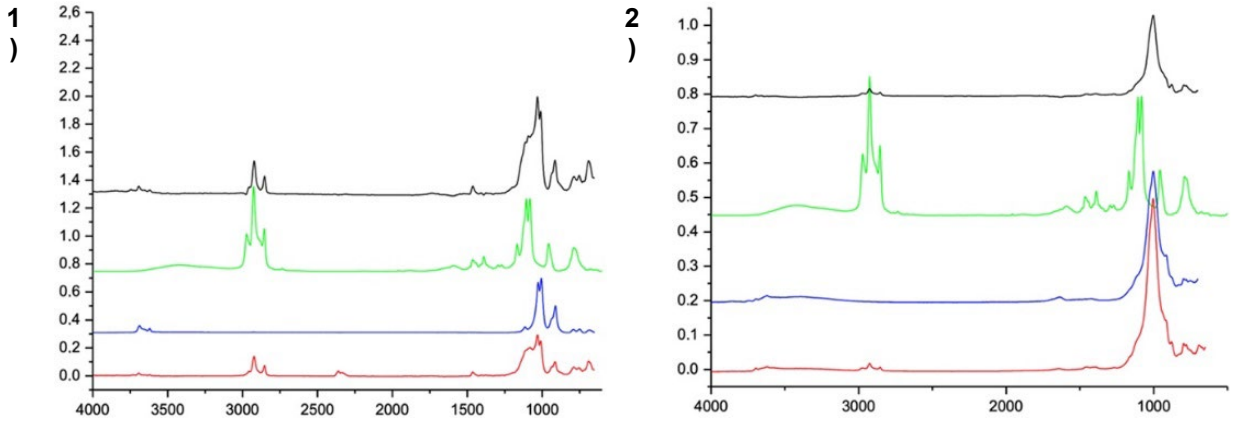

Figure 2. IR spectra: —— – difference spectrum; —— – dodecyltriethoxysilane; —— – clay; —— – clay modified by dodecyltriethoxysilane: 1 – kaolinite; 2 – montmorillonite.

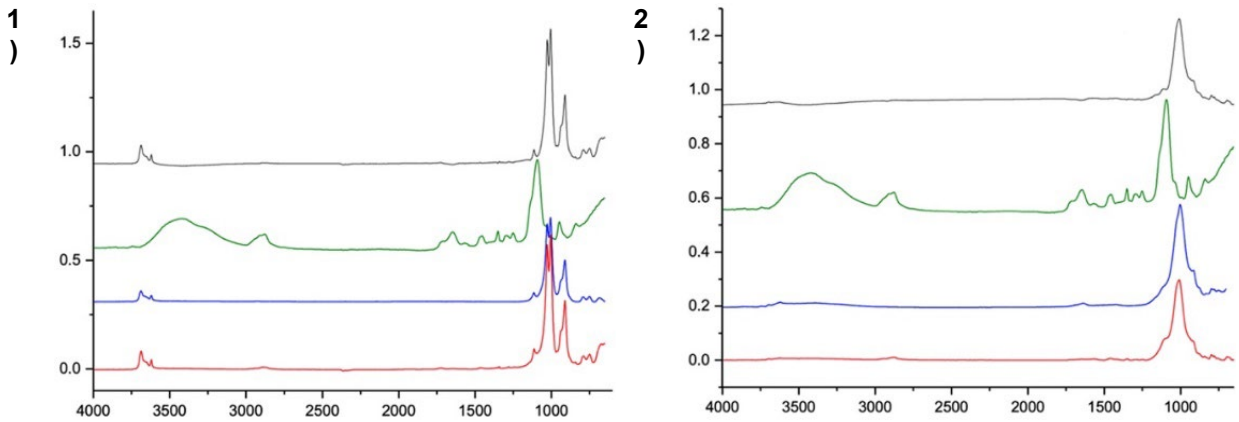

Figure 3. IR spectra: ——— – difference spectrum; ——— – polycarboxylate ester; ——— – clay; ——— – clay modified by polycarboxylate ester: 1 – kaolinite; 2 – montmorillonite.

It has been established that the complex modification consequence is chemical interaction (chemisorption) with the organosilane bonds formation, which ensure increased efficiency of the clay soils strengthening technology in road construction.

Based on the results of the IR spectroscopic analysis method (Fig. 2 and 3), it was determined that the band at 3700 cm^{-1} in the studied clays indicates the intrasurface OH groups presence located on the octahedral layers opposite tetrahedral oxygens surfaces, and the band at 3621 cm^{-1} may be attributed to internal OH groups located in a plane common to octahedral and tetrahedral layers [38]. Analysis of the given IR spectra shows that the main bands in them relate to the valence bonds of silicon with oxygen and hydrogen with oxygen. Oxygen atoms can be connected to two silicon atoms via Si-O-Si bridging bonds, or to one via non-bridging Si-O bonds. In particular, the bands at 1032 cm^{-1} and 1009 cm^{-1} are attributed to the stretching vibrations of Si-O-Si(Al) bridging bonds in the kaolinite clay crystal lattice and 1090 cm^{-1} and 990 cm^{-1} in montmorillonite clay [38, 39].

The chemical structure of modifiers dodecyltriethoxysilane and polycarboxylate superplasticizer was confirmed. In the dodecyltriethoxysilane spectrum stretching vibrations of bonds correspond to an intense peak at a frequency of 1093 cm^{-1} with a shoulder of 1120 cm^{-1} and peaks of ethyl groups stretching and bending vibrations at frequencies of 2990, 2910, 2840, 1450 cm^{-1}, corresponding to the aliphatic CH_2 and CH_3 groups of the monomer radical.

In the polycarboxylate superplasticizer spectrum the mainly contains the stretching vibrations in the region of 2840–2970 cm^{-1} and bending vibrations in the region of 1450–1470 cm^{-1} associated with aliphatic CH_2 and CH_3 groups of polyethylene glycol. The C-O-C ether bond stretching vibrations corresponds to an intense peak at 1125 cm^{-1}.

It has been established that the complex modification consequence is chemical interaction (chemisorption) with the organosilane bonds formation, which provide increased strengthening clay soils efficiency in road construction. When montmorilonite clay is modified by dodecyltriethoxysilane, the intense peak at a frequency of 1093 cm^{-1} with a shoulder of 1120 cm^{-1} disappeared, but the bands corresponding to the monomer radical remained. Analysis of the difference spectrum and spectrum of kaolinite clay modified by dodecyltriethoxysilane showed that no chemical interaction occurs.

When kaolinite and montmorillonite clays modified by polycarboxylate ether, the ether C-O-C bond complete disappearance was noted, which indicated the polymer chemical interaction (chemisorption) with clay minerals.

4. Conclusions

1. The joint influence of the dodecyltriethoxysilane and polycarboxylate ether modifying effect on kaolinite and montmorillonite clays has been established, which led to the manifestation about synergistic mechanism in strengthening clay soils. During the modification, the polyfunctional effect was noted, manifested in the processes of intercalation, chemisorption, splitting and reducing the clay minerals particle size. The completed research results will ensure the effectiveness of using soils with a clay minerals high content in road pavement structures.
2. A multifunctional effect was noted, characterized by an increase of diffraction maxima integral intensity on the modified clay soils diffraction patterns, associated with an interplanar distances increase in their structure as a result of intercalation processes. When kaolinite clay is modified

with polycarboxylate ether and dodecyltriethoxysilane, no changes are observed in the interplanar distance.

3. The positive effect of complex clays modification has been established, which consisted in reducing the kaolinite clay mineral particles size by 31.5 % and 40.0 %, and in montmorillonite clay by 48.9 % and 55.2 %, respectively.

4. It has been established that the complex modification consequence is chemical interaction (chemisorption) with the organosilane bonds formation, which ensure an increase the strengthening clay soils efficiency in road construction.

References

1. Abbey, S.J., Eyo, U.E., Okeke, C.A.U., Ngambi, S. Experimental study on the use of RoadCem blended with by-product cementitious materials for stabilisation of clay soils. Construction and Building Materials. 2021. 280. Article no. 122476. DOI: 10.1016/j.conbuildmat.2021.122476
2. Jiang, N.-J., Du, Y.J., Liu, K. Durability of Lightweight Alkali-Activated Ground Granulated Blast Furnace Slag (GGBS) Stabilized Clayey Soils Subjected to Sulfate Attack. Applied Clay Science. 2018. 161. Pp. 70–75. DOI: 10.1016/j.clay.2018.04.014
3. Behnood, A. Soil and clay stabilization with calcium-and non-calcium-based additives: a state-of-the-art review of challenges, approaches and techniques. Transportian Geotechnics. 2018. 17. Pp. 14–32. DOI: 10.1016/j.trgeo.2018.08.002
4. Amiri, M., Sanjari, M., Porhonar, F. Microstructural evaluation of the cement stabilization of hematite-rich red soil. Case Studies in Construction Materials. 2022. 16. Article no. e00935. DOI: 10.1016/j.cscm.2022.e00935
5. Zhang, Y., Zhong, X., Lin, J., Zhao, D., Jiang, F., Wang, M.-K., Ge, H., Huang, Y. Effects of fractal dimension and water content on the shear strength of red soil in the hilly granitic region of southern China. Geomorphology. 2020. 351. Article no. 106956. DOI: 10.1016/j.geomorph.2019.106956
6. Cai, Y., Xu, L., Liu, W., Shang, Y., Su, N., Feng, D. Field test study on the dynamic response of the cement-improved expansive soil subgrade of a heavy-haul railway. Soil Dynamics and Earthquake Engineering. 2020. 128. Article no. 105878. DOI: 10.1016/j.soildyn.2019.105878
7. Roshan, K., Choobbasti, A., Soleimani, K., Fakhrabadi, A. The effect of adding polypropylene fibers on the freeze-thaw cycle durability of lignosulfonate stabilised clayey sand. Cold Regions Science and Technology. 2021. 193. Article no. 103418. DOI: 10.1016/j.coldregions.2021.103418
8. Mousavi, S.S., Bhojaraju, C., Ouellet-Plamondon, C. Clay as a Sustainable Binder for Concrete – A Review. Construction Materials. 2021. 1. Pp. 134–168. DOI: 10.3390/constrmater1030010
9. Koohmishi, M., Palassi, M. Mechanical Properties of Clayey Soil Reinforced with PET Considering the Influence of Lime-Stabilization. Transportation Geotechnics. 2022. 33. Article no. 100726. DOI: 10.1016/j.trgeo.2022.100726
10. Singh, N.B. Clays and Clay Minerals in the Construction Industry. Minerals. 2022. 12. Article no. 301. DOI: 10.3390/min12030301
11. Wang, S., Gainey, L., Mackinnon, I.D.R., Allen, C., Gu, Y., Xi, Y. Thermal behaviors of clay minerals as key components and additives for fired brick properties: A review. Journal of Building Engineering. 2023. 66. Article no. 105802. DOI: 10.1016/j.jobe.2022.105802
12. Kausor, M.A., Gupta, S.S., Bhattacharyya, K.G., Chakrabortty, D. Montmorillonite and modified montmorillonite as adsorbents for removal of water soluble organic dyes: A review on current status of the art. Inorganic Chemistry Communications. 2022. 143. Article no. 109686. DOI: 10.1016/j.inoche.2022.109686
13. Zhu, Y., Iroh, J.O., Rajagopolan, R., Aykanat, A., Vaia, R. Optimizing the Synthesis and Thermal Properties of Conducting Polymer – Montmorillonite Clay Nanocomposites. Energies. 2022. 15. Article no. 1291. DOI: 10.3390/en15041291
14. Linhares Jr., J.A., Azevedo, A.R.G., Marvila, M.T., Teixeira, S.R., Fediuk, R., Vieira, C.M.F. Influence of processing parameters variation on the development of geopolymeric ceramic blocks with calcined kaolinite clay. Case Studies in Construction Materials. 2022. 16. Article no. e00897. DOI: 10.1016/j.cscm.2022.e00897
15. Maier, M., Sposito, R., Beuntner, N., Thienel, K. Particle characteristics of calcined clays and limestone and their impact on early hydration and sulfate demand of blended cement. Cement and Concrete Research. 2022. 154. Article no. 106736. DOI: 10.1016/j.cemconres.2022.106736
16. Huang, G., Lin, H., Li, J., Liu, J. Inducing hydrophobicity in saline soils: A comparison of hydrophobic agents and mechanisms. Powder Technology. 2023. 424. Article no. 118475. DOI: 10.1016/j.powtec.2023.118475
17. Roshan, K., Choobbasti, A., Soleimani, K., Fakhrabadi, A. The effect of adding polypropylene fibers on the freeze-thaw cycle durability of lignosulfonate stabilised clayey sand. Cold Regions Science and Technology. 2021. 193 (3). Article no. 103418. DOI: 10.1016/j.coldregions.2021.103418
18. Al-Kheetan, M.J., Rahman, M.M., Chamberlain, D.A. Moisture evaluation of concrete pavement treated with hydrophobic surface impregnants. International Journal of Pavement Engineering. 2020. 21 (14). Pp. 1746–1754. DOI: 10.1080/10298436.2019.1567917.
19. Sun, Z., Liu, Zh., Han, J., Wang, H., Zhang, H., Yan, J. Long-term effects of soft rock amendment on changes of soil aggregate cementing agents of sandy soil by SEM-EDS. Frontiers Environmental Science. 2023. 11. Article no. 1207781. DOI: 10.3389/fenvs.2023.1207781
20. Rakhimov, F., Ahmedov, V., Aminov, F. The method for producing hydrophobic compositions. Universum: chemistry and biology. 2020. 4 (70). Pp. 63–66.
21. Kosulina, T.P., Tsokur, O.S., Chernykh, V.F. The Use of Products Disposal of Bottoms Residues as a Hydrophobic Additive. Ecology and Industry of Russia. 2019. 23 (4). Pp. 36–40. DOI: 10.18412/1816-0395-2019-4-36-40
22. Misnikov, O. The hydrophobic modification of gypsum binder by peat products: Physico-chemical and technological basis. Mires and Peat. 2018. 21. Pp. 1–14. DOI: 10.19189/MaP.2017.OMB.300
23. Schröfl, C., Mechtcherine, V., Kaestner, A., Vontobel, P., Hovind, J., & Lehmann, E. Transport of water through Strain-hardening Cement-based Composite (SHCC) applied on top of cracked reinforced concrete slabs with and without hydrophobization of cracks – Investigation by neutron radiography. Construction and Building Materials. 2015. 76. Pp. 70–86. DOI: 10.1016/j.conbuildmat.2014.11.062

24. Lisichkin G.V., Olenin A.Y. Hydrophobization of inorganic materials by chemical modification of the surface. Russian Journal of Applied Chemistry. 2020. 93 (1). Pp. 5–19. DOI: 10.31857/S0044461820010016
25. Fic, S., Klonica, M., Szewczak, A. Effect of hydrophobization on the durability of building ceramics. Polimery. 2016. 61 (01). Pp. 46–48. DOI: 10.14314/polimery.2016.046
26. Ogurtsova, Y.N., Strokova, V.V., Labuzova, M.V. Hydrophobization of Concrete Using Granular Nanostructured Aggregate. IOP Conference Series: Materials Science and Engineering. 2017. 262. Article no. 012013. DOI: 10.1088/1757-899X/262/1/012013
27. Grabowska, K., Koniorczyk, M. The effect of hydrophobic treatment by organosilicon admixtures of cement mortar. Cement Wapno Beton, 2019. 24 (4). Pp. 320–329. DOI: 10.32047/CWB.2019.24.4.7
28. Vdovin, E., Bulanov, P., Stroganov, V., Mavliev, L. Physical and mechanical characteristics of modified soil cement with polycarboxylate superplasticizers. Proceedings of STCCE. 2022. Lecture Notes in Civil Engineering. 2023. 291. Pp. 125–133. DOI: 10.1007/978-3-031-14623-7_10
29. Chong, S.H. Development of constitutive model for simulation of cemented soil. Geotechnical and Geological Engineering. 2019. 37 (5). Pp. 4635–4641. DOI: 10.1007/s10706-019-00903-3
30. Plank, J., Sakai, E., Miao, C.W., Yu, C., Hong, J.X. Chemical admixtures – Chemistry, Applications and Their Impact on Concrete Microstructure and Durability. Cement and Concrete Research. 2015. 78. Pp. 81–99. DOI: 10.1016/j.cemconres.2015.05.016
31. Kanchanason, V., Plank, J. Effect of calcium silicate hydrate – polycarboxylate ether (C-S-H–PCE) nanocomposite as accelerating admixture on early strength enhancement of slag and calcined clay blended cements. Cement and Concrete Research. 2019. 119 (1). Pp. 44–50. DOI: 10.1016/j.cemconres.2019.01.007
32. Bhandari, I., Sharma, R., Sofi, A., Nighot, N. A systematic study on sustainable low carbon cement – Superplasticizer interaction: Fresh, mechanical, microstructural and durability characteristics. Heliyon. 2023. 9. Article no. e19176. DOI: 10.1016/j.heliyon.2023.e19176
33. Wang, L., Cheng, J., Jin, Zh., Sun, Q., Zou, R., Meng, Q., Liu, K., Su, Y., Zhang, Q. High-pressure hydrogen adsorption in clay minerals: Insights on natural hydrogen exploration. Fuel. 2023. 344. Article no. 127919. DOI: 10.1016/j.fuel.2023.127919
34. Vdovin, E., Bulanov, P., Stroganov, V., Morozov, V. Construction of road pavements using complex modified soil-cement. Construction of Unique Buildings and Structures. 2023. 109. Article no. 10927. DOI: 10.4123/CUBS.109.27
35. Vdovin, E., Bulanov, P.; Stroganov, V., Morozov, V. Complex modification of soil-cement for road pavements. Construction of Unique Buildings and Structures. 2023. 109. Article no. 10928. DOI: 10.4123/CUBS.109.28
36. Vdovin, E.A., Bulanov, P.E., Stroganov, V.F. Design of road pavements with layers of soil-cement modified with organosilicon. News KSUAE. 2024. 1 (67). Pp. 207–216. DOI: 10.48612/NewsKSUAE/67.20
37. Vdovin, E.A., Bulanov, P.E., Stroganov, V.F. Improving the characteristics of road soil-cement with organosilicon compounds. News KSUAE. 2023. 4 (66). Pp. 301–309. DOI: 10.52409/20731523_2023_4_301
38. Šaponjić, A., Šaponjić, Đ., Nikolić, V, Milošević, M., Marinović-Cincović, M., Gyoshev, S., Vuković, M., Kokunešoski, M. Iron (III) oxide fabrication from natural clay with reference to phase transformation g- → a-Fe2O3. Science of Sintering. 2017. 49 (2). Pp. 197–205. DOI: 10.2298/SOS1702197S
39. Chetverikova, A.G., Kanygina, O.N., Alpysbaeva, G.Z., Yudin, A. A., Sokabayeva, S.S. Infrared spectroscopy as the method for determining structural responses of natural clays to microwave exposure. Condensed Matter and Interphases. 2019. 21 (3). Pp. 446–454. DOI: 10.17308/kcmf.2019.21/1155
40. Stack, K.M., Milliken, R.E. Modeling near-infrared reflectance spectra of clay and sulfate mixtures and implications for Mars. Icarus. 2015. 250. Pp. 332–356. DOI: 10.1016/j.icarus.2014.12.009

Information about the authors:

***Evgeniy Vdovin**, PhD in Technical Sciences*
ORCID: https://orcid.org/0000-0002-0649-4342
E-mail: vdovin007@mail.ru

***Pavel Bulanov**, PhD in Technical Sciences*
ORCID: https://orcid.org/0000-0002-0149-8854
E-mail: pavel.bulanov1991@yandex.ru

***Victor Stroganov**, Doctor of Chemical Sciences*
ORCID: https://orcid.org/0000-0001-9680-6698
E-mail: Svf08@mail.ru

***Vladimir Morozov**, Doctor of Geological and Mineralogical Sciences*
E-mail: Vladimir.Morozov@kpfu.ru

Received: 23.03.2024. Approved after reviewing: 18.06.2024. Accepted: 22.06.2024.

Magazine of Civil Engineering

ISSN 2712-8172

journal homepage: http://engstroy.spbstu.ru/

Research article

UDC 624.07

DOI: 10.34910/MCE.128.10

Providing free vibrations and stability of a multi-span beam under temperature changes by selecting the support system

I.V. Kudryavtsev ✉ , ***V.A. Ivanov***, ***O.I. Rabetskaya***, ***A.E. Mityaev***

Siberian Federal University, Krasnoyarsk, Russian Federation

✉ *ikudryavcev@sfu-kras.ru*

Keywords: Euler–Bernoulli beam theory, multi-span beam, periodic structures, temperature, axial compression, free vibration, structural design, buckling, transverse oscillation, topology optimization, finite element method, pipeline

Abstract. This study presents a newly developed method for reasonable selection of boundary conditions and number of pinned intermediate supports for a straight multi-span beam. This method might help to obtain the required values of the first frequency of free vibrations and the critical load from the action of axial force, resulting from the changing the beam temperature. The method is based on known concepts of beam vibration and stability theories and uses support coefficients as a criterion for selecting the appropriate support system for a multi-span beam. These coefficients are obtained by solving the corresponding differential equations of the dynamic behavior of the beam and are determined only by the support conditions. Comparative calculations of the straight pipeline using the developed and finite element methods for beam and shell models were carried out, which showed good convergence. Normalization of the values of the support coefficients allowed to combine both conditions, for the first natural vibration frequency and the first critical force, and express it as a single criterion for the selection of the support system. The selection of the support system is shown as three general methods of fixing multi-beam beams with a constant span length. This approach can be applied to any straight beams and support conditions for which support coefficient values are known. To this end, a general algorithm for selecting a support system with known support coefficients and requirements for their normalization is given. The results obtained can be used in the calculation and design of any multi-span beam structures to control the values of their free vibration frequencies and stability by selecting an appropriate support system during the engineering design process.

Funding: The research was financially supported by Russian Foundation for Basic Research, Krasnoyarsk Territory and Krasnoyarsk Regional Fund of Science, project No. 20-48-242922. Available online: https://www.sf-kras.ru/konkursy/reestr/6277-razrabotka-proektnykh-metodov-obespecheniya-trebuemykh-dinamicheskikh-parametrov-mnogoproletnykh-sterzhnevykh-konstruktsij-posredstvom-obosnovannogo-vybora-skhemy-rasstanovki-i-vidov-opor-s-uchetom-vliyaniya-temperatury.

Citation: Kudryavtsev, I.V., Ivanov, V.A., Rabetskaya, O.I., Mityaev, A.E. Providing free vibrations and stability of multi-span beam at temperature changes by supports selection. Magazine of Civil Engineering. 2024. 17(4). Article no.12810. DOI: 10.34910/MCE.128.10

1. Introduction

A large number of extended periodic structures are subject to forced vibrations and temperature changes. These include pipelines, oil lines, steam lines, railway rails, pull rods, cables, beams, etc. Serviceability conditions for such structures ensure the permissible values of the first natural frequency of vibration f_1 and the first critical force P_{cr1} or temperature ΔT_{cr1} at which the loss of stability occurs:

$$f_1 \geq [f],\ P_{cr1} \geq [P] \text{ or } \Delta T_{cr1} \geq [\Delta T]. \quad (1)$$

In this paper, these multi-span structures are modeled on the basis of Euler–Bernoulli beam theory for cases of transverse free vibrations and stability loss. Theoretical foundation for calculating the vibrations and stability of multi-span beams have been described in many papers. This beam dynamic behavior is commonly calculated by partial differential equations with specified boundary conditions, which are determined by the supports of the beam [1–39]. As it is difficult to obtain an analytical solution to this problem, numerical calculation methods and specialized computer programs are used. They are mostly based on the finite element method [40–42]. At the same time, numerical methods allow to obtain only individual particular solutions. This complicates their use for quick qualitative assessment of structural decisions in order to meet serviceability conditions (1).

Recently, applied calculation methods and various reference books on dynamics were developed to help engineers conduct the necessary calculations without setting up and solving differential equations [43, 44]. However, almost all the literature on vibrations and stability is focused only on assessing the dynamic behavior of already existing structures with given supports without the possibility of their design calculation. Nevertheless, engineers mostly need to determine the required support system with boundary conditions and number of pinned intermediate supports for a given beam to ensure the serviceability conditions (1).

The literature on vibration protection [45–51] mainly considers the following vibration control methods: vibration isolation, additional damping, balancing, etc. In the optimal design of beam structures and topology optimization [52–76], the authors focus on making changes to the beam itself, wherein changing variables must be continuous and smooth, which is difficult for discrete changes in the number and type of supports. It is also true for beam stability calculations.

This paper is aimed at a new approach for a reasonable selection of a support system for a straight multi-span beam that provides the required values of the first natural vibration frequency and first critical force taking into account the temperature.

To achieve this goal, the following tasks were solved;

1) to develop a design calculation approach for a reasonable selection of a support system for a straight multi-span beam that provides its required dynamic behavior (the first natural vibration frequency and the first critical force) taking into account the temperature;
2) to get a single criterion based on support coefficients for the design approach;
3) to propose a method, which makes it possible for an engineer to quickly and reasonably perform a multifactor assessment or design of multi-span beams to achieve the required dynamic behavior;
4) to justify the method by comparative calculations of a pipeline using different approaches.

2. Methods

The equation of free vibrations of a beam takes into account the action of the axial force P (Fig. 1a) and thus looks as follows [2, 3]:

$$EJ_{\min}\frac{\partial^4 y}{\partial x^4} + P\frac{\partial^2 y}{\partial x^2} + m\frac{\partial^2 y}{\partial t^2} = 0. \quad (2)$$

As a function of the deflection $y(x,t)$ for the bending mode of free vibrations at the first natural frequency, the following equation should be considered:

$$y_1(x,t) = A\sin\left(\frac{x\pi}{l}\right)\sin(\omega t). \quad (3)$$

For an unambiguous solution of equation (2), setting four boundary conditions that reflect the beam restraint conditions on supports is necessary.

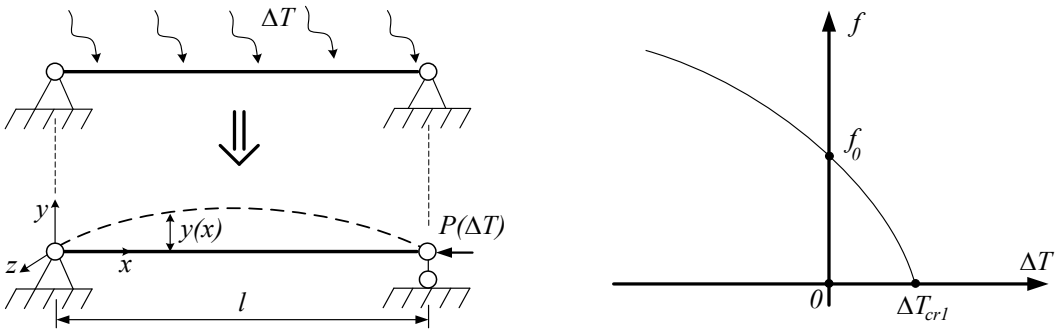

a) b)

Figure 1. Effect of the beam temperature on its dynamic state: a) temperature design diagram; b) frequency-temperature curve.

By substituting the deflection function (3) into equation (2) and temporarily taking $P = 0$ as well as the hinge restraint conditions, the solution for the first natural vibration frequency is calculated as follows:

$$f_1 = \frac{\alpha^2}{2\pi l^2} \cdot \sqrt{\frac{EJ_{\min}}{m}}. \tag{4}$$

When the axial compressive force P acts on the beam, the first natural vibration frequency can be defined by Galef's formula [78–80]:

$$f_{1(P<>0)} = f_{1(P=0)} \cdot \sqrt{1 - \frac{P}{P_{cr1}}}. \tag{5}$$

The axial force P is calculated through the temperature by equation [37]:

$$P = \alpha_t \cdot \Delta T \cdot ES. \tag{6}$$

The buckling force P_{cr1} for the first instability mode is calculated as follows [37]:

$$P_{cr1} = \frac{\pi^2 EJ_{\min}}{\mu^2 \cdot l^2}. \tag{7}$$

A typical curve of the dependence of the first natural vibration frequency on temperature is shown in Fig. 1b. By combining equations (4–7), the condition for the first natural vibration frequency of the beam is calculated, taking into account its temperature and the support restraints:

$$f_1(\Delta T) = \left(\frac{\alpha}{\pi l}\right)^2 \cdot \sqrt{\frac{E}{4m}\left(\pi^2 J_{\min} - \mu^2 \cdot l^2 \cdot \alpha_t \cdot \Delta T \cdot S\right)} \geq [f]. \tag{8}$$

The beam buckling corresponds to the case of its zero natural vibration frequency (Fig. 1b). In equation (8), this corresponds to the equality to zero of the expression in brackets under the root, which makes it possible to use this dependence for assessing stability. For example, the first critical temperature of a beam is defined as follows:

$$\Delta T_{cr1} = \frac{\pi^2 J_{\min}}{\mu^2 \cdot l^2 \cdot \alpha_t \cdot S} \geq [\Delta T]. \tag{9}$$

The obtained analytical dependence (8) ensures the fulfillment of all serviceability conditions (1).

2.1. Structural Design Approach

Let us consider the values of the support coefficients α and μ (Table 1) for three common support systems (Fig. 2) for multi-span beams [43, 44].

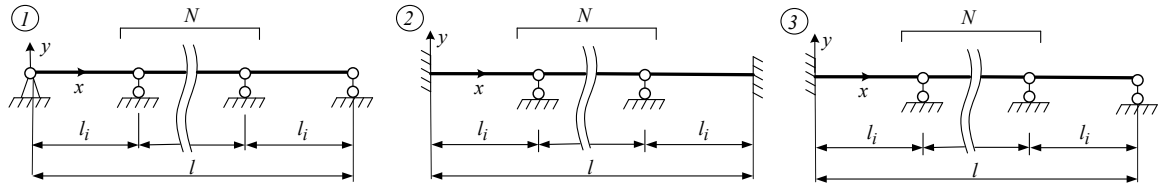

Figure 2. Patterns of beam support systems.

Table 1. Original values of the support coefficients α and μ.

Pattern no.	Coefficient	Number of intermediate supports, *N*										
		0	1	2	3	4	5	6	7	8	9	10
1	α						3.1416					
	μ						1					
2	α	4.730	3.927	3.557	3.393	3.310	3.260	3.230	3.210	3.196	3.186	3.180
	μ	0.5	0.699	0.814	0.879	0.917	0.939	0.954	0.964	0.971	0.977	0.978
3	α	3.927	3.393	3.261	3.210	3.186	3.173	3.164	3.159	3.156	3.153	3.151
	μ	0.7	0.879	0.939	0.964	0.977	0.983	0.988	0.99	0.992	0.994	0.996

If all intermediate supports (Fig. 2) are located equidistant from each other, the length of each span is calculated as follows:

$$l_i = \frac{l}{N+1}. \tag{10}$$

The values of the support coefficients α and μ in Table 1 make it possible to control the dynamic behavior of the beam by selecting their required values.

2.2. Normalization of Support Coefficients

The serviceability condition (8) includes two support coefficients α and μ, but it is necessary to derive a single criterion for the selection method of the appropriate support system. For this purpose, we normalize the initial values of the support coefficients in Table 1 for all patterns (Fig. 2). To do this, it is necessary to divide the initial values of the coefficients (Table 1) by the support coefficients of free beam and take into account equation (10):

$$\alpha' = \left(\frac{\alpha \cdot (N+1)}{\pi}\right)^2, \ \mu' = \left(\frac{N+1}{\mu}\right)^2. \tag{11}$$

Normalized values of the support coefficients α' and μ' for the patterns in Fig. 2 are shown in Table 2.

Table 2. Normalized values of the support coefficients α' and μ'.

Pattern no.	Coefficient	Number of intermediate supports, N										
		0	1	2	3	4	5	6	7	8	9	10
1	α'	1	4	9	16	25	36	49	64	81	100	121
	μ'	1	4	9	16	25	36	49	64	81	100	121
2	α'	2.267	6.250	11.54	18.66	27.75	38.77	51.80	66.82	83.83	102.8	124.0
	μ'	4	8.187	13.58	20.71	29.73	40.83	53.84	68.87	85.91	104.8	126.5
3	α'	1.563	4,666	9.697	16.71	25.72	36.72	49.70	64.71	81.75	100.7	121.7
	μ'	2.041	5.177	10.21	17.22	26.19	37.26	50.20	65.30	82.31	101.2	122.0

Now, the new support coefficients α' and μ' can be compared as both are in the numerator and already take into account the number of intermediate supports.

2.3. Single Criterion for the Structural Design Approach

The analysis of the data from Table 2 shows that the new values of the support coefficients are close to each other for each support pattern, and at $N > 2$ the difference in their values is within 2–3 %.

Moreover, with the increase in N, this difference rapidly decreases because the initial support coefficients (Table 1) rapidly converge to the characteristic constants:

$$\alpha = \pi,\ \mu = 1 \text{ at } N \to \infty. \tag{12}$$

This allows us to introduce a single criterion for the selection of the support system:

$$\alpha_{\min} = \alpha' = \mu'. \tag{13}$$

If condition (13) is substituted in equation (8), then we get a square equation relative to the sought coefficient $\alpha_{\min}$:

$$-\alpha_{\min}^2 \cdot \pi^2 EJ_{\min} + \alpha_{\min} \cdot l^2 \alpha_t \Delta TES + 4l^4 m\left[f\right]^2 = 0. \tag{14}$$

The solution of quadratic equation (14) with the required root sign is as follows:

$$\alpha_{\min} = C_{\Delta T} + \sqrt{C_{\Delta T}^2 + \frac{4m\left[f_1\right]^2 l^4}{\pi^2 EJ_{\min}}}, \tag{15}$$

where $C_{\Delta T}$ is the temperature effect coefficient:

$$C_{\Delta T} = \frac{\alpha_t \cdot \Delta T \cdot Sl^2}{2\pi^2 J_{\min}}. \tag{16}$$

If the temperature effect is irrelevant, we assume $\Delta T = 0,$ and the condition (15) is simplified:

$$\alpha_{\min} = \frac{2l^2\left[f_1\right]}{\pi}\sqrt{\frac{m}{EJ_{\min}}}. \tag{17}$$

To ensure all operability conditions (1), it is necessary to select from Table 2 such pattern and number of intermediate supports for which values of support coefficients α' and γ' are equal or more than the calculated value:

$$\min\left(\alpha',\ \mu'\right) \ge \alpha_{\min} = C_{\Delta T} + \sqrt{C_{\Delta T}^2 + \frac{4m\left[f_1\right]^2 l^4}{\pi^2 EJ_{\min}}}. \tag{18}$$

The selected support system for a beam with the corresponding values of the coefficients α' and μ' ensure the simultaneous fulfillment of both serviceability conditions (1), which can be verified by checking the first vibration frequency and the first critical force or temperature using the new dependencies:

$$f_1\left(\Delta T\right) = \frac{\alpha'}{2l^2}\cdot\sqrt{\frac{E}{m}\left(\pi^2 J_{\min} - \frac{1}{\mu'}\cdot l^2 \cdot \alpha_t \cdot \Delta T \cdot S\right)} \ge \left[f\right]; \tag{19}$$

$$P_{cr1} = \frac{\mu' E}{l^2}\left(\pi^2 J_{\min} - \frac{4l^4\left[f\right]^2 m}{\alpha'^2 E}\right) \ge \left[P\right]; \tag{20}$$

$$\Delta T_{cr1} = \frac{\mu'}{l^2 \cdot \alpha_t \cdot S}\left(\pi^2 J_{\min} - \frac{4l^4\left[f\right]^2 m}{\alpha'^2 E}\right) \ge \left[\Delta T\right]. \tag{21}$$

If we take the condition $\left[f\right] = 0$ in (19–21), the form of these equations is almost identical to their original version (4, 7, 9).

2.4. Algorithm for a Reasonable Selection of Support System for a Beam

The proposed design approach for normalizing the values of the support coefficients allows implementing the method for a reasonable selection of the support system for a beam to ensure the serviceability conditions (1). This method consists of the following steps:

1. Preparation of a set of possible patterns of beam support systems (as in Fig. 2).
2. Determination of the support coefficients α and μ for each pattern from the selected set based on the reference literature or by calculation.
3. Normalization of the values of the support coefficients α and μ for each pattern so that they take close values: $\alpha' \approx \mu'$.
4. Calculation of the minimum required value of the support coefficient $\alpha_{\min}$ (15).
5. Selection of a pattern from the obtained set so that the following condition is satisfied:

$$\min\left(\alpha',\ \mu'\right) \geq \alpha_{\min}.$$

Let us consider an example of calculating an extended structure by the developed method.

3. Results and Discussions

Consider a straight pipeline with a circular cross-section and the following characteristics: length l = 1.5 m, outer diameter D = 15 mm, wall thickness t = 1 mm, material: aluminum alloy E = 7.1 × 10^5 MPa, density ρ = 2,770 kg/m^3, and CTE α_t = 2.3 × 10^{-5}. Initially, the beam is rigidly fixed at both ends without intermediate supports. The objective is to select a support system that will provide the first natural vibration frequency $\left[f_1\right]$ = 250 Hz at a temperature ΔT = 90 °C. We perform the calculation by the developed method and verify the obtained results by the finite element method using the ANSYS software.

3.1. Analytical Solution by the Developed Method

First, let us check the current dynamic parameters of the beam under the initial restraint conditions. According to Table 2, these correspond to the support coefficients α' = 2.267 and μ' = 4. By dependences (19–21) at ΔT = 0 °C and $\left[f_1\right]$ = 0 Hz, we obtain the following initial dynamic characteristics of the beam:

$$f_1 = 39.76 \text{ Hz}, \quad \Delta T_{cr} = 18.79^{\circ}\text{C}. \tag{22}$$

Instability is sure to arise when heating the beam to T_{cr1} = 18.79 °C, which prevents us from using such initial restraint conditions. We cannot use initial restraint conditions at ΔT = 0 °C as, in this case, the first natural vibration frequency is only f_1 = 39.76 Hz. So it becomes necessary to select another support system. For this, according to the proposed method, it is necessary to calculate the required support coefficient according to equation (15):

$$\alpha_{\min} = 26.76. \tag{23}$$

From Table 2, we select a support system with $\min\left(\alpha',\ \mu'\right) > 26.76;$ for example, Pattern 2 with $N = 4,$ for which the support coefficients are equal:

$$\alpha' = 27.75;\ \mu' = 29.73. \tag{24}$$

Let us check the actual values of the first natural vibration frequency and the critical temperature of the beam using the equations (19) and (21):

$$f_2 = 290.16 \text{ Hz};\ \Delta T_{cr2} = 102.78^{\circ}\text{C}, \tag{25}$$

which fulfill the serviceability conditions of this task ($\left[f_1\right]$ = 250 Hz at ΔT = 90 °C).

In Fig. 3, the two curves show the dependences of the first vibration frequency on temperature for both variants (22, 25).

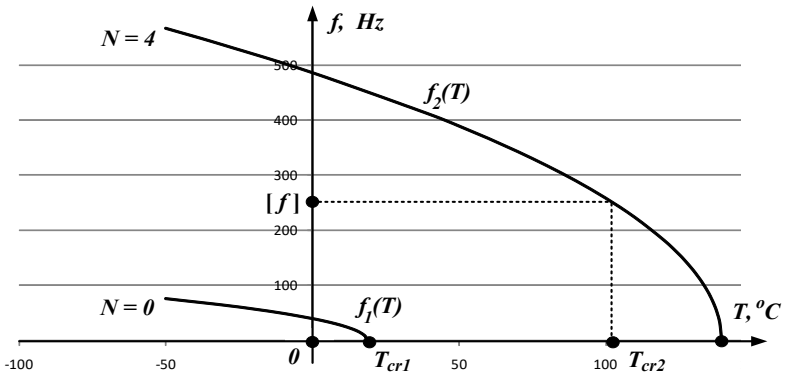

Figure 3. Dependence of the first natural vibration frequency on temperature.

In Fig. 3, the curve $f_2(N)$ for $N = 4$ clearly shows the rise of the first natural vibration frequency of the structure in the entire temperature range under consideration.

3.2. Numerical Solution of the Problem

Let us verify the obtained results using the finite element method (FEM) for the beam and shell models of the straight pipeline. The beam model has 1500 Beam189 finite elements, and the shell model has 14328 Shell281 finite elements. Fig. 4 shows some typical numerical calculation results for the shell model.

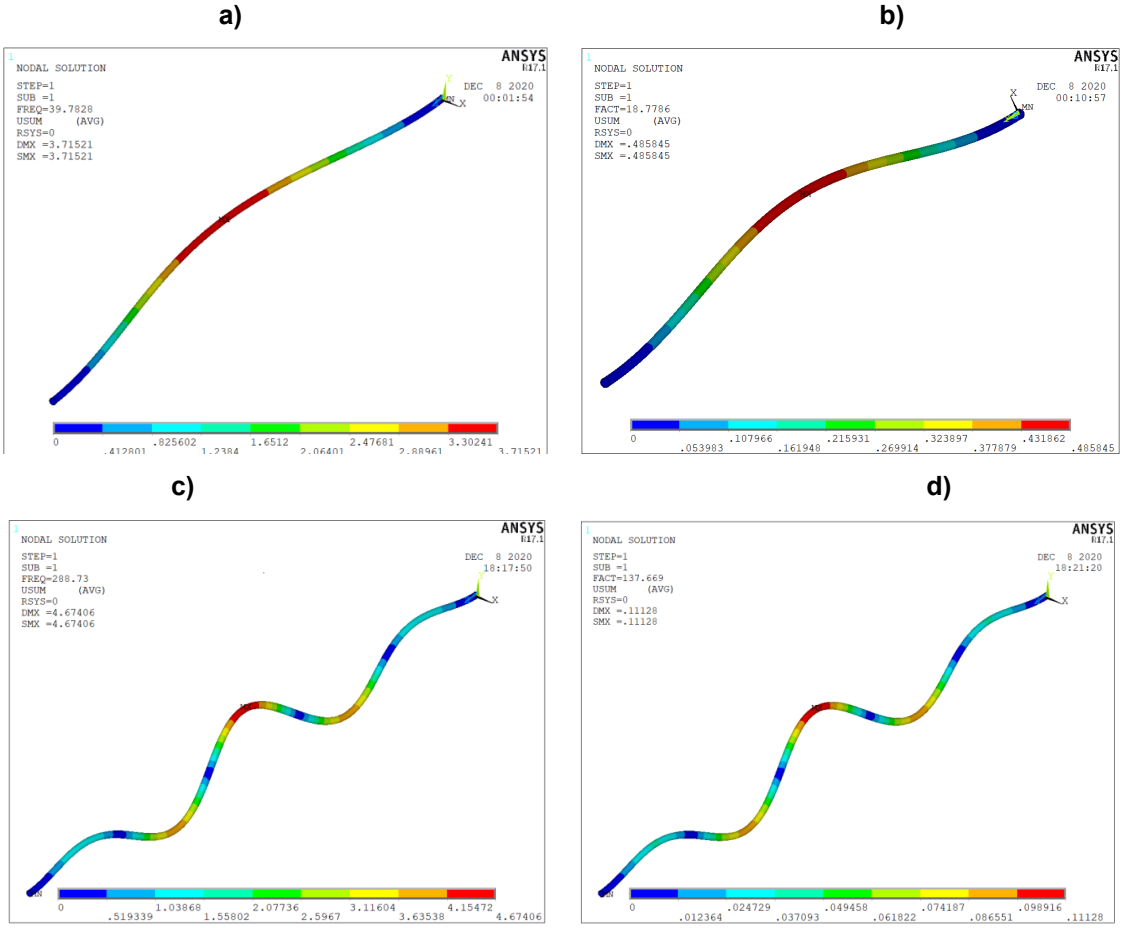

Figure 4. Results of the numerical calculation: a) first vibration mode at N = 0 and ΔT = 0˚C; b) instability at T_{cr1}, N = *0* and [*f*] = 0 Hz; c) first vibration mode at N = 4 and ΔT = 90˚C*;* d) instability at T_{cr2}, N = 4 and [*f*] = 0 Hz.

The numerical calculation results are summarized in Table 3.

Table 3. Comparison of the calculation results.

	f_1, Hz at ΔT = 0 ˚C	T_{cr1}, ˚C at [f] = 0 Hz	f_1, Hz at ΔT = 90˚C	T_{cr2}, ˚C at [f] = 0 Hz	T_{cr2}, ˚C at [f] = 250 Hz
	N = 0			N = 4	
Developed method	39.76	18.79	290.16	139.62	102.78
FEM, Beam4	39.75	18.78	290.39	139.93	102.91
Deviation, %	0.00961	0.00786	0.0812	0.219	0.119
FEM, Shell281	39.78	18.77	288.73	137.67	100.23
Deviation, %	0.0532	0.0353	0.494	1.40	1.52

The comparison of the calculation results obtained by the proposed method with numerical solutions by FEM shows that the maximum difference is 1.52 %.

Comparison of the proposed method with the papers of other authors shows a complete coincidence for cases when the solution is based on the differential equation (2) and the formula (5), for example, in [78–83]. This approach is correct for the Euler–Bernoulli beam theory, which has some limitations when used. For example, there are some conditions of the beam size ratios [84, 85]. Formula (5) also has its limitations, mostly depending on the ratio [86]:

$$\frac{Pl^2}{EJ_{\min}}. \tag{26}$$

In later works, other authors have developed refined solutions based on more complex dependencies [86–90]. However, the difference in results is less than 5 %, which is acceptable for beam theory, which usually implies a preliminary design calculation.

4. Conclusions

1. The paper developed a design calculation approach for a reasonable selection of a support system for a straight multi-span beam that provides its required dynamic behavior. A new method was developed to help engineers reasonably select the support system for straight multi-span beams, which ensures their serviceability under given requirements for the minimum first natural vibration frequency and the first critical force or temperature.
2. The proposed method has a simple analytical formulation, which also makes it possible for an engineer to quickly and reasonably perform a multifactor assessment or design of any multi-span beam to achieve the required dynamic behavior.
3. The method was justified by the comparative calculations of a pipeline by using the beam and shell models, which showed good convergence for all monitored parameters. Comparison of the method with the works of other authors also showed good convergence in all controlled parameters.
4. The proposed method is to be developed further for the plane multi-support beams consisting of straight and curved sections in order to ensure their dynamic, stressed, and deformed state.

References

1. Abramovich, H., Elishakoff, I. Application of the Krein's Method for Determination of Natural Frequencies of Periodically Supported Beam Based on Simplified Bresse–Timoshenko Equations. Acta Mechanica. 1987. 66(1–4). Pp. 39–59. DOI: 10.1007/BF01184284
2. Banakh, L.Y. Vibrations of Mechanical Systems with Regular Structure. Berlin: Springer, 2010. 262 p.
3. Benaroya, H., Nagurka, M., Han, S. Mechanical Vibration. London: CRC Press, 2017. 602 p.
4. Billing, J.R. Estimation of the natural frequencies of continuous multi-span bridges. Ontario: Ministry of transportation and communication, 1979. 20 p.
5. Bottega, W.J. Engineering Vibrations. New York: CRC Press, 2006. 750 p.
6. Cai, C.W., Cheung, Y.K., Chan, H.C. Transverse vibration analysis of plane trusses by analytical method. Journal of Sound and Vibration. 1989. 133(1). Pp. 139–150. DOI: 10.1016/0022-460X(89)90988-7
7. Chonan, S., Sasaki, M. Vibration and stability of elastically supported multi-span beams under conservative and non-conservative loads. Journal of Sound and Vibration. 1985. 99(4). Pp. 545–556. DOI: 10.1016/0022-460X(85)90539-5
8. Chuang, C.H., Hou, G.J. Eigenvalue sensitivity analysis of planar frames with variable joint and support locations. AIAA Journal. 1992. 30(8). Pp. 2138–2147. DOI: 10.2514/3.11192

9. Clough, R.E. Dynamics of Structures. 3th ed. New York: McGraw-Hill College, 1995. 752 p.
10. Geradin, M., Rixen, D.J. Mechanical Vibrations. London: John Wiley & Sons, 2015. 617 p.
11. Hagedorn, P. Vibrations and waves in continuous mechanical systems. New Jersey: John Wiley. & Sons, 2007. 388 p.
12. Den Hartog, J.P. Mechanical Vibrations. New York: Dover Publications. 1985. 449 p.
13. Inman, D.J. Engineering Vibration. New Jersey: Pearson Education, 2014. 720 p.
14. Kelly, S.G. Advanced Vibration Analysis. Boca Raton: CRC/Taylor & Francis, 2007. 637 p.
15. Lee, H.P., Ng, T.Y. In-Plane Vibration of Planar Frame Structures. Journal of Sound and Vibration. 1994. 172(3). Pp. 420–427. DOI: 10.1006/jsvi.1994.1185
16. Lin, H., Chang, S.C. Free vibration analysis of multi-span beams with intermediate flexible constraints. Journal of Sound and Vibration. 2005. 281(1–2). Pp. 155–169. DOI: 10.1016/j.jsv.2004.01.010
17. Lin, H., Tsai, Y. Free vibration analysis of a uniform multi-span beam carrying multiple spring-mass systems. Journal of Sound and Vibration. 2007. 302(3). Pp. 442–456. DOI: 10.1016/j.jsv.2006.06.080
18. Lin, Y.K. Free Vibration of a Continuous Beam on Elastic Supports. International Journal of Mechanical Sciences. 1962. 4(5). Pp. 409–423. DOI: 10.1016/S0020-7403(62)80027-7
19. Liu, H., Nguyen, H., Xiang, Y. Vibration analysis of a multi-span continuous beam with cracks. Applied Mechanics and Materials. 2012. 256–259. Pp. 964–972. DOI: 10.4028/www.scientific.net/AMM.256-259.964
20. Luo, J., Zhu, S., Zhai, W. Exact closed-form solution for free vibration of Euler–Bernoulli and Timoshenko beams with intermediate elastic supports. International Journal of Mechanical Sciences. 2022. 213. Article no. 106842. DOI: 10.1016/j.ijmecsci.2021.106842
21. Maurizi, M.J., Bambill, D.V., Bellés, P.M., De Rosa, M.A., Grossi, R.O., Marcelo, A.C., Zannier, L. Free vibrations of Bernoulli–Euler beams with intermediate elastic support: A concise thematic recension. Journal of Sound and Vibration. 2005. 281(3–5). Pp. 1238–1239. DOI: 10.1016/j.jsv.2004.06.014
22. Mead, D.J. Free wave propagation in periodically supported, infinite beams. Journal of Sound and Vibration. 1970. 11(2). Pp. 181–197. DOI: 10.1016/S0022-460X(70)80062-1
23. Miles, J. Vibration of beams on many supports. ASCE Journal of Engineering Mechanics. 1956. 82. Pp. 1–9.
24. Mills-Curran, W.C., Lust, R.V., Schmit, L.A. Approximations method for space frame synthesis. AIAA Journal. 1983. 21(11). Pp. 1571–1580. DOI: 10.2514/3.60154
25. Naguleswaran, S. Transverse vibration of an Euler–Bernoulli uniform beam on up to five resilient supports including ends. Journal of Sound and Vibration. 2003. 261(2). Pp. 372–384. DOI: 10.1016/S0022-460X(02)01238-5
26. Sen Gupta, G. Natural flexural waves and the normal modes of periodically-supported beams and plates. Journal of Sound and Vibration. 1970. 13(1). Pp. 89–101. DOI: 10.1016/S0022-460X(70)80082-7
27. Wang, D., Friswell, M.I., Lei, Y. Maximizing the natural frequency of a beam with an intermediate elastic support. Journal of Sound and Vibration. 2006. 291(3–5). Pp. 1229–1238. DOI: 10.1016/j.jsv.2005.06.028
28. Wang, R. Vibration of multi-span Timoshenko beams to a moving force. Journal of Sound and Vibration. 1997. 207(5). Pp. 731–742. DOI: 10.1006/jsvi.1997.1188
29. West, H.H., Mafi, M. Eigenvalues for Beam-Columns on Elastic Supports. Journal of Structural Engineering (United States). 1984. 110 (6). Pp. 1305–1320. DOI: 10.1061/(ASCE)0733-9445(1984)110:6(1305)
30. Zhao, Z., Wen, S., Li, F., Zhang, C. Free vibration analysis of multi-span Timoshenko beams using the assumed mode method. Archive of Applied Mechanics. 2018. 88(7). Pp. 1213–1228. DOI: 10.1007/s00419-018-1368-8
31. Zhu, L., Elishakoff, I., Lin, Y.K. Free and forced vibrations of periodic multispan beams. Shock and Vibration. 1994. 1(3). Pp. 217–232. DOI: 10.3233/SAV-1994-1302
32. Bayo, E., Loureiro, A. An efficient and direct method for buckling analysis of steel frame structures. Journal of Constructional Steel Research. 2001. 57(12). Pp. 1321–1336. DOI: 10.1016/S0143-974X(01)00040-2
33. Kobelev, V. Closed-form solution for optimization of buckling column. Mechanics Based Design of Structures and Machines. 2021. 51(10). Pp. 5596–5635. DOI: 10.1080/15397734.2021.2008259
34. Liu, Z., Hu, H., Huang, C. Derivative of Buckling Load with Respect to Support Locations. Journal of Engineering Mechanics. 2000. 126(6). Pp. 559–564. DOI: 10.1061/(ASCE)0733-9399(2000)126:6(559)
35. Şakar, G., Öztürk, H., Sabuncu, M. Dynamic stability of multi-span frames subjected to periodic loading. Journal of Constructional Steel Research. 2012. 70. Pp. 65–70. DOI: 10.1016/j.jcsr.2011.10.009
36. Thomsen, J.J. Vibrations and Stability. Advanced Theory, Analysis, and Tools. 2nd ed. London: Springer, 2003. 420 p. DOI: 10.1007/978-3-662-10793-5
37. Timoshenko, S.P., Gere, J.M. Theory of Elastic Stability, 2nd ed. New York: Dover Publications. 2009. 560 p.
38. Trahair, N.S. Buckling analysis design of steel frames. Journal of Constructional Steel Research. 2009. 65(7). Pp. 1459–1463. DOI: 10.1016/j.jcsr.2009.03.012
39. West, H.H., Mafi, M. Eigenvalues for Beam-Columns on Elastic Supports. Journal of Structural Engineering (United States). 1984. 110(6). Pp. 1305–1320. DOI: 10.1061/(ASCE)0733-9445(1984)110:6(1305)
40. Shrikhande, M. Finite Element Method and Computational Structural Dynamic. New Delhi: PHI Learning Private Limited, 2008. 234 p.
41. Moaveni, S. Finite Element Analysis: Theory and Application with ANSYS. 4th ed. New York: Pearson Education, 2015. 929 p.
42. Stolarski, T. Engineering Analysis with ANSYS Software. London: Butterworth-Heinemann, 2018. 553 p.
43. Blevins, R.D. Formulas for Dynamics, Acoustics and Vibration. London: John Wiley & Sons, 2016. 464 p.
44. Birger, I.A., Panovko, Y.G. Strength, stability, fluctuations. Moscow: Mashinostroenie, 1968. 567 p.
45. Baz, A.M. Active and Passive Vibration Damping. New York: John Wiley & Sons. 2019. 737 p.
46. Inman, D.J. Vibration with Control. Berlin, 2017. 426 p.
47. Barez, F. Dynamic Systems Vibration and Control. San Jose: San Jose State University, 2018. 283 p.
48. Genta, G. Vibration Dynamics and Control. New York: Springer New York, 2009. DOI: 10.1007/978-0-387-79580-5

49. Nashif A.D., Jones D.I. Vibration Damping. New York: John Wiley & Sons, 1985. 480 p.
50. Thorby, D. Structural Dynamics and Vibration in Practice. Boston: Butterworth-Heinemann, 2008. 419 p. DOI: 10.1016/B978-0-7506-8002-8.X0001-6
51. Yao, P.-F. Modeling and Control in Vibrational and Structural Dynamics: A Differential Geometrical Approach. Boca Raton: CRC Press, 2011. 417 p. DOI: 10.1201/b11042
52. Albarracín, C.M., Zannier, L., Grossi, R.O. Some observations in the dynamics of beams with intermediate supports. Journal of Sound and Vibration. 2004. 271(1–2). Pp. 475–480. DOI: 10.1016/S0022-460X(03)00631-X
53. Andreassen, E., Ferrari, F., Sigmund, O., Diaz, A. R. Frequency response as a surrogate eigenvalue problem in topology optimization. International Journal for Numerical Methods in Engineering. 2018. 113(8). Pp. 1214–1229. DOI: 10.1002/nme.5563
54. Aydin, E., Dutkiewicz, M., Öztürk, B., Sonmez, M. Optimization of elastic spring supports for cantilever beams. Structural and Multidisciplinary Optimization. 2020. 62(1). Pp. 55–81. DOI: 10.1007/s00158-019-02469-3
55. Bojczuk, D., Rebosz-Kurdek, A. Optimal design of bar structures with their supports in problems of stability and free vibrations. Journal of Theoretical and Applied Mechanics (Poland). 2014. 52(2). Pp. 533–546.
56. Dems, K., Turant, J. Sensitivity Analysis and Optimal Design of Elastic Hinges and Supports in Beam and Frame Structures. Mechanics of Structures and Machines. 1997. 25(4). Pp. 417–443. DOI: 10.1080/08905459708905297
57. Garstecki, A., Mróz, Z. Optimal Design of Supports of Elastic Structures Subjected to Loads and Initial Distortions. Mechanics of Structures and Machines. 1987. 15(1). Pp. 47–68. DOI: 10.1080/08905458708905108
58. Grandhi, R.V. Structural optimization with frequency constraints. Proceedings of 4th Symposium on Multidisciplinary Analysis and Optimization. Cleveland, 1992. AIAA-92-4813. DOI: 10.2514/6.1992-4813
59. Kennedy, G.J., Fu, Y. Topology Optimization with Natural Frequency Constraints using a Quadratic Approximation of a Spectral Aggregate. Proceedings of AIAA Science and Technology Forum and Exposition. San Diego: American Institute of Aeronautics and Astronautics, 2022. DOI: 10.2514/6.2022-2244
60. Kesson, B., Olhoff, N. Minimum stiffness of optimally located supports for maximum value of beam eigenfrequencies. Journal of Sound and Vibration. 1988. 120(3). Pp. 457–463. DOI: 10.1016/S0022-460X(88)80218-9
61. Kobelev, V. Some exact analytical solutions in structural optimization. Mechanics based design of structures and machines. 2017. 45 (1). Pp. 43–61. DOI: 10.1080/15397734.2016.1143374
62. Leader, M.K., Chin, T.W., Kennedy, G.J. High-Resolution Topology Optimization with Stress and Natural Frequency Constraints. AIAA Journal. 2019. 57(8). Pp. 3562–3578. DOI: 10.2514/1.J057777
63. Mróz, Z., Rozvany, G.I.N. Optimal design of structures with variable support conditions. Journal of Optimization Theory and Applications. 1975. 15 (1). Pp. 85–101. DOI: 10.1007/BF00933023
64. Olhoff, N. Optimal design with respect to structural eigenvalues. Proceedings of XVth Int. IUTAM Cong. Theoretical and Applied Mechanics. Amsterdam: North-Holland, 1980. Pp. 133–149.
65. Olhoff, N., Åkesson, B. Minimum stiffness of optimally located supports for maximum value of column buckling loads. Structural Optimization. 1991. 3(3). Pp. 163–175. DOI: 10.1007/BF01743073
66. Rao, S.S. Engineering Optimization: Theory and Practice. New York: John Wiley & Sons, 2009. 848 p. DOI: 10.1002/9780470549124
67. Rozvany, G.I.N., Mroz, Z. Column Design: Optimization of Support Conditions and Segmentation. Journal of Structural Mechanics. 1977. 5(3). Pp. 279–290. DOI: 10.1080/03601217708907315
68. Sergeyev O.A., Kiselev V.G., Sergeyeva S.A. Optimal design of 3d frame structures taking into account the stress and multiple natural frequency constraints. Magazine of Civil Engineering. 2016. 61(1). Pp. 74–81. DOI: 10.5862/MCE.61.7
69. Son, J.H., Kwak, B.M. Optimization of Boundary Conditions for Maximum Fundamental Frequency of Vibrating Structures. AIAA Journal. 1993. 31(12). Pp. 2351–2357. DOI: 10.2514/3.11935
70. Studziński, R., Pozorski, Z., Błaszczuk, J. Optimal Support System of Sandwich P|anels. Journal of Engineering Mechanics. 2015. 141(3). DOI: 10.1061/(ASCE)EM.1943-7889.0000857
71. Vanderplaats, G.N., Salajegheh, E. An efficient approximation technique for frequency constraints in frame optimization. International Journal for Numerical Methods in Engineering. 1988. 26(5). Pp. 1057–1069. DOI: 10.1002/nme.1620260505
72. Wang, B.P., Chen, J.L. Application of genetic algorithm for the support location optimization of beams. Computers and Structures. 1996. 58(4). Pp. 797–800. DOI: 10.1016/0045-7949(95)00184-I
73. Wang, C.Y. Minimum stiffness of an internal elastic support to maximize the fundamental frequency of a vibrating beam. Journal of Sound and Vibration. 2003. 259(1). Pp. 229–232. DOI: 10.1006/jsvi.2002.5100
74. Wang, D. Optimal Design of an Intermediate Support for a Beam with Elastically Restrained Boundaries. Journal of Vibration and Acoustics. Transactions of the ASME. 2011. 133(3). Article no. 031014. DOI: 10.1115/1.4003204
75. Won, K., Park, Y Optimal support positions for a structure to maximize its fundamental natural frequency. Journal of Sound and Vibration. 1998. 213(5). Pp. 801–812. DOI: 10.1006/jsvi.1997.1493
76. Zhu, J., Zhang, W. Maximization of structural natural frequency with optimal support layout. Structural and Multidisciplinary Optimization. 2006. 31(6). Pp. 462–469. DOI: 10.1007/s00158-005-0593-2
77. Amba-Rao, C.L. Effect of End Conditions on the Lateral Frequencies of Uniform Straight Columns. The Journal of the Acoustical Society of America. 1967. 42. Pp. 900–901. DOI: 10.1121/1.1910667
78. Galef, A.E. Bending Frequencies of Compressed Beams. Journal of the Acoustical Society of America. 1968. 44(2). P. 643. DOI: 10.1121/1.1911144
79. Bokaian, A. Natural frequencies of beams under compressive axial loads. Journal of Sound and Vibration. 1988. 126(1). Pp. 49–65. DOI: 10.1016/0022-460X(88)90397-5
80. Bokaian, A. Author's reply. Journal of Sound and Vibration. 1989. 131(2). P. 351. DOI: 10.1016/0022-460X(89)90499-9
81. Bokaian, A. Natural frequencies of beams under tensile axial loads. Journal of Sound and Vibration. 1990. 142(3). Pp. 481–498. DOI: 10.1016/0022-460X(90)90663-K
82. Pilkington, D.F, Carr, J.B. Vibration of Beams Subjected to End and Axially Distributed Loading. Journal of Mechanical Engineering Science. 1970. 12(1). Pp. 70–72. DOI: 10.1243/JMES_JOUR_1970_012_012_02

83. Saiidi, M., Douglas, B., Feng, S. Prestress Force Effect on Vibration Frequency of Concrete Bridges. Journal of Structural Engineering (United States). 1994. 120(7). Pp. 2233–2241. DOI: 10.1061/(ASCE)0733-9445(1994)120:7(2233)
84. Kudryavtsev, I.V., Brungardt, M.V., Kudryavtseva, Y.M., Kolotov, A.V., Rabetskaya, O.I. Boundary revision of a beam model for a thin-walled waveguide at bending vibration. Paper presented at the Journal of Physics: Conference Series. 2021. 1889(2). Article no. 022109. DOI: 10.1088/1742-6596/1889/2/022109
85. Mityaev, A.E., Kudryavtsev, I.V., Khomutov, M.P., Brungardt, M.V., Rabetskaya, O.I. Mutual influence of the supports stiffness and the first natural frequency at bending vibrations of a spring-hinged beam. IOP Conference Series: Materials Science and Engineering. 2021. 1155. Article no. 012101. DOI: 10.1088/1757-899X/1155/1/012101
86. Seshu, P., Dhuri, K.D. Corrected Formulas for Natural Frequencies of Cantilever Beams under Uniform Axial Tension. AIAA Journal. 2007. 45(6). Pp. 1435–1438. DOI: 10.2514/1.28937
87. Han, S.M., Benaroya, H., Wei, T. Dynamics of transversely vibrating beams using four engineering theories. Journal of Sound and Vibration. 1999. 225(5). Pp. 935–988. DOI: 10.1006/jsvi.1999.2257
88. Stephen, N.G. Beam vibration under compressive axial load-upper and lower bound approximation. Journal of Sound and Vibration. 1989. 131(2). Pp. 345–350. DOI: 10.1016/0022-460X(89)90498-7
89. Valle, J., Fernández, D., Madrenas, J. Closed-form equation for natural frequencies of beams under full range of axial loads modeled with a spring-mass system. International Journal of Mechanical Sciences. 2019. 153–154, Pp. 380–390. DOI: 10.1016/j.ijmecsci.2019.02.014
90. Williams, F.W., Banerjee, J.R. Flexural vibration of axially loaded beams with linear or parabolic taper. Journal of Sound and Vibration. 1985. 99(1). Pp. 121–138. DOI: 10.1016/0022-460X(85)90449-3

Information about the authors:

Ilya Kudryavtsev,
ORCID: https://orcid.org/0000-0001-7933-3710
E-mail: ikudryavcev@sfu-kras.ru

Viktor Ivanov,
E-mail: pi-prm@mail.ru

Olga Rabetskaya,
E-mail: olga_rabez@mail.ru

Alexander Mityaev,
E-mail: aemit@mail.ru

Received: 19.09.2021. Approved after reviewing: 09.04.2024. Accepted: 10.05.2024.